The Role of the Nano-Environmental Interface in ZnO and CeO_2 Nanoparticle Ecotoxicology

Submitted by

Nicholas David Leyland Walker

To the University of Exeter as a thesis for the degree of Doctor of Philosophy in Biological Sciences in June 2012.

Declaration:

This thesis is available for Library use on the understanding that it is copyright material and that no quotation from the thesis may be published without proper acknowledgement.

I certify that all material in this thesis which is not my own work has been identified and that no material has previously been submitted and approved for the award of a degree by this or any other University.

Signature: ....

“*Anyone who doesn’t take truth seriously in small matters cannot be trusted in large ones either”*

Albert Einstein

Abstract

An increase in nanotechnology has seen an associated rise in nanoparticles released into the environment. Their potential toxicity and exposure to humans and the environment, the field of nanoecotoxicology, is not yet well understood. The interactions at the nanoparticle surface will play a fundamental role in the nanoparticle behaviour once released into the environment. This study aims to characterise the particle surface interaction, determining key parameters influential in the nanoparticle fate.

Evanescent Wave Cavity Ring Down Spectroscopy techniques have been applied to study molecular interactions at the silica-water charged interface. The adsorption of the electronic spectrum of Crystal Violet has demonstrated the formation of a monolayer with different binding site orientation at the interface. The binding affinity for the chromophore was calculated as 29.15 ± 0.02 $\mathrm{kJmol^{-1}}$ at pH 9 and this was compared with other interface structures involving both inorganic and organic components. The study of the model interface was extended to the properties of CeO_2 nanoparticles, where the surface charge density was determined to be 1.6 ± 0.3 e^{-} nm^{-2}.The nanoparticle surface charge controls the suspension stability which was measured for CeO_2 nanoparticles giving a stability half-life of 330 ± 60 hours in pure water, and 3.6 ± 0.6 hours in ISOFish water.

Studies were extended to the toxicity of ZnO nanoparticles. An assay was developed to quantify the photo-electron production for nanoparticles exposed to UV light both in deionised water and soil suspensions with a photo-radical production yield of 19 ± 2 % and an electron production of 709 $e^{-}s^{-1}np^{-1}$ for a 100 $\mathrm{mgL^{-1}}$ suspension. The species-specific photo-radical assay was subsequently used to determine the rate of ZnO nanoparticle dissolution in water and soil suspensions. Comparable dissolution rates in complex cell growth media were also measured, detecting total zinc by Inductively Coupled Plasma Atomic Emission Spectroscopy, with comparable dissolution rates derived.

Acknowledgments

I would firstly like to thank my supervisor Professor Andrew Shaw for his guidance and support throughout my PhD. I would also like to thank Dr. Rouslan Olkhov for his constant help and knowledge, Dr. Bernard van Vuuren for ‘that phone call’ and keeping me entertained throughout the course of my PhD, as well as Tom, Lindsey, Jon, Rob and Max, for making the lab an enjoyable place to work.

I would like to thank the PROSPEcT project and the EPSRC for funding my research. Thanks also to the staff at the National Physics Laboratory, and Dr. Claus Svendsen for providing the soil samples for the experiments. Special thanks to Dr. Nicola Rogers and Dr. Maxine McCall at CSIRO, for making me feel so welcome in Australia.

Finally, I would like to thank my parents, Sarah and close family for their endless support, and a special mention to Sammy and Winnie for keeping me sane through tough times.

Table of Contents

Table of Figures

Table of Tables

Chapter 1
Introduction

Nanotechnology has progressed significantly in the last two decades with novel applications in many areas of society. Lagging behind the advance of nanotechnology is the understanding of the harmful effects nanomaterials may have on human health and the environment; the field of nanoecotoxicology. In particular, the mechanisms of toxicity and how nanoparticles interact with their local environment are poorly characterised and understood. Improving understanding must start with a detailed knowledge of the nano-environmental interface and its physical chemistry.

1.1 Nanotechnology

Nobel-prize winning physicist Richard Feynman proposed in his lecture entitled "*There's plenty of room at the bottom*" (*1*) the idea of manufacturing on a nano scale and the possibility in the future to manipulate atoms and molecules. Nanotechnology as a concept was introduced in 1974 by Norio Taniguchi (*2*), proposing engineering and product design at a subatomic molecular level, using nanostructured devices. A nanomaterial is defined as a structure that possesses at least one dimension within the nanoscale range, conventionally less than 100 nm (*3*), and may possess only one nano-dimension in the form of a thin film, two nano-dimensions such as carbon nanotubes, Figure 1.1 (A) or three nano-dimensions forming nanoparticles, Figure 1.1 (B). To put a nanoparticle in size context, a human hair is approximately 80,000 nm and a red blood cell is 7000 nm in diameter (*4*).

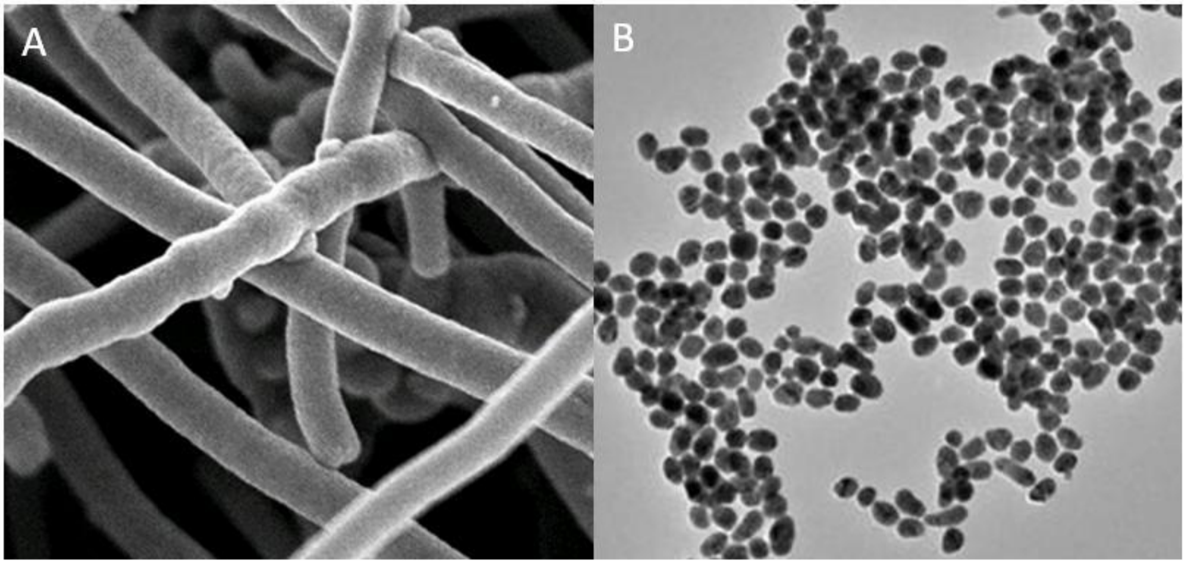

Figure 1.1 TEM images of different nanostructures, A - Carbon nanotubes, modified from the Materials Research Institute (*5*), and B – Gold Nanoparticles with a mean diameter of 40 nm, modified from Owens *et al.* (6)

The primary motivation for nanotechnology is harnessing the unique properties which nano scale particles possess, making them very different to their bulk counterparts. The most significant property is their large surface area to volume ratio, generating a high percentage of surface atoms or molecules (*7*). This enhances particle adsorption capacity and catalytic activity, generating greater environmental availability, with larger areas of the nanoparticle directly exposed (*8*). The nanoparticle size also enables electro-optical phenomenon to be observed (*7*) such as the localised surface plasmon resonance (LSPR) effects of particles (*9*), typically seen in Ag and Au nanoparticles. This unique property is controlled by the shape and size of the particle, with maximum excitation or scatter occurring at different wavelengths. Large scattering cross-sections of the particle plasmons generate strong extinction in the green region of the spectrum which causes the dark red colour observed in Au nanoparticles in a colloid compared to the bulk (*10*). The ability to control and tune these metal nanoparticle optical properties has seen a growth in development of nanoparticles as sensor applications in biological and medicinal science (*11*).

Since the introduction of nanotechnology, investment in industry worldwide has risen from $432 million in 1997 (*12*) up to $18 billion in 2008 (*13*), and with nano products entering the market at a rate of 3-4 a week (*14*), it is estimated that nanotechnology will become a $1 - 3 trillion industry by 2015 (*12, 13, 15*). A few examples of nanoparticles used in products are shown in Table 1.1, ranging from clothing to cosmetics.

Table 1.1 Examples of Nanoparticles currently used in Industry and commercial products

Nanoparticle	**Use in Nanotechnology**
Silver nanoparticles	Plasters and dressings for anti-bacterial properties (*12*) Clothes, particularly socks to kill odour producing bacteria (*16*)
Gold nanoparticles	Bio-sensors and electronics (*17, 18*) Fuel cells as a catalyst to remove carbon monoxide (*19*)
Titanium Dioxide nanoparticles	Solar cells (*20*) Electroluminescent devices (*21*) Chemical sensors (*22*) Paints (*14*) Cosmetics and sun screens (*23*)
Zinc Oxide nanoparticles	Optics and electronic materials (*24*) Sun screens (*23*)
Cerium Dioxide nanoparticles	Catalysts in fuels, their redox properties enable it to act as an efficient oxygen store (*25*)
Carbon nanotubes	Fuel cells (*26*) Site specific drug delivery (*27*)
Quantum Dots	Medicinal imaging and diagnosis (*12, 18*) Drug Delivery (*28*)

Given the widespread and increasing use in a number of different industries, the danger and exposure potential to human health and the environment needs to be understood – nanoecotoxicology.

1.2 Nanoecotoxicology

"Nanoparticles have greater potential to travel through the organism than other materials or larger particles" (29), and it is this property that is not yet well understood and presents a significant challenge. Nanoparticle passage through an organism may lead to unexpected exposure routes (*30*), causing potentially greater toxic consequences to living organisms compared to their bulk counterparts (*4*). This is the concept of nanotoxicology or nanoecotoxicology, the nanoparticle science which deals with effects in living organisms (*8*), formalised by Donaldson *et al.* in 2004 (*29*).

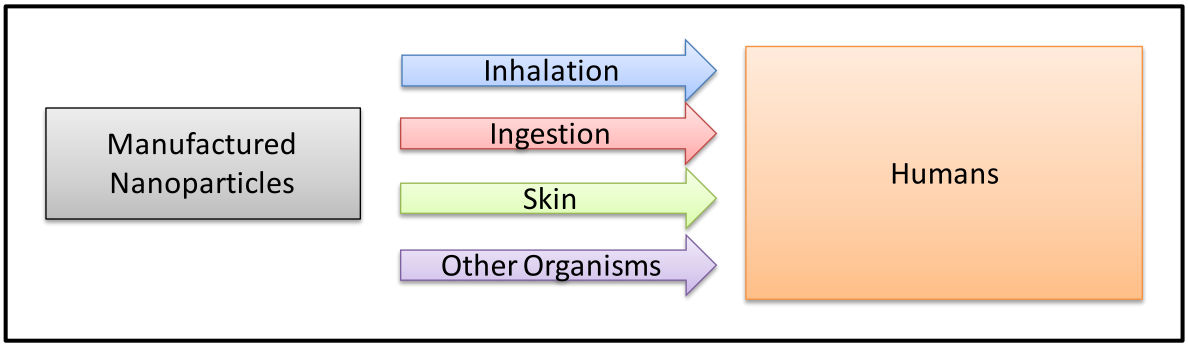

Figure 1.2 Potential nanoparticle exposure routes to Humans

Once nanoparticles have been introduced into the manufacturing process they have the potential to enter society and the environment through different pathways, both intentionally and accidently, Figure 1.2. The modes of human uptake can be deliberate in the form of digestion, with people voluntarily eating Ag nanoparticle tablets for their anti-bacterial properties (*31*), or beauty care products containing TiO_2 and ZnO particles actively applied to the skin (*32*). Other human uptake may be less deliberate, with CeO_2 nanoparticles released through exhaust emissions inhaled once airborne (*33*), and carbon nanotubes also inhaled, with their fibre-like form drawing comparisons with asbestos (*34, 35*). Exposure pathways may be less direct, with nanoparticles released into the environment taken up by other organisms and animals in the human food chain. Benn *et al.* (*16*) published evidence of Ag nanoparticles originally added to socks, subsequently released through washing into waste water systems, and ZnO nanoparticles in sun screen will also be continuously washed off the skin, able to enter various water systems (*23*), with potential exposure to organisms.

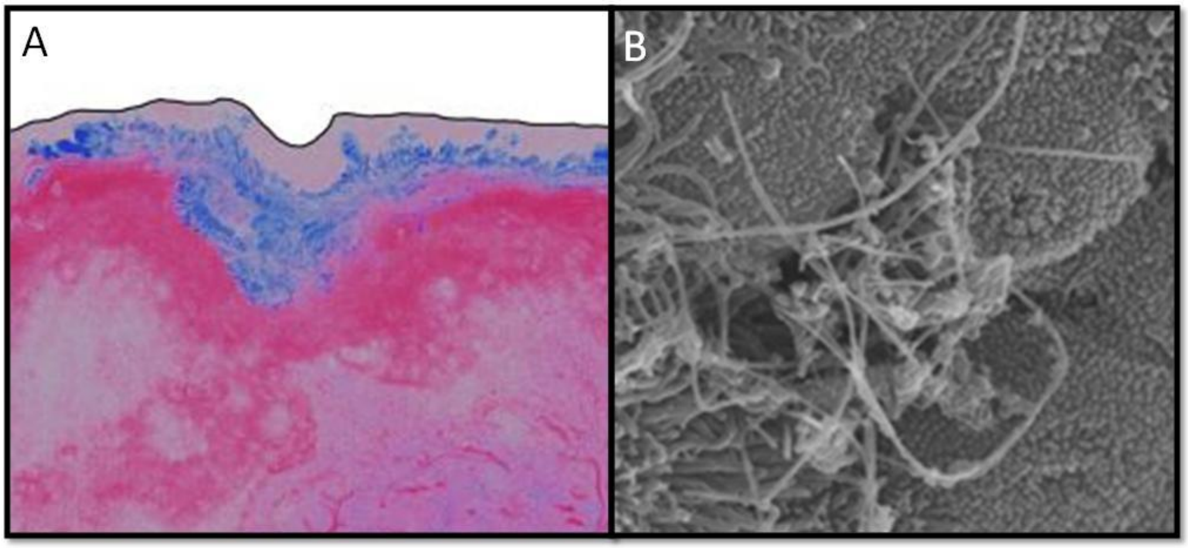

Figure 1.3 A – ZnO nanoparticles (blue) present under the surface of the skin, adapted from Timothy Kelfs image, published in Optical Science of America (*36, 37*), and B - Carbon nanotubes present in the lung of a mouse. Image modified from Robert Mercers CDC publication (*38*)

Toxic effects of nanoparticles have been demonstrated in humans following the uptake of a number of nanoparticle types. The inhalation of CeO_2 nanoparticles caused respiratory damage in lungs, with the nanoparticles also demonstrating the ability to move from the lungs into the blood (*33, 39*). TiO_2 nanoparticle uptake has led to cell death through oxidative stress in human bronchial epithelial cells (*24).* ZnO nanoparticles have been shown to travel through dermal barriers on the skin (*37, 40, 41*), Figure 1.3 (A), leading to a build-up in cells causing gene mutation. Carbon nanotubes are known to be the most toxic particles to humans causing lung damage (*42, 43*), where their tube-like shapes cause them to become trapped in the respiratory tract, Figure 1.3 (B). In other organisms Ag nanoparticles suspended in water proved toxic to both zebra fish (*44*) and daphnids (*45*). Individual nanoparticle toxicity may vary dramatically depending on their local environment, and by understanding nanoparticle surface interaction in that environment, information on their toxic potential can be obtained.

1.3 Nanoparticle Characterisation and Regulation

To determine nanoecotoxicology potential accurately, correct and specific characterisation is needed that will directly address toxicity mechanisms (*46*) and develop an understanding about how the nanoparticles interact in biologically and environmentally relevant dispersion media (*47*). Once this is achieved, the correct nanoparticle regulation and legislation can follow. At present there is an ever increasing list of tools and techniques used to characterise nanoparticles (*48, 49*), which do not appear to add to the understanding of toxicity potential. Table 1.2 lists a selection of techniques currently used for nanoparticle characterisation. To form a comprehensive safety document on nanoparticles in industry (*7*), the OECD formed the working party on manufactured nanoparticles (WPMN), bringing together countries to consider the environmental and human health aspects of manufactured nanoparticles. The WPMN included 30 OECD member countries and many non-members such as Brazil and Russia, and focussed on testing 14 different manufactured nanoparticles relevant in industry.

Table 1.2 Techniques for nanoparticle analysis and characterisation

Instrument and Technique	Characterisation	Advantages and disadvantages
Electron Microscopy (EM)	Images particles, giving shape and diameter parameters	High resolution, but preparation on slides can aggregate samples
Atomic Force Microscopy (AFM)	Images particles, giving diameter and surface area	High resolution 3D images, but can distort image
Dynamic Light Scattering (DLS)	Particle size in suspension	Inaccurate with broad particle size distribution
Brunauer Emmett Teller (BET)	Particle surface area characterisation	Very accurate, but only suitable for dry powder
Zetasizer	Determines surface charge of particles	Inaccurate with sample aggregation and background noise
Inductively Coupled Plasma – Mass Spectroscopy (ICP-MS)	Determines particle composition	Sample preparation can limit detection.
X-ray Spectroscopy	Surface chemistry	Only dry powder samples

Ecotoxicology test Protocols for Representative Nanomaterials in Support of the OECD Sponsorship Programme (**PROSPEcT**), was set up as the UK's contribution to the OECD programme to examine the environmental safety of nanoparticles used in industry in accordance with the agreed OECD WPMN. The project aimed to provide information on the global safety assessment of nanomaterials and protocols of specific nanoparticles in the environment, as part of the OECD WPMN, with work in this thesis a direct contribution to the PROSPEcT project. Specifically the PROSPEcT project was assigned to characterise two different nanoparticles; firstly, ZnO nanoparticles present in commercial sun screens (*7, 23*), Z-cote ZnO, Figure 1.4 (A) manufactured by BASF (*50*), and Nanosun ZnO supplied by Micrometrics Ltd (*51*), and secondly, CeO_2 nanoparticles used in diesel fuels (*52, 53*), Nanograin CeO_2, Figure 1.4 (B) provided by Umicore (*54*).

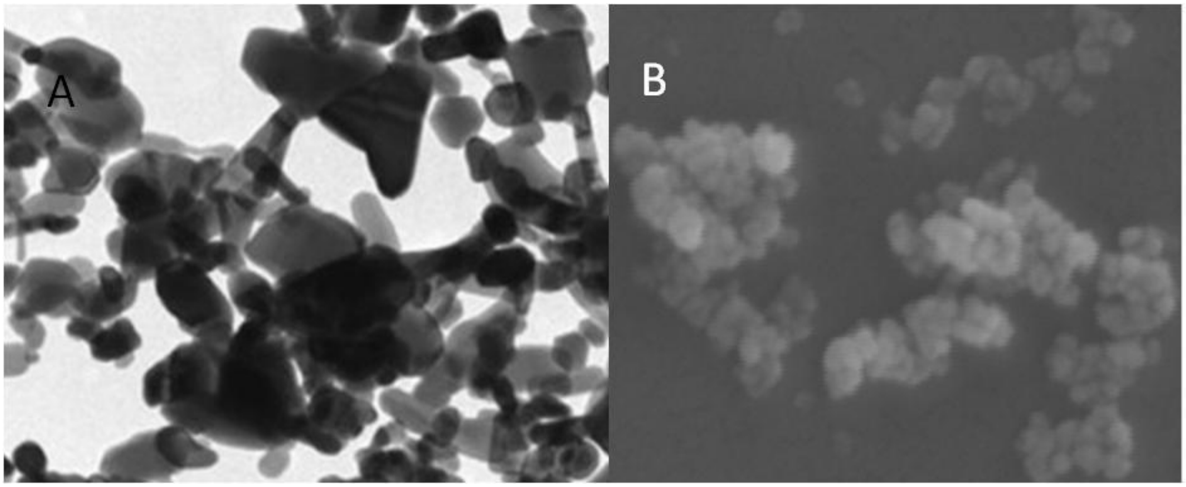

Figure 1.4 A – TEM image of BASF Z-cote ZnO nanoparticles, and B – SEM image of Umicore Nanograin CeO_2 nanoparticles

These nanoparticles may be released into the environment through a variety of pathways, Figure 1.5, and it is the different potential environmental interface structures that may be formed at the particle surface which need to be characterised to establish their properties. Humans may be directly exposed to both these nanoparticles. ZnO nanoparticles applied in sun screen formulations, may enter the body through the skin (*32*). The CeO_2 particles, once expelled into the atmosphere post combustion can be inhaled into the lungs (*33*). When entering a biological fluid the nanoparticle surfaces will become coated with proteins (*55*), forming a complex nano-bio interface, Figure 1.5. This interface may alter specific toxic properties such as ZnO nanoparticle dissolution and CeO_2 redox mechanisms, by forming stable layers around the particles once in the body.

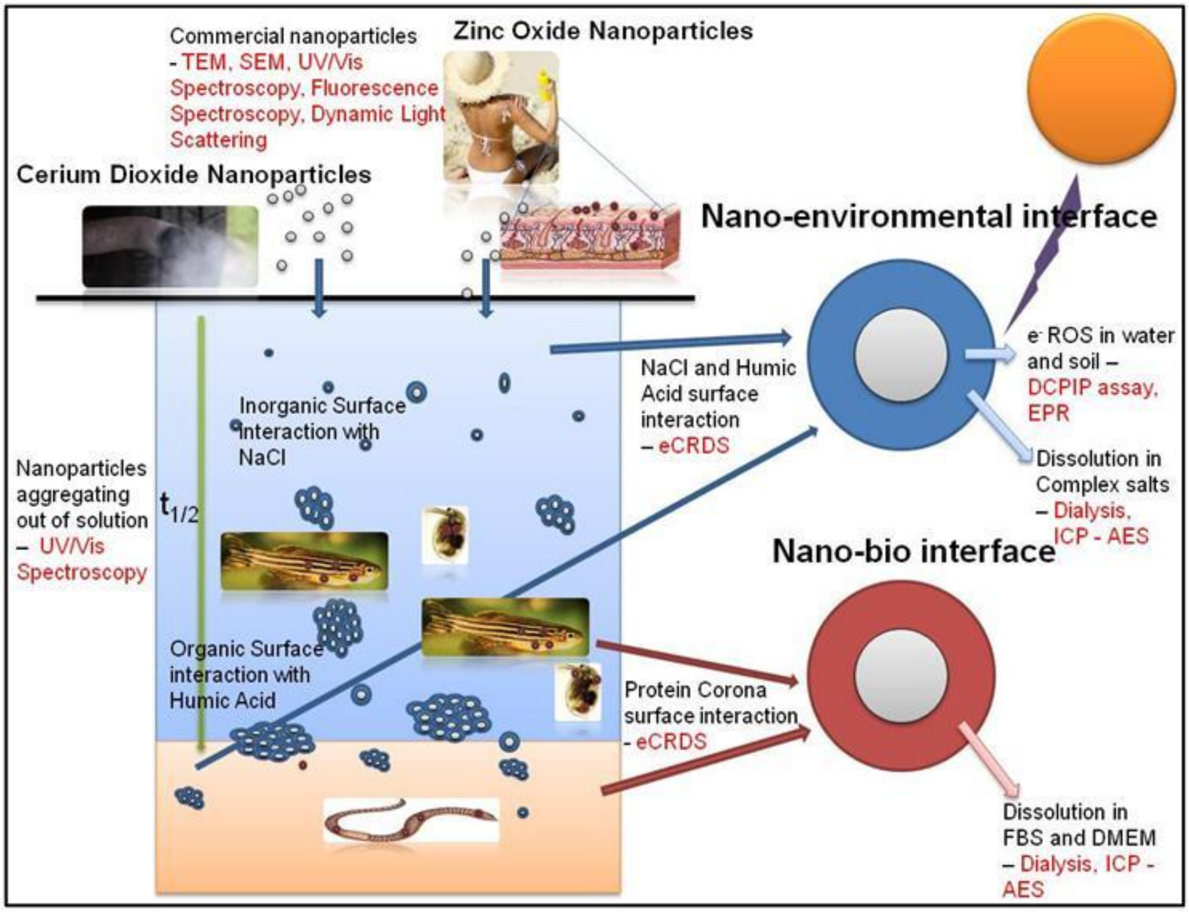

Figure 1.5 The role of the nano-environmental interface in ZnO and CeO_2 nanoparticle ecotoxicology

Particles not directly taken up into the body may migrate into the water systems, with ZnO nanoparticles washed off the skin surface and CeO_2 particles settling out of airborne exhaust fumes, Figure 1.5. Once in the water systems, the nanoparticle dispersion stability and aggregation properties become important in determining their availability to biological systems. The stability of nanoparticle dispersions are a direct consequence of the interaction of the organic and inorganic environments on the nanoparticle surfaces; the nano-environmental interface. This interface is decisive in assessing the potential bioavailability and toxicity of the nanoparticles (*8,* *56, 57*) and their lifetime in aqueous conditions. If the particles are stable in suspension then they may be available to fish and bacteria in water, but if they prove unstable and aggregate quickly, then sedimentary organisms may come into contact with particle aggregates. The nanoparticle stability life-times will then have a direct influence on potential toxicity mechanisms such as dissolution (*58*), or free radical generation through UV exposure (*59*).

1.3.1 Surface Characterisation techniques

Central to a molecular understanding of mechanisms of nanoecotoxicology is the accurate characterisation of nano-environmental interfaces (*7*). Interrogation of the interfacial structure and the surface properties of nanoparticles is complex but key in determining biological fate and toxic effects (*60*). Current state-of-the-art techniques for studying surface chemistry include various Attenuated Total Reflection (ATR) techniques (*61*) using thermal lens detection (*62*) and surface enhanced Infra-Red Adsorption Spectroscopy (*63*). They provide information about the identity of molecules on the surface and their vibrational spectra, and may provide characterisation on surface reactivity, although they are restricted to low sensitivity in the visible and UV range. Surface Enhanced Raman Spectroscopy (SERs) (*64-66*), is useful for detecting single molecules at a surface, enhancing the scattering of adsorbed molecules. The non-linear optical Second Harmonic Generation (SHG) and Sum Frequency Generation (SFG) processes can give high resolution optical interrogation of a surface, although may perturb the interface structure with high-power requirements.

For surface interrogation, Cavity Ring Down Spectroscopy (CRDS) (*67*) is favourable as a technique; it has high optical detection and sensitivity compared to ATR and UV-Vis spectroscopy techniques (*68*) and can be constructed to measure electronic spectroscopy of molecules in the interface in a relatively simple set-up. There are many types of CRDS set-up variations (*68-70*), and these will be explored in detail in Chapter 2, along with the experimental set-up of the Evanescent Wave

Cavity Ring Down Spectroscopy (EW-CRDS) technique implemented in this thesis (*71, 72*). Using the evanescent wave phenomenon, the cavity set-up will allow for a charged surface to be interrogated, observing the interaction and stability of charged layer formation, and can be used as a model for particle surface interaction in complex environmental media.

1.3.2 Nanoparticle Aggregation and Suspension Stability

The lifetime of nanoparticles in water systems determines their availability to aquatic organisms. Where particles have a long life time, toxicity may occur though ingestion, controlled by interaction with proteins in gills of fish, but where nanoparticles have a short life time, the issue quickly becomes a sediment problem. Determining particle stability requires an understanding of particle aggregation processes. The particles will form colloidal suspensions understood conventionally in terms of the DLVO theory, named after Derjaguin and Landau, Verwey and Overbeck (*73*), which states that a colloidal system is determined by the sum of the double layer repulsions and van der Waals attractive forces. Contributions to the interaction energy are attractive and repulsive and when the attractive energies overcome the repulsive contributions the particles aggregate, Figure 1.6.

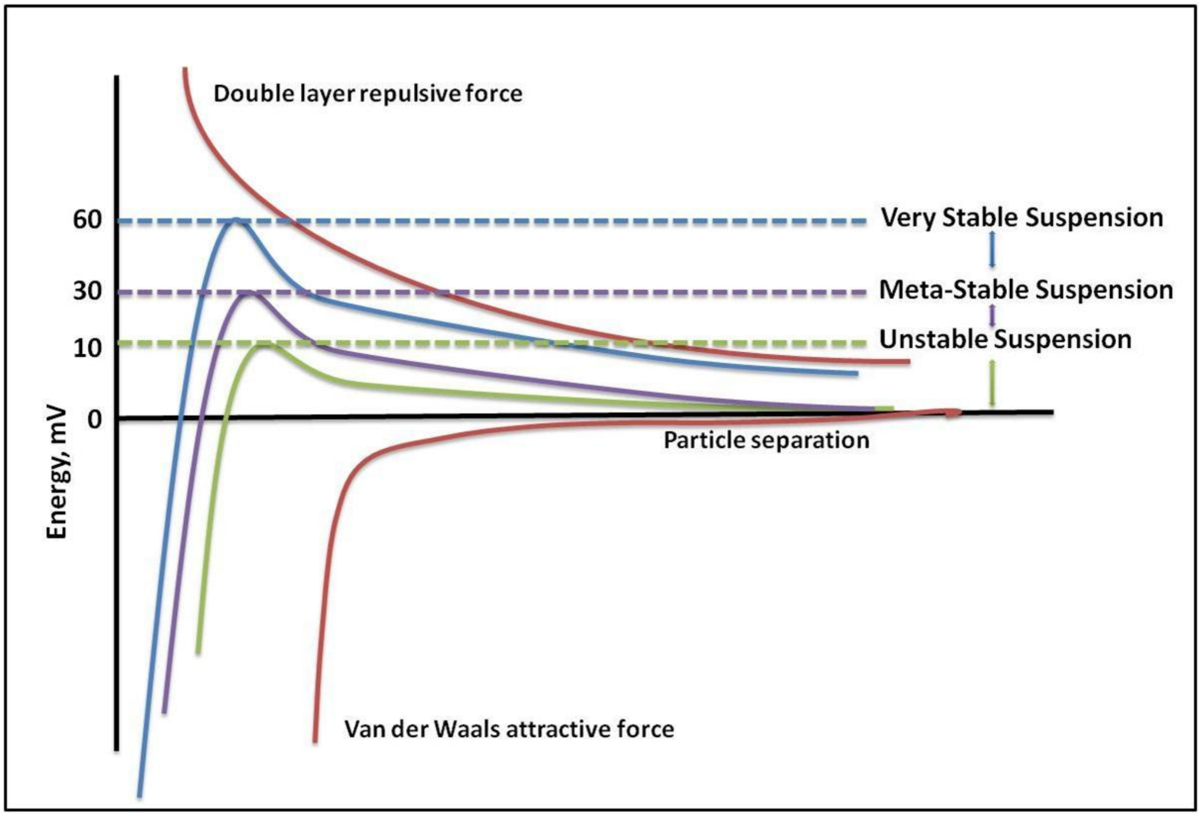

Figure 1.6 DLVO Theory showing the variation of interaction energy with particle separation, and the zeta potential range for nanoparticle colloidal stability

In suspension, there are high energy particle double layer repulsions, which maintain the suspension stability over long lifetimes. The potential stability of a colloid is conventionally indicated by the zeta potential (*74*). This is a measurement of the electric potential in the interfacial double layer, located at the slipping plane. It may be measured using a zetasizer, which directs a laser through the sample measuring the maximum drift velocity of the nanoparticle, its particle mobility, in an applied electric field (*47*). The mobility is related to zeta potential using the Smoluchowski equation (*75*):

$$U_{\mathrm{E}} = 4\pi\varepsilon_0\varepsilon_r \frac{\zeta}{6\pi\mu}(1+\kappa r)$$

Equation 1.1

Where U_E stands for particle mobility, ζ is the zeta potential, ε_o is the relative permittivity of a vacuum and ε_r is the relative permittivity of the test medium, μ is the solution viscosity, with *r* being the surface radius and *κ* representing the Debye-Huckel parameter. The magnitude of the zeta potential shows the potential stability of the colloidal system (*7*): a low zeta potential indicates an unstable suspension, Figure 1.6 leading to aggregation and agglomeration (*30*) with particles sedimenting out of suspension (*76*). A large zeta potential indicates a high level of repellence between particles maintaining distance and thus a very stable suspension, Figure 1.6. The taken value for a stable colloid is above +26mV/-26mV (*77*), a level greater than the level of thermal energy, RT at 298K. The stability of the nanoparticle colloid is environmentally interesting, as it will determine a life time that the particles are in suspension for, and thus available to uptake from aquatic organisms. Once aggregates are formed they will have their own unique properties (*78*), and may still be available to sedimentary organisms, entering into the food chain this way, with potentially toxic consequences.

The nanoparticle interaction energies in suspension are related to the surface potential which is in turn related to the total surface charge, with the charge understood in terms of the density of charged chemical groups on the surface. The surface charge is related to the surface potential by the Poisson's equation (*76*) given by Equation 1.2:

$$ze\rho = -\varepsilon_0 \varepsilon_r (d^2\psi / dx^2)$$

Equation 1.2

Where *z* is the valency, *ρ* is the number density of ions, ε_o is the relative permittivity of a vacuum and ε_r is the relative permittivity of the test medium, *ψ* is the electrostatic potential, and x is a point between two surfaces. This can then be combined with the Boltzmann distribution to relate the potential and counter-ion density between two surfaces.

To estimate the particle size including the density of the counter-ion layer formation in suspension, a technique called Dynamic Light Scattering (DLS) is used. DLS analyses the dynamic fluctuations of light scattering intensity caused by Brownian motion of particles in a sample (*47*) from which a mean particle hydrodynamic diameter is derived. The technique tends to overestimate the diameter, biased to larger aggregates by their large light-scattering cross-section (*47*) limiting complex size distribution characteristics (*48*). The role of size in suspension is therefore difficult to determine, lacking a reliable hydrodynamic size estimation technique. The only estimates of particle size therefore come from the imaging techniques Transmission Electron Microscopy (TEM) and Scanning Electron Microscopy (SEM) where both size and shape are resolved (*79*). Preparation of the samples for TEM produces images of the nanoparticle aggregates formed in the drying out on the TEM sample grid and are therefore not representative of the hydrodynamic diameter or degree of clustering (*47*). SEM in solution may provide a more reliable diameter but again the sample needs to be prepared on a surface to localise the particle which may also aggregate the suspension-phase species. Currently there is no reliable technique for the estimation of hydrodynamic diameter and whether it plays a critical role as a mechanism of nanoecotoxicology.

1.3.3 Nanoparticle Dissolution

The nanoscale of nanoparticles may provide new routes of entry into the body and passage through it potentially delivering nanoparticles containing locally high concentrations of heavy metals to tissue surfaces that have previously not been considered important in mechanisms of toxicity. Dissolution of nanoparticles in suspension or at a tissue surface can liberate heavy metals into the environment, which have well established toxicities. Ag nanoparticles have been shown to produce toxic Ag^+ ions when present in suspension (*31*), which will occur when the thermodynamic properties of a suspended media are favourable (*58*). The rate of nanoparticle dissolution depends on surface area (*80*), with an increase in surface molecules causing a faster rate of dissolution as surface molecules are able to solvate readily at the surface (*81*). Smaller particles have a higher proportion of molecules on the surface (*15*), with previous calculations indicating that for spherical 30 nm particles, surface molecules make up 10% of the total mass, rising to 50% of the total mass for 3 nm particles (*15, 80*). Dissolution rate is also dependent on nanoparticle topology, with rougher high energy surfaces dissolving at a faster rate than smooth surfaces (*60*).

Dissolution will be influenced by the suspension medium, specifically its pH and ionic strength (*82*). This will be further modified by the formation of the interface where ions and ligands may adsorb to the surface. In biological systems it has been demonstrated that the nanoparticle interface will become covered in proteins, forming a protein corona (*49, 83*). This surface interaction may form very stable interfaces reducing the rate at which ions can leave the surface, stabilising the pH and ionic strength locally (*84*) or act as a diffuse barrier slowing dissolution. Surface ligands may alternatively cause more surface molecules to undergo ion exchange, enhancing the movement of nanoparticle molecules into the bulk (*85*).

Techniques used to study the dissolution process detect the arrival of the dissolving ion into the suspension medium, These ultra-sensitive ion detection techniques include Optical Emission Spectroscopy (OES) (*86*), Atomic Adsorption (AA) (*87*), Inductively Coupled Plasma-Mass Spectrometry (ICP-MS) and Inductively Coupled Plasma – Atomic Emission Spectroscopy (ICP-AES). Studies using ICP-AES will be presented in this thesis for ZnO nanoparticles. To measure dissolution, samples need to be separated from the nanoparticles present. To separate them, dialysis (*58*) and syringe ultra-filtration techniques (*87*) are used, although other techniques such as ultra-centrifugation can also be effective. Despite accurate measures of ions in solution, there is at present no direct technique for determining the change in concentration of nanoparticles in suspension – a direct speciation assay for the nanoparticles themselves.

1.3.4 Nanoparticle Radical Generation – Reactive Oxygen Species

A second mechanism of nanoparticle toxicity important to the nanoparticles in the PROSPEcT project is the formation of photo-radicals at the nanoparticle surface, which then induce redox stress in organisms proximal to the nanoparticle (*88-91*). Free radicals are molecules or atoms with unpaired electrons which have increased redox reactivity and participate in a diverse reaction set often associated with a radical storm (*15, 92*). Photo-radicals are formed constantly in the earth's atmosphere, inducing redox chemistry that may be harmful to critical biological processes within the genome and proteome. The most commonly identified radicals are hydroxyl and superoxide species that are formed when photo-electrons encounter a water molecule or dissolved oxygen in the suspension medium, generically called Reactive Oxygen Species (ROS) (*13*). Many nano-materials have been shown to produce free radicals, including quantum dots (*93*), C_{60} fullerenes (*94, 95*) and ZnO and TiO_2 metal oxide nanoparticles (*96*). The mechanism for free radical generation in metal oxide nanoparticles is through photo-excitation at UV wavelengths of electrons in the band gap transition (*97*). In organisms this initiates an oxidative stress response such as inflammation responses *in vivo* releasing oxy radicals (*8, 98*). This production of ROS is now a major theory of toxicity (*41*).

Detection and identification of these short-lived species is a significant measurement challenge. The technique of choice is Electron Paramagnetic Resonance (EPR) using spin-trap molecules to stabilise species before measurement of their EPR spectrum. The identification of radicals depends on the efficiency of the spin-trap molecules to trap some or all of the species produced and the interpretation of the complex EPR spectrum (*92, 99, 100*). Less usefully, the presence of radicals may be detected and quantified by observing the colour changes in various redox-sensitive dyes. In this thesis, a redox dye 2,6-dichlorophenolindophenol (DCPIP), will be used to quantify radical production in nanoparticles, and observe nanoparticle size-dependent effects on radical generation. Jiang *et al.* has previously shown a correlation between the ROS response observed and an increase in particle size (*101*), indicating that the type and shape of nanoparticles may be influential to radical production.

1.3.5 Whole Organism Exposure Studies

The understanding of nanoecotoxicology as a field is evolving slowly because of a lack of appropriate characterisation techniques making it difficult to test the mechanism of toxicity at the molecular level. At present many nanoparticle cytotoxicity risk assessment studies are carried out both *in vivo* and *in vitro* (*102*). Research has examined toxic responses of whole cell sensors, monitoring mitochondrial activity (*103*) and genetic profiling of stress response through ROS detection (*104*). Studies have also looked at the change in inflammatory marker production using ELISA assays (*105*) for many nanoparticles including ZnO (*106*) and TiO_2 (*107*). However, *in vivo* and *in vitro* studies offer little correlation in results (*106*), with *in vitro* systems lacking the complex nature of actual organisms (*108*). In practice, the organisms will be exposed to nanoparticles vastly different in their appearance and characteristics after interaction with the environment and the current cytotoxicity studies are remote detection events from the source of the toxicity, the nanoparticle interface. To understand the nanoparticle toxicity potential in a relevant capacity, information on the interaction and stability at nanoparticle interfaces, protein corona formation and aggregation properties first need to be understood, meaning that the physical chemistry of the interface is central to our understanding of nanoecotoxicology.

1.4 Thesis Aims and Objectives

The aim of this thesis is to understand the physical chemistry of molecular interactions at the nanoparticle interface in complex environmental suspensions and their influence on nanoparticle ecotoxicology. To achieve this aim, the objectives of this thesis are to address the role of the interface in the understanding of the nanoparticle through its entire cycle, from its commercial use, through to its exposure in the environment, Figure 1.5. This thesis will attempt to explore different environmental parameters, developing a platform for measuring direct surface interactions at a charged interface, and specifically looking at ZnO and CeO_2 nanoparticle characteristics in environmentally relevant suspensions, addressing the question of nanoparticle stability, speciation and toxicity through radical production and dissolution measurements.

In **Chapter 2** a model charged interface will be explored, looking at the interaction of species at a silica surface. The interface will be characterised and adsorption and stability parameters at the interface and surface spectra for charged chromophores will be observed. This model will be developed in **Chapter 3,** introducing organic and inorganic parameters, looking at the availability of binding sites and competitive and cooperative binding interaction in different environmental conditions. The interface will then be used to characterise CeO_2 nanoparticle interaction in **Chapter 4**, observing direct nanoparticle surface interaction and aggregation properties, and competitive binding with a charged chromophore. Further characterisation techniques determining nanoparticle stability in different environmental media and aggregation properties of the particles will also be established. Toxicity mechanisms of ZnO nanoparticles will be explored in **Chapters 5 and 6**, with a DCPIP speciation assay quantifying the generation of radicals developed in **Chapter 5**, and the type of radical species generated observed using EPR spectroscopy. **Chapter 6** will monitor dissolution of the nanoparticles over time, using dialysis and syringe filtration techniques, analysed using ICP-AES. The unique radical generation property of the nanoparticle will also be used to determine nanoparticle presence in samples, and thus a dissolution timescales in both environmental and biological systems may be estimated.

References

1. Feynman, R. (1960) There's plenty of room at the bottom, *Engineering and Science 23*.
2. Taniguchi, N. (1974) The basic concept of Nano-Technology, *Japan Society of precision engineering 18*.
3. Bard, D, Mark, D, and Mahlmann, C. (2009) Current standardisation for nanotechnology, *Journal of physics: Conference series 170*, 012036.
4. (2004) Nanoscience and nanotechnologies: opportunities and uncertainties, The Royal Society & The Royal Academy of Engineering, London.
5. Materials Research Institute. materialsri.com/products.html.
6. Owens, D, Eby, J, and Peppas, N. (2006) Metal-polymer Nanocomposites for Therapeutic and imaging Applications, *Micro and Nanodevices for Trgeted Therapeutics*.
7. Powers, K W, Brown, S C, Krishna, V B, Wasdo, S C, Moudgil, B M, and Roberts, S M. (2006) Research Strategies for Safety Evaluation of Nanomaterials. Part VI. Characterization of Nanoscale Particles for Toxicological Evaluation, *Toxicological Sciences 90*, 296-303.
8. Oberdorster, G, Oberdorster, E, and Oberdorster, J. (2005) Nanotoxicology: An Emerging Discipline Evolving from Studies of Ultrafine Particles, National Institue of Environmental Health Sciences.
9. Kottmann, J r P, Martin, O J F, Smith, D R, and Schultz, S. (2001) Plasmon resonances of silver nanowires with a nonregular cross section, *Physical Review B 64*, 235402.
10. Wang, S, Lu, W, Tovmachenko, O, Rai, U S, Yu, H, and Ray, P C. (2008) Challenge in understanding size and shape dependent toxicity of gold nanomaterials in human skin keratinocytes, *Chemical Physics Letters 463*, 145-149.
11. Fisk, J D, Rooth, M, and Shaw, A M. (2007) Gold Nanoparticle Adsorption and Aggregation Kinetics at the Silica−Water Interface, *The Journal of Physical Chemistry C 111*, 2588-2594.

12. Ray, P C, Yu, H, and Fu, P P. (2009) Toxicity and Environmental Risks of Nanomaterials: Challenges and Future Needs, *Journal of Environmental Science and Health, Part C 27*, 1-35.

13. Lux, R. (2009) Nanomaterials State of the Market QI, *Lux research Inc, New York*.

14. Seaton, A, Tran, L, Aitken, R, and Donaldson, K. (2009) Nanoparticles, human health hazard and regulation, *Journal of The Royal Society Interface*.

15. Nel, A, Xia, T, Madler, L, and Li, N. (2006) Toxic Potential of Materials at the Nanolevel, *Science 311*, 622-627.

16. Benn, T M, and Westerhoff, P. (2008) Nanoparticle Silver Released into Water from Commercially Available Sock Fabrics, *Environmental Science & Technology 42*, 4133-4139.

17. Rosi, N L, and Mirkin, C A. (2005) Nanostructures in Biodiagnostics, *Chemical Reviews 105*, 1547-1562.

18. Corti, C, Holliday, R, and Thompson, D. (2002) Developing new industrial applications for gold: Gold nanotechnology, *Gold Bulletin 35*, 111-117.

19. Cameron, D, Holliday, R, and Thompson, D. (2003) Golds future role in fuel cell systems, *Journal of Power Sources 118*, 298-303.

20. Seow, Z L S, Wong, A S W, Thavasi, V, Jose, R, Ramakrishna, S, and Ho, G W. (2009) Controlled synthesis and application of ZnO nanoparticles, nanorods and nanospheres in dye-sensitized solar cells, *Nanotechnology 20*, 045604.

21. Haque, S A, Koops, S, Tokmoldin, N, Durrant, J R, Huang, J S, Bradley, D D C, and Palomares, E. (2007) A multilayered polymer light-emitting diode using a nanocrystalline metal-oxide film as a charge-injection electrode, *Advanced Materials 19*, 683-683.

22. Arnold, M S, Avouris, P, Pan, Z W, and Wang, Z L. (2002) Field-Effect Transistors Based on Single Semiconducting Oxide Nanobelts, *The Journal of Physical Chemistry B 107*, 659-663.

23. Daughton, C G, and Ternes, T A. (1999) Pharmaceuticals and personal care products in the environment: agents of subtle change, JSTOR, The National Institute of Environmental Health Sciences (NIEHS).
24. Bian, S-W, Mudunkotuwa, I A, Rupasinghe, T, and Grassian, V H. (2011) Aggregation and Dissolution of 4 nm ZnO Nanoparticles in Aqueous Environments: Influence of pH, Ionic Strength, Size, and Adsorption of Humic Acid, *Langmuir 27*, 6059-6068.
25. Park, E-J, Yi, J, Chung, K-H, Ryu, D-Y, Choi, J, and Park, K. (2008) Oxidative stress and apoptosis induced by titanium dioxide nanoparticles in cultured BEAS-2B cells, *Toxicology Letters 180*, 222-229.
26. Allsopp, M, Walters. A, and Santillo. D. (2007) Nanotechnologies and nanomaterials in electrical and electronic goods: A review of uses and health concerns, *Greenpeace Research*.
27. Pastorin, G, Wu, W, Wieckowski, S, Briand, J-P, Kostarelos, K, Prato, M, and Bianco, A. (2006) Double functionalisation of carbon nanotubes for multimodal drug delivery, *Chemical Communications*, 1182-1184.
28. Agnihotri, S A, Mallikarjuna, N N, and Aminabhavi, T M. (2004) Recent advances on chitosan-based micro- and nanoparticles in drug delivery, *Journal of Controlled Release 100*, 5-28.
29. Donaldson, K, Stone, V, Tran, C L, Kreyling, W, and Borm, P J A. (2004) Nanotoxicology, *Occupational and Environmental Medicine 61*, 727-728.
30. Maynard, A D, Warheit, D B, and Philbert, M A. (2011) The New Toxicology of Sophisticated Materials: Nanotoxicology and Beyond, *Toxicological Sciences 120*, S109-S129.
31. Tinkle, S S, Antonini, J M, Rich, B A, Roberts, J R, Salmen, R, DePree, K, and Adkins, E J. Skin as a route of exposure and sensitization in chronic beryllium disease.
32. Gulson, B, McCall, M, Korsch, M, Gomez, L, Casey, P, Oytam, Y, Taylor, A, McCulloch, M, Trotter, J, Kinsley, L, and Greenoak, G. (2010) Small Amounts of Zinc from Zinc Oxide Particles in Sunscreens Applied Outdoors Are Absorbed through Human Skin, *Toxicological Sciences 118*, 140-149.

33. Nemmar, A, Hoet, P H M, Vanquickenborne, B, Dinsdale, D, Thomeer, M, Hoylaerts, M F, Vanbilloen, H, Mortelmans, L, and Nemery, B. (2002) Passage of Inhaled Particles Into the Blood Circulation in Humans, *Circulation 105*, 411-414.
34. Maynard. A, D. (2006) Nanotechnology: a research strategy for addressing risk, *Woodrow Wilson International Cetre for scholoars*.
35. Jia, G, Wang, H, Yan, L, Wang, X, Pei, R, Yan, T, Zhao, Y, and Guo, X. (2005) Cytotoxicity of Carbon Nanomaterials: Single-Wall Nanotube, Multi-Wall Nanotube, and Fullerene, *Environmental Science & Technology 39*, 1378-1383.
36. Kelf, T A. *Optical Science of America Macquarie University*.
37. Song, Z, Kelf, T A, Sanchez, W H, Roberts, M S, Rika, J, Frenz, M, and Zvyagin, A V. (2011) Characterization of optical properties of ZnO nanoparticles for quantitative imaging of transdermal transport, *Biomed. Opt. Express 2*, 3321-3333.
38. Mercer, R. (2008) Should Nanotubes be handled in the work place like asbestos?, *Centres for Disease Control and Prevention*.
39. Dockery, D W. (2001) Epidemiologic evidence of cardiovascular effects of particulate air pollution, Brogan and Partners, Environmental health perspectives.
40. Ryman-Rasmussen, J P, Riviere, J E, and Monteiro-Riviere, N A. (2006) Penetration of Intact Skin by Quantum Dots with Diverse Physicochemical Properties, *Toxicological Sciences 91*, 159-165.
41. Xia, T, Kovochich, M, Brant, J, Hotze, M, Sempf, J, Oberley, T, Sioutas, C, Yeh, J I, Wiesner, M R, and Nel, A E. (2006) Comparison of the Abilities of Ambient and Manufactured Nanoparticles To Induce Cellular Toxicity According to an Oxidative Stress Paradigm, *Nano Letters 6*, 1794-1807.
42. Muller, J, Huaux, F o, Moreau, N, Misson, P, Heilier, J-F o, Delos, M, Arras, M, Fonseca, A, Nagy, J B, and Lison, D. (2005) Respiratory toxicity of multi-wall carbon nanotubes, *Toxicology and Applied Pharmacology 207*, 221-231.

43. Davoren, M, Herzog, E, Casey, A, Cottineau, B, Chambers, G, Byrne, H J, and Lyng, F M. (2007) In vitro toxicity evaluation of single walled carbon nanotubes on human A549 lung cells, *Toxicology in Vitro 21*, 438-448.
44. Asharani, P V, Wu, Y L, Gong, Z, and Valiyaveettil, S. (2008) Toxicity of silver nanoparticles in zebrafish models, *Nanotechnology 19*, 255102.
45. Griffitt, R J, Luo, J, Gao, J, Bonzongo, J-C, and Barber, D S. (2008) Effects of particle composition and species on toxicity of metallic nanomaterials in aquatic organisms, *Environmental Toxicology and Chemistry 27*, 1972-1978.
46. Hardman, R. (2006) A Toxicologic Review of Quantum Dots: Toxicity Depends on Physicochemical and Environmental Factors, *Environ Health Perspect 114*.
47. Murdock, R C, Braydich-Stolle, L, Schrand, A M, Schlager, J J, and Hussain, S M. (2008) Characterization of Nanomaterial Dispersion in Solution Prior to In Vitro Exposure Using Dynamic Light Scattering Technique, *Toxicological Sciences 101*, 239-253.
48. Allen, T. (2004) Particle size measurement - Surface area and pore size determination, Chapman and Hall, London.
49. Ratner, B D (2004) *Biomaterials Science: An introduction to materials in medicine*, Academic Press, San Diego.
50. BASF. GUP / PC - Z470, 67056, Ludwigshaften, Germany.
51. Micrometrics. 4356 Communications Drive, Norcross, GA 30093-2901, U.S.A.
52. Institute, H E. (2001) Evaluation of Human Health Risk from Cerium Added to Dielsel Fuel, pp 1-57.
53. Wakefield, G, Wu, X, Gardener, M, Park, B, and Anderson, S. (2008) Envirox fuel-borne catalyst: Developing and launching a nano-fuel additive, *Technology Analysis & Strategic Management 20*, 127-136.
54. Umicore. Broekstraat 31 rue du Marais, B-1000 Brussels, Belgium.
55. Kane, R S, and Stroock, A D. (2007) Nanobiotechnology: Protein-Nanomaterial Interactions, *Biotechnology Progress 23*, 316-319.

56. Vertegel, A A, Siegel, R W, and Dordick, J S. (2004) Silica Nanoparticle Size Influences the Structure and Enzymatic Activity of Adsorbed Lysozyme, *Langmuir 20*, 6800-6807.
57. Ehrenberg, M S, Friedman, A E, Finkelstein, J N, Oberdorster, G, and McGrath, J L. (2009) The influence of protein adsorption on nanoparticle association with cultured endothelial cells, *Biomaterials 30*, 603-610.
58. Franklin, N M, Rogers, N J, Apte, S C, Batley, G E, Gadd, G E, and Casey, P S. (2007) Comparative Toxicity of Nanoparticulate ZnO, Bulk ZnO, and ZnCl2 to a Freshwater Microalga (Pseudokirchneriella subcapitata): The Importance of Particle Solubility, *Environmental Science & Technology 41*, 8484-8490.
59. Serpone, N, Dondi, D, and Albini, A. (2007) Inorganic and organic UV filters: Their role and efficacy in sunscreens and suncare products, *Inorganica Chimica Acta 360*, 794-802.
60. Borm, P, Klaessig, F C, Landry, T D, Moudgil, B, Pauluhn, J r, Thomas, K, Trottier, R, and Wood, S. (2006) Research Strategies for Safety Evaluation of Nanomaterials, Part V: Role of Dissolution in Biological Fate and Effects of Nanoscale Particles, *Toxicological Sciences 90*, 23-32.
61. Milosevic, M. (2004) Internal Reflection and ATR Spectroscopy, *Applied Spectroscopy Reviews 39*, 365-384.
62. Shimosaka, T, Sugii, T, Hobo, T, Alexander Ross, J B, and Uchiyama, K. (2000) Monitoring of Dye Adsorption Phenomena at a Silica Glass/Water Interface with Total Internal Reflection Coupled with a Thermal Lens Effect, *Analytical Chemistry 72*, 3532-3538.
63. Huo, S-J, Xue, X-K, Li, Q-X, Xu, S-F, and Cai, W-B. (2006) Seeded-Growth Approach to Fabrication of Silver Nanoparticle Films on Silicon for Electrochemical ATR Surface-Enhanced IR Absorption Spectroscopy, *The Journal of Physical Chemistry B 110*, 25721-25728.
64. Nie, S, and Emory, S R. (1997) Probing Single Molecules and Single Nanoparticles by Surface-Enhanced Raman Scattering, *Science 275*, 1102-1106.

65. Sun, Z, Wang, C, Yang, J, Zhao, B, and Lombardi, J R. (2008) Nanoparticle Metal Semiconductor Charge Transfer in ZnO/PATP/Ag Assemblies by Surface-Enhanced Raman Spectroscopy, *The Journal of Physical Chemistry C 112*, 6093-6098.
66. Joo, S W. (2006) Adsorption of Bipyridine Compounds on Gold Nanoparticle Surfaces Investigated by UV-Vis Absorbance Spectroscopy and Surface Enhanced Raman Scattering, *Spectroscopy Letters 39*, 85-96.
67. O'Keefe, A, and Deacon, D A G. (1988) Cavity ring-down optical spectrometer for absorption measurements using pulsed laser sources, *Review of Scientific Instruments 59*, 2544-2551.
68. Schnippering, M, Neil, S R T, Mackenzie, S R, and Unwin, P R. (2011) Evanescent wave cavity-based spectroscopic techniques as probes of interfacial processes, *Chemical Society Reviews 40*, 207-220.
69. Mazurenka, M, Wilkins, L, Macpherson, J V, Unwin, P R, and Mackenzie, S R. (2006) Evanescent Wave Cavity Ring-Down Spectroscopy in a Thin-Layer Electrochemical Cell, *Analytical Chemistry 78*, 6833-6839.
70. Ball, S M, and Jones, R L. (2003) Broad-Band Cavity Ring-Down Spectroscopy, *Chemical Reviews 103*, 5239-5262.
71. O'Reilly, J P, Butts, C P, I'Anso, I A, and Shaw, A M. (2005) Interfacial pH at an Isolated Silica Water Surface, *Journal of the American Chemical Society 127*, 1632-1633.
72. Fisk, J D, Batten, R, Jones, G, O'Reilly, P, and Shaw, A M. (2005) pH Dependence of the Crystal Violet Adsorption Isotherm at the Silica-Water Interface, *J. Phys. Chem. B 109*, 14475-14480.
73. Adamczyk, Z, and Weronski, P. (1999) Application of the DLVO theory for particle deposition problems, *Advances in Colloid and Interface Science 83*, 137-226.
74. Attard, P. (2001) Recent advances in the electric double layer in colloid science, *Current Opinion in Colloid & Interface Science 6*, 366-371.
75. Sze, A, Erickson, D, Ren, L, and Li, D. (2003) Zeta-potential measurement using the Smoluchowski equation and the slope of the current time

relationship in electroosmotic flow, *Journal of Colloid and Interface Science 261*, 402-410.

76. Israelachvili, J N (1991) *Intermolecular and Surface Forces*, 2nd Edition ed., Academic Press, London.
77. Muller, R H, Hildebrand, G E, and Nitzsche, R. (1996) Zetapotential und Partikelladung in der Laborpraxis, *lavoisier*.
78. Muller, F, Peukert, W, Polke, R, and Stenger, F. (2004) Dispersing nanoparticles in liquids, *International Journal of Mineral Processing 74, Supplement*, S31-S41.
79. Goldstein, J I (2003) *Scanning electron microscopy and X-ray microanalysis*, Kluwer Academic/Plenum, New York [etc.].
80. Tang, R, Orme, C A, and Nancollas, G H. (2004) Dissolution of crystallites: surface energetic control and size effects, *Chemphyschem : a European journal of chemical physics and physical chemistry 5*, 688-696.
81. Tinke, A P, Vanhoutte, K, De Maesschalck, R, Verheyen, S, and De Winter, H. (2005) A new approach in the prediction of the dissolution behavior of suspended particles by means of their particle size distribution, *Journal of Pharmaceutical and Biomedical Analysis 39*, 900-907.
82. Lok, C-N, Ho, C-M, Chen, R, He, Q-Y, Yu, W-Y, Sun, H, Tam, P, Chiu, J-F, and Che, C-M. (2007) Silver nanoparticles: partial oxidation and antibacterial activities, *Journal of Biological Inorganic Chemistry 12*, 527-534.
83. Casals, E, Pfaller, T, Duschl, A, Oostingh, G J, and Puntes, V. (2010) Time Evolution of the Nanoparticle Protein Corona, *ACS Nano 4*, 3623-3632.
84. Fukushi, K, and Sato, T. (2005) Using a Surface Complexation Model To Predict the Nature and Stability of Nanoparticles, *Environmental Science & Technology 39*, 1250-1256.
85. Iller, R K. (1979) The Chemistry of silica: Solubility, polymerization, colloid and surface properties, and biochemistry, *Wiley New York*, 632 - 729.
86. Navarro, E, Piccapietra, F, Wagner, B, Marconi, F, Kaegi, R, Odzak, N, Sigg, L, and Behra, R. (2008) Toxicity of Silver Nanoparticles to Chlamydomonas reinhardtii, *Environmental Science & Technology 42*, 8959-8964.

87. Hoet, P, Bruske-Hohlfeld, I, and Salata, O. (2004) Nanoparticles - known and unknown health risks, *Journal of Nanobiotechnology 2*, 12.

88. Federici, G, Shaw, B J, and Handy, R D. (2007) Toxicity of titanium dioxide nanoparticles to rainbow trout (Oncorhynchus mykiss): Gill injury, oxidative stress, and other physiological effects, *Aquatic Toxicology 84*, 415-430.

89. Zweier, J L, Duke, S S, Kuppusamy, P, Sylvester, J T, and Gabrielson, E W. (1989) Electron paramagnetic resonance evidence that cellular oxygen toxicity is caused by the generation of superoxide and hydroxyl free radicals, *FEBS Letters 252*, 12-16.

90. Hu, C W, Li, M, Cui, Y B, Li, D S, Chen, J, and Yang, L Y. (2009) Toxicological effects of TiO2 and ZnO nanoparticles in soil on earthworm Eisenia fetida, *Soil Biology and Biochemistry 42*, 586-591.

91. Reddy, K M, Feris, K, Bell, J, Wingett, D G, Hanley, C, and Punnoose, A. (2007) Selective toxicity of zinc oxide nanoparticles to prokaryotic and eukaryotic systems, *Applied Physics Letters 90*, 213902-213902-213903.

92. Shibata, H, Ogura, Y, and Sawa, Y. (1998) Hydroxyl radical generation depending on O2 or H2O by a photocatalyzed reaction in an aqueous suspension of titanium dioxide, *Bioscience, biotechnology, and biochemistry 62*, 2306-2311.

93. Derfus, A M, Chan, W C W, and Bhatia, S N. (2003) Probing the Cytotoxicity of Semiconductor Quantum Dots, *Nano Letters 4*, 11-18.

94. Rancan, F, Rosan, S, Boehm, F, Cantrell, A, Brellreich, M, Schoenberger, H, Hirsch, A, and Moussa, F. (2002) Cytotoxicity and photocytotoxicity of a dendritic C60 mono-adduct and a malonic acid C60 tris-adduct on Jurkat cells, *Journal of Photochemistry and Photobiology B: Biology 67*, 157-162.

95. Yamakoshi, Y, Umezawa, N, Ryu, A, Arakane, K, Miyata, N, Goda, Y, Masumizu, T, and Nagano, T. (2003) Active oxygen species generated from photoexcited fullerene (C60) as potential medicines: O2-* versus 1O2, *Journal of the American Chemical Society 125*, 12803-12809.

96. Nagaveni, K, Sivalingam, G, Hegde, M S, and Madras, G. (2004) Photocatalytic Degradation of Organic Compounds over Combustion-

Synthesized Nano-TiO2, *Environmental Science & Technology 38*, 1600-1604.

97. Xia, T, Kovochich, M, Liong, M, Madler, L, Gilbert, B, Shi, H, Yeh, J I, Zink, J I, and Nel, A E. (2008) Comparison of the Mechanism of Toxicity of Zinc Oxide and Cerium Oxide Nanoparticles Based on Dissolution and Oxidative Stress Properties, *ACS Nano 2*, 2121-2134.
98. Xia, T, Kovochich, M, and Nel, A. (2006) The Role of Reactive Oxygen Species and Oxidative Stress in Mediating Particulate Matter Injury, *Clinics in occupational and environmental medicine 5*, 817-836.
99. Turchi, C S, and Ollis, D F. (1990) Photocatalytic degradation of organic water contaminants: Mechanisms involving hydroxyl radical attack, *Journal of Catalysis 122*, 178-192.
100. Lipovsky, A, Tzitrinovich, Z, Friedmann, H, Applerot, G, Gedanken, A, and Lubart, R. (2009) EPR Study of Visible Light-Induced ROS Generation by Nanoparticles of ZnO, *The Journal of Physical Chemistry C 113*, 15997-16001.
101. Jiang, J, Oberdorster, G, Elder, A, Gelein, R, Mercer, P, and Biswas, P. (2008) Does nanoparticle activity depend upon size and crystal phase?, *Nanotoxicology 2*, 33-42.
102. Kroll, A, Pillukat, M H, Hahn, D, and Schnekenburger, J r. (2009) Current in vitro methods in nanoparticle risk assessment: Limitations and challenges, *European Journal of Pharmaceutics and Biopharmaceutics 72*, 370-377.
103. Berridge, M V, Herst, P M, Tan, A S, and El-Gewely, M R. (2005) Tetrazolium dyes as tools in cell biology: New insights into their cellular reduction, In *Biotechnology Annual Review*, pp 127-152, Elsevier.
104. Jakubowski, W, and Bartosz, G. (2000) 2,7-dichlorofluorescin oxidation and reactive oxygen species: what does it measure?, *Cell Biology International 24*, 757-760.
105. Lequin, R M. (2005) Enzyme Immunoassay (EIA)/Enzyme-Linked Immunosorbent Assay (ELISA), *Clinical Chemistry 51*, 2415-2418.

106. Sayes, C M, Reed, K L, and Warheit, D B. (2007) Assessing Toxicity of Fine and Nanoparticles: Comparing In Vitro Measurements to In Vivo Pulmonary Toxicity Profiles, *Toxicological Sciences 97*, 163-180.

107. Tao, F, and Kobzik, L. (2002) Lung macrophage-epithelial cell interactions amplify particle-mediated cytokine release, *American journal of respiratory cell and molecular biology 26*, 499-505.

108. Hayashi, Y. (2005) Designing in vitro assay systems for hazard characterization. Basic strategies and related technical issues, *Experimental and Toxicologic Pathology 57, Supplement 1*, 227-232.

Chapter 2

Electronic Spectroscopy of Counter-ion Chromophore Molecules at the Silica-Water Interface

2.1 Introduction

Understanding the fate of nanoparticles in the environment is intrinsically linked to the structure and stability of the nano-environmental interface, formed by its surface properties and the molecules present in the environment in which it is placed. This interfacial structure controls the stability and ultimately the toxicity potential of the nanoparticles. The structure and composition of the nano-environmental interfaces are critically depended on their local environments, as discussed in Chapter 1, and we need to develop new techniques to characterise the molecular structures within the interface. Here we will discuss interface spectroscopic techniques developing a platform for observing and measuring charged species in different environments at the interface, using the pH-dependence of the silica-water interface as a model system from which extrapolations to the environment will be made in Chapter 3 and Chapter 4.

2.1.1 Silica-water interface

The silica-water interface is an ideal model interface as it has been extensively characterised previously (*1*), with many of its properties well known. The silica surface becomes negatively charged as a function of the local interfacial pH of the solution phase above it (*2*). The surface contains a number of hydroxyl groups present that will become negatively charged as the pH changes at the silanol sites, Equation 2.1.

$$SiOH + H_2O \leftrightarrow SiO^- + H_3O^+$$

Equation 2.1

Work to characterise these negatively charged silanol groups on a prism surface has shown greater dissociation as the interfacial pH is increased, leading to a larger surface negative charge and interface structure. Ong *et al.* published a variation of second harmonic generation as a function of pH suggesting the presence of two silanol sites, one with a pK_a of 4.5 for 19% of the sites, and the other with a pK_a of 8.5 for the remaining 81% (*1*).

Dong *et al.* speculated that this variation in silanol sites was related to the isolation of the different surface hydroxyl groups. They indicated that completely isolated groups made up the low percentage pK_a 4.5 groups, with the rest of the surface groups being in close proximity with a pK_a of 8.5 (*3*). Bolis *et al.* showed that the non-isolated hydroxyl groups would either hydrogen bond directly to one another or bond through a bridged water molecule (*4*). This was shown to depend on the distance between the sites, calculated to be less than 3.3 Ǻ apart for direct hydrogen bonding, and between 3.5 – 5.5 Ǻ apart for bridged bonding (*3*). Previous studies by Chuang *et al.* showed on a silica gel that of the 81% silanol groups in close proximity 46% were hydrogen bonded directly (*5*), meaning the other 35% formed hydrogen bonds by bridged water molecules (*3*).

Cross Polarisation Magic Angle Spinning Nuclear Magnetic Resonance (CP/MAS NMR) studies showed that these two types of silanol groups represent two different silanol structures, one that has two Si-OH groups pointing away from the surface, and two Si-OH groups pointing into the bulk, whilst the other structure has only one Si-OH group pointing away from the surface, Figure 2.1. These structures are referred to as Q2 and Q3 silanol sites respectively (*6*), with the Q3 sites having a pK_a of 5.10 making up 27% of the surface and the Q2 sites having a pK_a of 9.05 making up the remaining 73% of the silica surface (*6*).

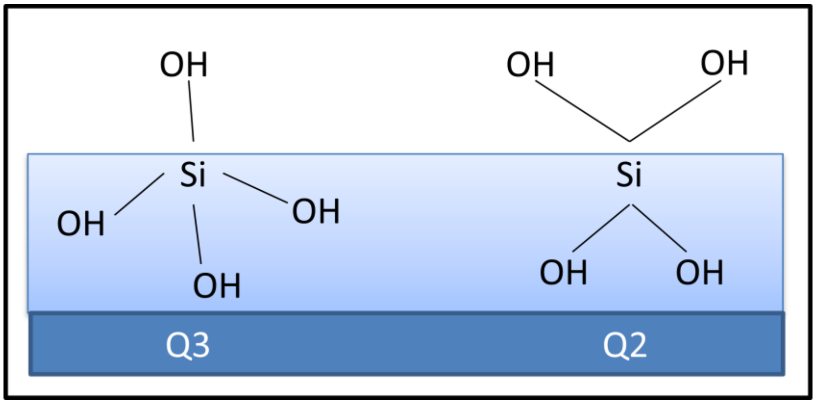

Figure 2.1 The Q2 and Q3 silanol sites available at the silica surface

The silica-water interface interactions have been shown previously to be highly significant in industrial research and environmental ecology (*7*). Work has looked at simple organics at the interface (*8*), and the contribution of surface charge and size of species on adsorption (*9*). The role of the interface in ecology has also been explored, looking at surfactant effects (*10*) and the influence of humic acid in the binding and transport of organic and inorganic contaminants (*11*). These interface effects will be explored further in Chapter 3.

The adsorption of molecules at the silica-water interface forms an interfacial structure which is best understood by the Gouy-Chapman-Stern (GCS) model (*12*). This is the concept of a surface double layer proposed by Stern, developing ideas put forward by Gouy and Chapman and previously by Helmholtz (*13*). Helmholtz originally designed a simple model with a single layer of charged ions adsorbed onto the surface. Gouy and Chapman introduced a diffuse double layer with the electric potential decreasing exponentially the further you are from the surface towards the bulk of the liquid. Stern combined both these ideas with the concept of an internal Stern layer of closely bound molecules directly on the surface followed by a lower energy association in a diffuse or Gouy-Chapman layer (GC), which had molecules less tightly bound to the surface, with the surface potential decaying exponentially to zero away from the surface into the bulk, Figure 2.2. Further extensions to the GCS model allows for division of the Stern layer into an inner and outer Helmholtz plane, with the inner Helmholtz plane (IHP) consisting of a tightly bound layer of species which are not hydrated, and the outer Helmholtz plane (OHP) consisting of more loosely bound hydrated molecules (*14*) (*15*).

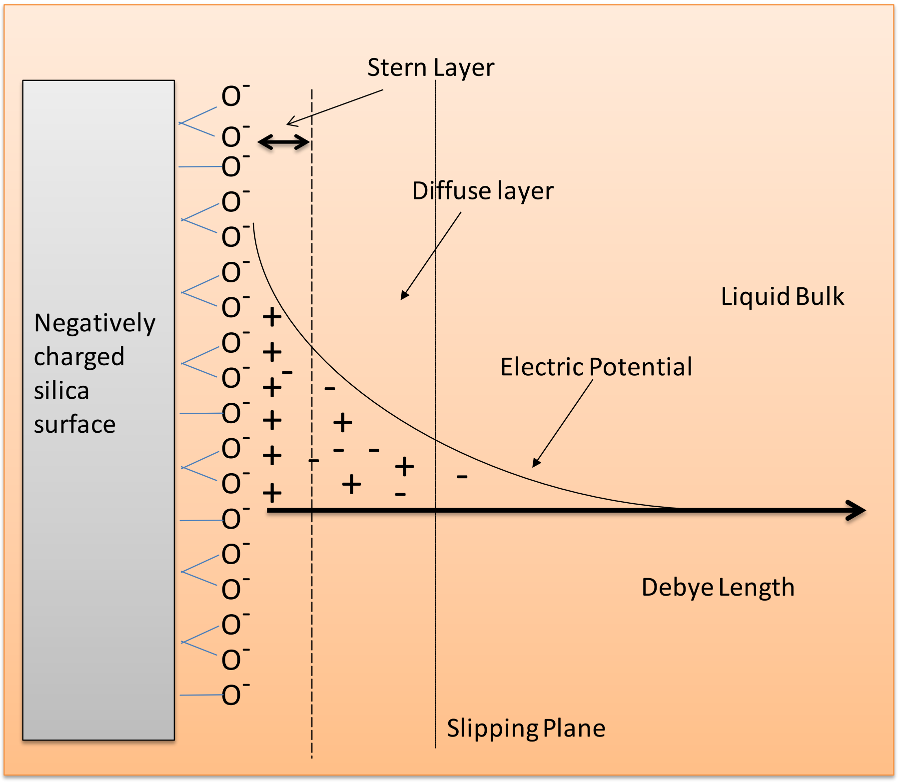

Figure 2.2 The Gouy – Chapman - Stern Charged Interface Model

At the surface, the ion distribution will be dominated by the positive counter-ions; however there will be a low concentration of negative co-ions to balance the surface charge. Further from the surface, counter-ion concentrations fall and co-ion concentration rises until at long distances from the surface the bulk solution is neutral. This distance, the diffuse double layer thickness, has an exponential decay length from the charged interface, the Debye length, with the boundary of the diffuse layer and solution bulk separated by the slipping plane, determined by the electronic potential at that point. The electric field strength will fall to zero at a distance depending on the ionic strength of the medium (*16*), with the magnitude of the Debye length depending solely on the liquid properties at the interface, with a Debye length in pure pH 7 water of approximately 1 µm (*16*).

The interfacial structure at the charged silica-water interface that will be studied in this chapter is a competitive binding adsorption process of positively charged species (*17*), interpreted using the GCS model (*12*). Cooperative binding will also occur on the surface as a consequence of steric hindrance effects, with co-ions and other charged species binding cooperatively onto the surface forming a charged bilayer (*6*), which can be determined by the Hill equation (*18*). The interaction of molecules in the Stern layer will be relatively stable with high electric potential in close proximity to the interface, however molecular interaction in the Gouy-Chapman layer may dissociate with steric effects of the Stern layer and the decreasing electronic potential away from the surface.

2.1.2 Interface Spectroscopy

Electronic spectroscopy of the adsorbed species may be studied by the ultra-sensitive absorption spectroscopy technique Cavity Ring Down Spectroscopy (CRDS). This technique was first demonstrated by O'Keefe and Deacon *(19)* in 1988, where they carried out various optical absorbance spectra measurements using a tuneable pulse laser. They demonstrated increased sensitivity measuring transition bands in gaseous molecular oxygen, detecting absorption signals of less than 1 part in 10^6 *(19).* The technique of CRDS is favourable compared to other gas phase spectroscopy set-ups (*20*), as it allows for a large increase in the magnitude of sensitivity over previous techniques and it is internally calibrated using the time base. Its high sensitivity technique can be used to measure electronic spectra directly in absorbance, and has proved important in looking at small numbers of molecules present in the gas phase (*21*). It is also insensitive, in principle, to shot-to-shot intensity fluctuations caused by the pulsed light source, compared with noise, relative to single pass techniques.

CRDS in its simplest form consists of a pulsed laser coupled into a linear, high finesse optical cavity which is formed by two high reflectivity mirrors of R > 99.99%, aligned optically opposite each other. The laser light pulse is coupled to the cavity through the back of the first mirror, trapping the radiation. At each reflection event some light is lost from the cavity and the light intensity in the cavity rings down. A photo-detector placed behind the second mirror detects the decaying light intensity which is captured on an oscilloscope. The rate of decay in the light intensity is determined by the reflectivity of the mirrors, and the length of the cavity. This decay may be approximated as a single exponential with a decay constant or ring-down time, τ. The empty cavity τ is determined by the reflectivity of the mirrors, and can be calculated using Equation 2.2 (*19*):

$$\tau = \frac{t_r / 2}{(1 - R)}$$

Equation 2.2

Where t_r is the round trip time of the cavity, and R is the reflectivity of the mirrors. The stability of the cavity and the smallest detectable change in τ allows for an accurate measurement of absorption to be determined, with the absorbing gas in the cavity causing the ring-down time τ to decrease with the additional optical loss (*22*).

Since O'Keefe and Deacon in 1988 there has been a huge development with CRDS extended to probe surface chemistry and measure the liquid state. Curran *et al.* has looked at the adsorption of bulk Silicon Dioxide by depositing thin low loss SiO_2 films onto the mirror surface directly (*23*), while Kleine *et al.* used a similar method, coating cavity mirrors with molecular films of iodine (*24*). Other variations in the solution phase include Alexander's liquid cavity using flowing liquid sheets (*25*), while Zare *et al.* simply filled the cavity with liquid analytes (*26*). Muir *et al.* inserted thin films of Oxazine on borosilicate substrates at Brewster's angle in between the cavity mirrors (*27*), and Xu *et al.* has also used a Brewster's angle cavity set-up to look at benzene (*28*).

The principle of CRDS was further developed to measure absorbance in the condensed phase by Pipino *et al.* (*29*). Here they incorporated an intra-cavity total internal reflection (TIR) element in the form of a Pellin-Broca prism to characterise the surface adsorption process of I_2. TIR is an optical phenomenon, occurring when radiation propagating in a medium reaches an interface with an optically rarer medium. The angle of incidence determines whether the radiation is transmitted or reflected, and will occur when the angle of incidence is greater than the critical angle; defined by the refractive indices n_1 and n_2 of the two media. At this point the angle of refraction is no longer transmitted across the media, causing all the light to be reflected (*30*). The consequence of having TIR intra-cavity is an evanescent wave; this will propagate at the prism surface in the sample, with a field intensity that decays exponentially with distance from the prism surface and a characteristic penetration depth, d_p (*31*). The interaction of the evanescent wave with molecules at the interface and within the penetration depth will then be coupled to the light intensity within the cavity. Any absorbance of the radiation by molecules in the penetration depth constitutes an additional loss to the cavity, leading to a change in the ring-down time, τ. This coupling allows for a CRDS variation of Attenuated Total Reflection (ATR) spectroscopy (*32*): evanescent wave cavity ring-down spectroscopy (EW-CRDS).

Following Pipino's use of an intra-cavity silica prism, there has been a large rise in different cavity set-ups and publications, with 100 papers published in 2004, up to over 50,000 papers currently published using CRDS in 2012 (*33*). They have used a variety of different prism configurations and orientations (*34-37*), which are well documented in Schnippering's review article (*20*), and include monolithic folded resonator cavities (*38*), ring cavities (*39-41*) and linear cavities used in this thesis and in other publications by the Shaw research group (*6, 17, 42-44*).

The EW-CRDS applications have predominantly been used to look at the kinetics of the interface adsorption of molecules, because of the high cavity sensitivity at the solid-liquid interface (*1, 6, 7, 17, 39, 43, 45-52*). Molecular adsorption at the silica-water interface has been extensively studied by the Shaw group looking at Crystal Violet interaction at the interface (*6, 17, 43*). Nile Blue has been studied, looking at the adsorption with pH at the interface (*43*), with Methylene Blue adsorption shown to lie in a planar orientation at the interface at low concentrations in the gas phase

(*53, 54*). The interaction of the fluorescent dye Rhodamine B at the silica interface was published by Chen *et al.* (*55*), as well as biologically relevant interfaces such as Haemoglobin interaction observed at the interface (*46*), with samples extracted from urine (*48*). Cytochrome C adsorption (*56*) and antigen antibody interaction (*57*) at the interface have also been studied. Work at the silica – water interface has been extended to look at different functionalised silica surfaces, as this can change the charge of the surface, and can also make the surface better defined in terms of its surface potential. Frey *et al.* looked at protein adsorption onto poly-L-lysine layers, with Mazurenka *et al.* also using poly-L-lysine to functionalise a silica surface (*58*). The same group studied adsorption of commercial gold nanoparticles on this functionalised surface (*58*), with layer formation also observed by Fisk *et al.* (*42*).

By using a tuneable pulsed laser in EW-CRDS interfacial absorbance spectra can be collected, which has predominantly been demonstrated by Pipino (*38, 59*), although the set-ups only have narrow wavelength scans. Thorpe *et al.* published a technique able to scan over the wavelength range 760 – 850 nm looking at the spectra of various molecules at the surface (*60*), which combined Fourier transform spectroscopy with CRDS. Another cavity technique has also been developed, Broadband Cavity Enhanced Absorption Spectroscopy (BB-CEAS). This involves the injection of continuous broadband radiation into the cavity, and can obtain surface spectra over broad wavelengths, which can then help to identify different shifts and broadening of spectra with changes in the surface dynamics (*61, 62*). Ball and Jones used their broadband cavity spectrometer to study absorption spectra in the gas phase *(63)*, Lehmann has used two Pellin – Broca prisms to look at absorption of calcium and barium fluoride across the full wavelength range (*64*), while Fielder measured Azulene in the gas phase over a spectral range of 500 - 700 nm using incoherent BB-CEAS (*65*). Van der Sneppen extended BB-CEAS to use the evanescent wave to study absorbance spectra of dye molecules using a supercontinuum laser source with an LED light (*62*).

In this thesis, an EW-CRDS experimental set-up using a Dove prism, with a tuneable pulsed laser will be developed. This may be adjusted enabling scanning of the visible wavelength range, depending on the anti-reflection coating of the mirrors and the prism, to monitor the changes in absorbance at the interface. It is also able to measure the adsorption and desorption of the molecules at a fixed wavelength and observe real-time kinetics at the surface, which has only been observed by a few studies previously (*41, 66*). The stability of the surface layers can then be observed, maximising the ability of the cavity to detect very small changes in absolute absorbance.

2.1.3 Aims and Objectives

The aim of this Chapter is to understand the molecular interactions at a charged interface, as this will relate specifically to the structure and stability of nano-environmental interfaces. This Chapter will detail the EW-CRDS experimental design and implementation for the measurement of electronic spectra to optimise the tuning range and sensitivity. In particular, we will measure the electronic spectra of two chromophore species as they interact with the Q2 and Q3 groups on the silica surface. It will then explore the surface interaction with the binding sites *(17)*, to investigate the structure of the layer formed.

The two cationic marker dyes used to interrogate the interaction at the negative silica surface will be Crystal Violet (CV) and Malachite Green (MG). These marker dyes were chosen as they have been used previously to characterise the silica surface (*3, 6*), and have solution electronic spectra with a λ_{max} within the wavelength range of the cavity. CV was used previously as its three amino-benzyl groups give it an evenly distributed charge density over the entire molecule. The MG structure has amine groups on only two of its three benzene rings, showing a stronger localised charge density on one side of the molecule. It is proposed that these structural changes will cause different binding and association at the interface. The work will look at the pH-dependence of the association and dissociation rates of both the CV and MG dyes on the surface, observing the absorbance change with available Q2 and Q3 silanol site interaction. The cavity has been calibrated to scan the wavelength range 580 – 680 nm, covering the chromophore solution spectra λ_{max}, enabling the measurement of the surface spectra of CV and MG as a function of pH.

The interaction of different charged species to a surface is very important in understanding the environmental processes of particles in solution phase, giving information on particle availability and toxicity in different media. By characterising the silica surface for molecule interaction and the formation and stability of a Stern layer, environmental parameters and particle interaction at an interface can be better understood in Chapters 3 and 4 respectively.

2.2 Evanescent Wave Cavity Ring-Down Spectrometer

The CRD Spectrometer consists of a tuneable OPO Plus laser of the range 410 – 720 nm coupling into a linear, high-finesse optical cavity. The cavity contains a Dove prism as a TIR element that preserves the linear configuration of the cavity, forming what has been called a Dove Cavity.

2.2.1 The Dove Cavity

A 10 Hz pump YAG laser (Surelite I, 14023), controlled by a Q-switch, produces a horizontal 355 nm pump laser for a Surelite OPO Plus (Continuum) optical parametric oscillator, which is tuneable using a non-linear (β-Barium Borate) crystal to produce coherent broadband radiation. The resulting beam entering the cavity is characterised by peak energy of 55 mJ and a pulse width of 3-5 nanoseconds. The EW-CRD spectrometer experimental setup is shown in Figure 2.3.

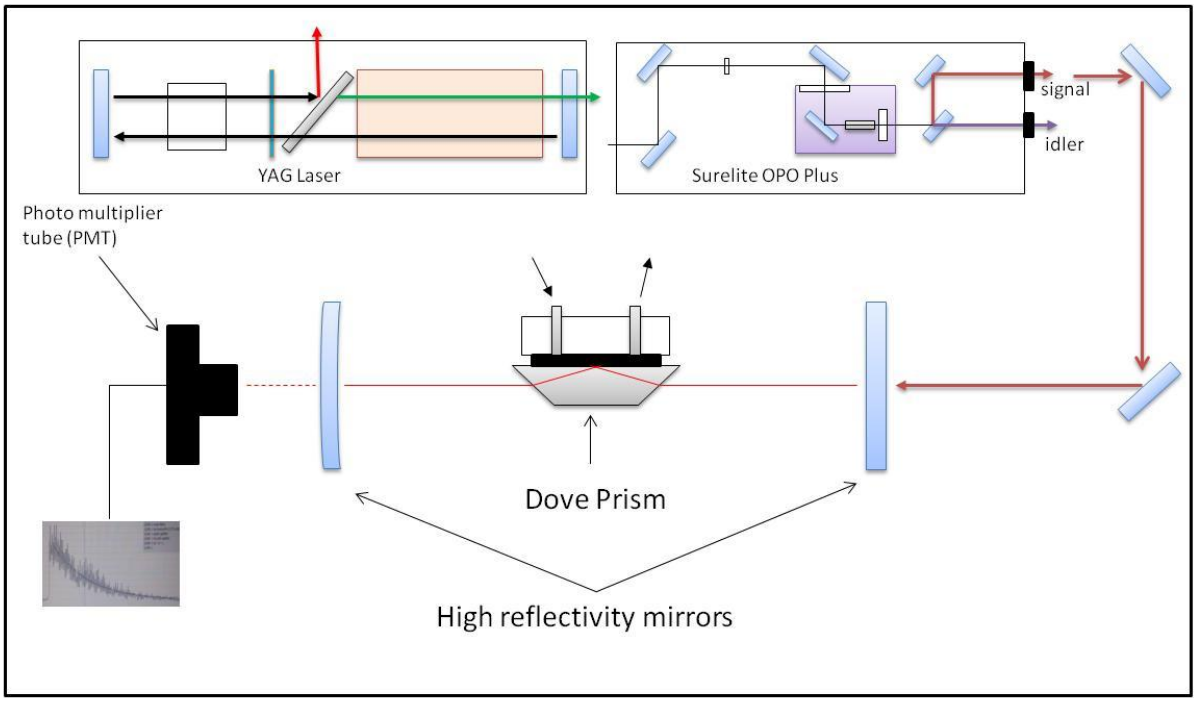

Figure 2.3 Schematic of the OPO Laser and EW-CRD Spectrometer

The laser light exits the Surelite OPO Plus and is steered by a series of bench mirrors into the cavity. The cavity, Figure 2.3, is constructed by two high reflectivity mirrors (*R*=0.9995, centred at 635 nm, Newport Optical Coatings) the entrance mirror is a plane mirror and the second mirror is a concave mirror with radius of curvature 1 m. They form a stable resonator when the length of the cavity is shorter than the radius of the curvature of the mirrors. Here the mirrors are placed 94 cm apart to form a stable optical cavity. The Dove prism was manufactured out of BK 7 optical glass, common in optics because of its high linear optical transmission in the visible range, and has dimensions 42.3 mm x 10 mm x 10 mm, and 14.1 mm x 10 mm entry and exit faces with an anti-reflection (AR) coating (<0.2 % *R*) centred at 635 nm for 45° angle of incidence *p*-polarised light, (custom coating from SLS optics). The prism is placed on an optical mount with precision rotation, in between two mirrors. The laser beam, approximately 2 ± 0.1 mm in diameter, is shaped into an ellipse through the prism, giving an interrogation area on the back of the prism explored by the laser beam of approximately 16.8 ± 0.8 mm^2, Figure 2.4.

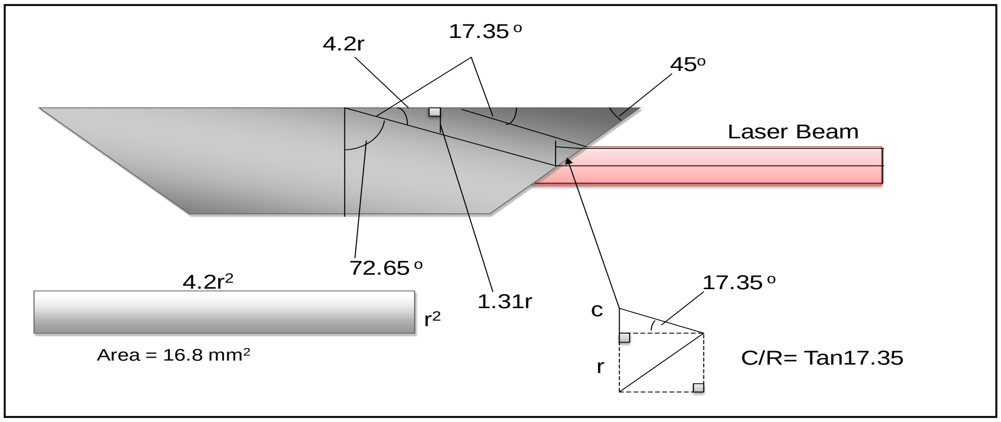

Figure 2.4 Calculation of the laser beam footprint at the surface interface

A flow cell was fabricated, consisting of a rubber O-ring placed on the top surface of the prism and attached by a Teflon block with in and out flow tubes giving an internal flow cell volume of 200 µL. The evanescent field propagates into the medium above the surface resulting from the TIR at the interface between two media, with refractive indices n_1 and n_2 and has a penetration depth which is dependent on the angle of incidence of the radiation and the wavelength of the radiation, as well as the ratio of the two refractive indices. The penetration depth, d_p is given by the Equation 2.3 (*31*):

$$d_p = \frac{\lambda}{2\pi((n_1 \sin(\vartheta))^2 - n_2{}^2)^{1/2}}$$

Equation 2.3

Where n_1 and n_2 are the refractive indices of the silica prism (1.51 at 635 nm) and water (1.333) (*67*), λ is the wavelength of the radiation and ϑ is the angle of incidence. Using this equation, interrogation of the silica surface at 635 nm gives a d_p of 235 nm in water. The liquid flow through the cell onto the surface was provided through a KD Scientific pump with a controllable flow rate typically set at 3.3 mL min^{-1}, allowing for concentration-limited kinetics, Figure 2.5.

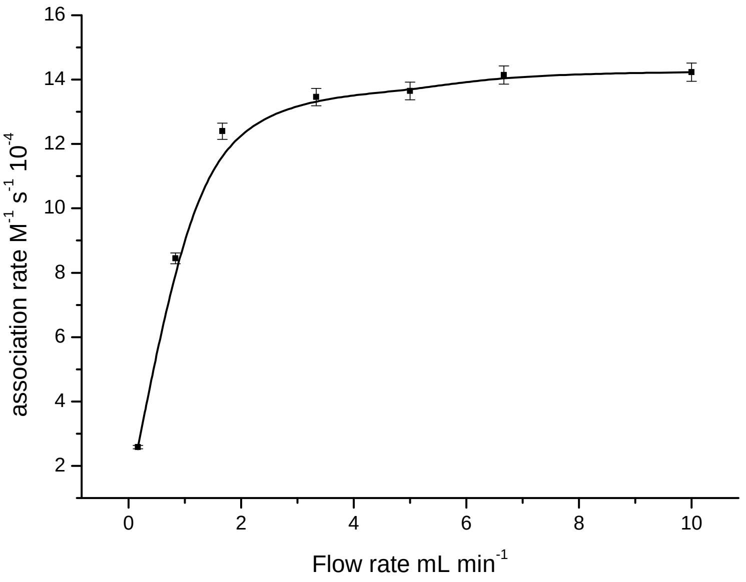

Figure 2.5 CV association rate constant at the silica surface as a function of flow rate showing concentration-limited kinetics for flow rates above 3 mL min^{-1}

The light intensity lost through the back of the second mirror of the cavity is collected by a photomultiplier tube (PMT) (Hamamatsu module H7732MOD, containing a R4632 PMT, rise time 0.78 ns). The PMT has a longpass filter (Thorlabs) in front of the optical entrance, preventing light shorter than 550 nm. The PMT output is an electric current which is measured as a voltage at the oscilloscope through the 50 Ω impedance channel (Lecroy Waverunner Oscilloscope, LT262). The voltage is digitalised at a rate of 1 GHz with a vertical signal depth of 8 bits. The ring-down trace is collected as an average curve over 25 sweeps on the oscilloscope to improve signal-to-noise ratio. The acquired trace is uploaded to a PC and fitted to a single exponential using a non-weighted Levenburg-Marquardt non-linear fitting routine written in Labview 7.1 (National Instruments, 2004). The characteristic decay function time, τ is then reported and averaged over 4 repeats giving an average τ and standard deviation, of $\tau \pm \sigma$ with a variation σ/τ of less than 1% (*59*).

The wavelength of the radiation entering into the cavity can be tuned by rotating the β-Barium Borate crystal in the Surelite OPO Plus. The rotation is controlled by a microstepping controller, which was calibrated manually, using a UV-Vis spectrometer to measure the wavelength of the radiation emitted from the cavity, Figure 2.6 (A). The variation of wavelength with microstepping controller turns was fitted to an exponential function which gave an accurate wavelength calibration over the range 570-680 nm, Figure 2.6 (B), with an error of <0.1 nm.

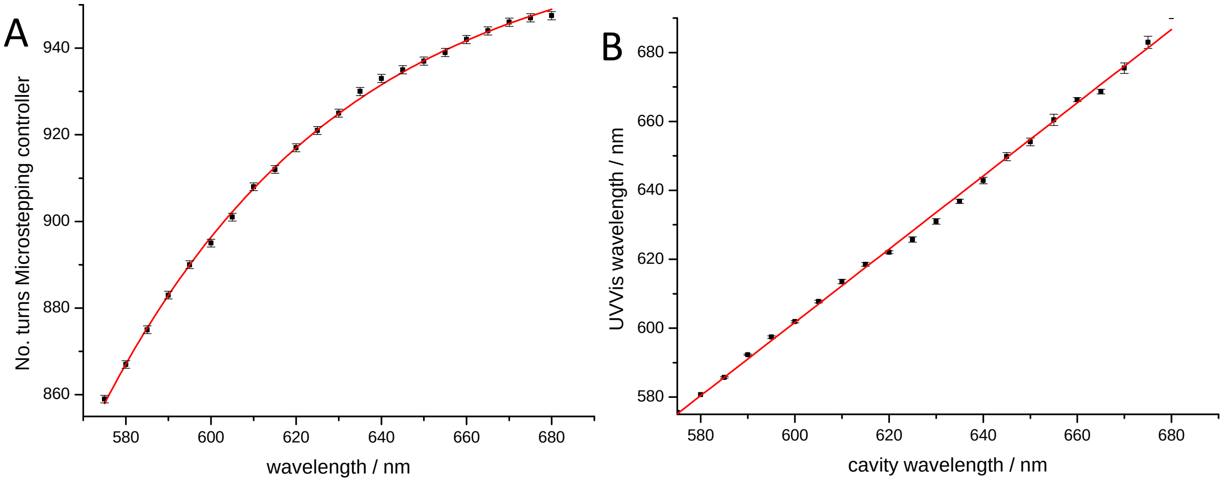

Figure 2.6 Calibration of the tuneable Surelite OPO Plus radiation wavelength entering into the cavity, A – showing the wavelength generated against the no. of turns of the microstepping controller, and B – showing the wavelength produced in the cavity

2.2.2 Dove Cavity Ring-down time, Cavity losses and Alignment

The τ in an empty cavity is determined by the reflectivity of the mirrors, using the previously mentioned Equation 2.2 to calculate the theoretical τ_{max} of the cavity. For the typical 94 cm cavity, the round trip time is 6.27 ns, and the mirror reflectivity is 0.9995. Using Equation 2.2, the current cavity setup gives a maximum ring-down time of 5.62 μs. After alignment of the cavity, data were collected showing the maximum τ for an empty cavity over the scanning range 580-710 nm, with a maximum τ value at 635 nm of 5.25 μs, Figure 2.7 (A) (a), in good agreement (93 ± 1 %) with the theoretical values. Any differences may be attributed to the wavelength dependence of the mirror coatings, cleanliness of the mirrors or nonideal optical alignment. The mirrors are centred at 635 nm, and the mirror reflectivity decreases away from this wavelength, causing the loss in τ observed.

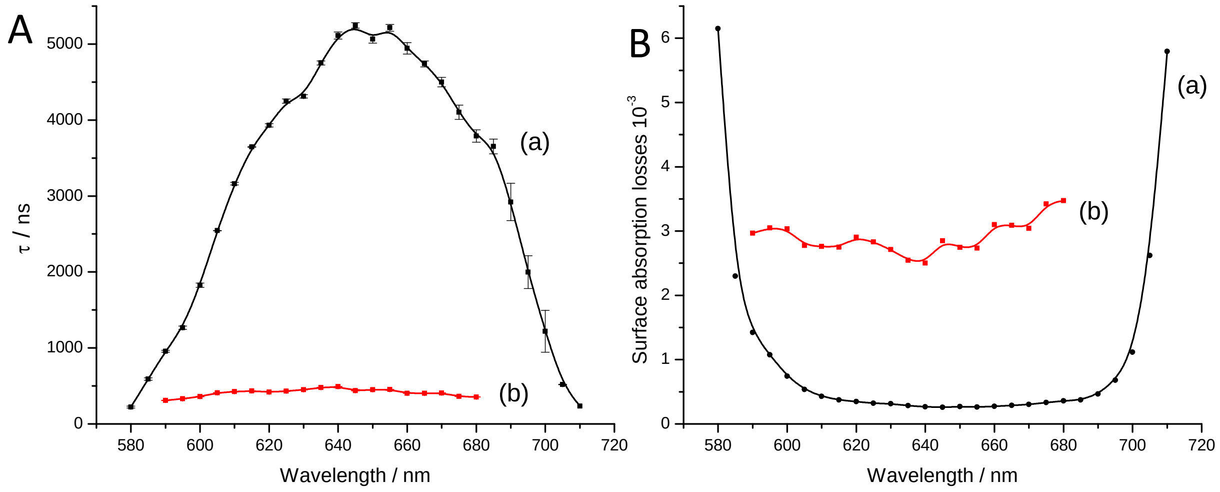

Figure 2.7 (A) shows the CRD τ spectrum in (a) the empty cavity over the range 580 – 710 nm, and (b) in the Dove cavity with the TIR element present, over the range 590 – 680 nm. (B) shows the absorbance losses associated with (a) τ of the empty cavity over the wavelength range 580 – 710 nm, and (b) in the Dove cavity over the range 590 – 680 nm.

When the TIR element is introduced further losses decrease τ. The theoretical τ of the cavity with the TIR element present can then be calculated with the optical losses from the prism, *L* using Equation 2.4:

$$\tau = \frac{t_r / 2}{(1 - R) + L}$$

Equation 2.4

The losses in the Dove prism predominantly come from the AR coatings on the 45^{o} faces of the prism and the associated losses from absorption of the light passing through the silica prism. There are also associated losses caused by surface diffraction from the top surface which can be estimated through scalar diffraction theory (*29*), and frustrated internal reflection at the interface (*68*).

The τ of the Dove cavity was scanned from 590 – 680 nm, Figure 2.7 (A) (b), with a maximum τ achieved with a TIR element in the cavity at 635 nm of 452 ns. This relates to cavity loses of 6.2 x 10^{-3}. The greatest losses from the anti-reflection coatings are 4 x 10^{-3} for a round trip (Table 2.1), and the theoretical losses for the adsorption through the prism are 8.54 x 10^{-3} (*69*), (*70*). Together with the losses from the reflectivity of the cavity mirrors, this gives a total cavity loss of 13 x 10^{-3}, indicating a theoretical τ with a TIR element of 216 ns.

The difference in the two τ values may be attributed to the extinction coefficient for the BK7 silica prism used, with the value likely to be nearer 1.5 x 10^{-3} M^{-1} cm^{-1} rather than the 2 x 10^{-3} M^{-1} cm^{-1} which was used in the theoretical model whilst the other improvements from τ come from the uncertainties in the AR losses and surface roughness, with well-polished anti – reflective surface coatings giving smaller surface losses. The actual cavity results obtained in Figure 2.7 (A) indicate a very well aligned cavity consistent with the theoretical models.

2.2.3 Evanescent Wave Cavity Ring-Down Electronic Spectroscopy

The absorbance of analyte molecules at the TIR surface-flow cell medium interface is calculated by the losses of the cavity and the change in the ring-down decay, converting τ to absorbance using Equation 2.5:

$$Abs = \frac{1}{2.303}\frac{L}{c}\left(\frac{1}{\tau} - \frac{1}{\tau_0}\right)$$

Equation 2.5

Where *L* is the length of the cavity, and *c* is the speed of light. 2.303 is the conversion factor for natural logarithms into base 10 logarithms, to be consistent with the definition of absorbance. To calculate the absorbance losses of the empty cavity setup, Equation 2.5 may be used, Figure 2.7 (B) (a). The absorbance losses shown represent the limiting range of the cavity mirrors in place, giving an absorbance value at 635 nm of 2.86 x 10^{-4}. The absorbance losses of the Dove cavity can also be observed, Figure 2.7 (B) (b), which shows much greater absorbance, of 2.5×10^{-3} at 635 nm, a contribution of the surface losses of the prism.

The Beer-Lambert law is used to derive the analyte concentration from measured absorbance (*19*) , Equation 2.6:

$$Abs = \varepsilon \, c \, l$$

Equation 2.6

Where ε is the molar extinction coefficient (M^{-1} cm^{-1}), *c* is concentration, and *l* is path length (cm).

2.2.4 Q-factor and Finesse of the cavity

The Q or Quality of the cavity setup may be used to characterise the number of round trip light passes in the cavity relative to the observed τ, Equation 2.7.

$$Q = \frac{\tau}{t_r}$$

Equation 2.7

The Q-factor of an empty cavity is 837, whereas with a prism, it is 72.

The finesse of the cavity is a measure of the mirror reflectivity, the higher the reflectivity of the mirrors, the higher finesse of the cavity. The finesse of the cavity is given by Equation 2.8, where *R* is the reflectivity of the mirrors.

$$F = \frac{\pi\sqrt{R}}{1-R}$$

Equation 2.8

For an empty cavity, the mirror losses give a finesse of 6281, and for the Dove cavity the finesse is 505.

2.2.5 Dove Cavity Parameters

The cavity is optimised to give an experimental set-up with the following optical parameters, summarised in Table 2.1, giving an empty cavity τ greater than 5 µs, with a cavity containing a TIR element having a typical ringdown time of 450 ns.

Table 2.1 Dove Cavity Parameters

Cavity Parameter	Parameter Value	Parameter Unit
Laser Beam peak Energy	55	mJ
Laser repetition rate	10	Hz
Mirror Reflectivity	0.9995	%
Cavity Length	0.94 ± 0.1	M
Beam diameter	2 ± 0.1	mm
Surface Interrogated area	16.8 ± 0.8	mm^2
Flow cell volume	200 ± 10	µL
Penetration depth at 635 nm	235	nm
Flow rate	3.3	mL min^{-1}
Theoretical empty cavity, τ	5.62	µs
Maximum τ obtained for empty Cavity at 635 nm	5.25 ± 0.1	µs
Prism coating reflectivity at 635 nm	0.2	%
Absorption Coefficient (ε) of BK7 at 635 nm (*69*), (*70*)	$2x10^{-3}$	M^{-1} cm^{-1}
Optical Path in Dove Prism	24.7	mm
Absorbance of BK7	8.54×10^{-3}	cm^{-1}
Total theoretical losses in cavity with TIR element	13×10^{-3}	
Minimum Theoretical τ with TIR element	216.2	ns
Maximum τ, achieved with TIR element in the cavity	452	ns
Total cavity losses	6.2×10^{-3}	
Q-factor of empty cavity	837	
Q-factor of cavity with TIR element	72	
Finesse of empty cavity	6281	
Finesse of cavity with TIR element	505	

2.3 Experimental Methods

2.3.1 Prism Cleaning Protocol

The prism was placed in *aqua regia* (Concentrated Hydrochloric Acid (HCl) and Nitric Acid (HNO_3) (both Fisher Scientific) (3:1)) to remove any residual organic species from the prism back surface. The prism was then thoroughly washed with Water, Decon (10%), Water, Methanol (Fisher Scientific), Water and propan-2-ol (IPA) (Fisher Scientific, Analytical reagent Grade) before being dried under nitrogen gas. Small amounts of Sodium Hydroxide (NaOH, Fisher Scientific) (1 M) were pipetted onto the prism surface and left overnight. The surface was washed with water and IPA and dried.

2.3.2 Surface Preparation for positively charged species

Crystal Violet (Aldrich ACS reagent, 95%) and Malachite Green (Fisher Scientific, 95%) solutions were prepared with ultrapure water (18 MΩ cm^{-1}) to the desired concentration range. Small volumes of NaOH (1 M) and HCl (1 M) solutions were used to vary the pH of the solutions and the water buffer without significantly altering concentration. The solution pH was monitored using a Jenway 3520 pH meter, with the electrode stored in Hanna Electrode Storage Solution, and Calibrated using Sigma Aldrich Buffer reference standards. The prism surface cleaning protocol was as follows: IPA, methanol, sodium dodecyl sulphate (1%) (SDS, Sigma-Aldrich, 99%) in methanol, water, 0.1 M HCl, 0.1 M NaOH, 0.1 M HCl, Water, IPA. pH adjusted ultrapure water was then passed over the prism until a stable baseline was obtained before commencing data collection.

A baseline τ, was recorded for the pH-adjusted water buffer. The CV and MG solutions were then prepared to the adjusted buffer pH levels, and run across the clean, negatively-charged silica surface. The association rate of the cationic dyes were monitored over time at 635 nm observing the change in τ, until the maximum surface coverage at the test pH was observed. At this point, the dye surface spectrum was recorded measuring τ over the wavelength range 575 nm – 680 nm at 5 nm intervals. At each of these wavelengths an average of 4 estimates of τ is made determining a mean, μ and standard deviation, σ for the value. The dissociation rate of the CV and MG species on the silica surface was then measured by switching the flow back to pH adjusted water buffer and monitoring the change in τ, with the dye spectrum also recorded for the dissociated surface.

2.4 Results

The surface interactions and electronic spectra of the positively-charged chromophore species CV and MG were investigated using the EW-CRDS detailed above (Chapter 2.2).

2.4.1 Crystal Violet interaction at the negatively charged interface

The solution phase spectra of CV, Figure 2.8, shows no change in the extinction coefficient with pH over the range 4-10, and gave a λ_{max} extinction coefficient ε_{583nm}= 7.5 ± 0.05 x 10^4 M^{-1} cm^{-1}.

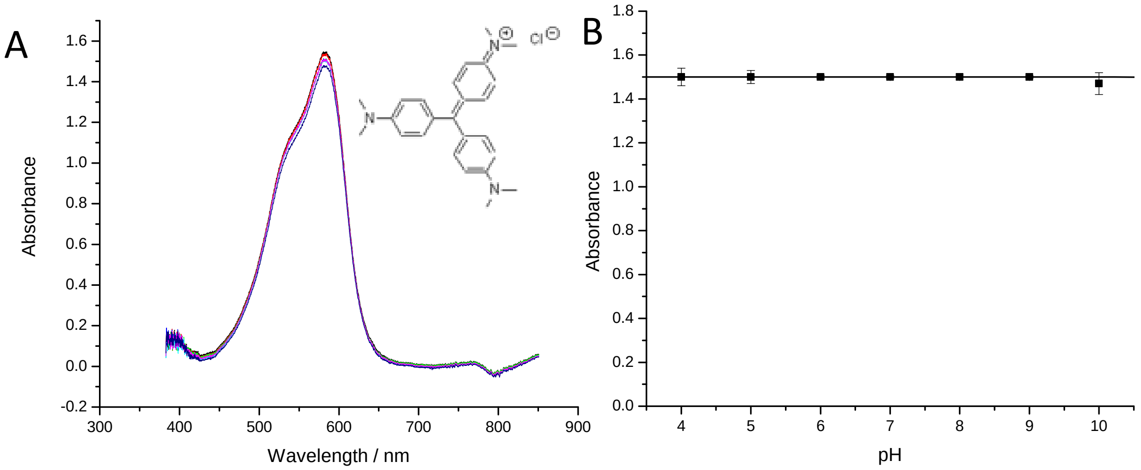

Figure 2.8 A - CV solution phase spectra from pH 4 – 10, and CV structure (inset), and B – the CV λ_{max} against bulk pH

The adsorption of CV to the silica-water interface was monitored at 635 nm and the electronic spectra measured over the range 585 - 675 nm. The association and dissociation kinetics of CV (20 μM) were measured as a function of bulk pH, and are shown in Figure 2.9 (A) at (a) pH 9 and (b) pH 5, indicating greater CV absorbance at higher pH. Switching to the free pH-adjusted buffer results in a significant decrease in the observed absorbance, and the final absorbance observed after the buffer wash off shows an increase with pH, with the uncertainty in the values obtained from the average of 100 successive data points obtained from the EW-CRDS. The full surface coverage, θ_1 absorbance values decrease from 4.69 ± 0.03 x 10^{-3} at pH 9, down to 9.2 ± 0.2 x 10^{-4} at pH 5, with the absorbance after wash off, θ_2 decreasing from 1.09 ± 0.03 x 10^{-3} to 6.8 ± 0.2 x 10^{-3} at the same pH values. The variation of θ_1 for CV (20 μM) is shown as a function of bulk pH, Figure 2.9 (B) (a), and for the absorbance following the wash with pH-adjusted buffer θ_2, Figure 2.9 (B) (b).

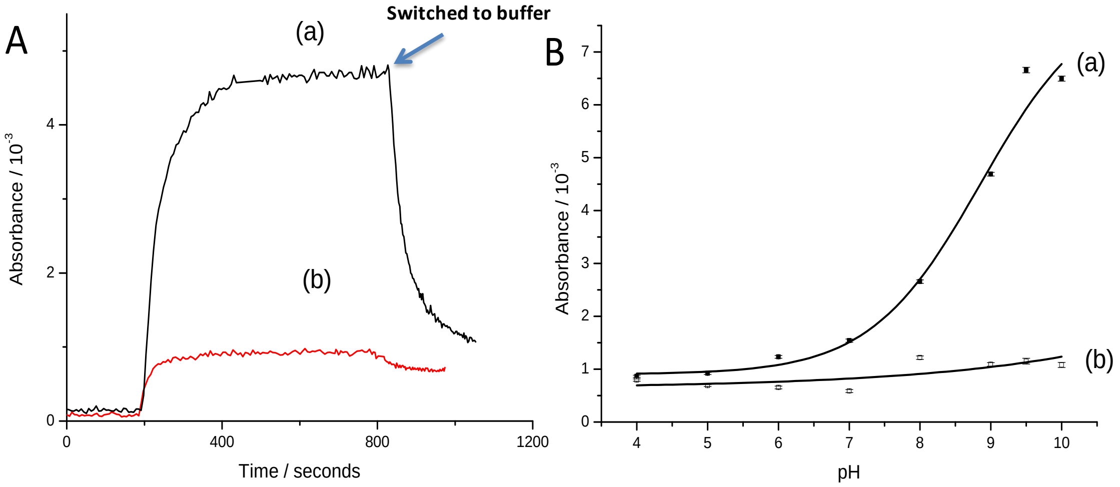

Figure 2.9 Variation of absorbance observed at 635 nm of CV (20 μM) at the silica-water interface as a function of bulk pH. A - association and dissociation on a silica surface at (a) pH 9 and (b) pH 5, and B - Adsorption Isotherms for (a) full surface coverage of CV (20 μM) on the silica surface θ_1 and (b) after water wash off of CV (20 μM) on the surface θ_2 *vs* pH

An electronic spectrum for the CV chromophore cation was measured after the surface adsorption kinetics had stabilised to θ_1, at each of the different pH values. Similar spectra were also recorded for CV θ_2. The electronic spectra for CV at θ_1 are shown in Figure 2.10 (A) at (a) pH 9 and (b) pH 5. The interface electronic spectra may be compared with the solution phase spectrum shown as the black line in Figure 2.10 which shows no variation with bulk pH. The interfacial electronic spectra show two maxima shifted from the solution phase spectrum, S_1 and S_2, one maximum observed shifted to the blue at 581 nm, S_1, a shift of 2 nm, and a further, more pronounced maximum in the red at 607nm, S_2, a shift of 24 nm. The $\theta_1 S_1$ peak decreases in intensity at lower pH, with an absorbance at pH 9 of 12.7 ± 0.06 x 10^{-3}, decreasing to 2.52 ± 0.06 x 10^{-3} at pH 5. The 24 nm red shift $\theta_1 S_2$ maximum shows a broadening of the shoulder into the red region observed as the pH is increased giving absorbance values at pH 9 of 9.36 ± 0.04 x 10^{-3}, down to 2.6 ± 0.1 x 10^{-3} for pH 5. Figure 2.10 (B) shows the spectra normalised to 1 at 607 nm, the S_2 peak maximum, for ease of comparison. The normalised spectra show the variation in the S_1 peak clearly, showing a normalised $\theta_1 S_1$ value of 1.36 ± 0.01 at pH 9, decreasing to 0.96 ± 0.01 at pH 5.

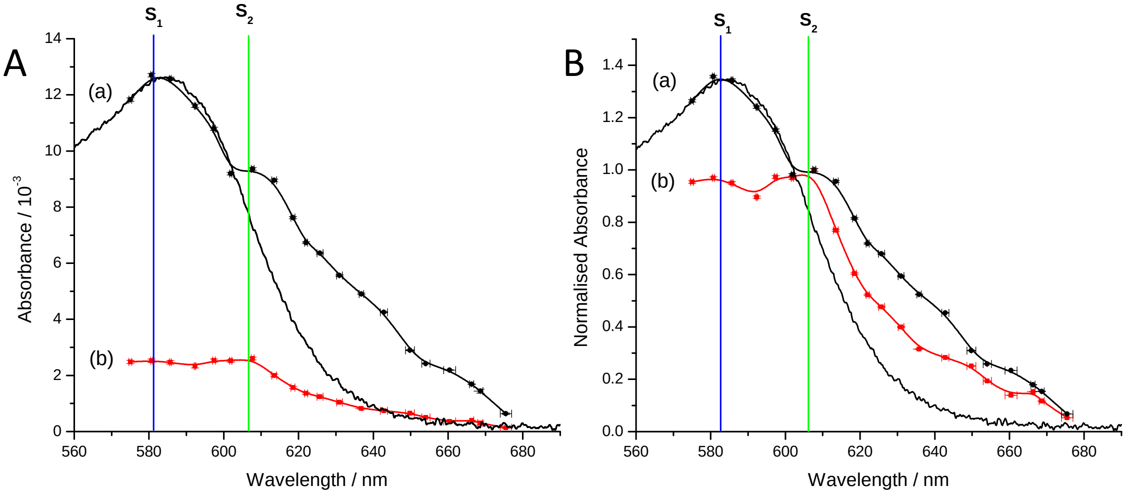

Figure 2.10 A – Electronic surface spectra of CV (20 μM) θ_1, at (a) pH 9 and (b) pH 5, and B – θ_1 normalised surface spectra at 607nm, with the CV solution phase shown in black

The CV θ_2 electronic spectra, Figure 2.11 (A) shows two maxima, S_1 and S_2 at the same wavelengths as previously. The spectra show a reduced broadening at longer wavelengths and a significant decrease in $\theta_2 S_1$ absorbance compared to $\theta_1 S_1$. At pH 9, Figure 2.11 (A) (a), $\theta_2 S_1$ shows an absorbance value of 4.26 ± 0.02 x 10^{-3}, and 3.98 ± 0.02 x 10^{-3} for $\theta_2 S_2$, with absorbance values of 1.72 ± 0.01 x 10^{-3} and

1.75 ± 0.04 x 10^{-3} for pH 5 θ_2S_1 and θ_2S_2 respectively. The spectra are again normalised at the maximum of the red shifted peak, Figure 2.11 (B) and show comparable θ_2 spectra at both pH's, with normalised θ_2S_1 values of 1.07 for pH 9 and 0.98 for pH 5.

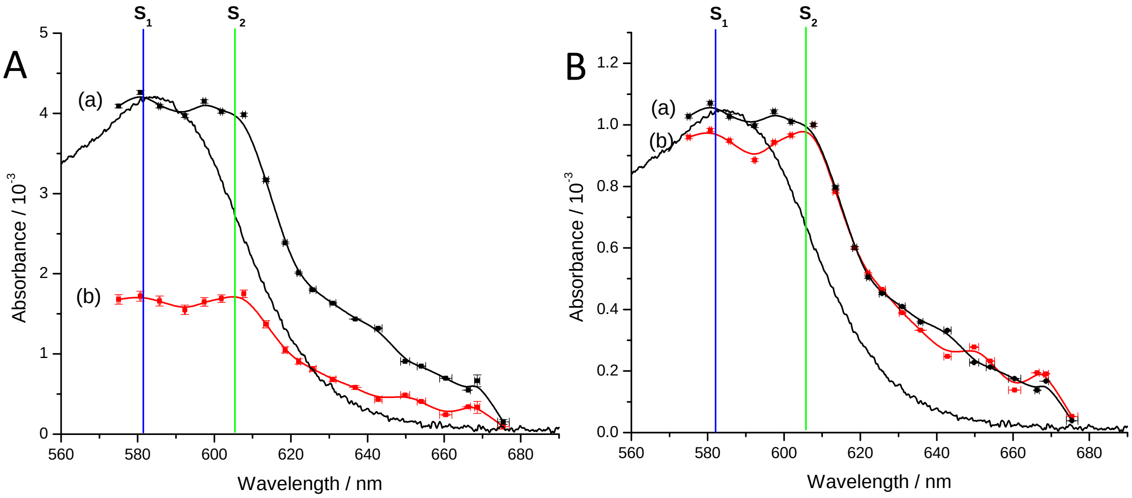

Figure 2.11 A – Electronic surface spectra of CV (20 µM) θ_2, at (a) pH 9, and (b) pH 5, and B – θ_2 normalised surface spectra at 607nm, with the CV solution phase shown in black

2.4.2 Malachite Green interaction at the negatively charged interface

The solution phase spectra of MG, Figure 2.12, also displayed no change within the error in the experimental pH range tested, and gave a λ_{max} extinction coefficient ε_{620nm}= 7.56 ± 0.05 x 10^4 M^{-1} cm^{-1}.

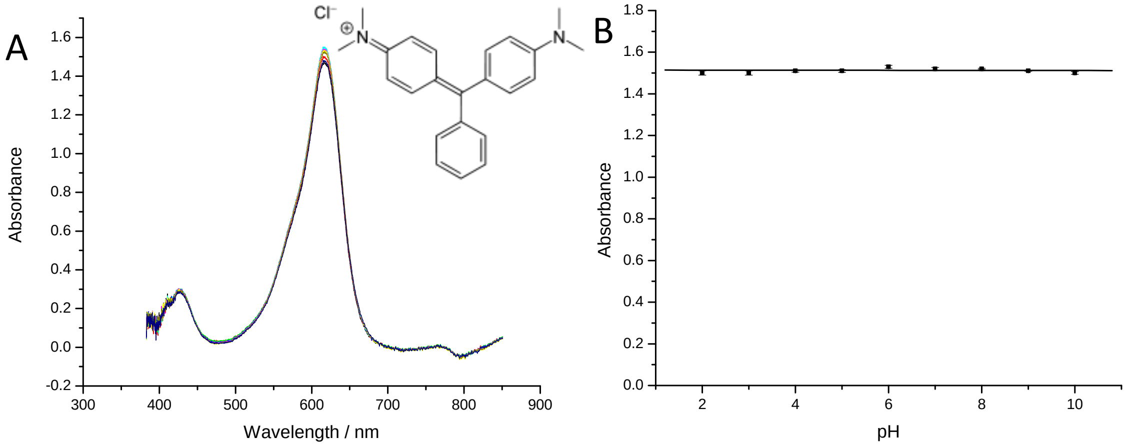

Figure 2.12 A - MG solution phase spectra from pH 2 – 10, and MG structure (inset), and B – the MG λ_{max} against bulk pH

Similar measurements monitoring the adsorption of MG (20 μM) were performed at 635 nm, shown in Figure 2.13 (A) (a) pH 9, and (b) pH 5. The adsorption kinetics for MG appear fast compared to CV, with larger surface absorbance, θ_1. There is also a significant change to θ_2 following the wash-off with the pH-adjusted buffer, with almost all of the MG removed off the surface. The θ_1 surface absorbance at pH 9 is 5.9 ± 0.1 x 10^{-3}, decreasing down to 2.4 ± 0.2 x 10^{-3} for pH 5, with very small θ_2 absorbance values of 2.1 ± 0.1 x 10^{-4} and 1.5 ± 0.2 x 10^{-4} at the same bulk pH values. The variation of surface adsorption for θ_1 and θ_2 with bulk pH are shown in Figure 2.13 (B) (a) and (b), showing an increasing absorbance trend with pH.

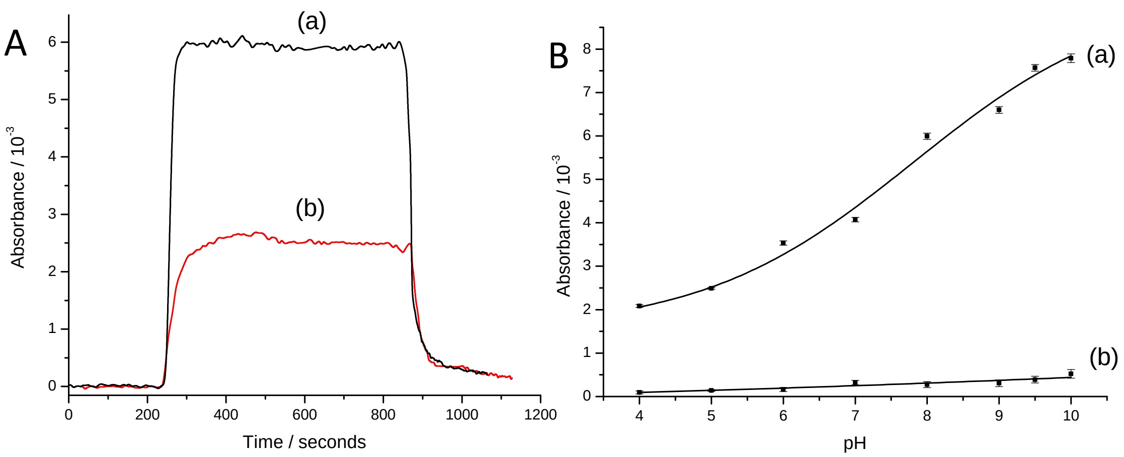

Figure 2.13 Variation of absorbance observed at 635 nm of MG (20 µM) at the silica-water interface as a function of bulk pH. (A) - Association and dissociation on a silica surface at (a) pH 9, and (b) pH 5, and (B) - Adsorption Isotherms for (a) full surface coverage of MG (20 µM) on the silica surface θ_1 and (b) after water wash off of MG (20 µM) on the surface θ_2 v pH

The θ_1 electronic surface spectra of MG (20 µM) was measured at each pH value over the wavelength range 580 nm – 675 nm, Figure 2.14, (a) pH 9 and (b) pH 5 with the MG solution phase spectra shown in black. The surface spectra show a complex, broad general shape with a blue-shifted maximum, $\theta_1 S_1$, at 609 nm which may be compared to the solution phase λ_{max} of 620 nm. This feature appears to grow and broaden further into both the blue and red shifted regions with increasing bulk pH. The absorbance observed at $\theta_1 S_1$ decreases with pH giving values of $8.8 \pm 0.1 \times 10^{-3}$ at pH 9 down to $3.6 \pm 0.2 \times 10^{-3}$ at pH 5. The spectra have been normalised to 609 nm at the maximum of the peak, to show the difference in the broadening of the surface spectra with pH.

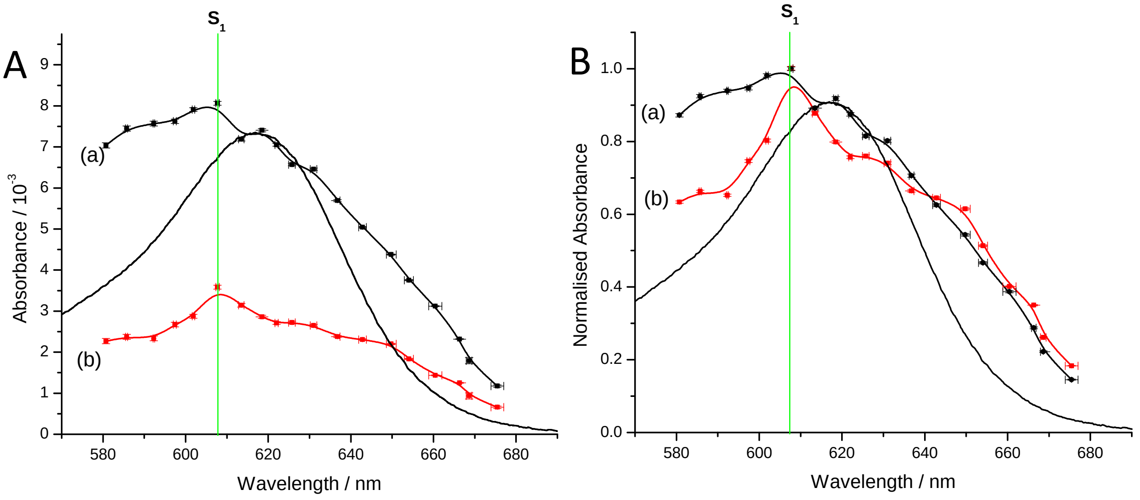

Figure 2.14 A – Electronic surface spectra of MG (20 μM) θ_1, at (a) pH 9 and (b) pH 5, and B – θ_1 normalised surface spectra at 609 nm, with the MG solution phase shown in black

There were no MG θ_2 electronic spectra obtained as the MG molecules appeared to almost completely dissociate off the surface, leaving minimal θ_2 absorbance.

2.5 Discussion

The association of the charged chromophores onto the silica surface will form an interface structure, which will depend on the bulk and interfacial pH. The surface will have greater negative charge at higher pH, corresponding to the two pK_a values of the silanol groups, producing an enhanced interfacial concentration of the counter-ion attracted by the surface potential (*6*). The positive chromophore will be attracted to this surface, balancing the electric charge, with the association kinetics at the interface then controlled by the surface potential and the interfacial concentration. There are many models for the structure of the charged interface, discussed in the introduction, with the ideas of a double layer at the interface, composed of a tightly bound Stern layer, with a weaker diffuse or GC layer away from the surface (*12, 14*). The interface model can be further developed, with the splitting of the Stern Layer into an inner and outer Helmholtz plane (*15*), while it has also been postulated that counter-ions can condense at the interface forming stable structures, counter-ion condensation (*71*). There are three possible interfacial structures of chromophores proposed here, molecules associated directly with the surface Q3 and Q2 sites, molecules present within the tightly ordered Stern layer, and molecules randomly orientated in the GC layer.

2.5.1 Crystal Violet Interface kinetics

The study of the interface kinetics of CV molecules was observed at a fixed concentration (20 μM) in relation to bulk pH. The interface adsorption for CV association at the silica surface to produce θ_1 total coverage appears to be exponential in shape, Figure 2.9 (A). The dissociation observed when flow is switched to running buffer shows CV dissociating slowly without getting completely dissociated with buffer, θ_2. The θ_1 surface coverage can be attributed to interaction in the GCS interface, total surface coverage. This includes stable molecules in the Stern layer, and less stable molecules in the GC layer. The molecules washed off are the low energy loosely bound interactions within the GC layer, leaving the θ_2 absorbance attributed to the stable molecules in the Stern layer. The difference in the θ_2 Stern layer stability is highlighted by observing the θ_1: θ_2 ratio, which gives values of 24.3:75.7 at pH 5 and 76.7:23.3 at pH 9 for CV. This indicates a more stable Stern layer formation at low pH, where you will only have Q3 silanol sites available, compare to at high pH, where over 75% of the CV structure interaction is a contribution of the θ_1 association.

An increase in maximum absorbance, θ_1 of the molecules on the surface was observed, as the pH was increased, Figure 2.9 (B) displaying a complex adsorption isotherm associated with the charge on the two types of silanol site present on the silica surface. The Q3 groups have a pK_a of 4.5 (*1*) and will be fully dissociated throughout the bulk pH range observed of the experiment. The Q2 sites have a higher pK_a, and will show minimal dissociation at low pH. As the bulk pH is increased, greater dissociation of Q2 groups will result in a higher number of negatively charged surface binding sites, attracting more positively charged chromophore molecules to balance the charge in the interfacial structure. The ratio of the silanol binding sites on the silica surface has been estimated by several techniques and found to be approximately 20:80 (*3, 6*). The ratio of silanol sites may be derived from the data shown in Figure 2.9 by comparing the ratio of the surface coverage θ_1 values at pH 5 and pH 9, showing a Q3:Q2 ratio of 21.3:78.7, in good agreement with previous determinations.

The rate of surface coverage of the CV at the silica surface is governed by both the adsorption and desorption processes as well as the bulk CV concentration. The rate of surface coverage can be written as:

$$\frac{d\theta}{dt} = k_a[CV][1-\theta] - k_d[\theta]$$

Equation 2.9

Here, k_a is the association rate constant, [CV] is the CV bulk concentration in solution, θ is the fractional surface coverage and k_d is the dissociation rate off the surface. In the initial stages, θ is very small ($\theta \rightarrow 0$), meaning the initial rate surface coverage can be written as:

$$\frac{d\theta}{dt} = k_a[CV]$$

Equation 2.10

Initial rate analysis of CV onto the silica surface was estimated, fitting lines to the initial linear feature of the adsorption curves obtained, with the uncertainty given by the error in the linear fit to the data. The k_a values for CV were plotted against pH, Figure 2.15 (A). CV displays a change with pH, giving a rate of 0.3 ± 0.04 M^{-1} s^{-1} at pH 5 up to 3.5 ± 0.2 M^{-1} s^{-1} at pH 9. The results indicate a non-linear trend in the rate, which is indicative of the change in the surface potential. This has been seen previously (*1*) and is expected, attributed to the different dissociation values of the Q2 and Q3 silanol groups at the surface.

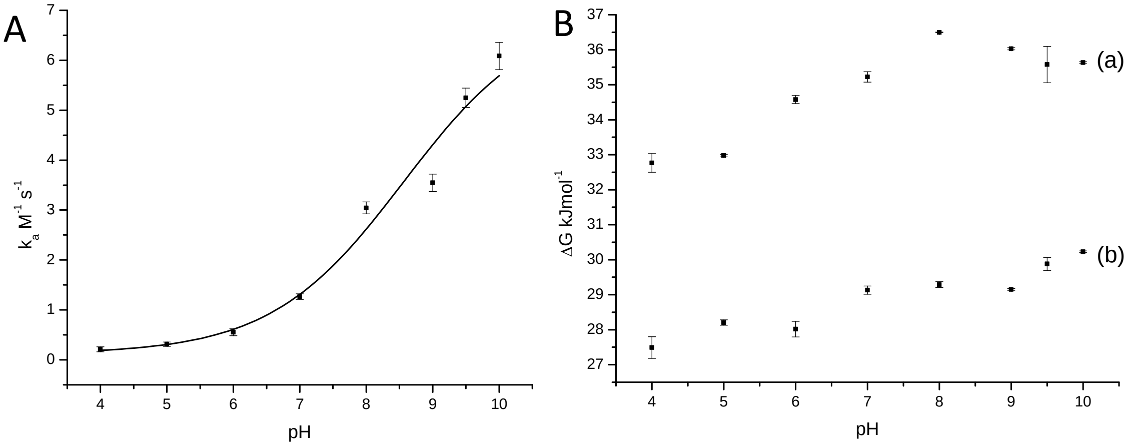

Figure 2.15 A - Variation of the association rate constant for CV (20 µM) with pH and B - Energy of interaction for CV (20 µM), (a) ΔG θ_2 and (b) ΔG θ_1

The dissociation rate for both the θ_1 and θ_2 surfaces were calculated, k_{d1} and k_{d2}, (not shown). The CV showed a θ_1 dissociation rate, k_{d1} of $3.5 \pm 0.4 \times 10^{-6}$ s^{-1} at pH 5 and $2.7 \pm 0.2 \times 10^{-5}$ s^{-1} at pH 9. There is greater dissociation at higher pH indicating the removal of a larger loosely bound GC layer formed with the greater surface potential at pH 9. The θ_2 dissociation rate k_{d2} was harder to derive, but showed values of $5.2 \pm 0.1 \times 10^{-7}$ s^{-1} and $1.7 \pm 0.1 \times 10^{-6}$ s^{-1} for CV, at pH 5 and 9.

The energy of interaction indicating structure stability was calculated by deriving the dissociation constant K_D, from which values the energy required to remove the molecules off the surface, the Gibbs free energy (ΔG), was derived. The Gibbs free energy is obtained from the enthalpy and entropy of the reaction observed, and calculated using Equation 2.11:

$$\Delta G = -RT \ln(K_D)$$

Equation 2.11

θ_1 and θ_2 interfacial binding energy values were derived for CV Figure 2.15 (B), with the k_{d1} values taken for the initial fast dissociation observed off the surface, to give a $\theta_1 K_D$, and the k_{d2} values derived from the slow dissociation observed, to give a $\theta_2 K_D$. The θ_1 interfacial binding energy varied from $27.5 \pm 0.2 - 29.9 \pm 0.1$ kJmol^{-1}, Figure

2.15 (B) (b) over the bulk pH range, with an increasing trend observed linked with greater surface potential. The θ_2 interfacial binding energy varied from 32.97 ± 0.03 – 36.02 ± 0.03 kJmol^{-1}, Figure 2.15 (B) (a). The interfacial binding energies observed indicate that the initial dissociation θ_1 requires lower energy, associated with the weaker binding interface in the GC layer, whereas the θ_2 energy is higher, showing a stronger binding attributed to Stern layer interaction of molecules.

2.5.2 Electronic Molecular Spectra of Crystal Violet at the Charged Silica-Water Interface

The structure of CV at the interface has been probed by measuring the electronic spectrum of CV at different pHs at both the full surface coverage θ_1 interface, Figure 2.10 and also the θ_2 interface after buffer wash off, Figure 2.11, to look at the molecular structure compared to solution phase and to observe differences at high and low pH. The CV surface spectra show two pronounced peaks, one close to the solution phase maximum slightly shifted in the blue region, S_1, and a second peak, significantly shifted 24 nm towards the red region, S_2 compared to bulk λ_{max}. The complete spectrum observed is broad, extending beyond 680 nm in the θ_1 interface, which significantly reduces when the θ_2 interface spectrum was measured. The shifts observed may be attributed to a Stark shift, which occur when there is a shift by a surrounding electronic field on molecules in close proximity, and is associated with a shift in surface spectrum (*72*).

The small blue shift indicates that molecules associated with this S_1 peak are similar to those in the bulk, randomly oriented with respect to the surface. They may therefore be assigned as the molecules close to the surface, within the penetration depth of the radiation. Molecules loosely associated within the GC layer, which are removed by the buffer causing a decrease in the S_1 peak, as well as some molecules in the Stern layer, which remain on the surface. The S_2 peak, showing a strongly red-shifted spectrum may be associated with a large Stark effect derived from the electric field present in the strongly associated interfacial structure. Large Stark effects have been observed (*72*) typically in fields as large as 500 kV cm^{-1}, whereas the interfacial electric field here is approximately 125 kV cm^{-1} depending on the surface charge and estimations of the relative permeability and interface dimensions. The S_2 spectrum may be a new molecular environment in which the delocalization volume for the electrons in the orbital's associated with the electronic transition is significantly larger. This shifted peak may be attributed to the molecules lying in a planar orientation directly associated with the Q2 and Q3 silanol groups in the Stern layer. Parida *et al.* have shown that dye molecules may associate at the interface in plane on plane orientation or end to end orientation, with different binding orientation resulting in hypsochromic and bathochromic shifts (*73*).

Previous work (*3, 47, 74*) has suggested that CV molecules may lie in a horizontal orientation on the silica surface, in particular on isolated Q3 binding sites and can form dimer structures through *π*-stacking in this planar formation (*74, 75*). This is because of its molecular structure, as the orientation of the molecules on the surface are controlled by the amino acid groups present (*76*); the CV molecule has a single positive charge across the pH range observed (*75, 77*), showing a symmetrical shape with one amino group present on each benzene ring, giving 3 amino-benzyl groups. Here there will be greater localised positive charge, but an evenly distributed charge over the whole structure, Figure 2.16.

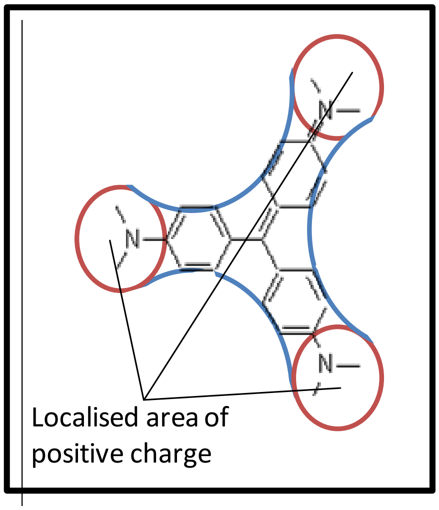

Figure 2.16 Charge density distribution on a CV molecule

The shifted S_2 peak is present both in the pH 9 and the pH 5 θ_1 and θ_2 spectra, Figure 2.10 and Figure 2.11, indicating that these molecules in planar orientation form stable complexes, which are not easily dissociated off the surface, Figure 2.17. It is likely that the planar orientation of the CV molecules will be on the isolated Q3 silanol groups, which will be present at all pH values. It has previously been demonstrated through polarised spectroscopy that Rhodamine dye molecules favoured planar formation when in isolation on the silica surface (*76*). Fan *et al.* (*47*) has also demonstrated that CV molecules may orientate themselves both in a planar and vertical position on isolated charged sites, but on the Q2 sites, where the charges are in close proximity the molecules were tilted off the surface at an angle of 40°, a feature of the CV molecules in close proximity.

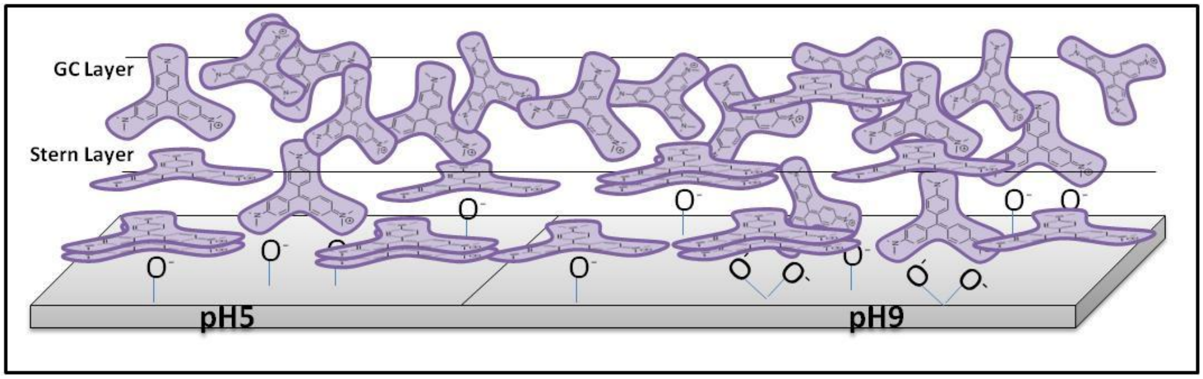

Figure 2.17 Schematic proposing the horizontal and vertical surface binding orientation of CV on low and high pH silica surfaces

The two shifted peaks observed in the CV spectra can be deconvolved into two spectra with Lorentzian shapes, with a fitted width of 40 nm, to extract the contribution of both peaks in the spectrum observed, Figure 2.18. At pH 9 the S_1 peak has an absorbance maximum of $11.5 \pm 0.3 \times 10^{-3}$ and an S_2 peak absorbance of $5.6 \pm 0.3 \times 10^{-3}$, showing a λ_{max} ratio of 2.1:1. Using Beer – Lambert law, and taking the extinction coefficient as $\varepsilon_{583nm} = 7.5 \pm 0.05 \times 10^4$ $M^{-1}cm^{-1}$, across the pH range, Figure 2.8, the θ_1 interfacial concentration can be estimated as 1.36 ± 0.02 molecules nm^{-2}. At pH 5 the S_1 and S_2 peak values were $1.92 \pm 0.01 \times 10^{-3}$ and $1.98 \pm 0.01 \times 10^{-3}$, showing a peak ratio of 0.97:1. This gave a θ_1 interfacial concentration at pH 5 of 0.31 ± 0.01 molecules nm^{-2}. These values decreased to 0.47 ± 0.02 molecules nm^{-2} and 0.21 ± 0.01 molecules nm^{-2} for pH 9 and 5 at $\theta_{2.}$

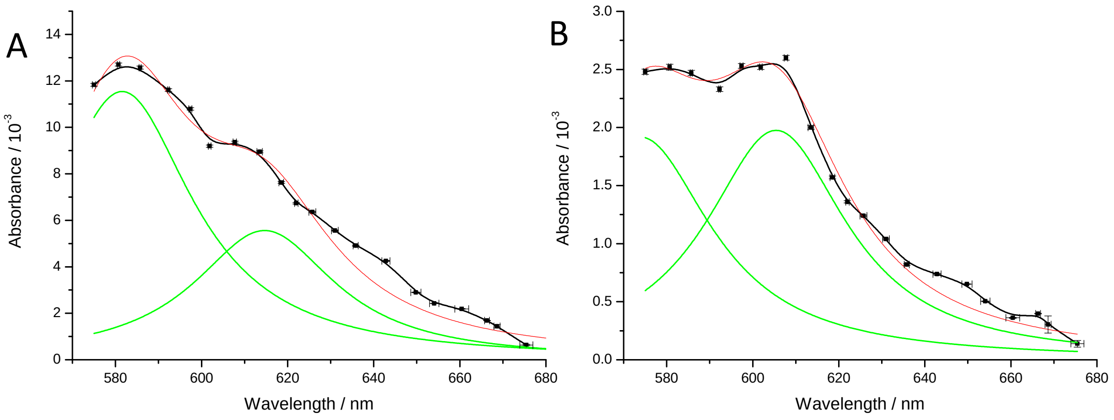

Figure 2.18 Showing the deconvolved CV absorbance spectra for A – pH 9 and B – pH 5

The silanol site density has previously been calculated to be in the region of 0.8 nm^{-2} (*3*) – 4 nm^{-2} (*43*), depending on the precise protocol of surface preparation. Here the silanol site density is taken as 2 nm^{-2} from previous work (*6*), which indicates that at pH 9 there will be approximately 2.72 molecules per silanol site, decreasing to 0.94 molecules per silanol site after wash off, indicative of a stable monolayer formed at the surface. With the interrogated area of the silica surface in the cavity estimated to be 16.8 ± 0.8 mm^2 (Section 2.2), the number of CV molecules interrogated at pH 9 is approximately $2.3 \pm 0.2 \times 10^{13}$.

2.5.3 Malachite Green Interface kinetics

The interface kinetics of MG were observed at a fixed concentration (20 µM) in relation to bulk pH. The interface adsorption for MG appears to be significantly faster and linear in shape compared to the CV surface adsorption, Figure 2.13. The dissociation observed is also different, showing almost immediate and complete MG wash off with buffer, θ_2, indicating an unstable GCS interface. The difference in the Stern layer stability can be observed by comparing the θ_1: θ_2 ratio, which gives values of 94.3:5.7 at pH 5 and 95.4:4.6 at pH 9 for MG, compared to 24.3:75.7 at pH 5 and 76.7:23.3 at pH 9 for CV, indicating that over 90% of the MG surface coverage is a contribution of the unstable θ_1 association. The adsorption isotherms displayed a similar increase in maximum absorbance θ_1 of the molecules on the surface as the pH was increased, Figure 2.14 (A), a feature of the two types of silanol site present on the silica surface. The ratio of silanol sites derived from the MG data, Figure 2.14 (B), comparing the ratio of the surface coverage θ_1 values at pH 5 and pH 9, show a Q3:Q2 ratio of 26.6:73.4, compared to 21.3:78.7 seen previously for CV.

The initial rate analysis of MG onto the silica surface was calculated and plotted against pH, Figure 2.19 (A). MG shows a significantly faster rate of surface association, with a k_a of 2.9 ± 0.4 M^{-1} s^{-1} at pH 5, rising up to 8.5 ± 1 M^{-1} s^{-1} at pH 9, compared to CV rates of 0.3 ± 0.04 M^{-1} s^{-1} at pH 5 and 3.5 ± 0.2 M^{-1} s^{-1} at pH 9. The dissociation rates were also faster (not shown), with a MG θ_1 k_{d1} of 5.1 ± 0.3 x 10^{-5} s^{-1} at pH 5 and 8.2 ± 0.6 x 10^{-5} s^{-1} at pH 9. θ_2 k_{d2} rates were not determined for MG, as the θ_1 structure was almost fully removed.

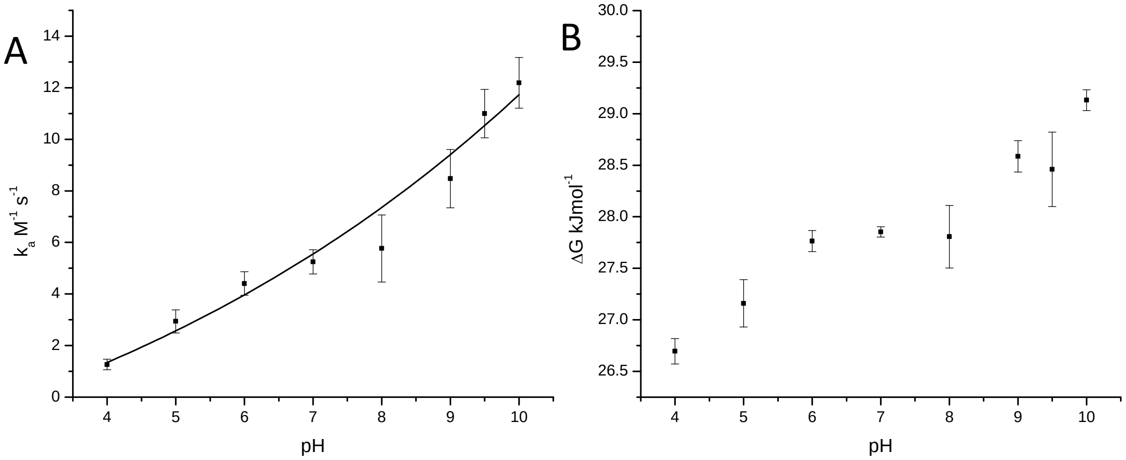

Figure 2.19 A - Variation of the association Rate Constants for MG (20 µM) with pH and B - Energy of interaction of MG (20 µM) for ΔG θ_2

The θ_1 interfacial binding energy values were derived for MG Figure 2.19 (B) displaying a variation from 26.7 ± 0.1 – 29.1 ± 0.1 $kJmol^{-1}$. These values are lower than for CV, with the MG molecules more easily dissociated, attributed to the complex planar and π-stacking binding structure of the CV in the interface.

2.5.4 Electronic Molecular Spectra of Malachite Green at the Charged Silica-Water Interface

The interface θ_1-spectrum of MG observed shows a definite maximum present at lower pH merging into a single broader feature at higher pH with a surface peak shifted 9 nm into the blue region, Figure 2.14 (A). The different features observed for MG may be attributed to the different charge density distribution of the molecules. Whereas CV has an evenly distributed charge density across the molecule, MG has only two areas of localised positive charge, with two amino-benzyl groups, Figure 2.20.

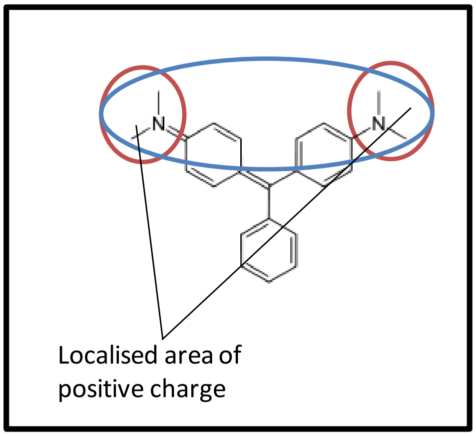

Figure 2.20 Charge density distribution on a MG molecule

The molecule therefore has an asymmetric charge distribution across the structure with one side having significantly greater positive charge. This suggests that the MG molecule is effectively polar indicating a strong preference for binding end on with the MG molecules unable to bind in close orientation on the Q2 and Q3 groups, compared to the planar orientation of the CV molecules. This can be seen in the broad features of the surface spectra, indicating weak randomly associated molecules in close proximity to the surface, Figure 2.21. This binding preference is also attributed to the unstable GCS layer structure, with the molecules easily dissociated, removing over 90% of the molecules off the surface.

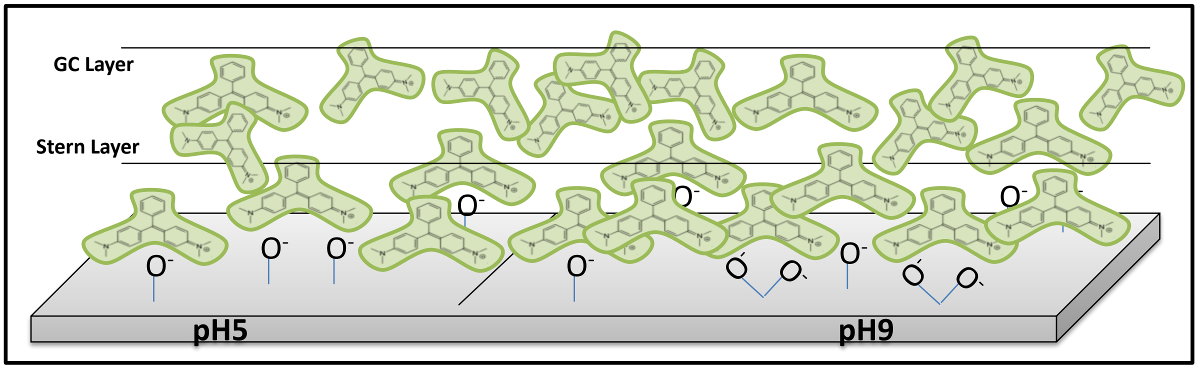

Figure 2.21 Schematic proposing the surface binding orientation of MG on low and high pH silica surfaces

As the surface spectra were broad and it was unclear if there were one, two or many different MG surface spectra at the interface, the interfacial concentration was calculated from the θ_1 maximum absorbance values, assuming $\varepsilon_{620nm} = 7.56 \pm 0.05 \times 10^4$ M^{-1} cm^{-1}, Figure 2.12, and gave interfacial concentration values of 0.6 ± 0.02 molecules nm^{-2} at pH 9 and 0.2 ± 0.01 molecules nm^{-2} at pH 5. These values show fewer MG molecules per silanol group, with 1.2 molecules per silanol compared to 2.72 molecules per silanol in the GCS layer, attributed to the ability of the CV able to get in close proximity to the silanol sites and form dimmers through π bonding, with molecules situated on top of one another.

2.6 Conclusions

The aim of this Chapter was to understand molecular interactions with the silica surface groups that make up the charged interface, as this model could then be related specifically to nanoparticle environmental interfaces. This chapter has developed the Dove cavity using EW-CRDS as a technique for surface interrogation, molecule association, stability and electronic spectra at the interface, using CV and MG chromophores. The silica surface has been shown to be influenced by solution pH, with a greater number of Q2 silanol sites available at higher pH giving a larger negative surface potential. The CV electronic spectra point towards a stable single molecular layer at the surface containing two electronic structures, with the CV molecules able to bind in a planar orientation in close proximity to the surface, causing a stark shift observed in the CV surface spectra, as well as end on away from the surface. A second loosely bound layer was identified, which was able to be removed off the surface, and displayed similar surface spectra features to the bulk solution phase molecules. Molecular interfacial concentrations indicated predominantly mono-layer formation at the surface, with 0.94 molecules per silanol site at pH 9. The association and dissociation rates, showed an unstable easily removed GC layer, and a more stable Stern layer and this simple interface model can now be used to investigate environmental parameters, looking at how competitive binding and ionic strength in organic or inorganic suspensions will influence CV interaction, surface availability and stability in Chapter 3.

References

1. Ong, S, Zhao, X, and Eisenthal, K B. (1992) Polarization of water molecules at a charged interface: second harmonic studies of the silica/water interface, *Chemical Physics Letters 191*, 327-335.
2. Iller, R K. (1979) The Chemistry of silica: Solubility, polymerization, colloid and surface properties, and biochemistry, *Wiley New York*, 632 - 729.
3. Dong, Y, Pappu, S V, and Xu, Z. (1998) Detection of Local Density Distribution of Isolated Silanol Groups on Planar Silica Surfaces Using Nonlinear Optical Molecular Probes, *Anal. Chem. 70*, 4730-4735.
4. Bolis, V, Cavenago, A, and Fubini, B. (1997) Surface Heterogeneity on Hydrophilic and Hydrophobic Silicas: Water and Alcohols as Probes for H-Bonding and Dispersion Forces *Langmuir 13*, 895-902.
5. Chuang, I S, and Maciel, G E. (1997) A Detailed Model of Local Structure and Silanol Hydrogen Bonding of Silica Gel Surfaces, *The Journal of Physical Chemistry B 101*, 3052-3064.
6. Fisk, J D, Batten, R, Jones, G, O'Reilly, P, and Shaw, A M. (2005) pH Dependence of the Crystal Violet Adsorption Isotherm at the Silica-Water Interface, *J. Phys. Chem. B 109*, 14475-14480.
7. Dong, Y, and Xu, Z. (1999) Investigation of Size and Charge Effects on the Adsorption of Organic and Inorganic Cations at Solid-Liquid Interfaces Using Nonlinear Optical Molecular Probes, *Langmuir 15*, 4590-4594.
8. Ali, M A, and Dzombak, D A. (1996) Competitive Sorption of Simple Organic Acids and Sulfate on Goethite, *Environmental Science & Technology 30*, 1061-1071.
9. Gabaldón, C, Marzal, P, Ferrer, J, and Seco, A. (1996) Single and competitive adsorption of Cd and Zn onto a granular activated carbon, *Water Research 30*, 3050-3060.
10. Howard, S C, and Craig, V S J. (2009) Adsorption of the Cationic Surfactant Cetyltrimethylammonium Bromide to Silica in the Presence of Sodium Salicylate: Surface Excess and Kinetics, *Langmuir 25*, 13015-13024.

11. Koopal, L K, Riemsdijk, W H v, and Kinniburgh, D G. (2001) Humic matter and contaminants : general aspects and modeling metal ion binding.
12. Bard, A J, and Faulkner, L R (2001) *Electrochemical Methods: Fundamentals and applications*, 2nd ed., Wiley & sons, New York.
13. Yates, D E, Levine, S, and Healy, T W. (1974) Site-binding model of the electrical double layer at the oxide/water interface, *Journal of the Chemical Society, Faraday Transactions 1: Physical Chemistry in Condensed Phases 70*, 1807-1818.
14. Stojek, Z, and Scholz, F. (2010) The Electrical Double Layer and Its Structure, *Electroanalytical Methods*, 3-9.
15. Nakamura, M, Sato, N, Hoshi, N, and Sakata, O. (2011) Outer Helmholtz Plane of the Electrical Double Layer Formed at the Solid Electrode–Liquid Interface, *ChemPhysChem 12*, 1430-1434.
16. Israelachvili, J N (1991) *Intermolecular and Surface Forces*, 2nd Edition ed., Academic Press, London.
17. Shaw, A M, Hannon, T E, Li, F, and Zare, R N. (2003) Adsorption of Crystal Violet to the Silica-Water Interface Monitored by Evanescent Wave Cavity Ring-Down Spectroscopy, *J. Phys. Chem. B*.
18. Van Volde, K E (1985) *Physical Chemistry*, 2nd ed., Prentice Hall, Englewood Cliffs, NJ.
19. O'Keefe, A, and Deacon, D A G. (1988) Cavity ring-down optical spectrometer for absorption measurements using pulsed laser sources, *Review of Scientific Instruments 59*, 2544-2551.
20. Schnippering, M, Neil, S R T, Mackenzie, S R, and Unwin, P R. (2011) Evanescent wave cavity-based spectroscopic techniques as probes of interfacial processes, *Chemical Society Reviews 40*, 207-220.
21. Spence, T G, Harb, C C, Paldus, B A, Zare, R N, Willke, B, and Byer, R L. (2000) A laser-locked cavity ring-down spectrometer employing an analog detection scheme, *Review of Scientific Instruments 71*, 347-353.

22. Romanini, D, and Lehmann, K K. (1993) Ring-down cavity absorption spectroscopy of the very weak HCN overtone bands with six, seven, and eight stretching quanta, *The Journal of Chemical Physics 99*, 6287-6301.

23. Curran, R, and Crook, T. (1988) Measurement of optical absorption in very thin liw-loss SiO2 films, *Materials Research Society*, 175.

24. Kleine, D, Lauterbach, J, Kleinermanns, K, and Hering, P. (2001) Cavity ring-down spectroscopy of molecularly thin iodine layers, *Applied Physics B: Lasers and Optics 72*, 249-252.

25. Alexander, A J. (2006) Flowing Liquid-Sheet Jet for Cavity Ring-Down Absorption Measurements, *Analytical Chemistry 78*, 5597-5600.

26. Hallock, A J, Berman, E S F, and Zare, R N. (2002) Direct Monitoring of Absorption in Solution by Cavity Ring-Down Spectroscopy, *Analytical Chemistry 74*, 1741-1743.

27. Muir, R N, and Alexander, A J. (2003) Structure of monolayer dye films studied by Brewster angle cavity ringdown spectroscopy, *Phys. Chem. Chem. Phys 5*, 1279.

28. Xu, S, Sha, G, and Xie, J. (2002) Cavity ring-down spectroscopy in the liquid phase, *Review of Scientific Instruments 73*, 255-258.

29. Pipino, A C R, Hudgens, J W, and Huie, R E. (1997) Evanescent wave cavity ring-down spectroscopy with a total-internal-reflection minicavity, *Review of Scientific Instruments 68*, 2978-2989.

30. O'Brien Ii, M J, Brueck, S R J, Perez-Luna, V H, Tender, L M, and Lopez, G P. (1999) SPR biosensors: simultaneously removing thermal and bulk-composition effects, *Biosensors and Bioelectronics 14*, 145-154.

31. Taitt, C R, Anderson, G P, and Ligler, F S. (2005) Evanescent wave fluorescence biosensors, *Biosensors and Bioelectronics 20*, 2470-2487.

32. Milosevic, M. (2004) Internal Reflection and ATR Spectroscopy, *Applied Spectroscopy Reviews 39*, 365-384.

33. Vallance, C. (2005) Innovations in cavity ringdown spectroscopy, *New Journal of Chemistry 29*, 867-874.

34. Czyżewski, A, Chudzyński, S, Ernst, K, Karasiński, G, Kilianek, Ł, Pietruczuk, A, Skubiszak, W, Stacewicz, T, Stelmaszczyk, K, Koch, B, and Rairoux, P. (2001) Cavity ring-down spectrography, *Optics Communications 191*, 271-275.

35. Ball, S M, Langridge, J M, and Jones, R L. (2004) Broadband cavity enhanced absorption spectroscopy using light emitting diodes, *Chemical Physics Letters 398*, 68-74.

36. Scherer, J J, Paul, J B, Jiao, H, and O'Keefe, A. (2001) Broadband Ringdown Spectral Photography, *Appl. Opt. 40*, 6725-6732.

37. Engeln, R, Berden, G, and Meijer, G. (1999) Fourier Transform and Polarization Dependent Cavity-Ringdown Spectroscopy, In *Cavity-Ringdown Spectroscopy*, pp 146-161, American Chemical Society.

38. Pipino, A C R. (2000) Monolithic Folded Resonator for Evanescent Wave Cavity Ringdown Spectroscopy, *Appl. Opt. 39*, 1449-1453.

39. Mazurenka, M, Wilkins, L, Macpherson, J V, Unwin, P R, and Mackenzie, S R. (2006) Evanescent Wave Cavity Ring-Down Spectroscopy in a Thin-Layer Electrochemical Cell, *Analytical Chemistry 78*, 6833-6839.

40. Powell, H V, Schnippering, M, Cheung, M, Macpherson, J V, Mackenzie, S R, Stavros, V G, and Unwin, P R. (2010) Probing Redox Reactions of Immobilized Cytochrome c Using Evanescent Wave Cavity Ring-Down Spectroscopy in a Thin-Layer Electrochemical Cell, *ChemPhysChem 11*, 2985-2991.

41. Zhang, M, Powell, H V, Mackenzie, S R, and Unwin, P R. (2010) Kinetics of Porphyrin Adsorption and DNA-Assisted Desorption at the Silica-Water Interface, *Langmuir 26*, 4004-4012.

42. Fisk, J D, Rooth, M, and Shaw, A M. (2007) Gold Nanoparticle Adsorption and Aggregation Kinetics at the Silica−Water Interface, *The Journal of Physical Chemistry C 111*, 2588-2594.

43. O'Reilly, J P, Butts, C P, I'Anso, I A, and Shaw, A M. (2005) Interfacial pH at an Isolated Silica Water Surface, *Journal of the American Chemical Society 127*, 1632-1633.

44. Rooth, M, and Shaw, A M. (2006) Interfacial pH and surface pKa of a thioctic acid self-assembled monolayer, *Physical Chemistry Chemical Physics 8*, 4741-4743.

45. Avena, M J, and Koopal, L K. (1999) Kinetics of humic acid adsorption at solid-water interfaces.

46. Everest, M A, Black, V M, Haehlen, A S, Haveman, G A, Kliewer, C J, and Neill, H A. (2006) Hemoglobin Adsorption to Silica Monitored with Polarization-Dependent Evanescent-Wave Cavity Ring-Down Spectroscopy, *The Journal of Physical Chemistry B 110*, 19461-19468.

47. Fan, H-F, Li, F, Zare, R N, and Lin, K-C. (2007) Characterization of Two Types of Silanol Groups on Fused-Silica Surfaces Using Evanescent-Wave Cavity Ring-Down Spectroscopy, *Analytical Chemistry 79*, 3654-3661.

48. Martin, W B, Mirov, S, Martyshkin, D, and Venugopalan, R. (2004) Evanescent cavity ring-down spectroscopy (e-CRDS) of hemoglobin absorption at the silica-water interface, In *Engineering in Medicine and Biology Society, 2004. IEMBS '04. 26th Annual International Conference of the IEEE*, pp 2345-2348.

49. Powell, H V, Schnippering, M, Mazurenka, M, Macpherson, J V, Mackenzie, S R, and Unwin, P R. (2008) Evanescent Wave Cavity Ring-Down Spectroscopy as a Probe of Interfacial Adsorption: Interaction of Tris(2,2-bipyridine)ruthenium(II) with Silica Surfaces and Polyelectrolyte Films, *Langmuir 25*, 248-255.

50. Shimosaka, T, Sugii, T, Hobo, T, Alexander Ross, J B, and Uchiyama, K. (2000) Monitoring of Dye Adsorption Phenomena at a Silica Glass/Water Interface with Total Internal Reflection Coupled with a Thermal Lens Effect, *Analytical Chemistry 72*, 3532-3538.

51. Wang, W, Gu, B, Liang, L, and Hamilton, W A. (2004) Adsorption and Structural Arrangement of Cetyltrimethylammonium Cations at the Silica Nanoparticle-Water Interface, *The Journal of Physical Chemistry B 108*, 17477-17483.

52. Weng, L, Van Riemsdijk, W H, and Hiemstra, T. (2008) Humic Nanoparticles at the Oxide−Water Interface: Interactions with Phosphate Ion Adsorption, *Environmental Science & Technology 42*, 8747-8752.

53. Li, F, and Zare, R N. (2005) Molecular Orientation Study of Methylene Blue at an Air/Fused-Silica Interface Using Evanescent-Wave Cavity Ring-Down Spectroscopy, *The Journal of Physical Chemistry B 109*, 3330-3333.

54. Hallock, A J, Berman, E S F, and Zare, R N. (2003) Ultratrace Kinetic Measurements of the Reduction of Methylene Blue, *Journal of the American Chemical Society 125*, 1158-1159.

55. Chen, M-S, Fan, H-F, and Lin, K-C. (2009) Kinetic and Thermodynamic Investigation of Rhodamine B Adsorption at Solid/Solvent Interfaces by Use of Evanescent-Wave Cavity Ring-Down Spectroscopy, *Analytical Chemistry 82*, 868-877.

56. Haselberg, R, van der Sneppen, L, Ariese, F, Ubachs, W, Gooijer, C, de Jong, G J, and Somsen, G W. (2009) Effectiveness of Charged Noncovalent Polymer Coatings against Protein Adsorption to Silica Surfaces Studied by Evanescent-Wave Cavity Ring-Down Spectroscopy and Capillary Electrophoresis, *Analytical Chemistry 81*, 10172-10178.

57. Wang, X, Hinz, M, Vogelsang, M, Welsch, T, Kaufmann, D, and Jones, H. (2008) A new approach to detecting biologically active substances with evanescent-wave cavity ring-down spectroscopy, *Chemical Physics Letters 467*, 9-13.

58. Mazurenka, M, Hamilton, S M, Unwin, P R, and Mackenzie, S R. (2008) In-Situ Measurement of Colloidal Gold Adsorption on Functionalized Silica Surfaces, *The Journal of Physical Chemistry C 112*, 6462-6468.

59. Pipino, A C R. (1999) Ultrasensitive Surface Spectroscopy with a Miniature Optical Resonator, *Physical Review Letters 83*, 3093-3096.

60. Thorpe, M J, Moll, K D, Jones, R J, Safdi, B, and Ye, J. (2006) Broadband Cavity Ringdown Spectroscopy for Sensitive and Rapid Molecular Detection, *Science 311*, 1595-1599.

61. Schnippering, M, Powell, H V, Zhang, M, Macpherson, J V, Unwin, P R, Mazurenka, M, and Mackenzie, S R. (2008) Surface Assembly and Redox Dissolution of Silver Nanoparticles Monitored by Evanescent Wave Cavity Ring-Down Spectroscopy, *The Journal of Physical Chemistry C 112*, 15274-15280.
62. van der Sneppen, L, Hancock, G, Kaminski, C, Laurila, T, Mackenzie, S R, Neil, S R T, Peverall, R, Ritchie, G A D, Schnippering, M, and Unwin, P R. Following interfacial kinetics in real time using broadband evanescent wave cavity-enhanced absorption spectroscopy: a comparison of light-emitting diodes and supercontinuum sources, *Analyst 135*, 133-139.
63. Ball, S M, and Jones, R L. (2003) Broad-Band Cavity Ring-Down Spectroscopy, *Chemical Reviews 103*, 5239-5262.
64. Lehmann, K K, Johnston, P S, and Rabinowitz, P. (2009) Brewster angle prism retroreflectors for cavity enhanced spectroscopy, *Appl. Opt. 48*, 2966-2978.
65. Fiedler, S E, Hoheisel, G, Ruth, A A, and Hese, A. (2003) Incoherent broad-band cavity-enhanced absorption spectroscopy of azulene in a supersonic jet, *Chemical Physics Letters 382*, 447-453.
66. McCain, K S, Schluesche, P, and Harris, J M. (2004) Poly(amidoamine) Dendrimers as Nanoscale Diffusion Probes in Sol Gel Films Investigated by Total Internal Reflection Fluorescence Spectroscopy, *Analytical Chemistry 76*, 939-946.
67. Thormahlen, I, Straub, J, and Grigull, U. (1985) Refractive Index of Water and Its Dependence on Wavelength, Temperature, and Density, *Journal of Physical and Chemical Reference Data 14*, 933-945.
68. Brandt, G B. (1974) Birefringent Coupler for Integrated Optics, *Appl. Opt. 13*, 1359-1362.
69. IPS, o. BK7 Schott Glass Specifications, (Optics, I., Ed.).
70. Cruz, R A, Jacinto, C, and CAtunda, T. (2006) High Sensitivity absorption measurements in liquids and solids, *Annals of Optics*.

71. Manning, G S. (2007) Counterion Condensation on Charged Spheres, Cylinders, and Planes *The Journal of Physical Chemistry B 111*, 8554-8559.

72. Flatt, M E, Kornyshev, A A, and Urbakh, M. (2008) Giant Stark effect in quantum dots at liquid/liquid interfaces: A new option for tunable optical filters, *Proceedings of the National Academy of Sciences 105*, 18212-18214.

73. Parida, S K, Dash, S, Patel, S, and Mishra, B K. (2006) Adsorption of organic molecules on silica surface, *Advances in Colloid and Interface Science 121*, 77-110.

74. Hoppe, R, Alberti, G, Costantino, U, Dionigi, C, Schulz-Ekloff, G n, and Vivani, R. (1997) Intercalation of Dyes in Layered Zirconium Phosphates. 1. Preparation and Spectroscopic Characterization of Zirconium Phosphate Crystal Violet Compounds, *Langmuir 13*, 7252-7257.

75. Del Nero, J, Galembeck, A, Silva, S B C, and Siva, J A P d. (2003) Dye incorporation in polyphosphate gels: synthesis and theoretical calculations, *Materials Research 6*, 335-340.

76. Bujdák, J, and Iyi, N. (2005) Molecular Orientation of Rhodamine Dyes on Surfaces of Layered Silicates, *The Journal of Physical Chemistry B 109*, 4608-4615.

77. Yurdakoc, M, Akcay, M, Tonbul, Y, and Yurdakoc, K. (1998) Acidity of Silica-Alumina Catalysts by Amine Titration, *Turk J Chem 23*, 319-327.

Chapter 3

Stability of the Organic and Inorganic Nano-Environmental Interfaces

3.1 Introduction

The structure and properties of the silica-water interface have been measured, using the electronic spectrum of the charged chromophore CV in Chapter 2. Accurate quantification of the number of CV molecules in the interface indicated the presence of only a single layer of CV tightly bound to the surface in two different configurations after wash off of the unstable GC layer. Significantly, we were also able to observe the binding kinetics of the charged chromophore in the formation of the interfacial structure and derive the binding energy at the surface. The studies on the model charged silica-water interface will now be extended to consider the interface structure and stability in the presence of inorganic and organic charged species. Understanding this nano-environmental interface is critically important in the characterisation of nanoparticle toxicity, as it will dominate the bio-availability, dispersion stability and exposure of the particles on immediate release into the environment. The key components which will contribute to the nano-environmental interface are the inorganic and organic components of the water environment present in rivers or the sea, and here sodium chloride (NaCl) and humic acid (HA) will be used to study the formation of charged inorganic and organic interfaces.

3.1.1 Inorganic Interface

The nanoparticle environmental surface charge and stability will be determined by the pH of the medium, its composition and critically its ionic strength (IS). IS is a measure of the ion concentration in solution and indicates how effectively the charge on a particular ion is shielded or stabilised by other ions. It depends on the numbers and charge on species in solution with more highly charged ions having a greater influence on particle dispersion stability, determining the distance between particles and the depth of surface double layers. The ionic strength of a solution is given by Equation 3.1:

$$IS = \frac{1}{2}\sum_i c_i {z_i}^2$$

Equation 3.1

Where *c* is the molar concentration (M) of each species, *i*, and *z* is its charge (*1*). IS in environmental conditions will be predominantly influenced by the content of inorganic salts present in the water. There is large variation in water salinity in different environments, with a salinity of 0.5% in river water (*2*), up to 27.6% in the Dead sea (*3*) and around 3.5% in sea water (*4, 5*). Specifically, there is 0.6 M NaCl and KCl in the oceans, with as much as 0.2 M NaCl and KCl present in animal fluids (*6*). The salinity of the aquatic environment can significantly affect the characteristics of materials suspended in it. Complex multivalent ions in inorganic solutions may cause an ion-shielding charge on the surface and enable stable counter-ion and co-ion layers to form, thus understanding the salt interaction at a silica water interface is important in predicting the fate of particles in suspension. Studies on a silica water interface under Atomic Force Microscopy have demonstrated that with an increase in NaCl concentration, greater adsorption of Na^+ ions were observed, neutralising the negatively charged silica surface at concentrations between 0.5 – 1 M (*7*). The same study also demonstrated an adsorption trend with cation radius, with larger K^+ ions neutralising the same silica surface at reduced concentrations between 0.2 – 0.5 M, and around 0.1 M for Cs^+ ions (*7*).

Previous work on nanoparticles has shown a significant change in nanoparticle dispersion stability with change in suspension salinity. Metin *et al.* (*8*) studied the aggregation of silica nanoparticles in solutions with different IS and cation / anion combinations, obtaining critical salt concentrations (CSC) above which the nanoparticle suspensions became unstable and sedimentation was observed.

Dickson *et al.* looked at aggregation and sedimentation processes of iron oxide (Fe_2O_3) nanoparticles in the presence of NaCl (*9*) using sonication dispersion techniques, and demonstrated a stability half-life of 30 hours with 0.1 M NaCl. Chowdhuy *et al.* showed significant aggregation of titanium dioxide (TiO_2) nanoparticles with IS (*10*), with aggregates observed in a 10 mM KCl nanoparticle suspension 5 times the size of a suspension with only 1 mM KCl. The results indicated that higher IS in suspension caused an increased rate of aggregation leading to the formation of larger particles and shorter dispersion lifetimes. If the nanoparticle suspension is only meta-stable then their bio-availability and potential toxicity mechanisms are significantly altered, with surface interactions then dominated by the sediment composition, and the nanoparticles will be incorporated into the food chain through uptake by sedimentary organisms.

3.1.2 Organic Interface

In addition to the inorganic salts component of aquatic environments, there is also a significant organic load. Humic substances are the major organic component in water environments making up around 30-50% of all organic matter in surface water (*11*), and 60-70% of organic matter in soil (*12*). They play an important role in the binding and movement of molecules in the natural environment (*13*), indicating their surface interactions with nanomaterials are important in understanding the nanoparticle fate and toxicity potential. The organic matter that is found in the environment can be divided into humic and non-humic substances (*14*). The non-humic materials include proteins and amino acids, whilst humic matter can be classified into humic acids, fulvic acids and humins (*14*). These humic structures are all similar, and consist of large covalently linked aromatic molecules, with a complex mixture of acids, including carboxyl groups and phenolate groups, as shown in Figure 3.1.

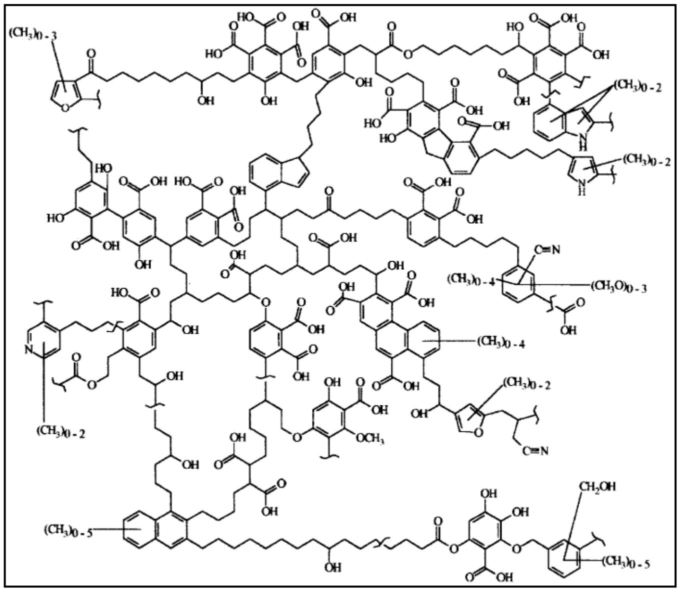

Figure 3.1 A complex image of a HA structure modified from *Schulten and Schnitzer (15)* and *Jones and Bryan (14)*

The differences in the three humic materials are their solubility and size, with fulvic acid completely soluble, humic acid soluble in pH > 2 and humins completely insoluble (*14*). Fulvic acids are smaller lower molecular weight examples of humic acids, with slightly higher oxygen content. Humic acid will be used in this work to replicate organic environmental conditions at the silica-water interface.

Large organic complexes of humic acids form through a long degradation process of dead plant and animal residue (*16*). They routinely form supramolecular structures held together by non-covalent forces, like van de Waals forces and *π*-stacking interactions. The humic acids combine with charged surfaces including nanoparticles (*17*), which will affect aggregation and desorption behaviour (*18*). Adsorption of humic acid at different interfaces has previously been studied, (*19*), with humic acid showing a strong affinity for oxide surfaces (*20*). Other hydrophilic (Fe_2O_3, Al_2O_3) surface interfaces have been observed (*21*) with Avena and Koopal (*21, 22*) using reflectometry to study the kinetics of the adsorption at these solid-water interfaces. Adsorption to hydrophilic surfaces is relatively fast at low pH (*23*) as there is strong interaction with carboxylate and phenol groups present (*24*), forming complexes with hydroxyl groups on the surface. Slower attachment is observed at high pH as there is increased electrostatic repulsion (*21*).

Tong *et al.* explored the interaction of fullerenes with humics, observing aggregation characteristics (*25*). The work showed that adsorption and desorption behaviour of the fullerenes was critical in determining their nano-bioavailability and toxicity, with rapid surface adsorption reducing nanoparticle exposure (*26*). Evidence has suggested enhanced fullerene nanoparticle suspension stability in humic acid, with steric hindrance maintaining distance between individual nanoparticle surfaces (*18*). These data sets were obtained using transmission electron microscopy (TEM), so the surface chemistry and aggregation in dispersion still remains relatively unclear. Other research has studied the interaction of humic acid with the ZnO nanoparticle interface, monitoring aggregation properties in solution with concentration variation of humic acid (*27*). Results showed that the nanoparticles coated with natural organic matter can in some cases increase the nanoparticle dispersion stability (*28*).

3.1.3 Aims and Objectives

The aim of this chapter is to observe competitive binding at the model surface, between CV and environmentally relevant species. The objectives are to measure the kinetics and thermodynamics of the binding of CV with respect to IS and HA and determine structural changes and interface stability.

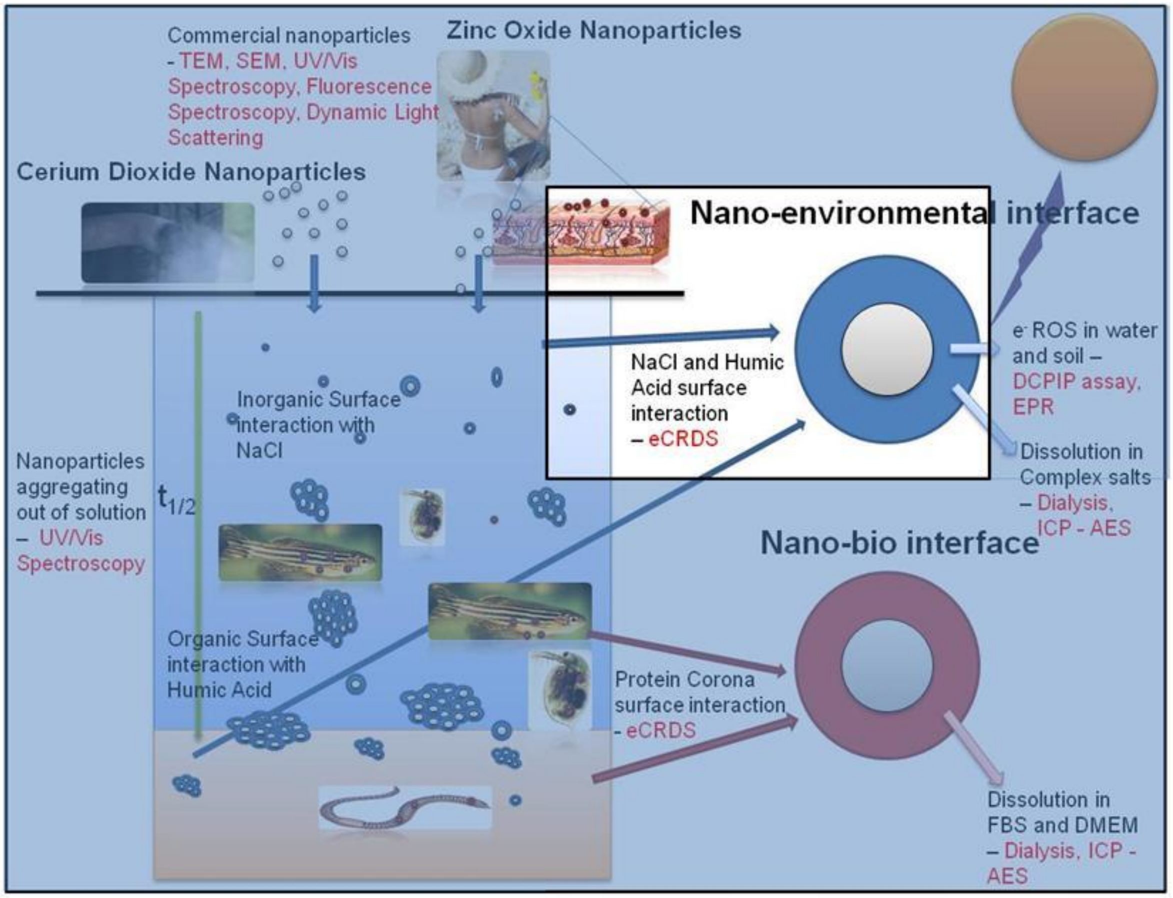

Figure 3.2 The characterisation of the nano-environmental interface using EW-CRDS, looking at surface interaction with NaCl and HA, as models for inorganic and organic nanoparticle environmental interaction

Knowledge of the formation and stability of organic and inorganic layers on a charged surface can then be applied to nanoparticle surfaces once dispersed in the environment, Figure 3.2. The experiments will address fundamental questions of the stability of molecules at the interface, which are relevant to the nanoparticle availability and stability in the environment. The stability of the CV-silica-water charged interface at pH 9 and pH 5 with respect to exchange reactions with the Na^+ cations will indicate if smaller charged ions will neutralise the surface preventing CV absorbance, pointing towards a stable inorganic interface or merely disrupt the GCS interface, with co-formation occurring, indicating the availability of charged surface sites in inorganic complexes. The interaction of HA with the CV will form a model organic interface, with the HA competitively and co-operatively binding with the CV chromophores, with aggregating properties also observed on the surface.

3.2 Experimental Methods

3.2.1 Evanescent Wave Cavity Ring-Down Spectroscopy

The principles of CRDS have been described in detail in Chapter 2 and elsewhere (*29*) so will not be repeated here; all experiments performed in this chapter have the same EW-CRDS procedures previously described. The prism cleaning and preparation procedures were also as used previously.

3.2.2 Competitive binding of Crystal Violet and Sodium Chloride

Crystal Violet CV (20 µM) was made up in deionised water (18 MΩ cm^{-1}). Sodium Chloride (NaCl) (Sigma Aldrich) was added to the experimental solutions at concentrations between 0 – 150 mM. The water buffer and CV solutions were adjusted to pH 9 and pH 5 using small volumes of NaOH (1 M) and HCl (1 M), with the solution pH monitored using a pH meter (Jenway 3520). After each experiment was performed, the prism surface was cleaned using IPA, Methanol, 1% SDS, HCl (0.1 M), NaOH (0.1 M), HCl (0.1 M), water and IPA, until the original baseline was regained.

The pH-adjusted buffer was run through the flow cell until a stable ring-down time, τ was achieved at the interrogation wavelength 635 nm. The baseline τ was then recorded for the buffer solution and a water surface baseline spectrum was collected. CV solutions made up in different concentrations of NaCl were run across the silica surface at a rate of 3.3 mL min^{-1}. The association of the CV was then monitored at 635 nm over time until full surface coverage was observed. Once τ had stabilised, an interfacial CV electronic spectrum was recorded over the range 575-670 nm in steps of approximately 5 nm.

3.2.3 Competitive binding of Humic Acid with Crystal Violet

Humic Acid (Sigma Aldrich), Figure 3.3, was dissolved in pH 9 deionised water (18 MΩ cm^{-1}), at concentrations between 0 - 1 gL^{-1}, with CV (20 µM) added to the solutions and the pH adjusted using NaOH (1 M) and HCl (1 M).

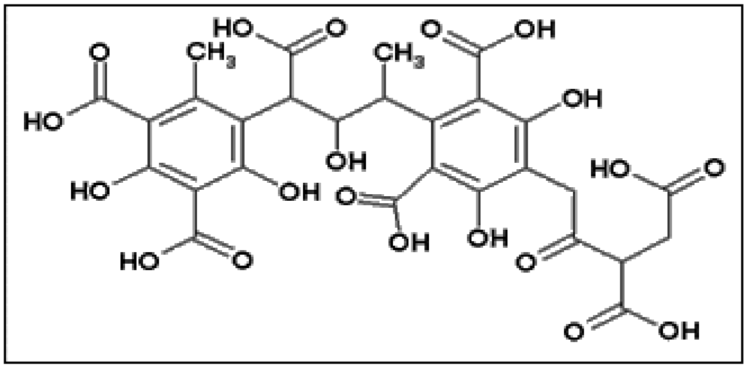

Figure 3.3 The model HA structure

The CV with HA solutions were run over the silica surface, until full surface coverage was observed. Once τ had stabilised, a surface spectrum was recorded for the CV with varying concentrations of HA. The silica surface was then cleaned using the previously stated cleaning protocol, before the process was repeated with different concentrations of HA in solution.

3.3 Results

3.3.1 Competitive binding of CV and NaCl at pH 9

The interaction of NaCl with CV was examined on a silica surface as an inorganic model of co-formation at a charged interface. Association and dissociation kinetics of different IS CV (20 µM) solutions were observed for a fully dissociated silica surface at pH 9. Figure 3.4 (A) shows a selection of competitive binding adsorption curves of CV onto the silica surface with, (a) 0 mM, (b) 20 mM, (c) 50 mM and (d) 150 mM of NaCl, leading to full surface coverage, θ_1. With increased NaCl concentration the absorbance decreases corresponding to a reduced concentration of CV in the interface. CV adsorbs to the silica surface at pH 9 with 0 mM NaCl with a maximum surface coverage, θ_1 of 4.3 ± 0.1 x 10^{-3}, Figure 3.4 (A) (a). This compares to 4.69 ± 0.03 x 10^{-3} for corresponding data in Chapter 2 indicative of the reproducibility of cavity and prism set-ups between experiments. In the presence of 150 mM NaCl, Figure 3.4 (A) (d), a θ_1 of 7.9 ± 0.2 x 10^{-4} is obtained, showing a 5.4 fold decrease in CV observed at the interface.

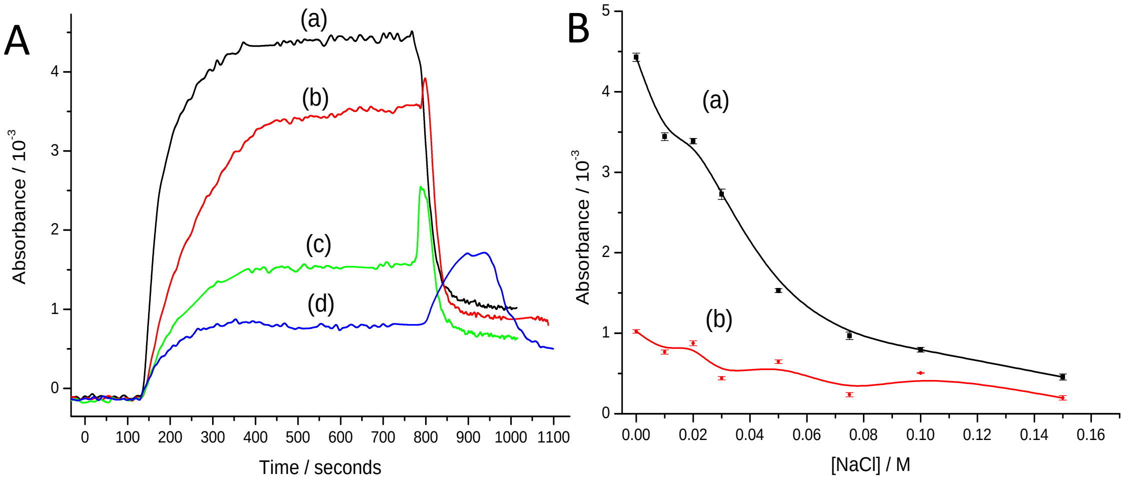

Figure 3.4 (A) - CV (20 μM) adsorption kinetics at pH 9, with increasing concentrations of NaCl (a) 0 mM (b) 20 mM, (c) 50 mM and (d) 150 mM, and (B) - Variation in surface coverage of CV adsorption isotherms for (a) full surface adsorption θ_1, and (b) surface adsorption after buffer wash off θ_2 v [NaCl]

Desorption kinetics and stability of the resulting CV-NaCl interface were observed when a pH 9 water buffer solution was flowed over the surface. A feature of the immediate response was a transient rise in the observed absorbance for 100 – 300 seconds, showing an initial increase above the stable θ_1 absorbance followed by a decrease to a new θ_2 absorbance. The effect was most pronounced for the higher concentrations of NaCl and not observed at all for the NaCl free solution. The θ_2 surface coverage is similar across the bulk pH range, decreasing from 1.02 ± 0.02 x 10^{-3} at 0 mM NaCl, Figure 3.4 (A) (a) down to 1.97 ± 0.26 x 10^{-4} for 150 mM NaCl, Figure 3.4 (A) (d); a 5.2 fold decrease. The absorbance isotherm, Figure 3.4 (B) shows the variation in absorbance observed against increasing IS solutions of NaCl, showing full surface coverage, θ_1, Figure 3.4 (B) (a) and surface coverage after wash off, θ_2, Figure 3.4 (B) (b), with both θ_1 and θ_2 displaying a decreasing trend with increasing NaCl concentration.

3.3.2 Electronic Spectra of CV and NaCl at pH 9

The θ_1 electronic spectra were recorded over the wavelength range 575 – 670 nm. Figure 3.5 (A) shows a selection of CV (20 µM) spectra with (a) 0 mM, (b) 20 mM, (c) 50 mM and (d) 150 mM NaCl in pH 9 solution, with the intensity of the spectra decreasing with increasing NaCl concentration. The θ_1 surface spectra, Figure 3.5 (A) show two shifted peaks, S_1 and S_2. The $\theta_1 S_1$ λ_{max} peak is at 581 nm, showing a shift of 2 nm with respect to the bulk spectrum of CV, and gives an initial absorbance value with 0 mM NaCl of $12.57 \pm 0.1 \times 10^{-3}$ decreasing down to $2.38 \pm 0.01 \times 10^{-3}$ with 150 mM NaCl in solution. The $\theta_1 S_2$ peak is at 607 nm, a red shift of 24 nm, and shows an initial absorbance at $9.36 \pm 0.04 \times 10^{-3}$ for 0 mM NaCl, decreasing to $2.33 \pm 0.01 \times 10^{-3}$ with 150 mM NaCl present in solution. Figure 3.5 (B) shows the spectra normalised at 607 nm, the wavelength of the red shifted S_2 peak, to highlight the observed spectra change with NaCl. The $\theta_1 S_1$ peak at 581 nm shows a normalised absorbance at 1.36 ± 0.01 for 0 mM NaCl, decreasing to 1.02 ± 0.01 with 150 mM NaCl present in solution, with the $\theta_1 S_2$ peaks normalised at 1.

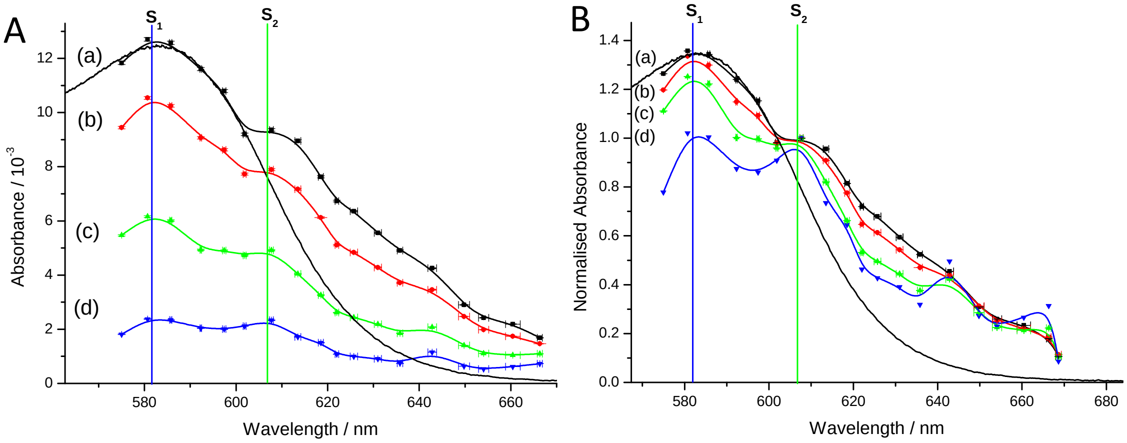

Figure 3.5 A Electronic surface spectra of CV (20 µM) θ_1 at pH 9 with different concentrations of NaCl, (a) 0 mM, (b) 20 mM, (c) 50 mM and (d) 150 mM, and (B) normalised at 607 nm, with the CV solution phase shown in black

Figure 3.6 (A) shows the θ_2 surface spectra after wash off. The θ_2 surface spectra show the same S_1 and S_2 peak shifts as shown for θ_1, however the peaks are narrower in the red region. The θ_2S_1 peak at 581 nm shows an absorbance of 5.19 ± 0.02 x 10^{-3} for 0 mM NaCl, decreasing down to a value of 1.35 ± 0.01 x 10^{-3} for 150 mM NaCl. The θ_2S_2 peak at 607 nm shows a decrease from 3.98 ± 0.01 x 10^{-3} to 1.56 ± 0.01 x 10^{-3} corresponding to an increase in NaCl in solution from 0 mM to 150 mM. Figure 3.6 (B) shows the normalised θ_2 surface spectra after wash off. The θ_2S_1 peak at 581 nm shows a normalised absorbance of 1.3 ± 0.02 for 0 mM NaCl, decreasing down to a value of 0.87 ± 0.02 for 150 mM NaCl. The θ_2S_2 peaks at 607 nm are all normalised at 1 across the concentration range.

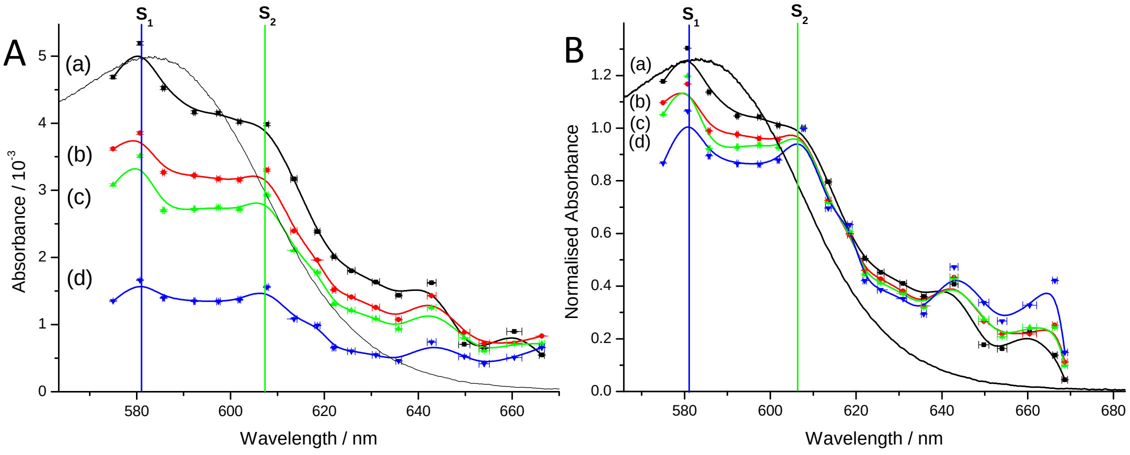

Figure 3.6 A - Electronic surface spectra of CV (20 µM) θ_2 at pH 9 with different concentrations of NaCl, (a) 0 mM, (b) 20 mM, (c) 50 mM and (d) 150 mM, and (B) normalised at 607 nm, with the CV solution phase shown in black

3.3.3 Competitive binding of CV and NaCl at pH 5

The silica surface at pH 9 has both Q2 and Q3 silanol groups available to bind to because of the two types of silanol binding sites, with pka’s of 4.5 and 8.4 discussed in Chapter 2. At pH 5, the silica surface will have fewer negatively charged sites available, and the ones available will be in greater isolation. The effect of co-formation between the sodium ions and the CV on the pH 5 silica surface was looked at to observe the different interaction on these isolated sites.

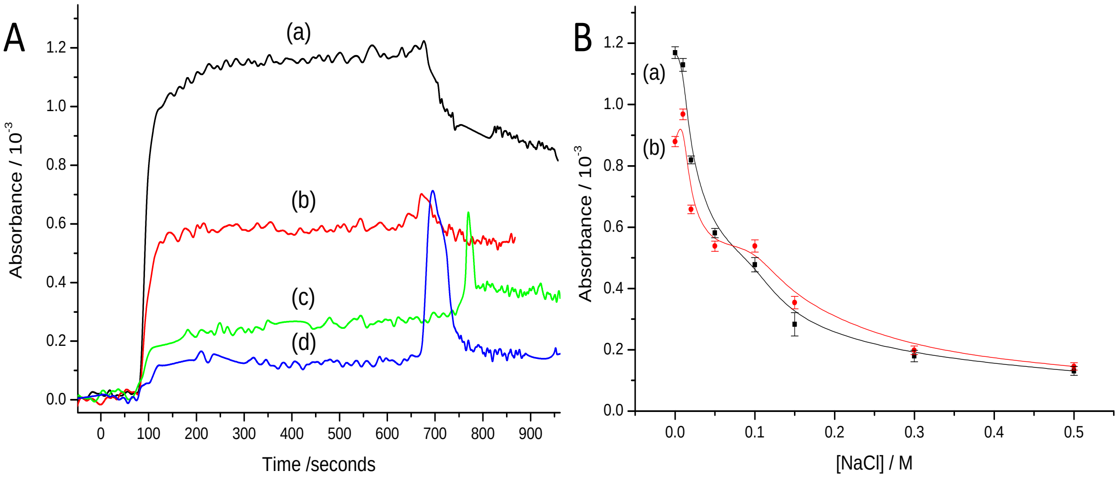

Figure 3.7 (A) - CV (20 µM) adsorption kinetics at pH 5, with increasing concentrations of NaCl (a) 0 mM (b) 50 mM, (c) 150 mM and (d) 500 mM, and (B) variation in surface coverage for CV-NaCl adsorption isotherms for (a) full surface adsorption θ_1, and (b) surface adsorption after buffer wash off θ_2 v [NaCl]

The observed adsorption at pH 5 of CV (20 µM) on the silica surface with (a) 0 mM (b) 50 mM, (c) 150 mM and (d) 500 mM NaCl, shows a decrease in surface adsorption as the NaCl concentration is increased, Figure 3.7 (A). The surface adsorption is considerably reduced compared to pH 9, with a θ_1 absorbance of 1.2 ± 0.1 x 10^{-3} with 0 mM NaCl in solution, down to 1.3 ± 0.1 x 10^{-4} with 500 mM NaCl present; a 9.2 fold decrease. The dissociation off the surface is minimal, with no significant change with the increase in NaCl in solution; however the small rise in surface absorbance was also seen here for the switch to buffer, before decreasing off the surface, appearing more prominent with increased NaCl. The θ_2 absorbance observed with 0 mM NaCl was 8.8 ± 0.2 x 10^{-4}, decreasing to 1.5 ± 0.1 x 10^{-4} with 500 mM present, Figure 3.7 (B); a 5.8 fold decrease.

3.3.4 Electronic Spectra of CV and NaCl at pH 5

The surface spectrum of CV (20 µM) at pH 5 was measured with varying concentrations of NaCl co-adsorbed to the silica-water interface. The θ_1 surface spectra, Figure 3.8 (A) shows CV (20 µM) with (a) 0 mM, (b) 50 mM, (c) 150 mM and (d) 500 mM NaCl in solution, with the spectra displaying two λ_{max} peaks, S_1 and S_2 at 581 nm and 607 nm. These peaks decrease in absorbance with increasing NaCl concentration, with S_1 and S_2 θ_1 absorbance values of $3.14 \pm 0.01 \times 10^{-3}$ and $3.12 \pm 0.01 \times 10^{-3}$ for 0 mM NaCl, decreasing to $1.20 \pm 0.01 \times 10^{-3}$ and $6.5 \pm 0.1 \times 10^{-4}$ with 500 mM NaCl in solution. Figure 3.8 (B), shows the spectra normalised at 607 nm, the wavelength of the red shifted peak. The black line for 0 mM NaCl displays normalised absorbance at S_1 of 1.01, with the S_2 peak normalised to 1, however, the blue line, showing the normalised 500 mM NaCl, indicates a large peak at 581 nm, as at such high concentrations of NaCl, the red shift peak S_2 has shifted further into the red region, distorting the spectra, giving a normalised absorbance at S_1 of 1.8 with the S_2 peak normalised to 1.

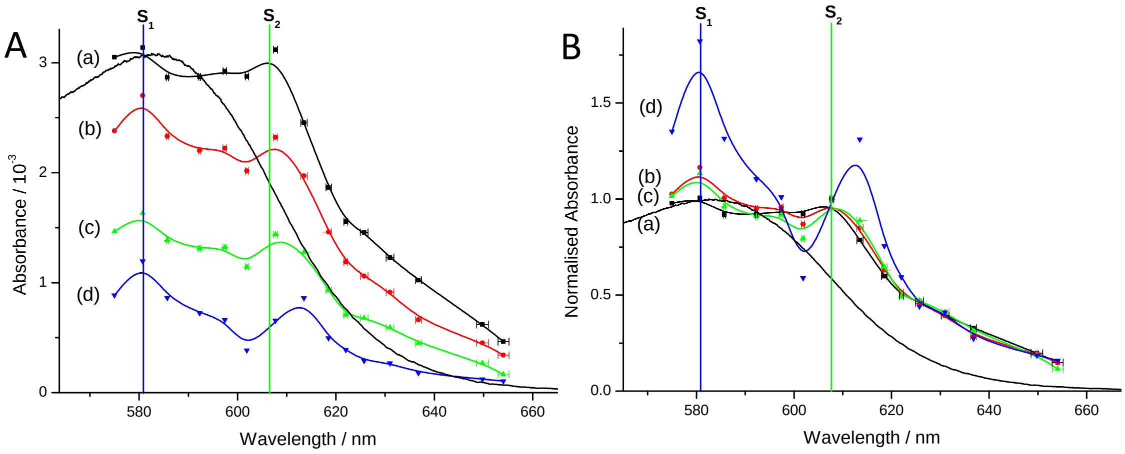

Figure 3.8 A - Electronic surface spectra of CV (20µM) θ_1 at pH 5 with different concentrations of NaCl, (a) 0 mM, (b) 50 mM, (c) 150 mM and (d) 500 mM, and (B) normalised at 607 nm, with the CV solution phase shown in black

The electronic spectra after wash off, θ_2 are shown in Figure 3.9 (A). The $\theta_2 S_1$ peak shows an absorbance value of $2.13 \pm 0.01 \times 10^{-3}$ for 0 mM NaCl, decreasing to $1.37 \pm 0.01 \times 10^{-3}$ for 500 mM NaCl. The $\theta_2 S_2$ peak absorbance values for 0 mM and 500 mM NaCl were $2.02 \pm 0.01 \times 10^{-3}$ and $0.78 \pm 0.01 \times 10^{-3}$ respectively. Figure 3.9 (B), shows the spectra normalised at 607 nm, the wavelength of the red-shifted peak, as before. The black line for 0 mM NaCl gives a normalised absorbance at S_1 of 1.05, with the S_2 peak normalised to 1, with the blue line again showing a large normalised feature at 581 nm due to the shift in the S_2 peak with high NaCl concentration, giving a normalised absorbance at S_1 of 1.75 with the S_2 peak normalised to 1.

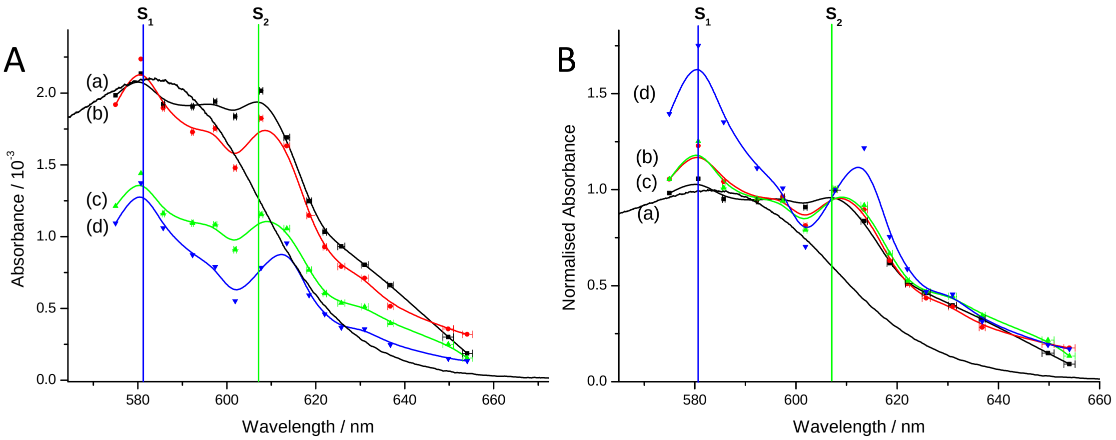

Figure 3.9 A - Electronic surface spectra of CV (20 µM) θ_2 at pH 5 with different concentrations of NaCl, (a) 0 mM, (b) 50 mM, (c) 150 mM and (d) 500 mM, and (B) normalised at 607 nm, with the CV solution phase shown in black

3.3.5 Crystal Violet and Humic Acid binding at a silica interface

To model a charged organic interface, the CV co-association onto a negatively charged silica surface with different concentrations of HA in solution was observed. Figure 3.10 (A) shows association monitored at 635 nm of CV (20 µM) at pH 9 on a silica surface with (a) 0 mgL^{-1}, (b) 5 mgL^{-1}, (c) 10 mgL^{-1}, (d) 25 mgL^{-1}, (e) 100 mgL^{-1} and (f) 1 gL^{-1} HA in solution.

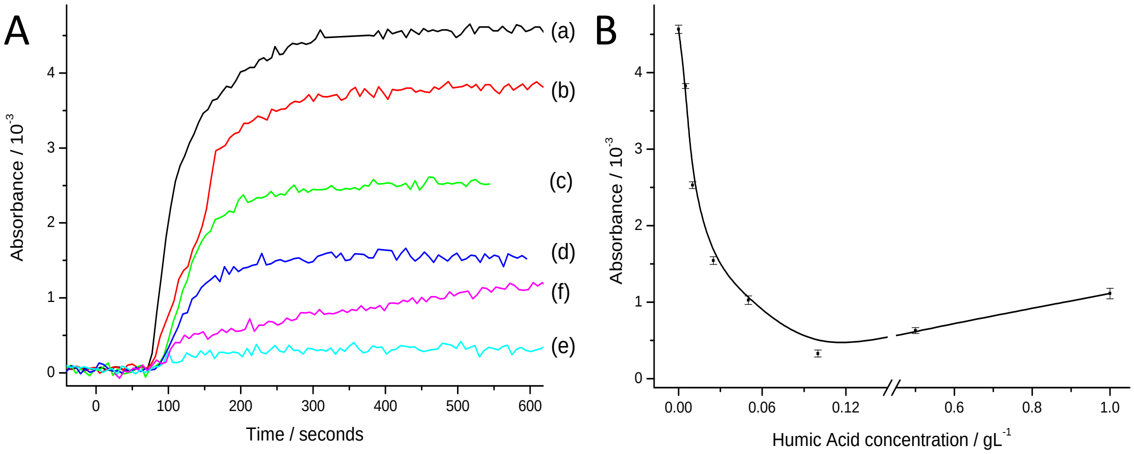

Figure 3.10 (A) - CV (20 µM) (pH 9) with a selection of difference concentrations of HA in solution on a silica surface, (a) 0 mgL^{-1} (b) 5 mgL^{-1}, (c) 10 mgL^{-1}, (d) 25 mgL^{-1}, (e) 100 mgL^{-1} and (f) 1 gL^{-1}, and (B) – surface coverage θ_1 v HA

The HA in solution reduces the CV observed at the interface, Figure 3.10 (A), with the θ_1 adsorption observed for 0 mgL^{-1} HA of 4.57 ± 0.05 x 10^{-3}, decreasing to 3.2 ± 0.4 x 10^{-4} with 100 mgL^{-1} HA in solution; a 14.3 fold decrease. With a further increase in HA concentration in solution the surface absorbance appears to increase, up to 1.1 ± 0.1 x 10^{-3} with 1 gL^{-1} in solution. However, the association curve appears less exponential in shape, and is slowly increasing on the surface over time, Figure 3.10 (A) (f). This trend in surface adsorption is shown in Figure 3.10 (B) plotted against HA concentration. There is no θ_2 dissociation shown, as the switch to the pH 9 water buffer appeared to show no change in absorbance.

Surface spectra of CV at θ_1 were recorded over the wavelength range 575 – 685 nm, Figure 3.11 (A), with different concentrations of HA, (a) 0 mgL^{-1}, (b) 5 mgL^{-1}, (c) 10 mgL^{-1}, (d) 25 mgL^{-1} (e) 100 mgL^{-1} and (f) 1 gL^{-1} in solution. The spectra show that with increased HA concentration, the CV adsorption on the surface decreases. The spectra shows two peaks observed at 581 nm and 607 nm, S_1 and S_2 as before, which have absorbance values of 12.7 ± 0.01 x 10^{-3} and 9.36 ± 0.04 x 10^{-3}, with 0 mgL^{-1} HA in solution, Figure 3.11 (A) (a). These values decrease significantly with HA in solution, with the S_1 peak most prominently removed, giving S_1 and S_2 absorbance values of 6.87 ± 0.02 x 10^{-3} and 6.58 ± 0.02 x 10^{-3} with 5 mgL^{-1} HA, Figure 3.11 (A) (b). There is a further decrease to 0.53 ± 0.02 x 10^{-3} and 0.63± 0.02 x 10^{-3} with 100 mgL^{-1} HA, Figure 3.11 (A) (e). At HA concentrations above 100 mgL^{-1} there appears to be a change in the spectra observed, with the S_1 and S_2 peaks no longer well defined, with values of 1.25 ± 0.02 x 10^{-3} and 1.8 ± 0.02 x 10^{-3} for 1 gL^{-1}, Figure 3.11 (A) (f), and a peak λ_{max} observed at 654 nm of 2.45 ± 0.02 x 10^{-3}.

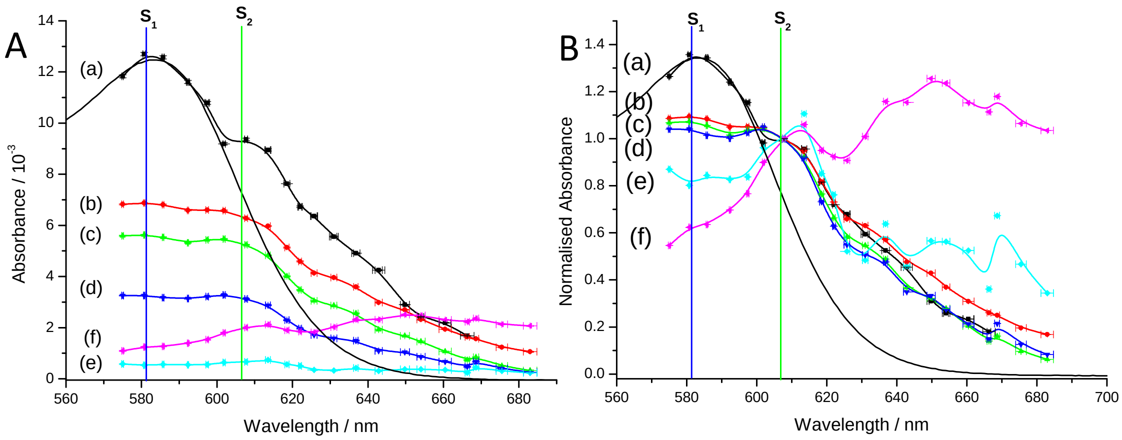

Figure 3.11 A - Surface spectra of CV (20 μM) with different concentrations of HA, (a) 0 mgL^{-1}, (b) 5 mgL^{-1}, (c) 10 mgL^{-1} , (d) 25 mgL^{-1}, (e) 100 mgL^{-1} and (f) 1 gL^{-1}, and B – normalised at 607 nm, with CV (20 μM) in solution shown as a solid black line

The spectra were normalised to 607 nm, Figure 3.11 (B), the absorbance peak of S_2, with the normalised absorbance for 0 mgL^{-1} showing an S_1 absorbance value of 1.36, decreasing to 0.8 with 100 mgL^{-1} HA. At 1 gL^{-1} the S_1 absorbance was 0.69, with all S_2 absorbance peaks normalised to 1.

3.4 Discussion

The CV-silica-water interface structure studied in Chapter 2 indicated a stable θ_2 Stern layer, with CV molecules able to bind directly to Q2 and Q3 silanol sites on the silica surface. The θ_1 formation, showed evidence of molecules associated in a less stable GC layer, also shown in the electronic spectrum, with the GC layer appearing to decrease at the interface relative to the surface potential. By introducing NaCl at different concentrations into the interface, the positively charged Na^+ cations will compete with the CV molecules for the Q2 and Q3 sites cooperatively. The Na^+ cations are significantly smaller than CV and may completely occupy negatively charged silica sites, neutralising these sites effectively. Alternatively they may undergo co-formation with the CV molecules forming a complex layer, resulting in a charged GCS interface with different binding affinities. The presence of NaCl at the interface will affect the rate of formation and stability of the GC layer and the Stern layer formation, and can be used as a simple inorganic surface model in understanding molecule interaction in inorganic environments. Here, both the fully dissociated silanol surface at pH 9 and the partially dissociated surface at pH 5 were interrogated with NaCl, observing the competitive binding associated with a high and low surface charge interface.

3.4.1 NaCl interaction at a pH 9 silica surface

The interface kinetics of CV molecules with increasing IS were observed at pH 9, Figure 3.4. The adsorption appears exponential, Figure 3.4 (A), with the θ_1 surface absorbance decreasing with higher NaCl concentration at the interface. The desorption kinetics display an increase in absorbance with buffer switch. This is presumed to be a combination of the compressing of the interfacial structure, as well as the water buffer increasing the dissociation rate of the Na^+ ions, allowing for an observed increase in the CV concentration at the interface over time, distorting the dissociation. This rise is followed by the removal of the unstable molecules bound in the GC layer, leaving a stable Stern layer. The Stern layer stability can be compared by observing the θ_1:θ_2 ratio, which gives values of 76.3:23.7 with 0 mM NaCl, and 75.1:24.9 with 150 mM NaCl, comparable with a value of 76.7:23.3 previously. This demonstrates that three quarters of the association observed is a feature of the θ_1 absorbance, which is not influenced considerably with NaCl. The decrease in the θ_1 surface coverage with NaCl concentration, Figure 3.4 (B) indicates greater competing at the interface for negative binding sites, with an increase in Na^+ ions adsorbing onto the silica surface preventing CV molecular interaction. Greater surface adsorption has been observed previously using Atomic

Force Microscopy, with increasing NaCl concentrations neutralising the negative surface charge at concentrations between 0.5 - 1 M (*7*).

The initial rate analysis of association of CV with NaCl was observed, with the rate constant k_a plotted against NaCl concentration, Figure 3.12 (A). This gave a value of 3.3 ± 0.2 M^{-1} s^{-1} with 0 M NaCl, in comparison to 3.5 ± 0.2 M^{-1} s^{-1} in Chapter 2. The k_a decreased to 0.23 ± 0.01 M^{-1} s^{-1} with 150 mM NaCl. This decrease suggests that the association rate of CV is influenced by the competing and hindrance of the NaCl in solution, preventing direct adsorption at the Q2 and Q3 sites, as well as a reduction in surface potential. This leads to weaker surface attraction and a slower rate of interaction.

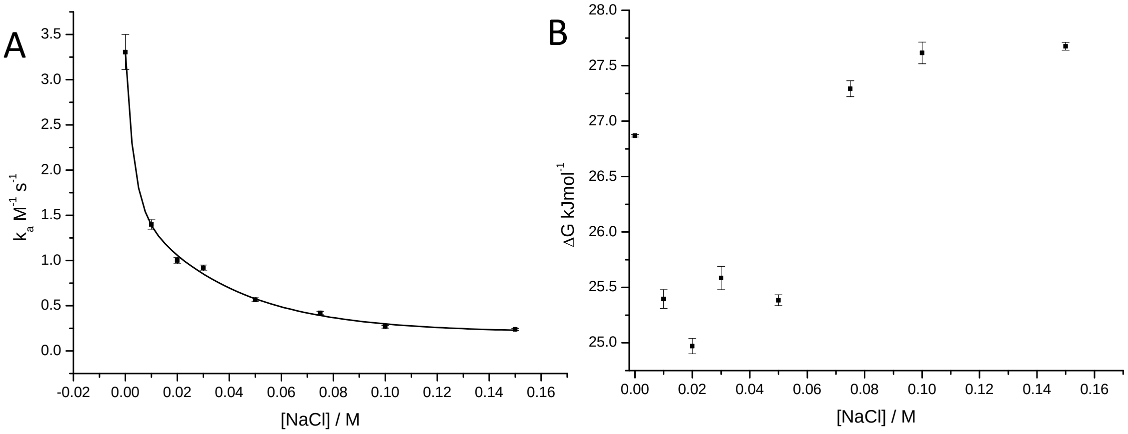

Figure 3.12 A – CV (20 µM) (pH 9) Association Rate Constant k_a v [NaCl], and B – CV (20µM) pH 9 θ_1 interfacial binding energy ΔG v [NaCl]

The stability of the silica-water interface with NaCl concentration was observed by calculating the energy of interaction, deriving the affinity constant K_D, from the association rate constant k_a and the dissociation rate, k_d. The k_d was difficult to determine because of the distorted compression of the interface, so a line was fitted to the data after the initial rise had settled, to give a θ_1 k_d. The θ_1 k_d shows an initial fast dissociation rate from 6.4 ± 0.4 x 10^{-6} s^{-1} with 0 mM NaCl, decreasing to 3.4 ± 0.2 x 10^{-6} s^{-1} with 150 mM NaCl in solution (not shown).

θ_1 interfacial binding energy values were then derived for CV with NaCl at pH 9, Figure 3.12 (B). The data showed an initial drop in ΔG from 26.9 ± 0.02 – 25 ± 0.1 $kJmol^{-1}$, with increasing NaCl from 0 – 20 mM, with the NaCl at the interface appearing to destabilise the CV structure making it easier to displace the CV molecules off the surface. As the NaCl concentration increases from 30 mM up to 150 mM, the ΔG rises from 25.6 ± 0.15 - 27.7 ± 0.05 $kJmol^{-1}$, with higher concentrations of NaCl increasing the stability of the interface. It is postulated that with higher concentrations of NaCl, the CV and Na^+ ions form a lattice structure at the interface, preventing dissociation of the closely adsorbed CV molecules in the Stern layer, meaning that a stable inorganic layer is formed on the surface.

3.4.2 Electronic Molecular Spectra of Crystal Violet with NaCl at a pH 9 Charged Silica-Water interface

The electronic structures on the silica interface were measured for θ_1, Figure 3.5 (A) and θ_2, Figure 3.6 (A). The electronic structure of CV in Chapter 2 suggested that the red shifted feature observed in the CV surface spectra was caused by interaction of the CV molecules in close proximity to the surface, and the two features present were deconvolved to estimate the peak contribution to the absorbance observed. The electronic structures observed with NaCl concentration at pH 9 display the same two shifted peaks, which decreased in intensity with NaCl. The spectra have been normalised to 607 nm, the wavelength of the S_2 peak, for θ_1, Figure 3.5 (B) and θ_2, Figure 3.6 (B), to observe the change in spectral shape. The shape of the CV θ_1 surface spectra displays a more dominant S_1 peak compared to S_2 for CV with no NaCl present, similar to chapter 2, decreasing with increasing NaCl. The ratio of the S_1:S_2 peaks for 0 mM NaCl were 1.36:1, decreasing to 1.02:1 with 150 mM NaCl in solution. This effect is the influence of the NaCl at the interface, decreasing the surface potential, resulting in a reduced GC layer. The θ_2 surface spectra, Figure 3.6 (A), displays the same S_1 and S_2 peak surface formation, although the width of the peaks are more comparable with θ_1 absorbance with high NaCl concentration. The ratio of the S_1:S_2 peaks for 0 mM NaCl are 1.3:1, decreasing to 0.87:1 with 150 mM NaCl, showing the decrease in the S_1 peak with NaCl.

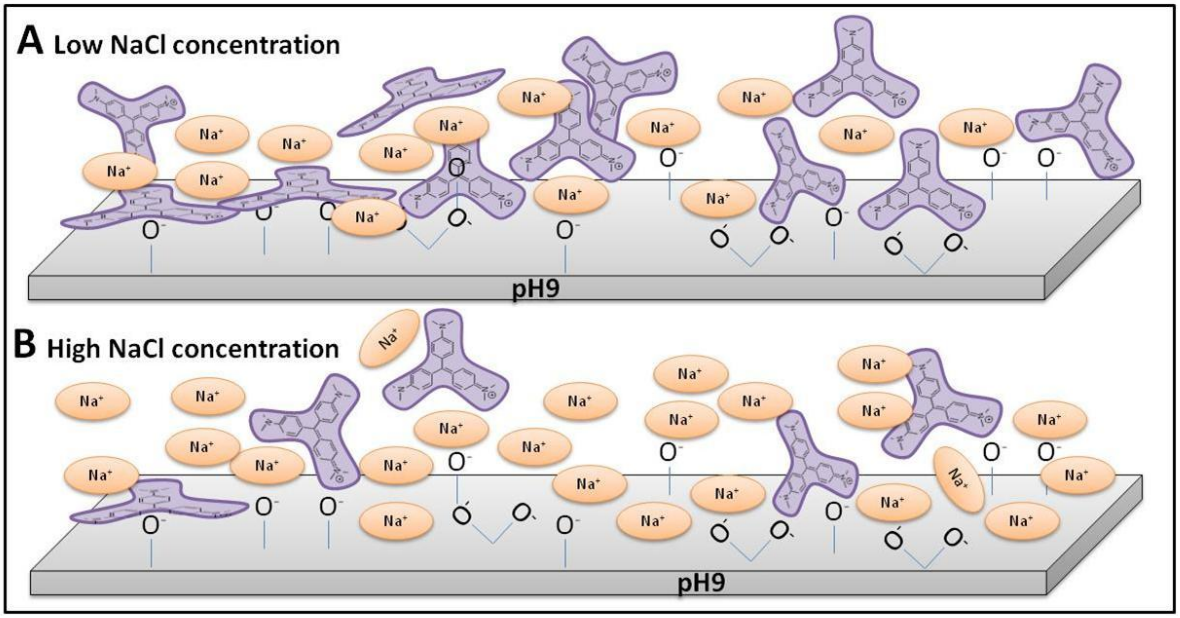

Figure 3.13 Schematic to show the surface interaction of CV and NaCl with the Q2 and Q3 binding sites at low and high NaCl concentration.

Using the extinction coefficient from the deconvolution of the spectra derived previously (section 2.3), the spectra observed indicate a CV interfacial concentration of 1.34 molecules nm^{-2} with 0 mM NaCl, for θ_1 at pH 9, decreasing to 0.25 molecules nm^{-2} with 150 mM NaCl; a 5.3 fold decrease in concentration. This is a change from 2.25 x 10^{16} to 4.2 x 10^{12} CV molecules interrogated at the interface, with the addition of 150 mM NaCl. The influence of NaCl on the θ_2 surface absorbance was smaller, with a decrease in θ_2 interfacial concentration from 0.55 molecules nm^{-2} down to 0.14 molecules nm^{-2}; a 3.8 fold concentration decrease. This indicates that even at the highest concentrations of NaCl, 2.53 x 10^{12} CV molecules will still be able to interact with the negatively charged surface. This suggests that the Na^+ ions have a lower binding energy at the surface, and will dissociate, undergoing constant exchange reactions, with the vacant sites filled by more permanent CV adsorption. This leads to the eventual co-formation of a CV-NaCl stable lattice, rather than direct competitive binding between the two charged species and the complete neutralisation of the charged surface by the Na^+ ions, Figure 3.13.

3.4.3 NaCl interaction at a pH 5 silica surface

The absorbance of CV (20 µM) at pH 5 is smaller than at pH 9 as only the Q3 silanol sites will be dissociated, decreasing the number of negative binding sites and corresponding to a lower overall negative surface potential. The interface kinetics were observed at pH 5 with increasing IS, Figure 3.7, with the θ_1 interfacial absorbance decreasing with NaCl concentration. The dissociation displays the same feature as previously, showing an initial rise, before minimal dissociation off the surface, giving θ_2 values comparable with θ_1. The Stern Layer stability comparing the θ_1:θ_2 ratio, give values of 26.6:73.4 with 0 mM NaCl, and 0:100 for 500mM NaCl, with a higher θ_2 value achieved after wash off. This demonstrates that at pH 5, the increase in NaCl at the interface stabilises the charged layer formed, with the CV molecules that are able to bind at the interface, not easily removed.

The rate of association of CV at pH 5 was observed by fitting a line to the data obtained. The association rate constants (k_a) were plotted against NaCl concentration, Figure 3.14 (A). It shows a decrease in k_a, from 0.62 ± 0.01 M^{-1} s^{-1} with 0 mM NaCl, down to 0.04 ± 0.01 M^{-1} s^{-1} with 500 mM NaCl in solution, with a decreasing association rate observed as a greater number of Na^+ ions occupied silanol sites at the interface.

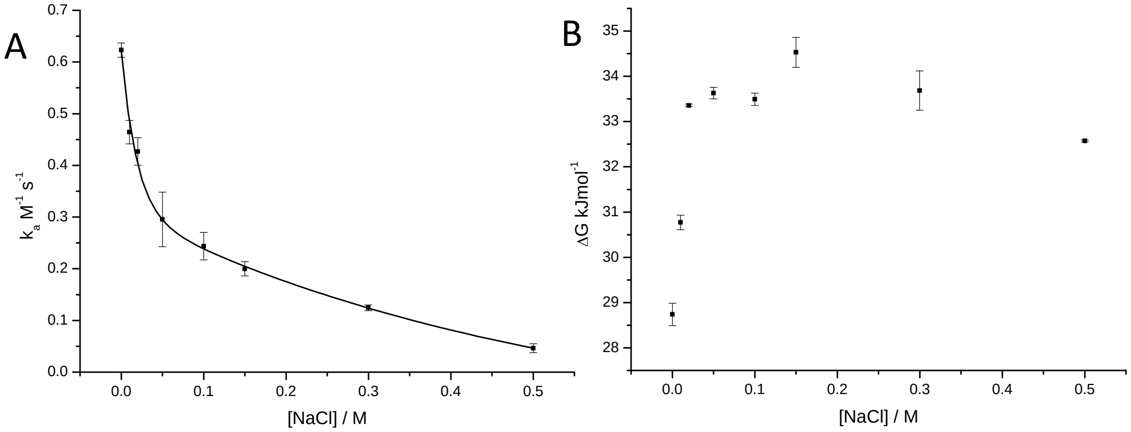

Figure 3.14 A – CV (20 µM) (pH 5) Association Rate Constant k_a v [NaCl], and B – CV (20 µM) pH 5 θ_1 interfacial binding energy ΔG v [NaCl]

The stability of the silica-water interface at pH 5 with NaCl concentration was observed by calculating the energy of interaction, deriving the affinity constant K_D, from the association rate constant, k_a and the dissociation rate, k_d. The dissociation was again difficult to calculate, because of the observed sudden increase and decrease in absorbance with buffer switch, but lines were fitted to the data after the rise had settled to its original point, to give θ_1 k_d. The θ_1 k_d decreased from $5.7 \pm 0.7 \times 10^{-6}$ with 0 mM NaCl in solution, down to $9 \pm 1 \times 10^{-8}$ with 500 mM NaCl in solution, (not shown).

The θ_1 interfacial binding energy values were derived for CV with NaCl at pH 5, Figure 3.14 (B), showing an initial rise in ΔG from 28.7 - 33.4 kJmol^{-1} with the increase in NaCl from 0 – 20 mM, appearing to increase the surface stability of the CV interface. This increase in the surface stability is attributed to the co-formation at the surface of the Na^+ with the CV molecules, resulting in a lower dissociation rate, and a corresponding enhanced ΔG value. The ΔG value remains high with increasing NaCl, giving a ΔG of 32.6 kJmol^{-1} with 500 mM NaCl. This interfacial binding energy strengthens the idea of a stable CV-NaCl lattice layer being formed at the interface.

3.4.4 Electronic Molecular Spectra of Crystal Violet with NaCl at a pH 5 Charged Silica-Water interface

The pH 5 θ_1 surface absorbance spectra for CV (20 µM) with NaCl concentration are shown in Figure 3.8, and for θ_2 absorbance in Figure 3.9. At pH 5, only the Q3 silanol sites are available, corresponding to a smaller S_1 peak compared to pH 9, Figure 3.8 (A) (a). This compares with previous surface spectra at pH 5, attributed to a decrease in surface potential, corresponding to a reduced GC layer. The spectra have been normalised at 607 nm, Figure 3.8 (B), which shows similar θ_1 S_1:S_2 peak ratios at 0 mM NaCl of 1:1, however at high NaCl concentration, the S_2 peak shifts further into the red, causing a distorted normalised spectrum, with the θ_1 S_1:S_2 peak ratio for 500 mM NaCl of 1.8:1. This shift is caused by very high NaCl concentration at the interface, influencing the CV molecular interaction. The θ_2 surface spectra of pH 5 are very similar to the θ_1 surface spectra as there is minimal surface wash off observed. The θ_2 S_1:S_2 peak ratio at 0 mM NaCl is 1.05:1, while the S_2 peak is further shifted into the red region for 500 mM NaCl, giving a θ_2 S_1:S_2 peak ratio of 1.75:1.

Previous results have shown θ_1 and θ_2 interfacial concentrations at pH 5, of 0.31 molecules nm^{-2} in the GCS layer, and 0.21 molecules nm^{-2} in the Stern layer, obtained from the deconvolved peak analysis. The interfacial concentration of molecules observed at pH 5 with NaCl show 0.37 molecules nm^{-2} with 0 mM NaCl, and 0.14 molecules nm^{-2} with 500 mM NaCl, a decrease from 6.22×10^{12} to 2.35×10^{12} CV molecules interrogated at the interface. The high NaCl interfacial concentration analysis should be viewed cautiously however, as the peaks have shifted with high NaCl concentration, meaning the peak contribution will be distorted compared to the previous analysis. There is minimal change in the observed θ_1: θ_2 values with wash off, with θ_2 interfacial concentration decreasing from 0.25 to 0.16 molecules nm^{-2}, indicative of the stable interface observed.

These pH 5 concentrations and the concentrations from the pH 9 data set previously point to the co-formation of CV-NaCl complexes at the interface, showing that even at the highest concentration of NaCl at the interface of 500 mM, the Na^+ ions do not simply neutralise the interface charge, but instead form a stable layer with CV molecules. For charged nanoparticle surfaces in strong inorganic environments, this indicates that complex but incomplete stable layers will form at the surface. These will influence suspension stability, aggregation properties and toxicity mechanisms, which will be explored in Chapters 4, 5 and 6.

3.4.5 Humic acid interaction at a pH 9 silica surface

CV and HA solutions were made up at pH 9 to assess the co-adsorption to the fully dissociated negatively charged silica surface. The phenol and carboxyl groups present on HA have reported pK_a values of 8 and 4 respectively (*30*), meaning they will be negatively charged and will be associated to the surface as a co-ion to CV. In addition, CV may associate with the HA in solution before interaction with the negatively charged silica-water interface through the positive CV charge, or aggregation of HA at higher concentrations.

At low concentrations of HA in solution, the CV will bind onto the silica surface, and similar adsorption traces are observed comparable with no HA in solution, Figure 3.10 (a), (b), (c) and (d). The decrease in θ_1 absorbance observed with increased HA concentration can be attributed to steric hindrance by the HA preventing CV interaction on the silanol groups. Previous studies by Jiang *et al.* observed deposition with organic matter at a silica surface, demonstrating that HA hindered the deposition of other molecules attributed to steric hindrance (*31*). The absorbance observed may also be decreased through partial neutralisation of the surface with the HA occupying silanol sites, as well as fewer CV molecules binding directly on the silica surface as they will interact with the negative carboxyl and phenolate groups on the HA structure in suspension, Figure 3.15. As the concentration of HA is further increased in solution above 100 mgL^{-1}, a different adsorption trend over time is observed, with aggregation kinetics of the HA seen compared to the CV charged molecular binding curves previously. This will happen as at high concentrations the HA will form large complexes of supramolecular structures, which will be held together by non-covalent forces such as van der Waals forces, and *π* stacking.

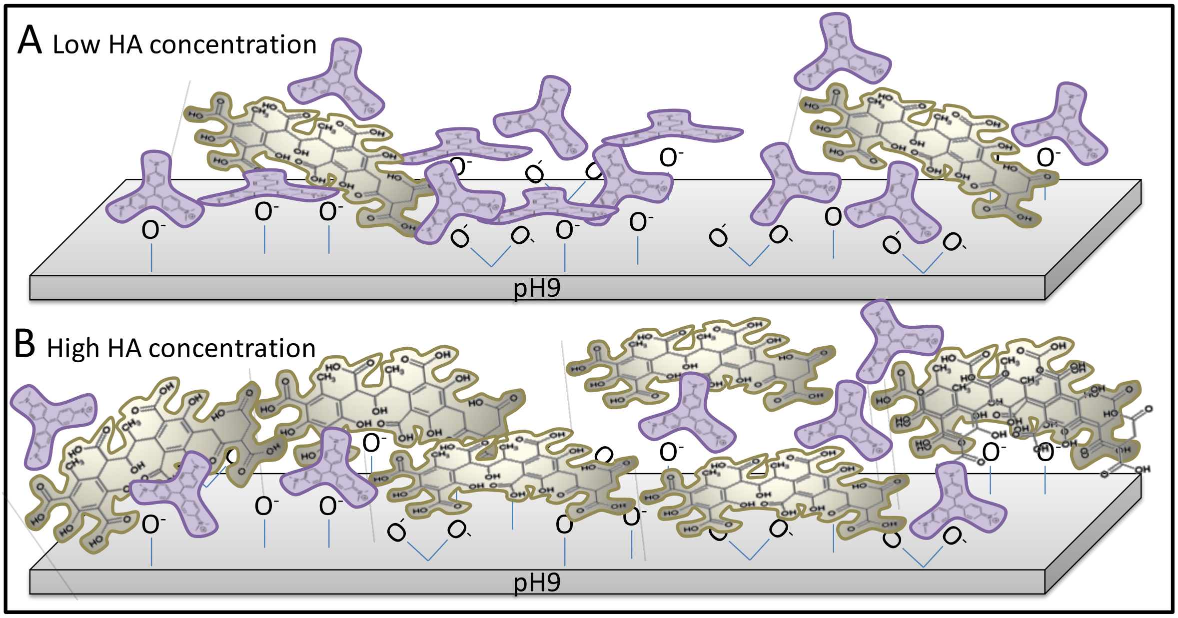

Figure 3.15 Schematic to show the surface interaction of CV and HA on the Q2 and Q3 binding sites at pH 9.

To observe the influence of the HA on the rate of association and formation of a CV layer at the interface, lines were fitted to the data from Figure 3.10 (A), and plotted as association rate constants against HA concentration, Figure 3.16. The rate decreases from 3 ± 0.1 M^{-1} s^{-1} to 0.04 ± 0.01 M^{-1} s^{-1} between 0 – 100 mgL^{-1}, and may be attributed to an interaction of more CV molecules in solution with the HA, meaning a decrease in CV concentration in the bulk, and also the hindrance of the large HA molecules at the interface, discussed previously. At high concentrations the rate of association rises slowly again, because of the increase in θ_1 absorbance observed in Figure 3.10 (A), rising back up to a rate of 0.19 ± 0.01 M^{-1} s^{-1} with 1 gL^{-1} HA present in solution, attributed to the aggregation of HA at the interface.

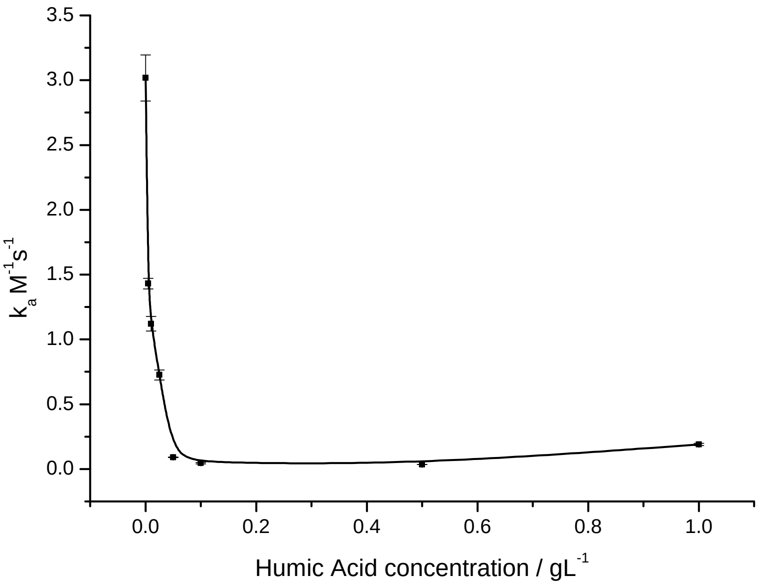

Figure 3.16 Rate of association k_a of CV (20 μM) (pH 9) v [Humic Acid]

The surface structures of CV with different concentrations of HA are shown in Figure 3.11 (A). The CV spectra with 0 mgL^{-1} HA displays the prominent S_1 and S_2 peaks seen previously, Figure 3.11 (a). At low HA concentrations, between 0 -100 mgL^{-1}, Figure 3.11 (A) (b-e), you have two peaks S_1 and S_2 at 581 nm and 602 nm. These are the 2 nm blue shifted peak observed in the CV pH 9 surface structure previously, and a 19 nm red shifted peak, similar to the red shifted peak before. The previously prominent S_1 peak in the CV interface spectra is less dominant with HA in solution, decreasing considerably, even with the lowest concentration of HA, resulting in surface spectra similar to a pH 5 interface. With increasing HA concentration, the S_1:S_2 peak ratio decreases, indicating the change in S_1 peak absorbance corresponding to a decreased GC layer formation. The interfacial concentration of CV molecules can be derived at the interface, using the data deconvolved in Chapter 2. With no HA in suspension, the spectrum indicates a CV interfacial concentration of 1.33 molecules nm^{-2}. This decreases down to 0.74 molecules nm^{-2} with 5 mgL^{-1} HA present in suspension, and 0.06 molecules nm^{-2} with 100 mgL^{-1} HA, a 14.2 fold decrease, a total of 1 x 10^{12} molecules present at the surface.

The CV interfacial concentration for the 1 gL^{-1} HA spectra was not calculated, as it shows no CV adsorption trend, Figure 3.11 (f). The S_1:S_2 adsorption ratio of 0.69:1, confirms the assumption that the change in surface kinetics observed previously were a result of the aggregation of HA onto the silica surface at high concentration. With the spectra normalised at 607 nm, the aggregated HA structure is clearly shown at concentrations above 100 mgL^{-1}.

3.5 Conclusions

The interaction of the CV chromophore at the silica interface in organic and inorganic suspensions, suggest that the components of the environment will have a direct influence on a particle surfaces charge and interaction. In the inorganic interface, the NaCl showed competitive binding with the CV, with an affinity towards the negative silanol sites. At high NaCl concentrations, comparable to NaCl concentrations found in the oceans (*6*), the Na^+ cations appear to form a stable lattice on the surface in co-formation with CV molecules. This is relevant to the environment as it indicates that in inorganic media, nanoparticle surfaces may form rapid inorganic layers, causing partial neutralisation of surface charge. This will reduce surface repulsion, creating instability and increasing nanoparticle aggregation. Once nanoparticles aggregate in suspension, they are likely to sediment out relatively quickly; meaning the relevant characterisation that needs to be made is observing nanoparticle interaction with the sediment.

In the organic interface, the CV appeared to interact with the HA molecules in solution, and were prevented from surface interaction with the silica surface at HA concentrations above 100 mgL^{-1}. The HA formed a stable aggregated layer on the charged surface, preventing charge particle interaction. This indicates that for nanoparticles in organic suspensions, a complex organic layer can form at the particle charged surface, which may completely encapsulate the particles, in an organic layer around the particle, meaning the surface availability and interaction of the particles may be irrelevant.

References

1. Solomon, T. (2001) The Definition and Unit of Ionic Strength, *Journal of Chemical Education 78*, 1691.
2. van Bennekom, A J, and Wetsteijn, F J. (1990) The winter distribution of nutrients in the Southern Bight of the North Sea (1961-1978) and in the estuaries of the scheldt and the rhine/meuse, *Netherlands Journal of Sea Research 25*, 75-87.
3. Steinhorn, I. (1983) In Situ Salt Precipitation at the Dead Sea, *Liminology and Oceanography 28*, 580-583.
4. Kohout, F A, Hathaway, J C, Folger, D W, Bothner, M H, Walker, E H, Delaney, D F, Frimpter, M H, Weed, E G A, and Rhodehamel, E C. (1977) Fresh Ground Water Stored in Aquifiers under the continental shelf: Implications from a deep test, Nantucket Island, Massachusetts, *JAWRA Journal of the American Water Resources Association 13*, 373-386.
5. McLean, P H, Smith, G W, and Wilson, M J. (1990) Residence time of the sea louse, Lepeophtheirus salmonis K., on Atlantic salmon, Salmo salar L., after immersion in fresh water, *Journal of Fish Biology 37*, 311-314.
6. Israelachvili, J N (1991) *Intermolecular and Surface Forces*, 2nd Edition ed., Academic Press, London.
7. Dishon, M, Zohar, O, and Sivan, U. (2009) From Repulsion to Attraction and Back to Repulsion: The Effect of NaCl, KCl, and CsCl on the Force between Silica Surfaces in Aqueous Solution, *Langmuir 25*, 2831-2836.
8. Metin, C, Lake, L, Miranda, C, and Nguyen, Q. (2010) Stability of aqueous silica nanoparticle dispersions, *Journal of Nanoparticle Research 13*, 839-850.
9. Dickson, D, Liu, G, Li, C, Tachiev, G, and Cai, Y. (2011) Dispersion and stability of bare hematite nanoparticles: Effect of dispersion tools, nanoparticle concentration, humic acid and ionic strength, *Science of The Total Environment 419*, 170-177.

10. Chowdhury, I, Hong, Y, Honda, R J, and Walker, S L. (2011) Mechanisms of TiO2 nanoparticle transport in porous media: Role of solution chemistry, nanoparticle concentration, and flowrate, *Journal of Colloid and Interface Science 360*, 548-555.
11. Thurman, E M, and Malcolm, R L. (1981) Preparative isolation of aquatic humic substances, *Environmental Science & Technology 15*, 463-466.
12. Woodwell, G M, Whitaker, R H, Reiners, W A, Likens, G E, Delwich, C C, and Botkin, D B. (1978) Biota and the World carbon budget, *Journal Name: Science; (United States); Journal Volume: 199:4325*, Medium: X; Size: Pages: 141-146.
13. Koopal, L K, Riemsdijk, W H v, and Kinniburgh, D G. (2001) Humic matter and contaminants : general aspects and modeling metal ion binding.
14. Jones, M N, and Bryan, N D. (1998) Colloidal properties of humic substances, *Advances in Colloid and Interface Science 78*, 1-48.
15. Schulten, H R, and Schnitzer, M. (1993) A state of the art structural concept for humic substances, *Naturwissenschaften 80*, 29-30.
16. Stevenson, F J (1982) *Humics Chemistry: Genesis, Composition and reactions,* , New York.
17. Zhang, Y, Chen, Y, Westerhoff, P, and Crittenden, J. (2009) Impact of natural organic matter and divalent cations on the stability of aqueous nanoparticles, *Water Research 43*, 4249-4257.
18. Chen, K L, and Elimelech, M. (2008) Interaction of Fullerene (C60) Nanoparticles with Humic Acid and Alginate Coated Silica Surfaces: Measurements, Mechanisms, and Environmental Implications, *Environmental Science & Technology 42*, 7607-7614.
19. Varadachari, C, Chattopadhyay, T, and Ghosh, K. (1997) Complexation of Humic Substances with Oxides of Iron and Aluminum, *Soil Science 162*, 28-34.
20. Vermeer, A W P, van Riemsdijk, W H, and Koopal, L K. (1998) Adsorption of Humic Acid to Mineral Particles. 1. Specific and Electrostatic Interactions, *Langmuir 14*, 2810-2819.

21. Avena, M J, and Koopal, L K. (1999) Kinetics of humic acid adsorption at solid-water interfaces.
22. Avena, M J, and Koopal, L K. (1998) Desorption of Humic Acids from an Iron Oxide Surface, *Environmental Science & Technology 32*, 2572-2577.
23. Gu, B, Schmitt, J, Chen, Z, Liang, L, and McCarthy, J F. (1995) Adsorption and desorption of different organic matter fractions on iron oxide, *Geochimica et Cosmochimica Acta 59*, 219-229.
24. Francis, R, Livens. (1991) Chemical reactions of metals with humic material, *Environmental Pollution 70*, 183-208.
25. Tong, Z, Bischoff, M, Nies, L, Applegate, B, and Turco, R F. (2007) Impact of Fullerene (C60) on a Soil Microbial Community, *Environmental Science & Technology 41*, 2985-2991.
26. Chen, J, Patil, S, Seal, S, and McGinnis, J F. (2006) Rare earth nanoparticles prevent retinal degeneration induced by intracellular peroxides, *Nat Nano 1*, 142-150.
27. Bian, S-W, Mudunkotuwa, I A, Rupasinghe, T, and Grassian, V H. (2011) Aggregation and Dissolution of 4 nm ZnO Nanoparticles in Aqueous Environments: Influence of pH, Ionic Strength, Size, and Adsorption of Humic Acid, *Langmuir 27*, 6059-6068.
28. Keller, A A, Wang, H, Zhou, D, Lenihan, H S, Cherr, G, Cardinale, B J, Miller, R, and Ji, Z. Stability and Aggregation of Metal Oxide Nanoparticles in Natural Aqueous Matrices, *Environmental Science & Technology 44*, 1962-1967.
29. Zalicki, P, and Zare, R N. (1995) Cavity Ring-Down Spectroscopy for Quantitative Absorption-Measurements, *J. Chem. Phys. 102*, 2708-2717.
30. Yonebayashi, K, and Hattori, T. (1988) Chemical and biological studies on environmental humic acids, *Soil Science and Plant Nutrition 34*, 571-584.
31. Jiang, X, Tong, M, Li, H, and Yang, K. (2010) Deposition kinetics of zinc oxide nanoparticles on natural organic matter coated silica surfaces, *Journal of Colloid and Interface Science 350*, 427-434.

Chapter 4

CeO_2 Nanoparticle Characterisation and Interaction at the Silica-Water Interface

4.1 Introduction

The structure of a negatively charged interface has been considered, characterising the interaction of the chromophore counter-ion CV at a silica surface as a function of bulk solution pH. The interfacial structure analysis was extended to organic and inorganic interfaces, demonstrating that in different environmental conditions, a charged surface would quickly form stable organic and inorganic complexes. In this chapter, CeO_2 nanoparticles, which have positively charged surfaces, will be characterised considering the effect of surface charge on suspension stability, and the aggregation properties of the nanoparticles in environmentally relevant media.

CeO_2 is a nanoparticle extensively used in industry, as a polishing agent for mirrors and optics (*1*), in glass and ceramics (*2*), and in solar cells (*3*). It is predominantly used in diesel fuels increasing combustion efficiency at high temperatures (*4*), with the mechanism associated with cerium's two valence states (Ce^{3+} and Ce^{4+}) (*5*). It is able to switch oxidation states forming Ce_2O_3 from CeO_2 relatively easily, Equation 4.1, and subsequently able to re-adsorb oxygen, making it a good oxygen store, and enhancing the combustion process by oxidising carbon (*6*).

$$4CeO_2 \leftrightarrow 2Ce_2O_3 + O_2$$

Equation 4.1

It has been shown to increase fuel efficiency in a study on Envirox™, a fuel containing CeO_2 nanoparticles, increasing total miles per gallon by 5-9% (*4, 7*). It is also used in catalytic converters decreasing harmful particle matter to harmless gases (*8*), reducing hydrocarbons to CO_2 and H_2O, soot to CO_2, and nitrogen oxides to N_2 (*6*). Logothetidis *et al.* published evidence that there was increased fuel efficiency with decreased particle size (*9*), attributed to an increase in oxygen vacancy at the particle surface (*10*). High thermal stability (MP, 2600°C (*6*)) of CeO_2 means it is not destroyed in the combustion process, and will enter the environment through exhaust emissions. The nanoparticles, post combustion, will inevitably have a degree of soot layer formation around the particle surface, influencing initial particle availability, depending on its stability and potential removal through interaction with the environment. CeO_2 nanoparticles are toxic to humans (*11*), with CeO_2 nanoparticle emissions shown to have adverse impacts on cardiac and respiratory health on inhalation (*12*).

CeO_2 in the bulk has a large lattice energy (*1*) of 12661 kJ mol^{-1} (*13*), which is assumed to be similar to the lattice energy of the nanoparticle and accounts for the poor particle solubility in water (*14*). This has important consequences for nanoecotoxicology of CeO_2 nanoparticles: these nanoparticles are unlikely to dissolve releasing Ce^{3+}/Ce^{4+} ions and will instead persist in the environment for long periods (*15, 16*). Once released in the air as exhaust emissions, there are two predominant exposure routes of CeO_2 to humans, through inhalation and by ingestion either directly or by eating organisms that have taken up nanoparticles further down the food chain. Respiratory effects on humans and animals have been extensively studied, with particles deposited in the alveoli in the lungs (*17*) resulting in oxidative stress toxicity observed in the bronchial epithelial cells (*12, 18, 19*). Lin *et al.* also observed increased cell membrane damage in human bronchi (*20*), and evidence of diffusion through the cell membranes into the blood stream (*21*). Airborne nanoparticles will eventually settle out of the atmosphere, with research showing higher concentrations of CeO_2 nanoparticles in soil adjacent to busy roads (*12*). Once in the soil, the nanoparticles can enter the water table leading to liquid phase toxicity, including cell death on exposure to bacteria in the water systems through oxidative stress (*22*), and can be taken up by aquatic organisms and sedimentary organisms into the human food chain, shown in Figure 4.1.

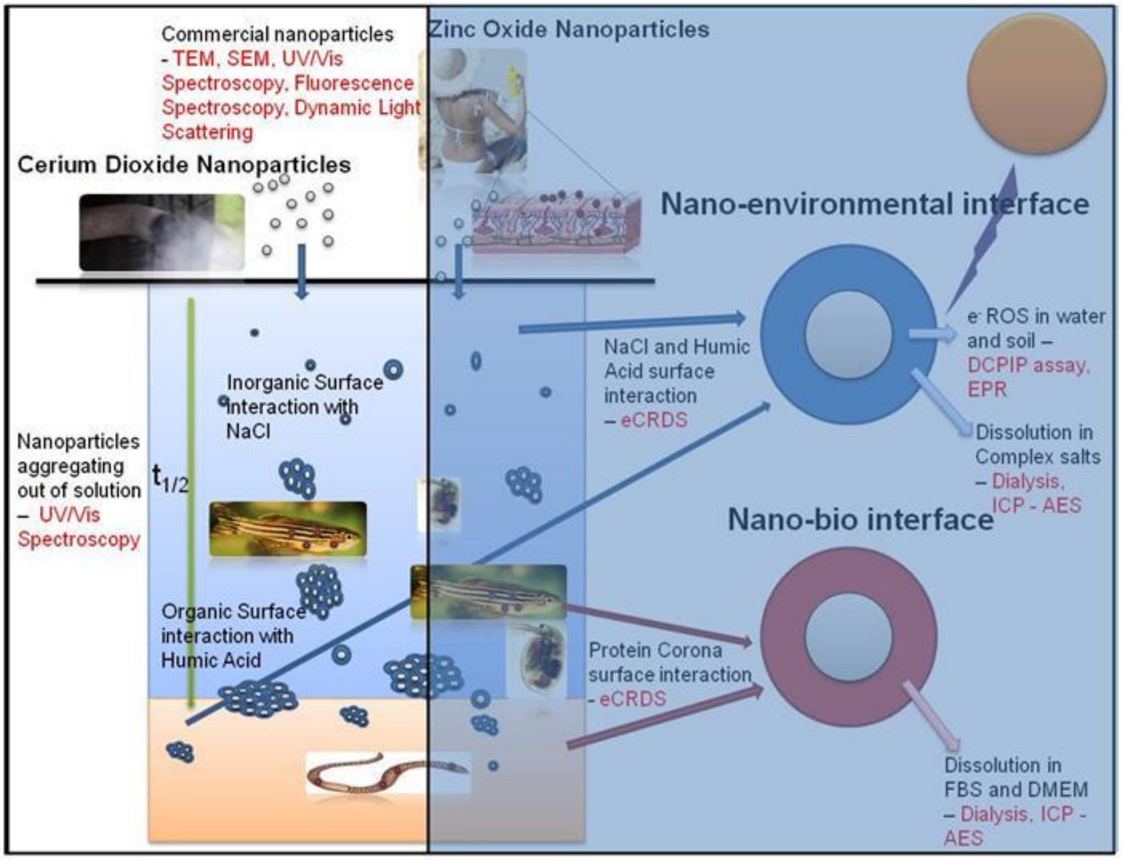

Figure 4.1 Thesis Schematic, showing the commercial nanoparticle dispersion into the environment, highlighting the important characterisation techniques used to determine the nanoparticle stability in the environment.

4.1.1 CeO_2 Nanoparticle Characterisation

CeO_2 as diesel additives will be emitted into the environment with a coating of residue from combustion chemistry, and this is extraordinarily difficult to characterise. Once the nanoparticles are airborne inhalation will solubilise the nanoparticles into solution covering their surfaces with lung surfactants, making the primary mechanism of interaction with the human lung alveoli in the solution phase, whilst nanoparticles not inhaled, are likely to settle into the soil or water systems. To understand the effects of the CeO_2 nanoparticles in aqueous environments, characterisation of dispersion stability and aggregation is required (*23*), as these parameters will influence the length of time the nanoparticles are available in a particular environment and thus their bio-availability, Figure 4.1. The key parameter that will influence nanoparticle stability in suspension is the surface charge (*24*), with the surface chemistry also significant as it will directly influence the particle toxicity (*25*). We have thus performed characterisation studies of the pure CeO_2 nanoparticle surfaces to act as model interactions, addressing the CeO_2 nanoparticle surface chemistry and interface structure in suspension.

Nanoparticles dispersed in a liquid form a colloid, the stability of which is currently understood using the DLVO theory, discussed in Chapter 1. Once the CeO_2 nanoparticles are dispersed in a suspension a charged double layer will form on the particle surface with the dissociation of surface groups, generating a surface potential, Figure 4.2. This surface potential will attract counter ions from the bulk suspension onto the surface and form a double layer structure, with an inner Stern layer, consisting of a strong, closely bound counter-ion layer, and then a second more loosely bound mobile layer further away from the surface, the diffuse layer.

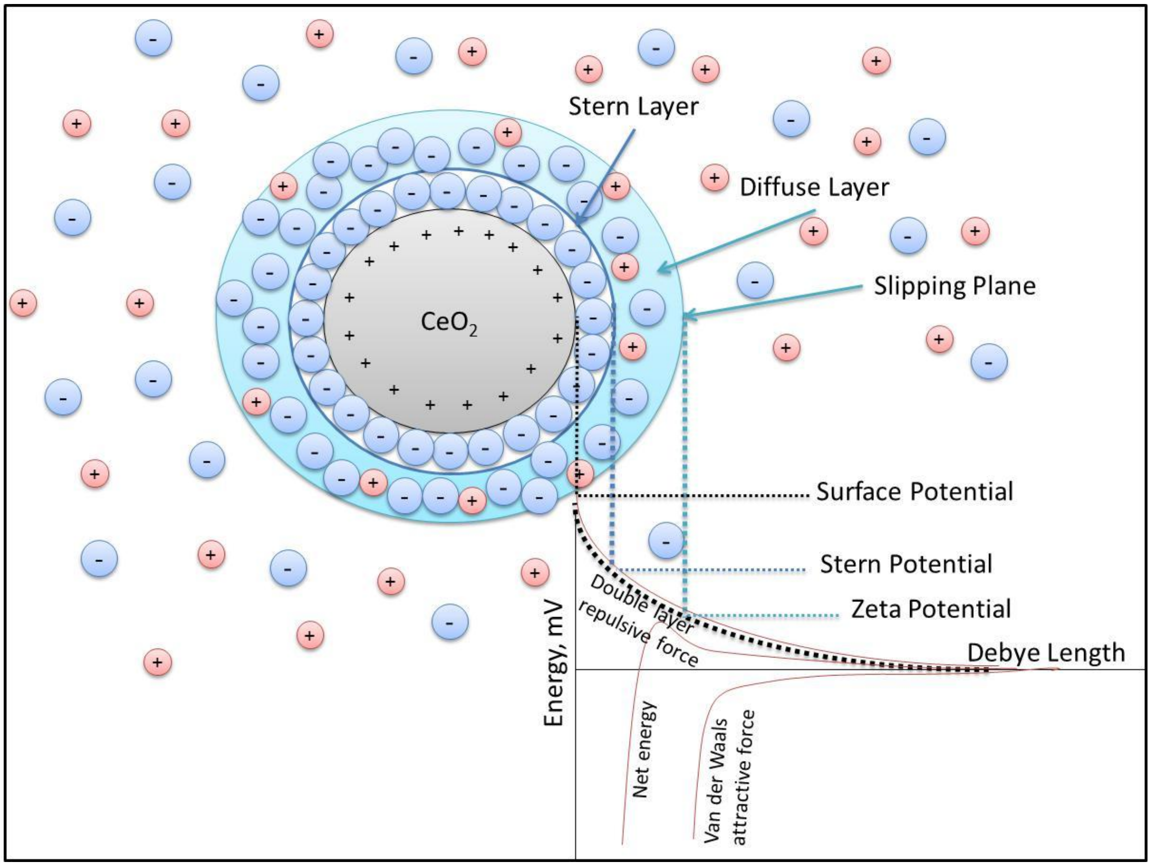

Figure 4.2 Formation of the charged nanoparticle surface double layers responsible for colloidal suspension stability

To observe effects at the charged surface, zeta potential measurements will be taken over time. The zeta potential, discussed in Chapter 1, shows the potential difference between the bulk solution attractive forces and repulsive forces of the double layer indicating the stability of the particles. The zeta potential defines the boundary of the diffuse layer, the slipping plane, showing the strength of the repulsive forces relative to the distance from the surface, the Debye length. Unstable particles in suspension will undergo aggregation, the interaction of particles to form a larger particle with an external surface area significantly smaller than the total surface area of the individual nanoparticles (*26*) and may form reversibly, flocculation, or irreversibly, coagulation. The aggregation of particles will alter the associated nanoparticle characteristics with the increase in size and the reduction of the surface area to volume ratio. To observe the aggregation of the CeO_2 nanoparticles in suspension, Dynamic Light Scattering (DLS) and UV-Vis spectroscopy techniques will be used. These properties are measured over time to assess the stability and lifetime of the suspension in deionised water and as a function of ionic strength in the solution. The complexity of the medium will be increased to include a biologically relevant salts medium used in Fish exposure studies, consisting of 4 different salts in suspension, ISOFish water (*27*).

Charged interface studies will be extended to observe the adsorption of CeO_2 nanoparticles at the silica interface as a model for the interaction with soil particles. There has been extensive previous research of nanoparticle interaction at charged surfaces, predominantly with gold and Ag nanoparticles used to develop biosensors (*28-31*) looking at aggregation and monolayer formation. Here competitive binding on the silica surface between the nanoparticles and a charged chromophore, CV were studied at the interface. The 635 nm cavity configuration documented in Chapter 2, is not suitable for observing direct CeO_2 nanoparticle interaction as the CeO_2 nanoparticles display a λ_{max} within the UV range, so a cavity configuration with mirrors and prisms centred at 420 nm to coincide with the shoulder of the CeO_2 bandgap has been implemented.

4.1.2 Aims and Objectives

Nanograin CeO_2 particles were chosen as part of the PROSPEcT research project, identifying and characterising specific nanoparticles used in fuel-additives. The aim of this chapter is to characterise the CeO_2 nanoparticle surface interactions in suspension, and their consequences on the particle availability in the environment. The objectives of this chapter are to establish a stable nanoparticle dispersion protocol in suspension, measuring the life-time of the nanoparticle suspension by monitoring the UV-Vis absorbance at the CeO_2 bandgap. The role of environmentally relevant media will also be observed on particle surface interaction and aggregation properties. This characterisation will be achieved using UV-Vis spectroscopy, DLS and Zetasizer techniques in collaboration with the National Physics Laboratory (NPL) (*32, 33*). Another objective will observe the adsorption of nanoparticles to a pH 7 soil surface, with the silica-water interface as a model interface, using EW-CRDS and visualised through Electron Microscopy. Finally, information on the cooperative binding of CeO_2 nanoparticles at a charged interface in the presence of other charged species will be established to address the factors that control the interaction of CeO_2 nanoparticles in the Environment.

4.2 Materials and Experimental Methods

4.2.1 Materials

The CeO_2 nanoparticles characterised and used in this chapter were Nanograin CeO_2 particles (CB250#41#05) provided by Umicore (Olen, Belgium) as part of the on-going PROSPEcT project. The nanoparticle characterisation by the manufacturers specified a nanoparticle size of 70 ± 11 nm when dispersed in water, measured by X-ray disc centrifuge (XDC), a Brunauer-Emmett-Teller (BET) particle surface area of 30 ± 3 m^2g^{-1} and X-ray photo-electron spectroscopy (XPS) composition values of $Ce^{4+}[CeO_2]$ 93.1%: $Ce^{3+}[Ce_2O_3]$ 6.9% (*34*). The ISOFish water is a salts medium made up of Calcium Chloride ($CaCl_2$) 4.87 mM, Magnesium Sulphate ($MgSO_4$) 1.92 mM, Sodium Bicarbonate ($NaHCO_3$) 1.54 mM and Potassium Chloride (KCl) 0.15 mM, made up in deionised water (18 MΩ cm^{-1}), at pH 7.

4.2.2 Nanoparticle Dispersion Protocol

The CeO_2 nanoparticles were dispersed using a dispersion protocol designed in collaboration with the National Physics Laboratory (NPL), to optimise nanoparticle dispersion stability (*35*). A mass of dry powder equivalent to the desired final concentration was weighed into a polypropylene universal tube. The contents of the tube were mixed into a paste with a few drops of Millipore deionised water using a metal spatula. The paste was then suspended in 15 mL Millipore deionised water and sonicated with an ultra-sonic probe (Cole-Parmer ® 130-Watt Ultrasonic

Processors (50/60 Hz, VAC 220) EW-04714-51) for 2 × 10 seconds at 90% amplitude to separate the nanoparticle aggregates. Finally, the sonicated suspension was mixed into the end volume of Millipore deionised water using a glass stirring rod. Once the nanoparticles were dispersed into the test media, they were stored in the dark until required.

4.2.3 UV-Vis Spectroscopy

The absorbance spectroscopy of the suspensions were performed using a Lambda 850 UV-Vis spectrometer (Perkin Elmer, Seer Green, UK), analysed using UV winlab software (version 5.1.5), with a slit width of 2 nm. The spectrometer was calibrated using Holmium glass standards (UR-HG, serial # 9392, Starna Scientific). All UV-Vis spectroscopy measurements were repeated in triplicate.

4.2.4 Zeta Potential and Dynamic Light Scattering

The dynamic light scattering (DLS) and zeta potential measurements of samples were obtained using a Zetasizer Nano ZS (Malvern Instruments, UK), with both measurements taken in unison. The data was analysed using Malvern Instrument Dispersion Technology software (Version 4).

4.2.5 EW-CRDS Cavity Configuration

The 635 nm EW-CRDS configuration used in both chapter 2 and chapter 3, was used here without modification, for examining nanoparticle interaction with CV at the silica interface. The EW-CRDS was also modified for a 420 nm configuration detailed below.

Light from the previously discussed fundamental YAG laser and Surelite OPO Plus is launched through a free space single mode fibre launch platform (Thorlabs, KT110). The light is collimated using a 400-600 nm Collimator (f-2.0mm, Thorlabs, CFC-2X-A), and through a mounted aspheric lens (AR: 400-600 nm, Thorlabs, C230TME-A). The collimated light is guided through the side of the cavity using a single mode fibre patch cable, 400-550 nm, FC/PC, Thorlabs, P1-450A-FC-1), with the blue light launched from the anti-reflection coating of one of the Dove prism faces (42.3 mm x 10.0 mm x 10.0 mm), with coatings of AR (<0.5%R) at 400-440 nm (4%deg.p-pol, SLS Optics Ltd) on both the entrance and exit faces. The cavity consists of high reflectivity (R>99.995%) 1” diameter concave mirrors, with bandwidth 400-430 nm (CRD Optics, Inc. 901-0010-0415), spaced 140 cm apart, Figure 4.3.

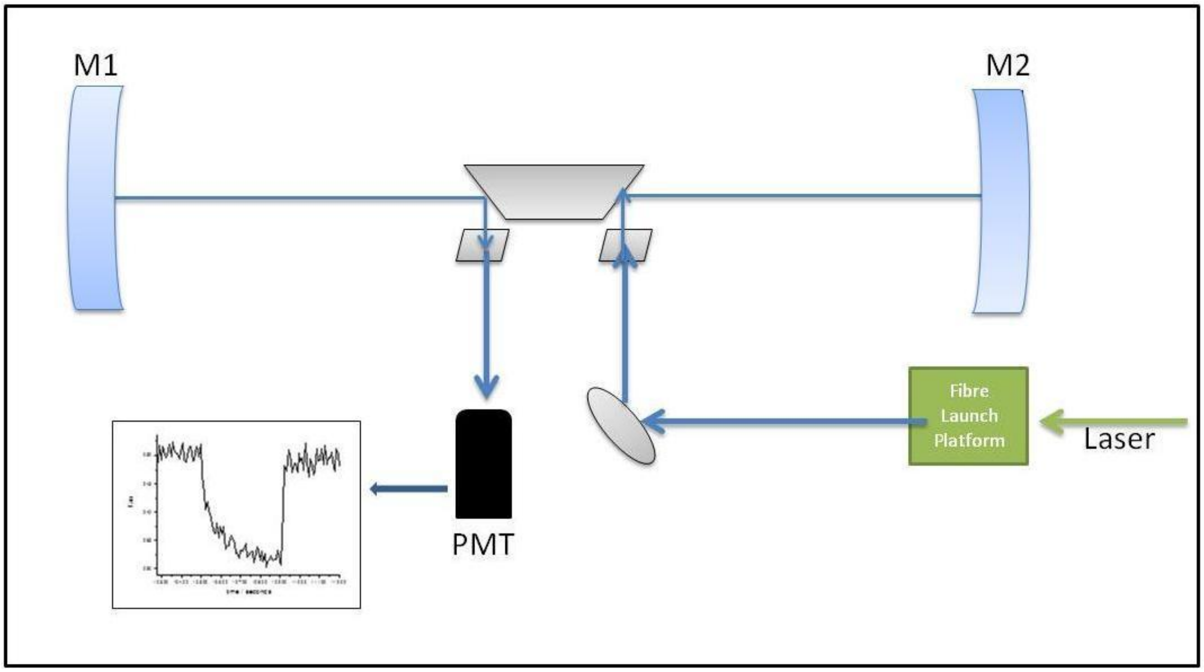

Figure 4.3 EW-CRDS set-up using a fibre-launch platform through anti-reflection coatings of the Dove prism, at 420 nm

The wavelength of the radiation entering the cavity was controlled by rotating the β-Barium Borate crystal in the Surelite OPO Plus. The micro-stepping controller was calibrated manually; measuring the radiation wavelength emitted using a UV-Vis spectrometer between 410 – 500 nm, Figure 4.4 (A) and converted to a wavelength-step calibration curve, Figure 4.4 (B).

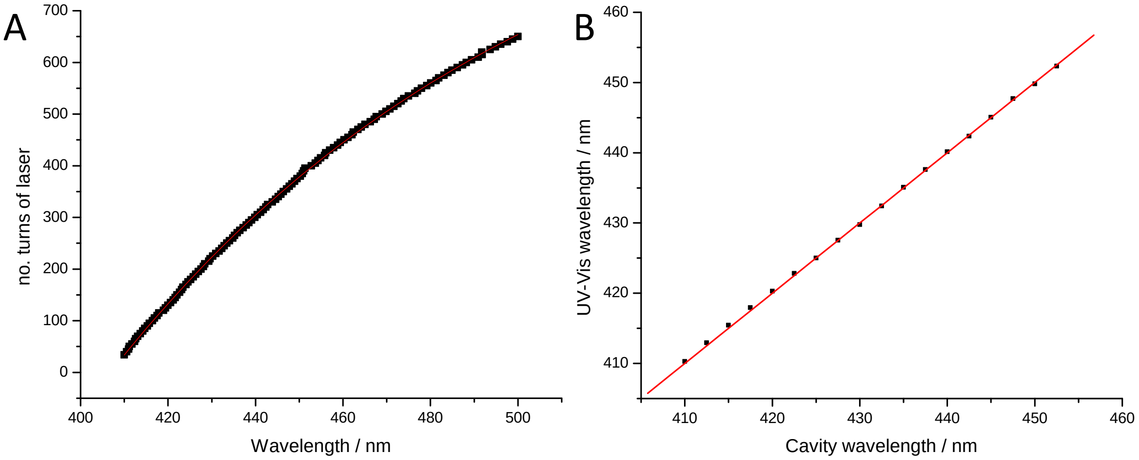

Figure 4.4 Calibration of the tuneable Surelite OPO Plus radiation wavelength entering into the cavity, A – shows the wavelength recorded against the number of turns of the microstepping controller, and B – showing the measured wavelength produced for the radiation entering into the cavity

Using Equation 2.2 the ring down time τ can be calculated; for the 140 cm cavity setup, with a round trip time of 9.34 ns, and mirror reflectivity of 0.9995, the current cavity setup gives a maximum theoretical τ of 8.37 µs. Inclusion of the Dove prism TIR element with 45° anti-reflection coatings has a theoretical τ of 279 ns, using Equation 2.4. Practically, the average τ obtained during the experiments was 200 ns. The differences here can be attributed to the losses through the surface scatter on the top surface of the prism, and the cleaning of the prism anti-reflective surface coatings, discussed in Chapter 2.2.

4.2.6 Scanning Electron Microscopy Imaging of Nanoparticles

The nanoparticle samples were deposited onto the prism surface from the flow cell where the extinction was measured. The sample was subsequently washed for a period of hours with flowing buffer before the prism was removed and allowed to dry in air. The protocol was designed to minimise aggregation during the drying process and to reflect the surface morphology of the sample preparation. The nanoparticles deposited on the prism surface were imaged using Scanning Electron Microscopy

(SEM). The prism was initially coated with a thin layer of Au by sputter coating for 2 minutes using a Polaron SC515 SEM coating system. The Au covered silica prisms were then imaged with a Hitachi 3200 N SEM with an EDS system (Oxford Instruments).

4.3 Results

4.3.1 Cerium dioxide nanoparticle Characterisation and suspension stability

Suspensions of CeO_2 nanoparticles were prepared according to the dispersion protocol in deionised water. The UV-Vis spectrum was measured in the range 250 – 800 nm and shows a λ_{max} at 312 nm, Figure 4.5 (A). The nanoparticles were dispersed at five different concentrations and showed a linear variation in λ_{max} in the concentration range observed, Figure 4.5 (B), with the extinction spectrum shape and wavelength of λ_{max} remaining constant over the concentration range. Measuring the nanoparticle suspension extinction using UV-Vis Spectroscopy can give a direct measurement of concentration of nanoparticles in solution, Beer-Lambert Law (*36*). Here the fit of the slope (R^2 0.999) corresponds to an extinction coefficient; ε_{312nm} = $18.9 \pm 0.1 \times 10^{-3}$ L mg^{-1} cm^{-1}.

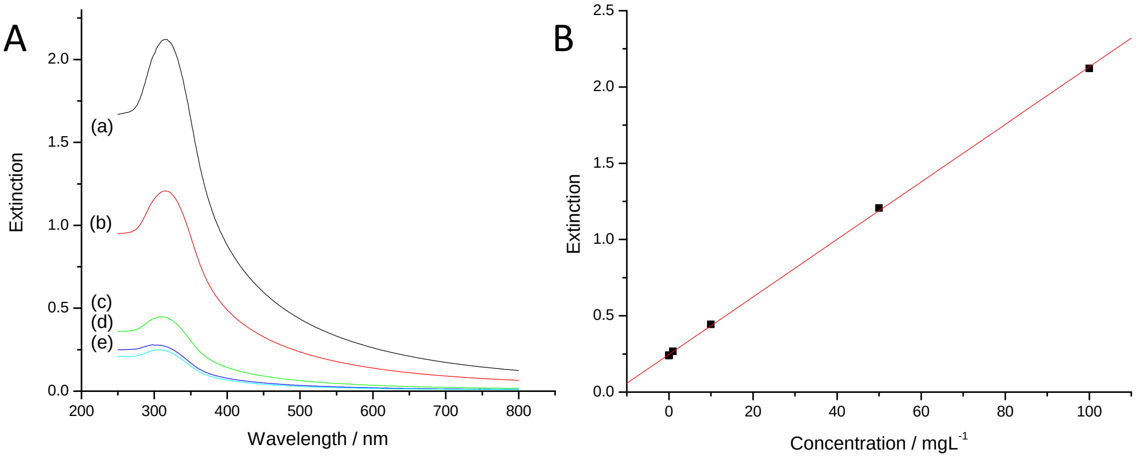

Figure 4.5 A - CeO_2 nanoparticles dispersed in deionised water observed under UV-Vis Spectroscopy at different concentrations, (a) 100 mgL^{-1} (b) 50 mgL^{-1} (c) 10 mgL^{-1} (d) 1 mgL^{-1} (e) 0.1 mgL^{-1}, and B - showing λ_{max} extinction at 312 nm against concentration

The CeO_2 nanoparticles were further dispersed in suspension according to the protocol, at a concentration of 50 mgL^{-1} in both deionised water and ISOFish water. Over the course of three days, aliquots of the suspensions were collected, and the UV-Vis spectrum was measured to produce a time course. Figure 4.6 (A) shows the extinction spectra observed for the deionised water sample at different time-points, with the ΔExt (312 nm) of the CeO_2 nanoparticles in deionised water against time shown in Figure 4.6 (B). The nanoparticle spectra appeared to remain relatively stable over time, with the extinction at *t* = 0 falling by 11 ± 3 % after 3 days.

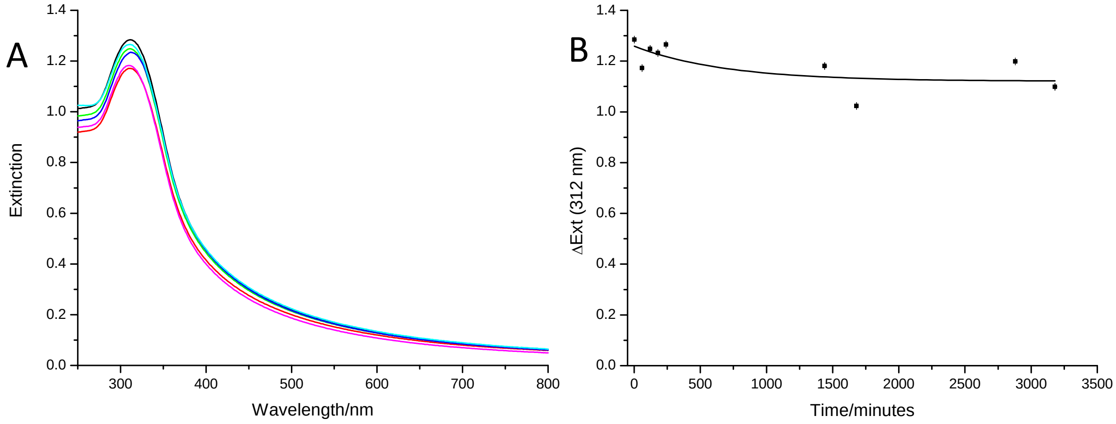

Figure 4.6 A – Extinction spectra of a CeO_2 nanoparticle (50 mgL^{-1}) suspension observed in deionised water at different time points, and B – ΔExt (312nm) of a CeO_2 nanoparticle (50 mgL^{-1}) suspension in deionised water over time.

The nanoparticles dispersed in the ISOFish water showed a broader UV-Vis extinction spectrum, with a small red shift in λ_{max} to 325 nm, Figure 4.7 (A). The measured extinction at λ_{max} was significantly lower in the ISOFish water than deionised water, with *t* = 0 values of 0.68 ± 0.01 and 1.28 ± 0.01 respectively. The extinction decreases quickly over time, Figure 4.7 (B) displayingextinction close to the instrumental detection limit of 0.08 ± 0.01 after 24 hours, remaining relatively unchanged with a value of 0.1 ± 0.01 after 72 hours.

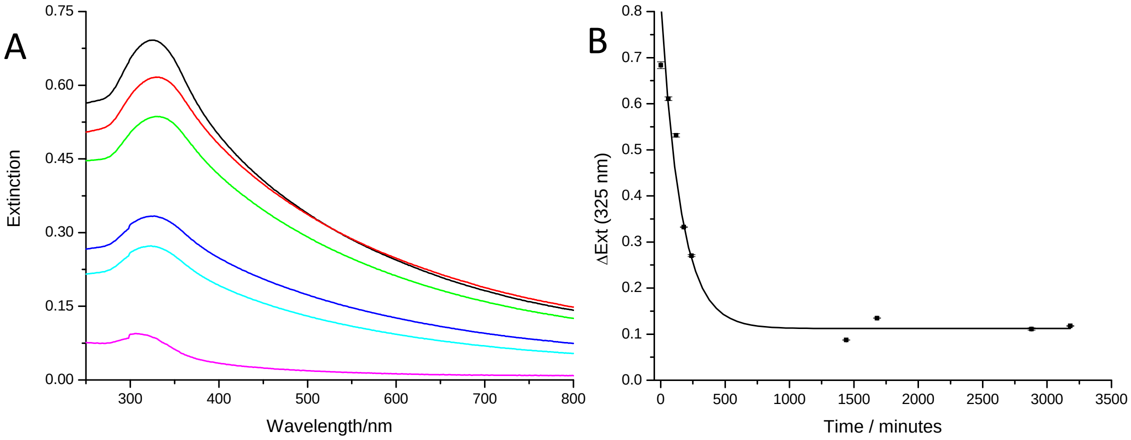

Figure 4.7 A – Extinction spectra of a CeO_2 nanoparticle (50 mgL^{-1}) suspension observed in ISOFish water at different time points, and B – ΔExt (312 nm) of a CeO_2 nanoparticle (50 mgL^{-1}) suspension in ISOFish water over time.

At each of the time points in the time course aliquots from each suspension were removed and further characterised by zeta potential and DLS. The zeta potential measurements recorded for the nanoparticles dispersed in deionised water, Figure 4.8 (a), show an initial potential of 14.1 ± 0.3 mV, rising up to 30.7 ± 0.4 mV.

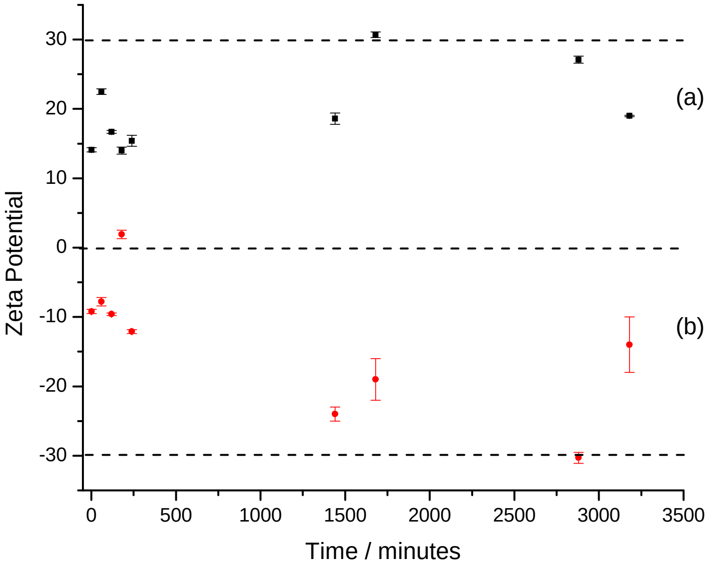

Figure 4.8 The zeta potential measurements of the CeO_2 nanoparticle suspensions (a) in deionised water and (b) in ISOFish water

The zeta potential observed in ISOFish water, Figure 4.8 (b) gives a negative value of -9.2 ± 0.3 mV at *t* = 0, with a final value recorded of -14 ± 4 mV. The day 2 and day 3 mean particle diameter and zeta potential measurements for the ISOFish water suspension have large error bars given the small extinction and hence mass left in suspension at this time, seen in Figure 4.7 (B).

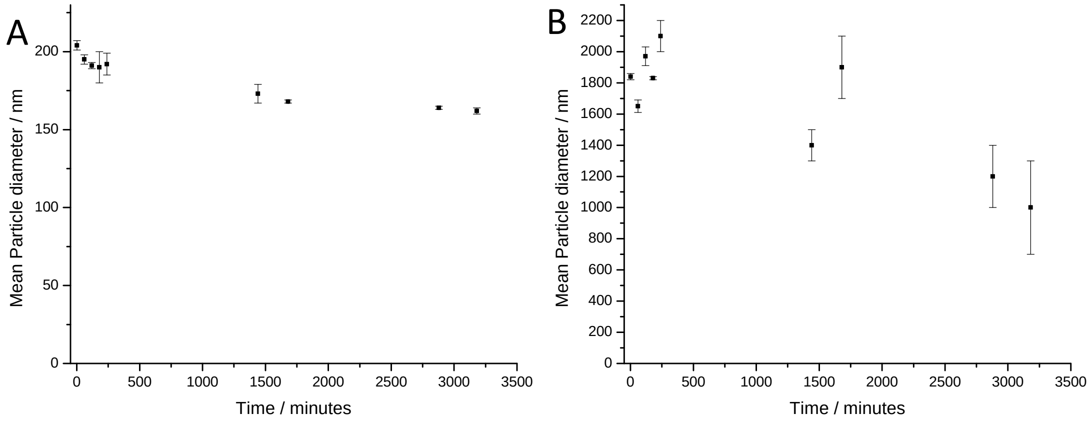

Figure 4.9 DLS measurements showing particle size observed for the CeO_2 nanoparticle (50 mgL^{-1}) suspensions over time in (a) deionised water and (b) ISOFish water

The DLS measurements, Figure 4.9 indicate a variation in particle diameter in the suspensions. The nanoparticles suspended in deionised water, Figure 4.9 (A) show a consistent small mean particle diameter, of 204 ± 3 nm at t = 0, remaining nearly constant throughout the time course, falling to 162 ± 2 nm after 72 hours. In comparison, nanoparticles suspended in ISOFish water, Figure 4.9 (B) show a mean particle size over 9 times larger than in deionised water, with a value at t = 0 of 1840 ± 20 nm. This rises to a maximum value of 2100 ± 100 nm, and remains high throughout the time course with a final reading of 1000 ± 100 nm after 72 hours.

4.3.2 Adsorption of CeO_2 Nanoparticles to the Silica-Water Interface

CeO_2 nanoparticle suspensions were prepared in deionised water with concentrations in the range 0.01 – 1 gL^{-1}, with varying bulk pH adjusted to pH 7 with small volumes of NaOH (1 M) and HCl (1 M). Made up in this suspension, the particles have been previously shown to have a positive net surface charge, with an isoelectric point of 8.5 ± 0.5 (*32*). A pH 7 water buffer was initially introduced over the surface to stabilise the silica-water interface as measured by a stable τ. The CeO_2 suspension was then introduced to the flow cell and the adsorption of the nanoparticles to the silica surface were monitored at 420 nm to produce time-dependent adsorption kinetics shown in Figure 4.10 (A).

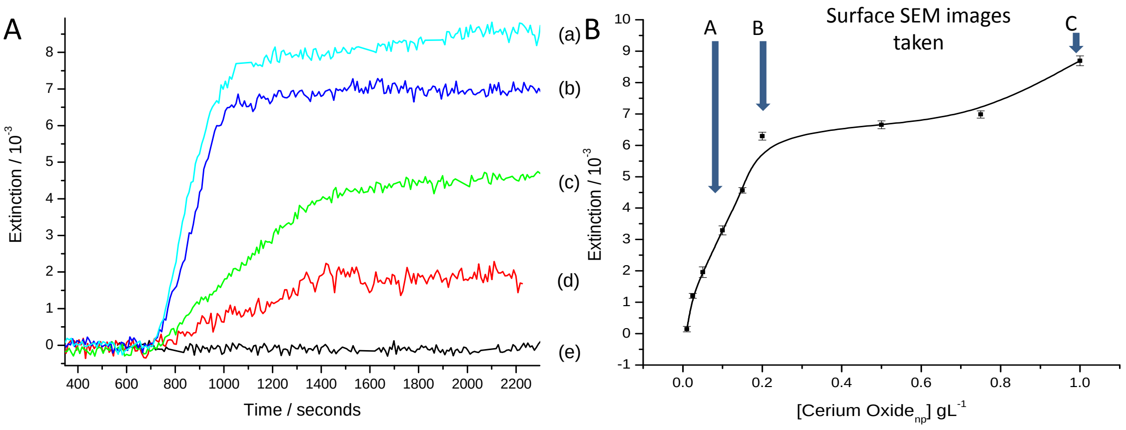

Figure 4.10 A – CeO_2 nanoparticle surface adsorption on a negatively charged silica surface, monitored at 420 nm at different concentrations, (a) 1 gL^{-1}, (b) 750 mgL^{-1}, (c) 150 mgL^{-1}, (d) 50 mgL^{-1}, and (e) 10 mgL^{-1}, and B – the θ_{max} adsorption isotherm against CeO_2 nanoparticle concentration

The extinction observed in Figure 4.10 (A), indicates slow adsorption to the surface at low dispersion concentrations, showing pseudo-Langmuir-adsorption kinetics. At higher concentrations, the adsorption kinetics are fast, appearing to reach a single surface capacity for the given pH. Figure 4.10 (B) shows the variation of the θ_{max} value observed on the silica surface against concentration, producing an isotherm for the CeO_2 nanoparticles at the silica surface, determined by taking the average of 100 data points after 3.5 minutes. The isotherm showed an initial rise in extinction from $1.4 \pm 0.8 \times 10^{-4}$ to $6.3 \pm 0.1 \times 10^{-3}$ for concentrations up to 200 mgL^{-1}, before a further rise up to $8.7 \pm 0.1 \times 10^{-3}$ at the highest concentration tested of 1 gL^{-1}.

The adsorbed nanoparticle morphology was imaged at three different dispersion concentrations. The images show an increasing degree of aggregation of the nanoparticles present on the silica surface at three different nanoparticle concentrations, Figure 4.11 (A) 100 mgL^{-1}, (B) 200 mgL^{-1} and (C) 1 gL^{-1}.

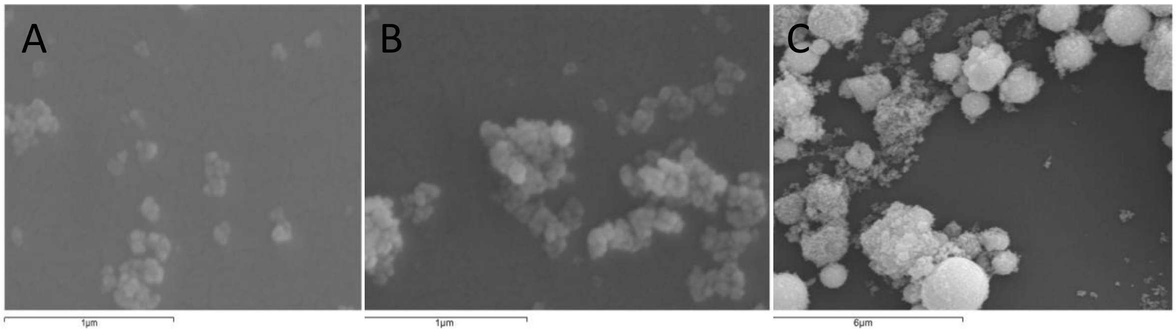

Figure 4.11 SEM images of the silica surface with different concentrations of CeO_2 nanoparticles present on the surface, (A) 100 mgL^{-1}, (B) 200 mgL^{-1} and (C) 1 gL^{-1}. The scale bar for A and B is 1 μm and 6 μm for C

The nanoparticle images for the low suspension concentrations in Figure 4.11 (A) appear to show single particles and small aggregate clusters of 5-10 nanoparticles, with a mean diameter of 112 ± 61 nm. The image displays approximately 100 nanoparticles present in the 4.32 μm^2 area of the image, corresponding to a θ_{max} of $3.29 \pm 0.14 \times 10^{-3}$. With increasing suspension concentration, the images show greater nanoparticle aggregation on the surface. The particles in Figure 4.11 (B) show 30 larger aggregates with a mean diameter of 181 ± 174 nm, with over 400 nanoparticles on the surface, corresponding to a θ_{max} of $6.29 \pm 0.12 \times 10^{-3}$. Finally, where linear adsorption kinetics are observed, the particles show significant aggregation, Figure 4.11 (C). An estimated 27 large aggregated nanoparticle spheres of between 1 – 3 μm can be seen in the image, with 90% of the interaction occupied by large nanoparticle aggregates and diameters consistent with them containing up to 2×10^5 particles each.

4.3.3 Competitive Binding of CeO_2 nanoparticles with the Chromophore counter-ion Crystal Violet

The competitive binding at the silica interface between positively charged CeO_2 nanoparticles and CV was observed using the 635 nm EW-CRDS configuration detailed in Chapter 2 and Chapter 3. At 635 nm the nanoparticles will show minimal extinction and the resulting kinetic traces inform on the changing charge at the co-operatively forming interface. CeO_2 nanoparticle suspensions were dispersed over the concentration range 0 – 300 mgL^{-1} and a fixed concentration of CV (50 µM) in deionised water using the protocol detailed previously, with the suspension pH adjusted to pH 7. The suspensions were introduced to the flow cell over the silica surface that had been pre-equilibrated at pH 7, and adsorption was monitored over time.

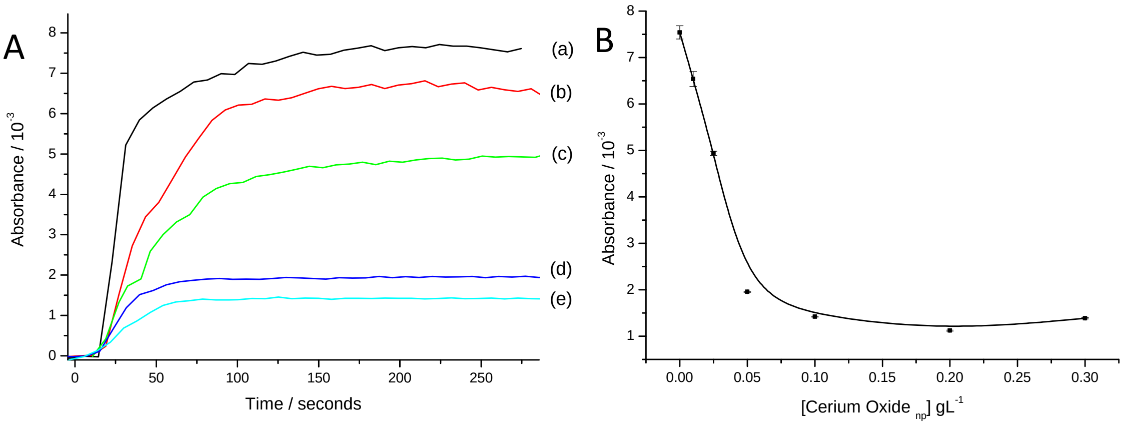

Figure 4.12 A – Competitive binding between CV (50 µM) and CeO_2 nanoparticle concentration, (a) CeO_2 (0 mgL^{-1}), (b) CeO_2 (10 mgL^{-1}), (c) CeO_2 (25 mgL^{-1}), (d) CeO_2 (50 mgL^{-1}) (e) CeO_2 (100 mgL^{-1}), and B – θ_{max} adsorption isotherm of CV (50 µM) at 635 nm against CeO_2 nanoparticle concentration

Figure 4.12 (A), shows CV (50 µM) adsorption curves with different concentrations of CeO_2 in dispersion, (a) 0 mgL^{-1}, (b) 10 mgL^{-1}, (c) 25 mgL^{-1}, (d) 50 mgL^{-1} and (e) 100 mgL^{-1}. As the concentration of nanoparticles added to the suspension is increased, the CV adsorption decreases. The θ_{max} of CV adsorption is shown in Figure 4.12 (B). The θ_{max} initially decreases linearly from 0 mgL^{-1} to 50 mgL^{-1}, showing θ_{max} values of 7.51 ± 0.04 x 10^{-3} down to 1.95 ± 0.01 x 10^{-3} respectively. The absorbance values observed at higher concentrations of CeO_2 appear to show no significant change, with a final θ_{max} value of 1.39 ± 0.01 x 10^{-3} seen for 300 mgL^{-1} CeO_2 in suspension.

4.4 Discussion

Determining the CeO_2 nanoparticle behaviour in suspension is fundamental in assessing its availability in the environment and its potential toxicity mechanisms. The objectives of the chapter looked to establish a protocol for the dispersion of CeO_2 nanoparticles into a suspension, to observe the stability and aggregation properties over time, and the influence of more complex media on the suspension parameters. The nanoparticle interactions with the model silica-water charged interface, representing an inorganic surface in the environment, were also observed, with clustering and aggregation effects visualised through SEM imaging.

4.4.1 Cerium dioxide Characterisation and stability

The CeO_2 nanoparticles suspended in deionised water show a broad extinction spectrum with a narrower λ_{max} extinction peak, a feature of a wide band gap semiconductor. They have a band gap of 5.5 eV (*37*), corresponding to an adsorption peak at 312 nm, Figure 4.5 (A). The extinction λ_{max} increases linearly with nanoparticle concentration in the range 0.1 – 100 mgL^{-1}, with the intercept of the calibration curve at 0.25 ± 0.01, Figure 4.5 (B). The non-zero intercept may be an artefact of nanoparticle residue present on the cuvette, or residual scatter from the nanoparticle extinction spectrum. In the concentration range observed, the spectrum may be considered to be a contribution from the band-gap absorption with an approximately Lorentzian absorption feature on a rising $1/\lambda^4$ scatter spectrum.

The nanoparticle dispersions in deionised water showed a stable suspension over 3 days, with an estimated half-life, $t_{1/2}$ of 330 ± 60 hours, Figure 4.6 (B). In deionised water the nanoparticles will have positively charged surfaces, balanced by OH^- in the water, giving rise to a surface potential that results in inter-particle Columbic repulsive forces, described by the DLVO theory. The nanoparticle repulsion can be quantified by the zeta potential values of the particles in suspension. The zeta potential for the deionised water sample, Figure 4.8 (a), increases with time to 30.7 ± 0.4 mV observed after 2 days. This indicates that the suspension stability is increasing as the suspension matures. However, an increasing stability appears to contradict the UV-Vis spectrum time dependence, which shows a steady decrease over time. The increase in zeta potential may be attributed to the sedimentation of larger aggregate particles that are not stable in the suspension, leaving the more stable single particles or very small clusters to dominate the zeta potential measurement. The DLS measurements provide information on the nanoparticle sizes in the suspension, indicating a particle hydrodynamic diameter, D_H of around 200 nm, Figure 4.9 (A) derived from the Stokes-Einstein equation (*38*). The results indicate that the observed particle size is likely to consist of a small cluster of nanoparticles, rather than individual nanoparticles in suspension.

The extinction spectrum of the nanoparticles dispersed in ISOFish water displays a 13 nm red shift in the band maximum λ_{max} to 325 nm, and a 46.8 ± 0.4 % fall in the extinction at t=0, of 0.68 ± 0.007 compared to 1.28 ± 0.001 in deionised water, Figure 4.7 (A). This broadening of the λ_{max} feature in the spectrum has previously been attributed to particle aggregation in suspension (*39*). The nanoparticle suspension is unstable in ISOFish water, with the nanoparticles showing a suspension half-life, $t_{1/2}$ of 3.6 ± 0.6 hours, having completely sedimented in 2 to 3 days. Suspension instability with increasing ionic strength is well known (*40, 41*) and may be explained as a collapse of the GCS interface to a bi-layer with a significantly reduced Debye length (*42*). The Debye length in pure water is approximately 1 µm, and this can decrease to 0.3 nm in a 1 M NaCl solution (*42*). As a result the nanoparticles can interact closely with one another, overcoming repulsive forces and forming unstable aggregates, which sediment out of suspension.

The zeta potential for the ISOFish suspension is negative, around -20 mV, whereas the zeta potential for the suspension in deionised water is positive, 30 mV. Previous studies have observed a similar sign change in the zeta potential with Xia *et al.* obtaining a value of +15 mV for CeO_2 nanoparticles in water and –10 mV for nanoparticles dispersed in DMEM, (*43*). The switch has been attributed to sulphate and chloride counter ion interactions from the ISOFish water forming a negatively charged inorganic surface corona. The zeta potential measurements are derived from the drift velocity in a medium, through the Smoluchowski equation (*44*), and consequently, by themselves the zeta potential values should be viewed as an unreliable measure of the nanoparticle stability properties as it depends critically on the environmental medium. The results may also appear misleading as values near -30 mV are observed at latter time-points, where the majority of particles have precipitated out of suspension. These results highlight the problem with nanoparticle characterisation with the different techniques producing contrasting results.

4.4.2 CeO_2 Nanoparticle Interactions with the Silica-Water Interface

The surface charge of the CeO_2 nanoparticles is derived predominantly from the Ce^{4+} charge centres (Ce^{4+} 93.1%:Ce^{3+} 6.9%)(*34*). The nanoparticles will be attracted to the negatively charged silica-water interface, our model soil surface, and will compete with any other counter-ions in suspension. By flowing a nanoparticle suspension over the silica surface, the adsorption and aggregation kinetics can be observed directly using EW-CRDS. Similar measurements have been performed for Au (*30, 31*), and Ag nanoparticle aggregation (*45*), at charged interfaces, with aggregation forming during the neutralisation of the silica-water interface.

The interaction of the CeO_2 nanoparticle suspensions observed in these results can be interpreted in terms of single nanoparticle adsorption, surface clustering and aggregation of the suspensions, depending on the nanoparticle concentrations, Figure 4.10 (c-e). The nanoparticle adsorption kinetic curves follow pseudo-Langmurian trends at low concentrations, with the particle association rising up to a θ_{max}, neutralising the charged surface. The nanoparticles are irreversibly bound to the surface with no measureable dissociation over three hours, $k_d > 10^{-7}$ s^{-1}. The very slow dissociation indicates a surface binding energy in excess of 50 kJ mol^{-1}. Similar aggregation with Au nanoparticles (*30, 31*) observed minimal dissociation indicating that here the nanoparticles are irreversibly adsorbed to the model soil surface.

As the concentration of the bulk suspension is increased, a higher θ_{max} surface coverage is observed, which indicates that a greater number of nanoparticles are required to neutralise the same fixed number of charges at the surface, Figure 4.10 (B). This is a consequence of nanoparticle aggregation. The nanoparticles have a charged counter-ion interface, with an overall positive charge, and at low nanoparticle concentrations individual nanoparticles adsorbed to the negatively charged sites will neutralise the surface. The SEM image for 100 mgL^{-1} CeO_2 nanoparticle suspension, Figure 4.11 (A), indicates that the surface is neutralised here by single nanoparticles.

At increased nanoparticle bulk concentrations, the nanoparticle density will be higher, with individual nanoparticle surfaces in closer proximity, resulting in surface aggregation. The aggregated nanoparticles will have a lower charge per mass, which will result in a higher number of nanoparticles required to neutralise the same negatively charged silica surface. This increased nanoparticle aggregation and clustering at the interface will adsorb and scatter more light, with a higher θ_{max} extinction value observed for the neutralisation of the same silica surface, Figure 4.10 (B). The SEM image showing a 200 mgL^{-1} CeO_2 nanoparticle concentration, Figure 4.11 (B) displays a greater number of surface aggregates and nanoparticle clusters, resulting in the increased θ_{max} observed in the isotherm.

A further θ_{max} extinction increase is observed in the isotherm at the highest nanoparticle concentration. This is a feature of nanoparticle solution phase aggregation, with the particles forming spherical micron sized aggregates, which sediment onto the surface, rather than surface aggregation leading to neutralisation. Figure 4.11 (C) displays the effect of the solution phase aggregation, with large spherical CeO_2 aggregates visible in the image, as well as surface aggregation observed. These large aggregates are likely to have a significantly larger extinction cross-section compared to the single nanoparticles resulting in an increase in the scatter contribution; the second rise in the θ_{max} extinction isotherm, Figure 4.10 (B).

The CeO_2 nanoparticle interfacial concentration can be estimated from the low CeO_2 concentration (100 mgL^{-1}) SEM image displaying individual nanoparticles, Figure 4.11 (A). The surface volume is assumed to be $1.2 \pm 0.2 \times 10^{-6}$ cm^3, calculated from the surface area interrogated by the laser beam footprint on the reverse face of the Dove prism (Chapter 2.2) and an interface thickness controlled only by the diameter of the nanoparticle, 70 ± 11 nm. From the image, 100 nanoparticles are observed in 4.32 μm^2, a total of $3.8 \pm 0.4 \times 10^8$ nanoparticles interrogated at the surface, from which a surface concentration of 0.55 ± 0.12 μM can be calculated. The derived extinction coefficient is then given as $\varepsilon_{420nm} = 8.5 \pm 1.4 \times 10^{10}$ M^{-1} cm^{-1}. This large value describes the combined absorption band gap feature and residual scatter and can be compared with literature values obtained for Au nanoparticles of $1.71 \pm 0.12 \times 10^{10}$ M^{-1} cm^{-1} (*31*).

An initial rate analysis was performed for the CeO_2 kinetic adsorption trends, Figure 4.13. At low nanoparticle concentrations up to 200 mgL^{-1} there is evidence of linear binding kinetics observed, with the 0 – 200 mgL^{-1} data fitted to a linear function, R^2 0.989. At higher concentrations a slight deviation from linearity is observed. The complete data set was fitted with a power function, displaying an order of reaction with respect to CeO_2 of 0.82 ± 0.06.

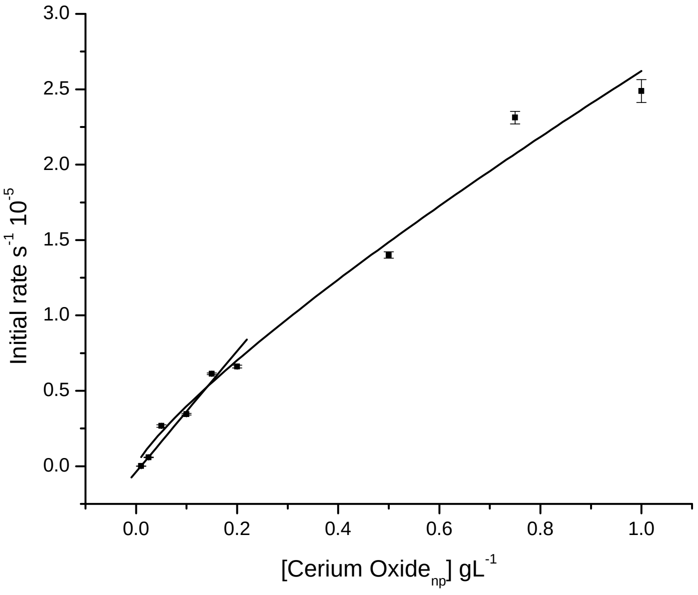

Figure 4.13 Initial rate analysis of CeO_2 nanoparticle surface adsorption against nanoparticle concentration

The non-linear trend at high concentrations can be attributed to the increased particle mass arriving at the surface, with steric hindrance caused by the repulsive forces of the large aggregated clusters, reducing the rate of adsorption. It has also been demonstrated that where the colloidal suspension has a large disparity between nanoparticle size, the greater diffusivity of the small particles means they adsorb to the surface at a faster rate, resulting in the observed decrease in adsorption rate with larger aggregates (*46*).

4.4.3 Competitive binding of Cerium dioxide nanoparticles with Crystal Violet

The concentration of CV molecules required to neutralise the silica surface can be calculated, assuming the extinction coefficient estimated in Chapter 2. Using the same interfacial volume from the CeO_2 calculations previously the CV concentration required to neutralise the silica surface, Figure 4.12 (A) (a), is 14 ± 1 mM. This CV concentration is 2.5 ± 0.6 x 10^4 times larger than the interfacial concentration of 100 mgL^{-1} CeO_2 previously demonstrated to neutralise the same fully dissociated silica surface, assuming a silanol site density of 2 e^- nm^{-2}. This suggests that each CeO_2 nanoparticle possesses approximately 2.5 ± 0.6 x 10^4 surface charges localized to Ce^{4+} groups giving a surface Ce^{4+} charged density of 1.64 ± 0.26 e^- nm^{-2}. This is comparable to a surface charge of 1e^- nm^{-2} observed for the Au nanoparticles determined by Fisk *et al* (*31*). The surface charge density is a fundamental property of the particle and is independent of the medium in which the particle is suspended, with the assumption that the particle counter-ion distribution does not significantly neutralise the silica-surface.

The CV θ_{max} at the surface displays a decreasing trend with an increase in CeO_2 nanoparticle concentration in suspension, Figure 4.12. With an increase in nanoparticle concentration, greater surface aggregation has been observed, Figure 4.11. As discussed previously, the aggregated particles possess a lower charge per mass compared to their individual counterparts, resulting in a greater concentration of nanoparticles present at the interface. Subsequently, fewer CV molecules are adsorbed, with a smaller θ_{max} observed. The concentrations estimated for CV at the surface decrease from 12.2 ± 0.3 mM in the presence of 10 mgL^{-1} CeO_2 to 2.6 ± 0.2 mM for the highest concentration of 300 mgL^{-1} CeO_2. Using the CeO_2 nanoparticle surface charge density calculated previously, the interfacial concentration of CeO_2 nanoparticles displacing the CV molecules to neutralise the surface may be estimated. This gives a CeO_2 interfacial concentration of 75 ± 3 nM for 10 mgL^{-1} CeO_2 in suspension with CV (50 μM), increasing to 0.46 ± 0. 2 μM for 300 mgL^{-1} CeO_2 in suspension, Figure 4.12. These concentrations are lower than the concentrations observed for the CeO_2 surface adsorption with no competing charged species, Figure 4.10. This is an effect of the competing CV on the surface charge and subsequent reduced surface aggregation.

4.5 Conclusions

The aim of this work was to characterise the CeO_2 nanoparticles in environmentally relevant suspensions, observing their stability and aggregation properties. Important suspension half-life parameters have been compared in complex ISOFish water and deionised water. The nanoparticle half-life in ISOFish water indicates that CeO_2 nanoparticles will quickly leave the water column and become part of the sediment within hours. This suggests that the most likely route to toxicity, if any, will be ingestion of aggregates into the food chain, through sedimentary organisms. By observing the nanoparticle aggregation on a silica interface the nanoparticle surface charge density was able to be derived. This characteristic is a unique property of the nanoparticle and can be used to predict the nanoparticle activity with charged surfaces in suspension. It is arguably a better characteristic of the nanoparticle than medium-dependent measurements, and may be used to predict the nanoparticle interaction in the presence of other charged surfaces.

References

1. Limbach, L K, Bereiter, R, Muller, E, Krebs, R, Galli, R, and Stark, W J. (2008) Removal of Oxide Nanoparticles in a Model Wastewater Treatment Plant: Influence of Agglomeration and Surfactants on Clearing Efficiency, *Environmental Science & Technology 42*, 5828-5833.
2. Gao, F, Lu, Q, and Komarneni, S. (2006) Fast Synthesis of Cerium Oxide Nanoparticles and Nanorods, *Journal of Nanoscience and Nanotechnology 6*, 3812-3819.
3. Park, E-J, Choi, J, Park, Y-K, and Park, K. (2008) Oxidative stress induced by cerium oxide nanoparticles in cultured BEAS-2B cells, *Toxicology 245*, 90-100.
4. Institute, H E. (2001) Evaluation of Human Health Risk from Cerium Added to Dielsel Fuel, pp 1-57.
5. Kilbourn, B T (2003) *Cerium and Cerium compunds*, John Wiley and sons, New York.
6. Energenics. (2012) Catalysis Catalytic function of Cerium Oxide, *Envirox Energenics Europe limited*.
7. Wakefield, G, Wu, X, Gardener, M, Park, B, and Anderson, S. (2008) Envirox fuel-borne catalyst: Developing and launching a nano-fuel additive, *Technology Analysis & Strategic Management 20*, 127-136.
8. Hei. (2001) Evaluation of human health risk from cerium added to diesel fuel, (Press, F., Ed.), North Andover MA.
9. Logothetidis, S, Patsalas, P, and Charitidis, C. (2003) Enhanced catalytic activity of nanostructured cerium oxide films, *Materials Science and Engineering: C 23*, 803-806.
10. Sayle, T X T, Parker, S C, and Catlow, C R A. (1994) Surface Segregation of Metal Ions in Cerium Dioxide, *The Journal of Physical Chemistry 98*, 13625-13630.
11. Hoecke, K V, Quik, J T K, Mankiewicz-Boczek, J, Schamphelaere, K A C D, Elsaesser, A, Meeren, P V d, Barnes, C, McKerr, G, Howard, C V, Meent, D V D, RydzynÌ• ski, K, Dawson, K A, Salvati, A, Lesniak, A, Lynch, I,

Silversmit, G, Samber, B r D, Vincze, L, and Janssen, C R. (2009) Fate and Effects of CeO2 Nanoparticles in Aquatic Ecotoxicity Tests, *Environmental Science & Technology 43*, 4537-4546.

12. Park, B, Donaldson, K, Duffin, R, Tran, L, Kelly, F, Mudway, I, Morin, J-P, Guest, R, Jenkinson, P, Samaras, Z, Giannouli, M, Kouridis, H, and Martin, P. (2008) Hazard and Risk Assessment of a Nanoparticulate Cerium Oxide-Based Diesel Fuel Additive:A Case Study, *Inhalation Toxicology 20*, 547-566.
13. Jenkins, H D B (1998) *A Ready-Reference book of Chemical and Physical Data (CRC Handbook of Chemistry and Physics*, 79th ed., CRC Press, Florida.
14. EPA. (2009) Toxicological review of cerium oxide and cerium compounds, U.S.
15. Bian, S-W, Mudunkotuwa, I A, Rupasinghe, T, and Grassian, V H. (2011) Aggregation and Dissolution of 4 nm ZnO Nanoparticles in Aqueous Environments: Influence of pH, Ionic Strength, Size, and Adsorption of Humic Acid, *Langmuir 27*, 6059-6068.
16. Schmidt, J, and Vogelsberger, W. (2006) Dissolution Kinetics of Titanium Dioxide Nanoparticles: The Observation of an Unusual Kinetic Size Effect, *The Journal of Physical Chemistry B 110*, 3955-3963.
17. Peters, A, von Klot, S, Heier, M, Trentinaglia, I, Harmann, A, Wichmann, H E, and Lawel, H. (2004) Exposure to Traffic and the Onset of Myocardial Infarction, *New England Journal of Medicine 351*, 1721-1730.
18. Eom, H-J, and Choi, J. (2009) Oxidative stress of CeO2 nanoparticles via p38-Nrf-2 signaling pathway in human bronchial epithelial cell, Beas-2B, *Toxicology Letters 187*, 77-83.
19. Brunner, T J, Wick, P, Manser, P, Spohn, P, Grass, R N, Limbach, L K, Bruinink, A, and Stark, W J. (2006) In Vitro Cytotoxicity of Oxide Nanoparticles: Comparison to Asbestos, Silica, and the Effect of Particle Solubility, *Environmental Science & Technology 40*, 4374-4381.

20. Lin, W, Huang, Y-w, Zhou, X-D, and Ma, Y. (2006) Toxicity of Cerium Oxide Nanoparticles in Human Lung Cancer Cells, *International Journal of Toxicology 25*, 451-457.
21. Hirst, S M, Karakoti, A S, Tyler, R D, Sriranganathan, N, Seal, S, and Reilly, C M. (2009) Anti-inflammatory Properties of Cerium Oxide Nanoparticles, *Small 5*, 2848-2856.
22. Thill, A, Zeyons, O l, Spalla, O, Chauvat, F, Rose, J m, Auffan, M l, and Flank, A M. (2006) Cytotoxicity of CeO2 Nanoparticles for Escherichia coli. Physico-Chemical Insight of the Cytotoxicity Mechanism, *Environmental Science & Technology 40*, 6151-6156.
23. Jiang, J, Oberdörster, G, and Biswas, P. (2009) Characterization of size, surface charge, and agglomeration state of nanoparticle dispersions for toxicological studies, *Journal of Nanoparticle Research 11*, 77-89.
24. Handy, R, von der Kammer, F, Lead, J, Hassellöv, M, Owen, R, and Crane, M. (2008) The ecotoxicology and chemistry of manufactured nanoparticles, *Ecotoxicology 17*, 287-314.
25. van Ravenzwaay, B, Landsiedel, R, Fabian, E, Burkhardt, S, Strauss, V, and Ma-Hock, L. (2009) Comparing fate and effects of three particles of different surface properties: nano-TiO(2), pigmentary TiO(2) and quartz, *Toxicology Letters 186*, 152-159.
26. Chemicals, C. (2009) Environment Directive, (Nanoparticles, W. P. o. M., Ed.), p 7, OECD.
27. ISO (1996) *Water quality-Determination of the acute lethal toxicity of substances to a freshwater fish, Part 3: Flow-through method.*, Geneva.
28. Rosi, N L, and Mirkin, C A. (2005) Nanostructures in Biodiagnostics, *ChemInform 36*, no-no.
29. O'Reilly, J P, Butts, C P, I'Anso, I A, and Shaw, A M. (2005) Interfacial pH at an Isolated Silica Water Surface, *Journal of the American Chemical Society 127*, 1632-1633.

30. Mazurenka, M, Hamilton, S M, Unwin, P R, and Mackenzie, S R. (2008) In-Situ Measurement of Colloidal Gold Adsorption on Functionalized Silica Surfaces, *The Journal of Physical Chemistry C 112*, 6462-6468.
31. Fisk, J D, Rooth, M, and Shaw, A M. (2007) Gold Nanoparticle Adsorption and Aggregation Kinetics at the Silica−Water Interface, *The Journal of Physical Chemistry C 111*, 2588-2594.
32. Tantra, R, Jing, S, Pichaimuthu, S, Walker, N, Noble, J, and Hackley, V. (2011) Dispersion stability of nanoparticles in ecotoxicological investigations: the need for adequate measurement tools, *Journal of Nanoparticle Research 13*, 3765-3780.
33. (NPL), N P L. Hampton Road, Teddington, Middlesex TW11 0LW, UK.
34. Tantra, R. (2010) Interim Report on the Physio-chemical characterisation of PROSPEcT nanomaterials.
35. Prospect. (2010) Protocol for Nanoparticle Dispersion, *Ecotoxicology Test Protocols for representative Nanomaterials in support of the OECD Sponsorship programme*.
36. Pavia, D L, Lampman, G M, Kriz, G S, and Vyvyan, J A (2008) *Introduction to Spectroscopy*, 4th Edition ed., Brooks Cole, Belmont.
37. Gu, H, and Soucek, M D. (2007) Preparation and Characterization of Monodisperse Cerium Oxide Nanoparticles in Hydrocarbon Solvents, *Chemistry of Materials 19*, 1103-1110.
38. www.malverninstruments.com.
39. Nguyen, D T, Kim, D J, Myoung, G S, and Kim, K S. (2009) Experimental measurements of gold nanoparticle nucleation and growth by citrate reduction of HAuCl4, *Adv. Powder Technology 21*, 111-118.
40. Chowdhury, I, Hong, Y, Honda, R J, and Walker, S L. (2011) Mechanisms of TiO2 nanoparticle transport in porous media: Role of solution chemistry, nanoparticle concentration, and flowrate, *Journal of Colloid and Interface Science 360*, 548-555.

41. Metin, C, Lake, L, Miranda, C, and Nguyen, Q. (2010) Stability of aqueous silica nanoparticle dispersions, *Journal of Nanoparticle Research 13*, 839-850.

42. Israelachvili, J N (1991) *Intermolecular and Surface Forces*, 2nd Edition ed., Academic Press, London.

43. Xia, T, Kovochich, M, Liong, M, Madler, L, Gilbert, B, Shi, H, Yeh, J I, Zink, J I, and Nel, A E. (2008) Comparison of the Mechanism of Toxicity of Zinc Oxide and Cerium Oxide Nanoparticles Based on Dissolution and Oxidative Stress Properties, *ACS Nano 2*, 2121-2134.

44. Sze, A, Erickson, D, Ren, L, and Li, D. (2003) Zeta-potential measurement using the Smoluchowski equation and the slope of the current time relationship in electroosmotic flow, *Journal of Colloid and Interface Science 261*, 402-410.

45. Schnippering, M, Powell, H V, Zhang, M, Macpherson, J V, Unwin, P R, Mazurenka, M, and Mackenzie, S R. (2008) Surface Assembly and Redox Dissolution of Silver Nanoparticles Monitored by Evanescent Wave Cavity Ring-Down Spectroscopy, *The Journal of Physical Chemistry C 112*, 15274-15280.

46. Krenn, J R, B., L, H., D, G., S, M., S, A., L, and R., A F. (2002) Non-diffraction-limited light transport by gold nanowires, *Europhys. Lett. 60* 663-669.

Chapter 5

ZnO Nanoparticle Toxicity – Photo-radical Generation

5.1 Introduction

The second nanoparticle to be considered in the PROSPEcT project is ZnO. ZnO nanoparticles dispersed in liquid media have two different potential mechanisms for toxicity. Firstly, ZnO nanoparticles in suspension will dissolve over time releasing Zn^{2+} ions into the local environment at potentially toxic levels. Secondly, the generation of photo-electrons when nanoparticle surfaces are exposed to UV light may generate radicals in solution leading to toxic redox stress responses in organisms. The second toxicity mechanism is a nanoparticle-specific property, and it is this property which will be considered in detail, quantifying and identifying the photo-radicals produced

5.1.1 Zinc Oxide Nanoparticles

Metal oxide nanoparticles have been introduced into industry for use in chemical sensors (*1*), optics and electronic materials (*2*), and many other products for their unique properties. In particular, ZnO and Titanium dioxide (TiO_2) nanoparticles are extensively used in the cosmetic industry (*3*), with their wide band gaps giving them the ability to absorb light in the potentially harmful UVA and UVB light regions of the electromagnetic spectrum, protecting the skin from UV-induced damage (*4*). The nanoparticles are aesthetically favoured in UV protecting agents compared to bulk material given their small size and large volume–to-surface area ratio, and once thinly spread on the skins surface, the visible light is not scattered giving a clear colourless appearance. The nanoparticles exposed to the sun may also generate photo-radicals, with potentially toxic effects in certain environments. This potential toxicity in suspension is relevant as nanoparticles will be continuously release into the environment from sun screen products, washed off into the water systems (*5*). It is important to identify how long the nanoparticles remain in the environment, the nanoparticle-medium interactions, and the toxicity mechanisms observed in different media.

The photo-radical generation properties of metal oxides are well known, (*6*) initially observed through the decolourisation of organic binders in paints, caused by the generation of oxygen species from long exposure of TiO_2 to sunlight (*7*). The large bandgap in semi-conductor metal oxide nanoparticles generate a broad absorbance spectrum with a maximum in the UV range. This results in the promotion of electrons from the valance band into the conduction band when exposed to radiation with a wavelength shorter than the band gap transition. ZnO has a band gap of 3.37 eV (*8*), corresponding to an excitation wavelength of approximately 375 nm (*9*), and will generate photo-radicals under exposure to UV radiation, with the potential to interact with molecules in its local environment generating radical species (*10*).

In water systems the electrons in the excited state of the conduction band will interact with water molecules close to the nanoparticle surface, as well as dissolved oxygen, to produce a set of radicals. Previously, under UV light TiO_2 nanoparticles in water have been demonstrated to form a number of reactive oxygen species (ROS) including $O_2^{-}\bullet$, H_2O_2 and •OH (*11, 12*). These radicals has been used for their anti-pathogenic behaviour against viruses (*13*), bacteria and tumour cells (*14*). They have also been demonstrated to be low-cost photo-catalysts for the degradation of organic material in aqueous solutions (*15*). However, the radicals generated from the metal oxides, in particular the •OH radical, are some of the strongest oxidising agents known to chemistry (*16*), and can react with molecules in and on cells, upsetting the cellular metabolism and triggering an oxidative stress response, which is toxic to animals and plants (*14, 17, 18*).

Oxidative stress is caused when there is an imbalance between the body's ability to dispose of ROS and repair the damage caused and the production of ROS in the body. When present in cosmetics on human skin, ZnO nanoparticles exposed to UV light, have displayed damage to the double helical DNA structure caused by the ROS, mutating the supercoiled DNA form (*19*), which may subsequently be responsible for skin cancers such as malignant melanoma (*20*). Other effects have shown that free radicals can cause tissue damage, reacting with polyunsaturated fatty acids and result in protein damage. This can result in cardiovascular diseases and cell damage. In ecotoxicological studies, nanoparticle exposures have demonstrated negative physiological effects on rainbow trout (*Oncorhynchus*) (*21*) and earthworms (*E. Fetida*) (*22*), with ROS causing cell toxicity leading to cell death (*23*). Bacterial systems have also been monitored, with the presence of ZnO nanoparticles leading to inhibition of *E.coli* growth (*24*). The study of nanoparticle radical toxicity in soil ecosystems is limited (*25-27*). Lu *et al.* reported that radicals generated by TiO_2 nanoparticles improved soybean growth, increasing germination and stimulating its antioxidant system (*28*), whilst TiO_2 nanoparticles also promoted photosynthesis and growth of spinach (*29*). In contrast *Lin et al.* looked at the nanoparticle effect on ryegrass, where radical production led to cell disfigurement (*30*).

The investigation of radical production has previously been studied by measuring the colour change and degradation of redox dyes. Wang *et al*. monitored Methyl Orange degradation using ZnO nano-crystalline particles (*31*), Jang *et al.* reported degradation of Methylene Blue under UV light (*32*), while the degradation of Eosin Y dye has also been observed with increased concentrations of ZnO (*33*). The mechanism of degradation of these dyes is not known and is therefore not stoichiometric with the production of radicals.

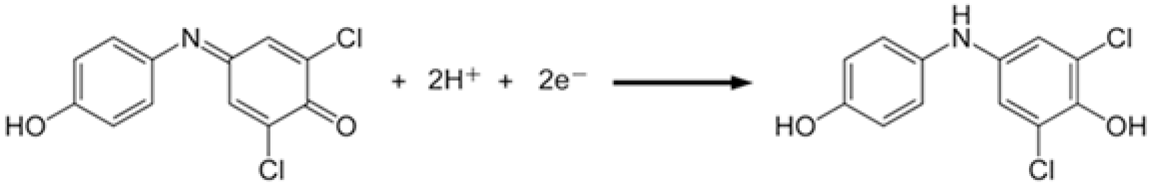

Figure 5.1 The stoichiometric radical reduction of 2, 6-dichlorophenolindophenol (DCPIP)

By contrast, the reduction of the redox dye 2, 6-dichlorophenolindophenol (DCPIP) is quantitative, requiring exactly 2 electrons to reduce one molecule (*34*), Figure 5.1 with the radicals entering the HOMO in the molecular orbital and disrupting the *π*-bonding electron system (*31, 35*)**.** The DCPIP absorbance spectrum has a maximum at 595 nm producing a dark blue solution in its oxidised form and changes to colourless when reduced. This colour change alters the absorbance spectrum, which may then be monitored over time to observe photo-radical production of ZnO nanoparticles.

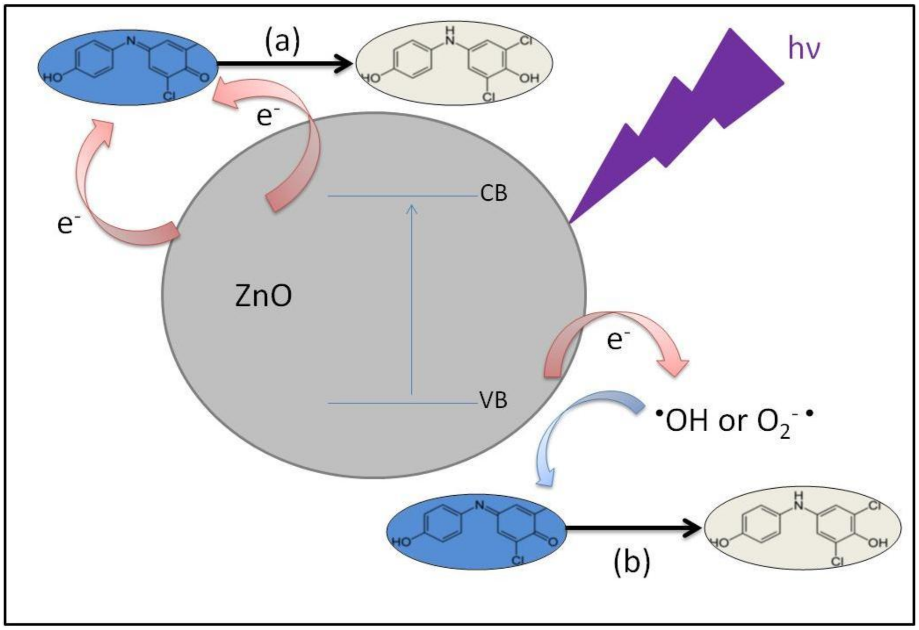

Figure 5.2 Schematic showing the potential reduction mechanisms of DCPIP by ZnO nanoparticles under UV light, (a) the photo-electrons generated from the nanoparticle directly reducing the DCPIP molecules from blue to clear solution, or (b) the photo-electrons react with the water and oxygen molecules producing ROS which then cause DCPIP reduction. VB; valance band, CB; conduction band

There are two possible mechanisms postulated for the reduction of DCPIP by the ZnO, Figure 5.2. One mechanism is that under UV light the nanoparticles release surface electrons which reduce the DCPIP directly, Figure 5.2 (a). The second, more likely mechanism is the photo-electrons produced on the surface will cause a radical storm and react with H_2O and O_2 forming radical species in solution, particularly O_2^{-}• and •OH, Figure 5.2 (b), which in turn reduce DCPIP. There may also be direct reduction of DCPIP by electrons excited from the nanoparticles, but as the concentration of water is approximately 10^6 greater than DCPIP, it is suggested that this process will be negligible. Identification of the photo-radicals produced is difficult as they possess short lifetimes, and need to be stabilised, so the technique of spin trapping the radicals and identification under Electron Paramagnetic Resonance (EPR) is the most effective method (*36*).

5.1.2 Electron Paramagnetic Resonance

EPR Spectroscopy has been extensively used to study radical generation in cells (*14, 23, 37, 38*), and for metal nanoparticle radical production, both in the gas phase (*12*) and suspension (*10, 12, 39*). Like Nuclear Magnetic Resonance (NMR), EPR uses the interaction of paramagnetic species with an external magnetic field to split the energy levels of the molecular orbitals into their magnetic sub-states labelled by the m_J quantum numbers (*40*). When microwave radiation is resonant with the Zeeman splitting, an absorption transition is observed. Thus, EPR is sensitive to molecules containing unpaired electrons (*41*) and the detailed structure of the molecular Zeeman levels.

EPR spectroscopy detects radicals and paramagnetic species directly (*40*), but it is limited to the observation of free radicals which have relatively long half-lives. To detect radicals with shorter half-lives, an indirect method of spin trapping is used (*36*). Here a nitrone or nitroso compound reacts with a free radical producing a nitroide, with greater stability compared to a free radical (*14*). The spin trap 5, 5-Dimethyl-1-pyrroline *N*-oxide (DMPO), has been used previously to trap superoxide and hydroxyl radicals produced through photo radical excitation of metal oxide nanoparticles (*10, 12, 39*). DMPO is a 5 membered cyclic nitrone which will react with the superoxide to form a DMPO-OOH adduct or with the hydroxyl radical to produce a DMPO-OH adduct, Figure 5.3 (*38*).

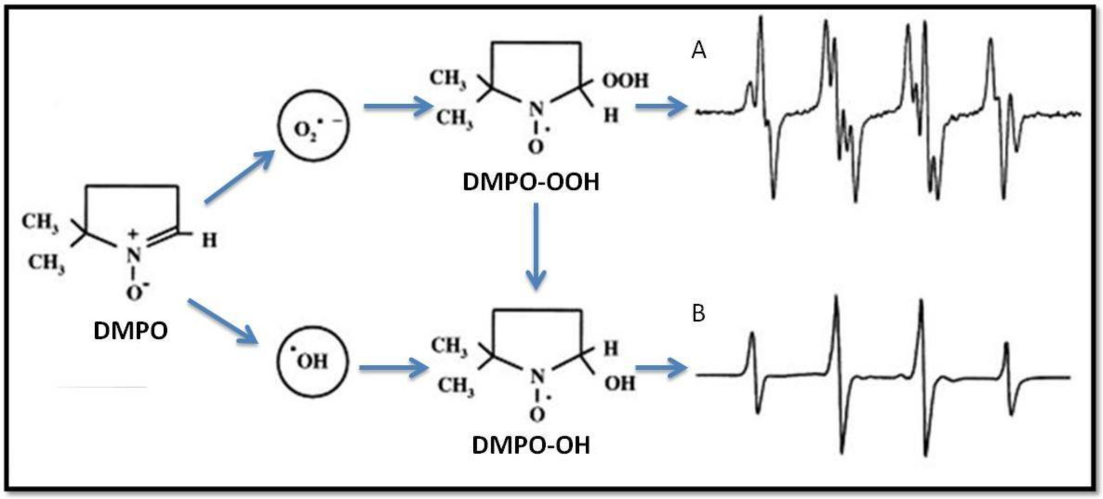

Figure 5.3 DMPO spin trap showing, A - the formation of a DMPO-OOH adduct with interaction with O_2^-• radicals, and B – the formation of a DMPO-OH adduct with interaction with •OH radicals, or subsequently from the DMPO-OOH adduct. Modified from Togashi *et al.* (*14*)

The superoxide spin trap has a short half-life of approximately 60 seconds and subsequently decays into the stable DMPO-OH adduct (*38*). In the DMPO-OH adduct hyperfine coupling is observed from the nuclei, with both the central nitrogen atom coupling (I =1) and β proton coupling ($I = {}^1/_2$) occurring, to give two hyperfine splitting constants (*16*). They both have the same value causing overlapping of the central lines resulting in a four line quartet spectrum with a 1:2:2:1 intensity ratio (*16*), and a hyperfine splitting constant ($a_N = {}^{\beta}a_H = 14.9$ G) (*14, 16, 38, 39, 42*).

5.1.3 Aims and Objectives

This work aims to identify and quantify the photo-radical production processes from ZnO nanoparticles dispersed in suspension when exposed to UV light, Figure 5.4. The objectives are to design a quantitative assay of photo-radical production, based on the stoichiometric reduction of DCPIP and determine the photo-radical change in relation to concentration, nanoparticle size and organics in suspension.

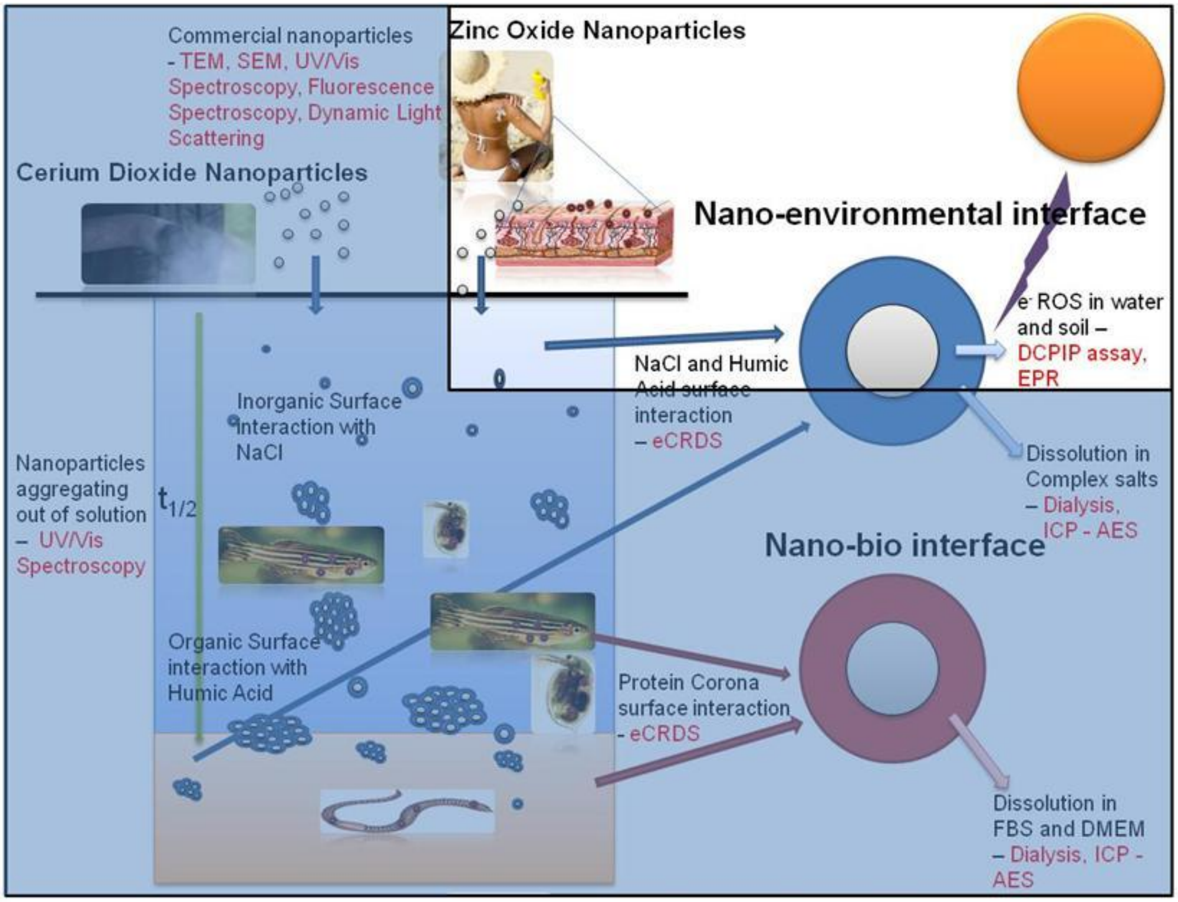

Figure 5.4 Thesis overview, showing ZnO nanoparticles used in cosmetics, released into the water systems, and exposed to UV rays from the sun, where the nanoparticles will generate surface radicals, which can be observed through the reduction of DCPIP in suspension and trapped using EPR.

This assay will be used to determine photo-radical production rates of the PROSPEcT ZnO nanopowders, and the identity of the radicals produced will then be determined using Electron Paramagnetic Resonance (EPR) in collaboration with the EPSRC National Research Facility and Service at the University of Manchester (*43*).

5.2 Experimental Methods

5.2.1 Materials

The Z-cote ZnO nanopowder was provided by BASF (ZC25#37#05) under the PROSPEcT project and used without modification. The Z-cote ZnO nanopowder has a mean particle diameter of 150 ± 60 nm measured here by TEM imaging Figure 5.5, and a BET particle surface area of 12-24 m^2g^{-1}. The Nanosun ZnO nanopowders were provided by Microniser (CAS 1314-13-2) in three sizes, 30 ± 5 nm, 80 ± 5 nm and 200 ± 5 nm in diameter measured by SEM imaging. In addition, a cobalt doped nanoparticle was also provided by Microniser, using Nanosun 80 ± 5 nm with a 3.4 % cobalt doping. A commercial Sun Screen product, produced by Invisible Zinc® was provided by Dr Maxine McCall (CSIRO) (*44*) and was used as supplied. Zinc Chloride ($ZnCl_2$) (Fluka Analytical) was used as purchased. 2, 6-Dichlorophenolindophenol (DCPIP) was purchased from Fluka Analytical (33125, 90% purity), and used as received. 5, 5-Dimethyl-1-pyrroline *N*-oxide (DMPO) was purchased from Sigma Aldrich. The soil was characterised and provided by Claus Svendsen (Centre for Ecology & Hydrology) (*45*). The soil had a sandy texture with a mean content of 51.5 % coarse sand, 40.2 % fine sand, 3.5 % clay and 4.7 % silt. This soil had a low organic carbon content of 4 % and a total nitrogen content of 0.13 %. (*45*). The pH of the soil was adjusted to pH 7 for the nanoparticle exposures. All dispersions were prepared in ultrapure deionised water from a Millipore Water Direct Quv3 and resistivity of 18 $M\Omega\ cm^{-1}$, and adjusted to pH 7 using NaOH (1 M) and HCl (1 M) unless otherwise directly stated.

5.2.2 ZnO Nanoparticle Suspension and Soil Suspension Preparation Protocol

The nanopowders were suspended in deionised water using the procedure detailed in the PROSPEcT Protocol for nanoparticle dispersions (*46*) and detailed in Section 4.2, which is optimised to produce a stable and homogeneous dispersion. For dispersions with soil, the required mass of soil was weighed out and ground with a pestle and mortar until it resembled a fine powder. It was then added to the required nanoparticle mass and dispersed using the protocol detailed above.

5.2.3 Electron Microscopy

A 5 µL volume of the nanoparticle suspension was aliquotted onto a copper / palladium mesh grid, which was subsequently dried under a 30 W lamp. Imaging of the mesh grid with the nanoparticles on was then carried out using transmission electron microscopy, (TEM) (1400 TEM, JEOL), and the images were analysed using Gatan Digital Micrograph Software.

5.2.4 UV-Vis Spectroscopy

UV-Vis spectra of the suspensions were measured in curvettes (1 cm optical path length) in a UV-Vis spectrometer (spectronic Unicam) with Vision 32 software, or alternatively measured with a Thorlabs OSLI-EC Fiber Illuminator and a Thorlabs spectrometer (SPI-USB, MOO229529) connected with an optical fibre (Thorlabs, M14L01). Each measurement was recorded with a sample reference, containing the corresponding dispersion medium.

5.2.5 ZnO Nanoparticle DCPIP Photo-radical Assay Protocol

The ZnO nanoparticle suspensions and ZnO nanoparticle with soil (1 gL^{-1}) suspensions in deionised water were prepared in the concentration range 1-100 mgL^{-1}. The photo-electron production was observed in triplicate using the redox sensitive dye DCPIP which was added to the suspensions at a concentration of 50 µM and stirred into the nanoparticle suspension, to give a dark blue colour. The suspensions were divided into two plastic containers covered in aluminium foil to prevent interference in the assay from ambient lighting. One container had no light, the dark suspension, while the second container covered with aluminium foil was exposed to UV light from an LED located in the lid of the container; the exposed suspension. The LED (Marl, 260019) had a peak wavelength of 370 nm, and was driven by a constant-current power source to provide an optical power output of 1 mW. Both solutions were stirred at 600 rpm at laboratory temperature. Samples of 1 mL in volume were removed from both the control and exposure suspensions at 10 minute intervals over a time course of 80 minutes and the extinction change at 595 nm was monitored using a UV-Vis spectrometer.

5.2.6 Electron Paramagnetic Resonance

The sample spectra were measured on a Bruker EMX Premium X Electron Paramagnetic Resonance Spectrometer, and the data was analysed using WIN-ACQ software. The samples were placed in 2 mm EPR tubes, and were covered in foil to prevent ambient lighting from affecting the samples. The UV light was directed from above the sample for the irradiated exposures. Four different nanoparticle samples were tested by EPR. These were Z-cote ZnO nanoparticles, Z-cote ZnO nanoparticles with soil, Nanosun ZnO nanoparticles, and Cobalt doped Nanosun ZnO nanoparticles, all dispersed in deionised water at pH 7, using the dispersion protocol detailed previously. A sample of Invisible Zinc® sun screen was also measured using a small volume of IPA to allow transfer to the EPR tube. All the samples were individually placed in an EPR tube with DMPO (0.1 M). For each sample a dark negative control baseline was recorded and a UV exposed sample spectrum recorded.

The instrument parameters for measurement of each sample are listed in Table 5.1 with only small variations. The peak intensity was calculated by double integration of the peak signal, and the intensity expressed in arbitrary units. The results displayed are an average of 100 scans, both in the baseline and in the UV exposed samples, with the baseline removed from the sample spectra to show the effect of the UV light on the individual samples.

Table 5.1 EPR Instrument Parameters

Parameter	Value	Units
Centre Field	3373	G
Sweep width	65	G
Frequency	9.46 – 9.87	GHz
Power	2	mW
Resolution	1024	Pt
Temperature	290	K
Receiver gain	1×10^6	
Modulation frequency	100	kHz
Modulation amplitude	1	G
Conversion	40	ms
Time constant	20.48	ms
Sweep time	40	s
No. of scans	100	

5.3 Results

5.3.1 Nanoparticle Characterisation

The Z-cote ZnO nanoparticles suspended in deionised water were imaged using TEM, Figure 5.5. The image shows spheres, rods and other non-uniform shapes present in the nanopowder, consistent with the manufacturer's size specifications of 150 ± 60 nm. The image is not representative of the nanoparticles in suspension, because of sample drying artefacts; however, the image shows considerable variation in size and shape.

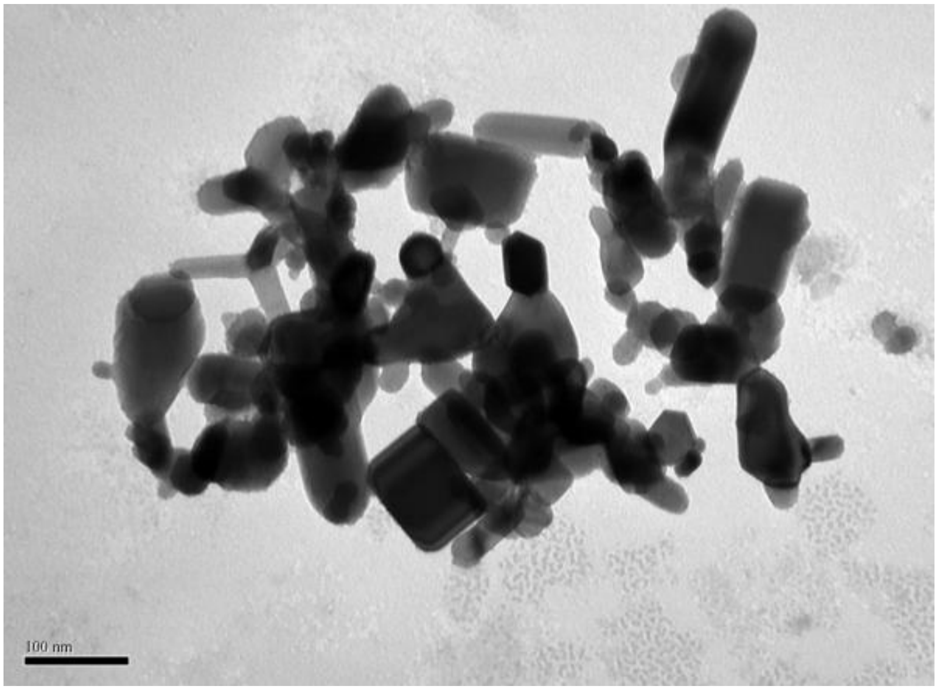

Figure 5.5 A TEM image of Z-cote ZnO nanoparticles showing a non-uniform particle size distribution with a mean diameter of 150 ± 60 nm. The scale bar is 100 nm

The nanoparticle suspensions observed were white or semi-opaque depending on the concentration of the suspension. The UV-Vis extinction spectrum of the nanoparticles dispersed in deionised water, displays a broad extinction upon which a narrower extinction feature with λ_{max} at 375nm is observed, Figure 5.6.

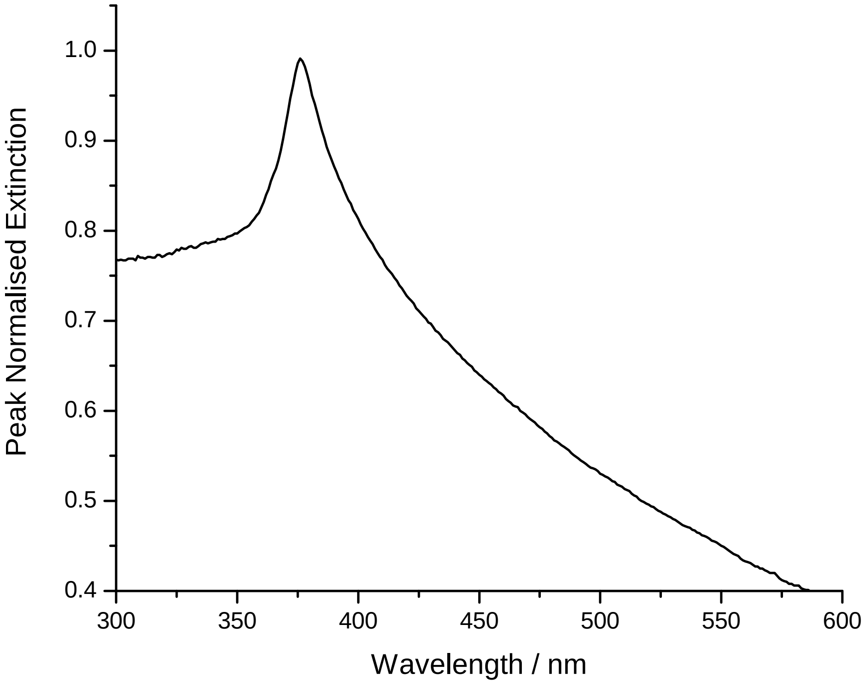

Figure 5.6 Peak Normalised UV-Vis extinction spectra for a Z-cote ZnO (100mgL^{-1}) suspension in deionised water showing a λ_{max} at 375nm

5.3.2 DCPIP Assay Controls

The UV-Vis spectrum of Z-cote ZnO nanoparticles in suspension with DCPIP shows a broad absorption curve with λ_{max} at 595 nm with the DCPIP in its oxidised form. Under UV light the DCPIP is reduced, monitored by a decrease in the λ_{max} (595 nm) extinction value over time, Figure 5.7.

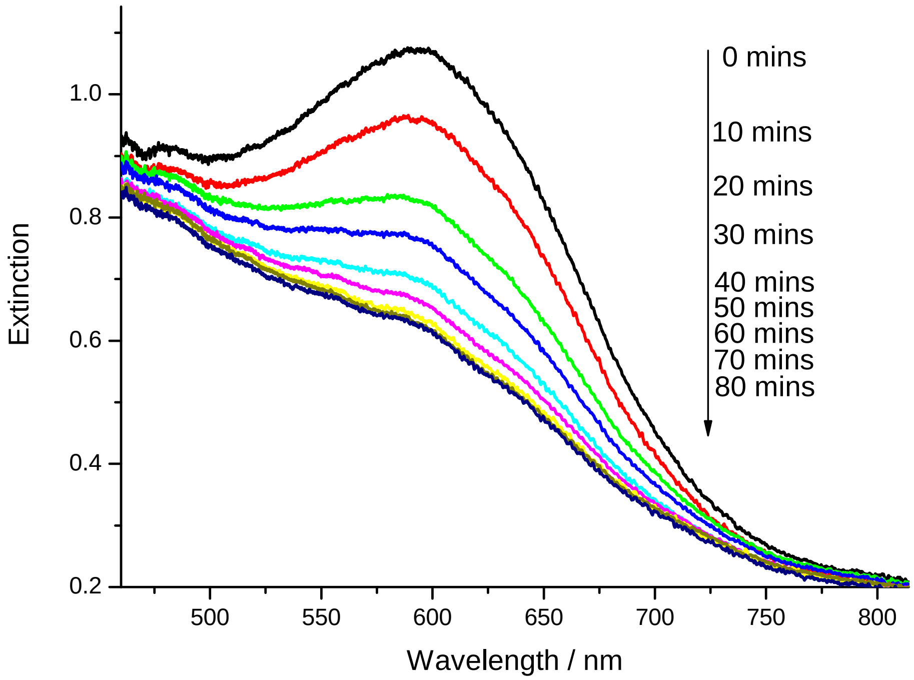

Figure 5.7 Example spectra taken from an 80-minute exposure, showing the contributions to the measured extinction from the dispersion scatter and the DCPIP producing a total extinction spectrum from 400 – 800 nm, λ_{max} = 595 nm

The DCPIP reduction was monitored at 595 nm over a time course of 80 minutes for dark and light assay controls, Figure 5.8 (a-g) and displayed no variation within the experimental error ($<10^{-2}$). Two example samples of Z-cote nanoparticle suspensions in deionised water, with and without soil present, Figure 5.8 (h and i) exposed to UV light are included here to display the exponential decrease over time observed in reduced DCPIP samples.

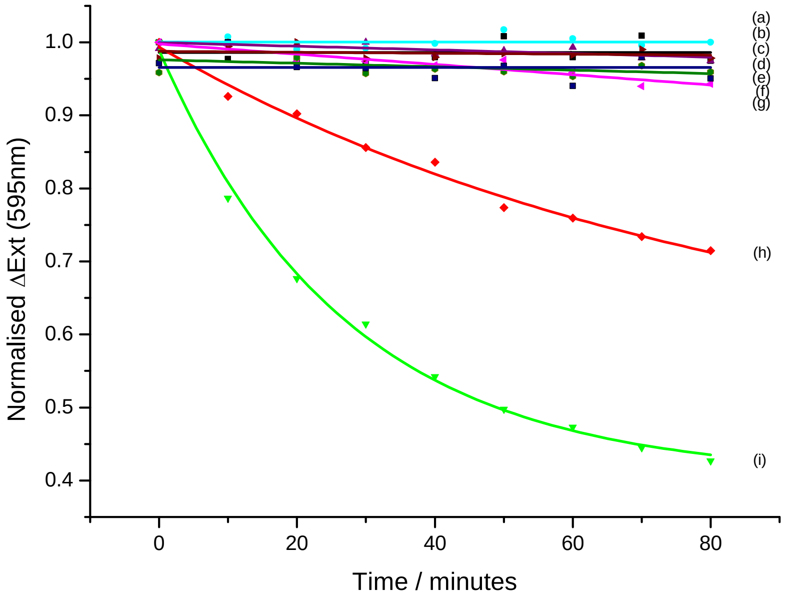

Figure 5.8 the observed photo-reduction of DCPIP followed in extinction at 595 nm for the assay controls dispersed in deionised water: (a) soil sample (1 gL^{-1}) under UV light (Black), (b) soil sample (1 gL^{-1}) in the dark (Light Blue), (c) Z-cote ZnO (100 mgL^{-1}) in the dark (Purple), (d) ZnCl$_2$ (100 mgL^{-1}) under UV light (Pink), (e) ZnCl$_2$ (100 mgL^{-1}) in the dark (Maroon), (f) DCPIP (50 μM) under UV light (Dark Green), (g) DCPIP (50 μM) in the dark (Dark Blue), (h) an example Z-cote ZnO suspension containing soil under UV light (Red), and (i) an example Z-cote ZnO suspension under UV light (Light Green).

5.3.3 ZnO Nanoparticle Concentration-Dependent DCPIP Photo-radical Assay

ZnO nanoparticle concentration-dependent measurements were performed over a time course of 80 minutes, for Z-cote concentrations in the range of 1-100 mgL^{-1} in deionised water, Figure 5.9 (A) and over the same concentration range with soil (1 gL^{-1}) suspended in deionised water, Figure 5.10 (A). The dark controls were subtracted, to produce a series of extinction *vs.* time profiles. The ΔExt (595 nm) over 80 minutes was plotted against nanoparticle concentration with lines fitted to the data Figure 5.9 (B) and Figure 5.10 (B).

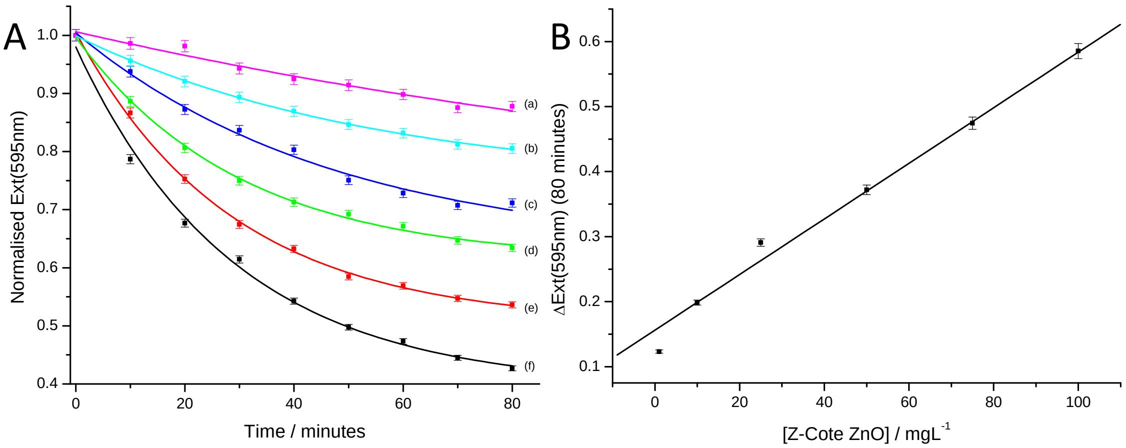

Figure 5.9 A – Photo-reduction of DCPIP followed in extinction at 595 nm for different concentrations of Z-cote ZnO nanoparticle suspensions in deionised water, (a) 1 mgL^{-1}, (b) 10 mgL^{-1}, (c) 25 mgL^{-1}, (d) 50 mgL^{-1}, (e) 75 mgL^{-1} and (f) 100 mgL^{-1}, and B – ΔExt (595 nm) after 80 minutes against concentration, with an R^2 value of 0.993

The results displayed a linear increase in observed DCPIP colour change with nanoparticle concentration in suspension, both for the nanoparticles suspended in deionised water, Figure 5.9 (B) and the nanoparticles and soil suspended in deionised water, Figure 5.10 (B), although there is evidence of non-linear behaviour at low concentrations close to the assay sensitivity maximum. The lines, gave fit accuracy, R^2 values of 0.993 and 0.989 respectively, with slopes of 4.4 ± 0.2 x 10^{-3} mgL^{-1}s^{-1} for the nanoparticle suspension without soil, Figure 5.9 (B) and 3.9 ± 0.2 x 10^{-3} mgL^{-1}s^{-1} for the nanoparticles with soil suspension, Figure 5.10 (B)

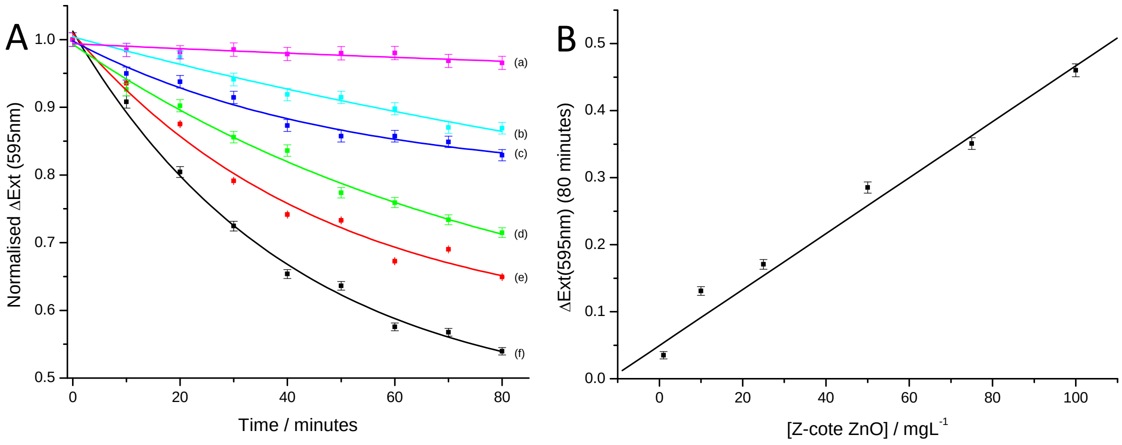

Figure 5.10 A – Photo-reduction of DCPIP followed in extinction at 595 nm for different concentrations of Z-cote ZnO nanoparticle and soil (1 gL^{-1}) suspensions in deionised water, (a) 1 mgL^{-1}, (b) 10 mgL^{-1}, (c) 25 mgL^{-1}, (d) 50 mgL^{-1}, (e) 75 mgL^{-1} and (f) 100 mgL^{-1}, and B – ΔExt (595 nm) after 80 minutes against concentration, with an R^2 value of 0.989

5.3.4 Photo-electron production rate from ZnO Nanoparticle Size on the rate of Photo-electron production

The Z-cote ZnO material consists of a variety of nanoparticle sizes and shapes with a significant variation in the photoelectron production rates averaged together in the Z-cote reduction measurements. A more systematic analysis of size-dependent photoelectron production was performed on a series of nanoparticles with better-defined size distributions provided by Nanosun. The material specifications show particle diameters of 30 ± 5 nm, 80 ± 5 nm or 200 ± 5 nm. Additionally, Cobalt doped (3.4 %) Nanosun (80 ± 5 nm) nanoparticles were also tested under the assay. Nanoparticle suspensions were produced for each of the materials at a concentration of 100 mgL^{-1} containing DCPIP (50 µM). The reduction was monitored at 595 nm as before and ΔExt (595 nm) measurements constructed from the control experiments, Figure 5.11. The cobalt doped Nanosun data, Figure 5.11 (a), shows no extinction change within experimental error (< 10^{-2}) over the 80 minute period. A clear diameter-dependent trend was observed for the remaining nanoparticles with 30 nm nanoparticles showing the smallest change and the 200 nm nanoparticles showing the largest change over the time course, Figure 5.11 (b-d).

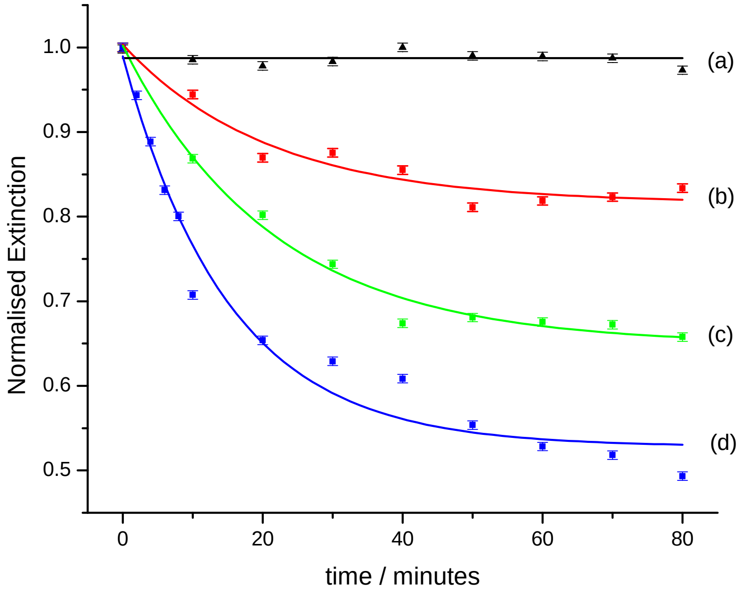

Figure 5.11 Normalised ΔExt (595 nm) over time of different size nanoparticles (a) Cobalt doped (3.4 %) Nanosun 80 ± 5 nm, (b) Nanosun 30 ± 5 nm, (c) Nanosun 80 ± 5 nm and (d) Nanosun 200 ± 5 nm

5.3.5 Spin-trapping EPR Spectra of ZnO photo-radicals

The DCPIP assay shows the production of photo-electrons by the ZnO nanoparticles as measured by the quantitative reduction of DCPIP but nothing about the identity of any radicals formed. Electrons generated by the nanoparticles may form a variety of radical intermediates. EPR spectra of ZnO nanoparticle suspensions exposed to UV light were recorded in collaboration with The EPSRC National EPR Research Facility in Manchester using a radical trapping technique with DMPO to trap •OH and O_2^-• radicals (*14*). The DMPO-OH adduct can form directly from the addition of •OH showing a characteristic 1:2:2:1 quartet spectrum, or indirectly reacting with O_2^-• to form initially a DMPO-OOH intermediate which degrades to DMPO-OH (*14*). We performed a series of measurements of photo-radical spin-trap spectra with two different types of ZnO nanoparticles, Nanosun ZnO and Z-cote ZnO nanoparticles in deionised water suspensions, a Z-cote ZnO nanoparticle-soil suspension and a cobalt doped Nanosun ZnO nanoparticle suspension. In addition, we looked at the photo-radical generation from the commercially available Invisible Zinc® sun screen.

Initially a water control was run, Figure 5.12 (a) producing a flat line in the magnetic field. An 80 nm Nanosun ZnO nanoparticle (100 mgL^{-1}) suspension was prepared to which 0.1 M DMPO was added. A dark control was acquired, averaging 100 scans, Figure 5.12 (b). A sample spectrum exposed to UV light was acquired with the dark control subtracted to produce the 1:2:2:1 quartet EPR spectra, Figure 5.12 (c). A Z-cote ZnO (100 mgL^{-1}) suspension and a Z-cote ZnO (100 mgL^{-1}) with 1 gL^{-1} soil suspension were both prepared in the same way with the dark controls subtracted, and indicated a 1:2:2:1 quartet, shown in Figure 5.12 (d) and Figure 5.12 (e) respectively.

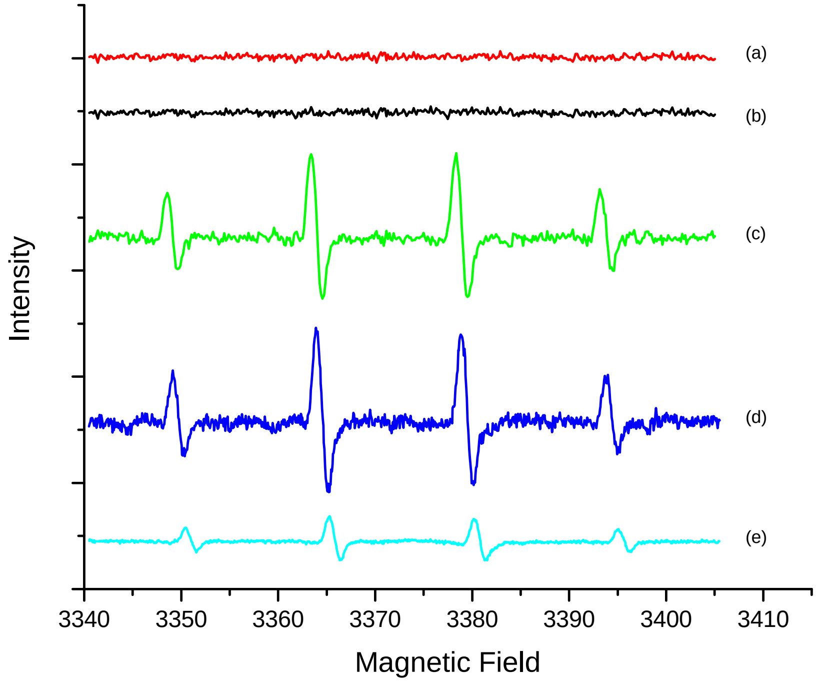

Figure 5.12 EPR spectra showing (a) a water control spectrum, (b) Nanosun 80 nm (100 mgL^{-1}) spectrum in the dark, (c) Nanosun 80 nm (100 mgL^{-1}) UV excited spectrum minus the dark control, (d) Z-cote ZnO 150 nm (100 mgL^{-1}) UV excited spectrum minus the dark control, and (e) Z-cote ZnO 150 nm (100 mgL^{-1}) with soil (1 gL^{-1}) UV excited spectrum minus the dark control

Cobalt doped Nanosun ZnO (80 ± 5 nm) nanoparticles were suspended in deionised water (100 mgL^{-1}) and EPR spectra collected as before, Figure 5.13. The sample shows a significant dark control change in intensity at 3378 G, Figure 5.13 (a). This change is present in the UV exposed sample as well, Figure 5.13 (b) and may be an instrumental artefact or an effect of the cobalt. Subtraction of the dark control recovers the same 1:2:2:1 quartet as previously, Figure 5.13 (c).

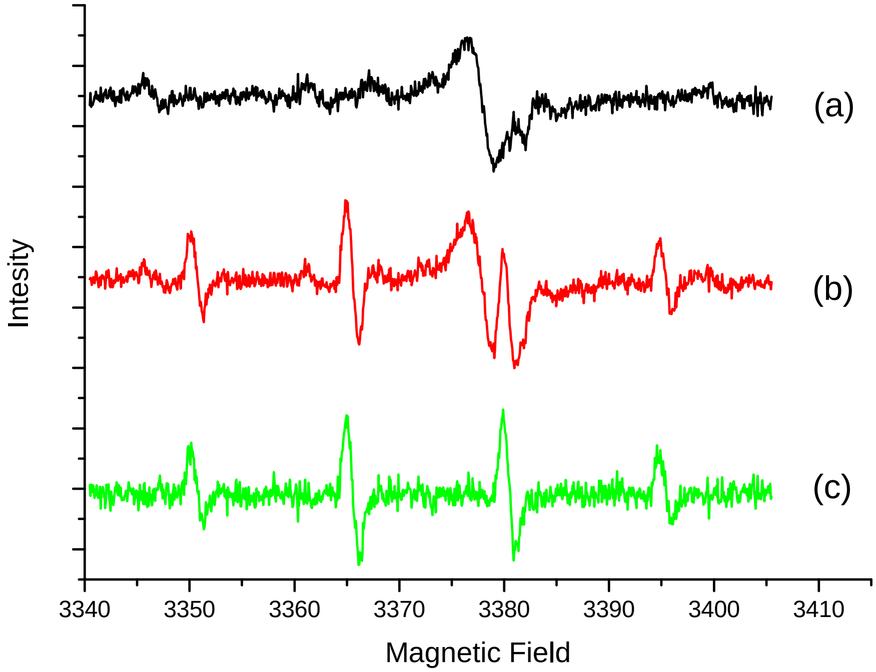

Figure 5.13 EPR spectra showing Cobalt doped Nanosun ZnO (100 mgL^{-1}) nanoparticles dispersed in deionised water, with DMPO (0.1 M), showing (a) the dark control spectrum, (b) the UV excited spectra, and (c) the UV excited spectrum minus the dark control spectrum

Finally, EPR spectra of the commercially available Invisible Zinc® sun screen were collected using the same protocol as previously. The sample was too viscous to place into the ERP tube, so small quantities of IPA were added to the sun screen sample together with DMPO (0.1 M). The dark control shows multiple low intensity peaks in the sample, Figure 5.14 (a). After irradiation, these peaks appear to increase, whilst new peaks are also formed, Figure 5.14 (b). Subtraction yields a very complex spectrum with components of the 1:2:2:1 quartet peak attributed to the •OH radical observed, Figure 5.14 (a) (1) (2) (3) (4). There are other larger peaks unassigned in the spectrum, additional radicals stabilised by the spin-trap reagent.

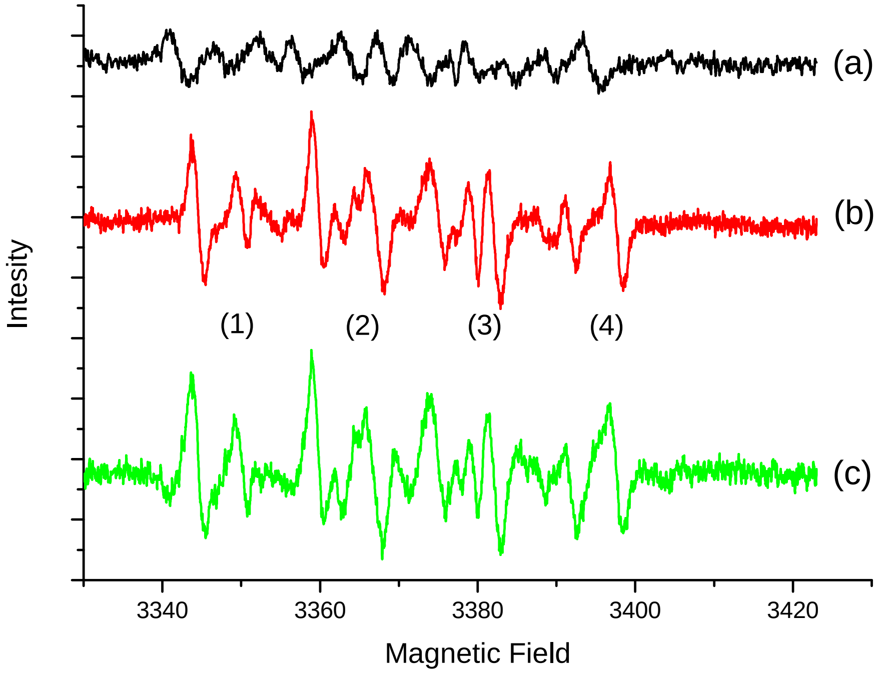

Figure 5.14 EPR spectra of Invisible Zinc® sun screen in IPA with DMPO (0.1 M), showing (a) the dark control spectrum (b) the UV excited spectra, and (c) the UV excited spectrum minus the dark control spectrum, with (1) (2) (3) and (4) indicating the DMPO-OH quartet peaks

5.4 Discussion

The aim of this chapter was to identify and quantify photo-radical production of ZnO nanoparticles. The ZnO nanoparticles in deionised water show a broad extinction spectrum with a sharp λ_{max} centred at 375 nm, which is assigned as the band gap transition (*9*), Figure 5.6. The spectrum shows strong extinction in both the UVA (313 – 400nm) and UVB (280 - 360 nm) spectral regions explaining their use in sun screens, with minimal extinction at visible wavelengths which is cosmetically desirable. The band gap transition leads to the production of photo-radicals (*31*) assumed to be the origin of the photo-radical mechanisms leading to redox toxicity responses in whole organisms, the ROS species. It is therefore important to identify the radicals produced by ZnO nanoparticles in water suspensions and to quantify the rates of production. An assay has been developed for observing the photo-radical effect of the nanoparticles, demonstrating the influence of concentration, nanoparticle size, and organic environments on the amount and rate of reduction of DCPIP observed.

5.4.1 ZnO nanoparticle DCPIP Photo Reduction Assay

The assay developed to investigate radical formation under UV light used DCPIP as a radical sensor, blue in its stable oxidised form, turning colourless when reduced (*34*), Figure 5.15**.** The suspension of DCPIP with nanoparticles in the test media gave a broad but prominent extinction λ_{max} at 595nm, a contribution from the adsorption spectrum of DCPIP and the ZnO suspension, providing an internal calibration for nanoparticle dissolution and sedimentation over the time course. This peak maximum was shown to be stable and maintained a consistent shape over time when left in a dark sealed container. When exposed to UV light the colour change in solution was monitored by the decreasing λ_{max}. This extinction peak produced no shifts in wavelength, decreasing its prominence and extinction value over time as the DCPIP was reduced. The controls Figure 5.8**,** showed no destabilising of the redox properties of the DCPIP on its own under UV light, or in the soil used in some sampling. The $ZnCl_2$ solution control confirmed that the reduction observed was an effect of the nanoparticle and not in fact a feature of Zn^{2+} ions dissolved in solution, with no DCPIP reduction observed. As the controls were stable over 80 minutes, any observed changes could be attributed as a direct result of the radical production of nanoparticles in suspension.

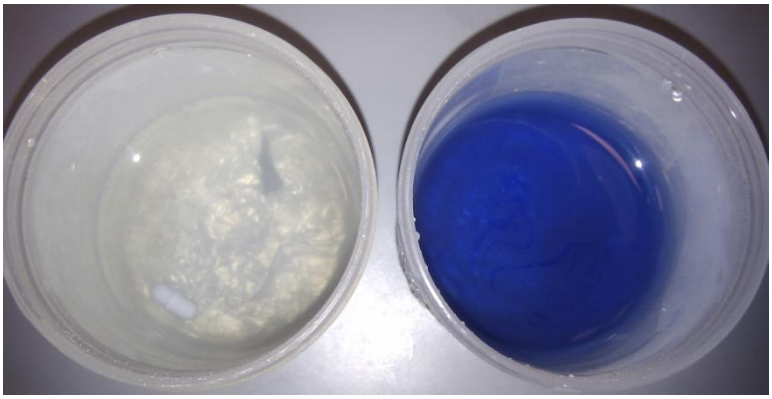

Figure 5.15 An image showing the colour change of DCPIP observed when it is reduced. The clear suspension (left) shows the nanoparticle suspension with DCPIP in its reduced form after exposure to UV light, whilst the blue suspension (right) shows the nanoparticle suspension with DCPIP kept in the dark over the same time period, showing no reduction of DCPIP

The effect of nanoparticle concentration in suspension on observed colour change was monitored by subtracting any instability observed in the dark suspension from the change in DCPIP extinction at 595 nm after 80 minutes, to give ΔExt (595 nm). By subtracting the dark controls, the assay becomes self-correcting for ZnO dispersion stability. The variation of ΔExt (595 nm) for the ZnO suspensions with concentration show a good linear dependence (R^2 = 0.993) indicating an accurate calibration of the ZnO mass with ΔExt (595 nm), Figure 5.9 (B), suggesting it has the potential to be a good species-specific ZnO nanoparticle assay. The assay displays non-linear effects at very low concentrations, showing sensitivity limitations of the assay at concentrations lower than 1 mgL^{-1}. The addition of soil particles to the suspension produces a systematic shift in the observed ΔExt (595 nm), Figure 5.10 (B) indicating a “shadowing effect” where the increased nanoparticle concentration reduced the radiation power arriving at the surface of the nanoparticles and therefore the amount of photo-radical production.

A second way of assessing the ZnO concentration has been considered: monitoring the concentration dependence of the derived exponential fitted rate constant, for both nanoparticles in deionised water, Figure 5.16(a) and with soil in deionised water, Figure 5.16 (b). Both calibration curves are linear with good R^2 values of 0.998 and 0.989, with slopes of $3.3 \pm 0.2 \times 10^{-6}\ s^{-1}$ and $2.0 \pm 0.3 \times 10^{-6}\ s^{-1}$

respectively. The rate analysis showed a significant rate divergence at higher concentrations, with soil in suspension. The rate of ZnO (100 mgL^{-1}) in deionised water is 1.7 times faster than with soil in suspension. This disparity indicates the soil particle hindering of the reduction process, nanoparticle surface absorbance and a suspension density increase.

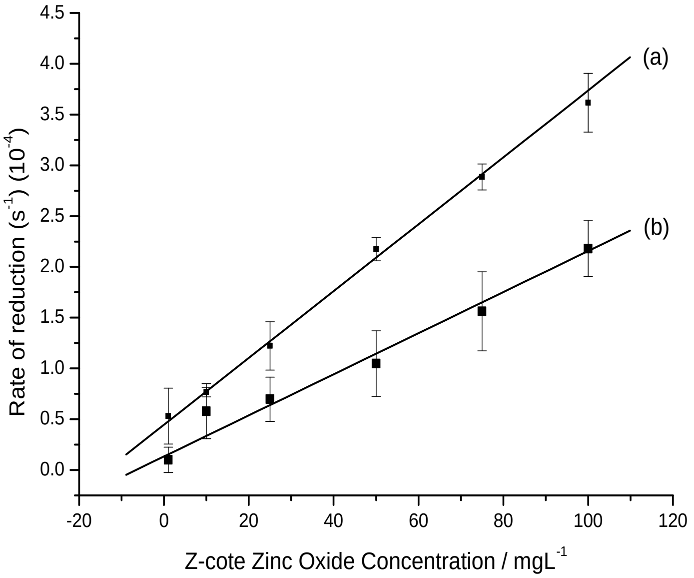

Figure 5.16 Rate of reduction of DCPIP (50 μM) against concentration of Z-cote ZnO nanoparticles in (a) Millipore deionised water, and (b) with soil (1 gL^{-1}) suspended in Millipore deionised water

The stoichiometric assay allows investigation of the photo-physical properties of the nanoparticles in suspension, providing important parameters for understanding potential toxicity. The ΔExt (595 nm) is directly proportional to the change in the DCPIP concentration; hence the number of moles of DCPIP reduced can be calculated. From this number, the rate of photo-electron/radical production can be calculated per nanoparticle assuming exactly 2 e^- are required to reduce one DCPIP molecule. The number of electrons generated per photon can then be calculated giving an estimated photo-electron yield from the nanoparticles in suspension.

For a 100 mgL^{-1} ZnO nanoparticle suspension in water 2.87 x 10^{-5} moles of DCPIP are reduced over 80 minutes; this requires an electron production of 3.58 x 10^{14} e^-s^-

[1]. Given that the diameter of the Z-cote ZnO nanoparticles is approximately 150 nm, and assuming nanoparticle density is the same as the bulk, ρ = 5.606 g cm^{-3} (*47*) then the number of electrons generated per particle may be calculated as 709 e^{-} s^{-1}. The photo-electron yield with an optical output of 1 mW is then 19 ± 2 %, Table 5.2. The accuracy and limitation of the derived properties come from the large discrepancy in the particle diameter, with the size distribution error. There are also assumptions made in the calculations that all the electrons produced are captured by the DCPIP through the radical intermediates, although collection efficiency for the electrons when surrounded by solution phase DCPIP is expected to be high (*48, 49*).

Table 5.2 Photo-physical properties of 100 mgL^{-1} ZnO nanoparticles in deionised water with DCPIP

Property	**Number**	**Units**
Nanoparticle size	150 ± 60	nm
ZnO Density	5.606	g cm^{-3}
Mass of 1 nanoparticle	9.9×10^{-15}	g particle $^{-1}$
Volume of sample	50	mL
Number of nanoparticles in assay	5.05×10^{11}	
MW of DCPIP	268	g mole^{-1}
DCPIP concentration	50	µM
ΔExt (595 nm)	0.574	
No. mols DCPIP used	2.9×10^{-5}	Mols
No. Molecules DCPIP per second	1.8×10^{14}	molecules s^{-1}
No. electrons per second	3.6×10^{14}	$e^{-}s^{-1}$
Energy of a 375 nm photon	5.3×10^{-19}	J photon
No. photons produced (LED 1 mW)	1.88×10^{15}	photon s^{-1}
Photo-electron yield	0.198	e^{-} photon^{-1}
Percentage yield	19 ± 2	%
Electrons per nanoparticle per second	709	$e^{-}s^{-1}np^{-1}$

It is hard to compare the results directly, as this is a novel assay, and gives important information on the relevant toxicity of the nanoparticles, aiming to answer questions asked in Chapter 1 on the relevant and important properties and characteristics needed to be measured to characterising nanoparticles.

5.4.2 Nanoparticle size effects on radical generation

The results so far have used Z-cote ZnO nanoparticles which have very large error in size and shape. The photo-radical properties are expected to be dependent on these parameters. Different nanoparticles, Nanosun ZnO which had a spherical uniform shape and well-defined size distribution error were used to monitor the importance and significance of size on the potential radical generation of a nanoparticle suspension. The results obtained indicate that the photo-radical yield of the Nanosun nanoparticles increase with nanoparticle diameter, Figure 5.11, with ΔExt (595 nm) 3 times larger for 200 nm nanoparticles compared to 30 nm nanoparticles, Table 5.3. The rate parameters derived from an exponential fit to each ΔExt (595 nm) trace may be used to calculate the initial rate of reduction of DCPIP as a function of nanoparticle diameter, Table 5.3. The photo-electron yield demonstrates a 2.5-fold increase from 30 nm to 200 nm nanoparticle diameter. The influence of size is an efficiency effect, with the photons more likely to interact with larger nanoparticles in suspension.

Table 5.3 Nanosun ZnO nanoparticle photo-electron properties

Nanoparticle size (nm)	Normalised ΔExt (595nm)	Rate of DCPIP reduction s^{-1}	Rate error	Photoelectron Yield %	Yield error
30	0.166	0.8	0.002	6.5	0.4
80	0.342	1.6	0.002	12.3	0.3
200	0.506	3	0.004	16.1	0.2

Commercially, the smaller size could be important but there is a balance between the rate of radical production and the UVA protection efficiency. The Co^{2+}-doped nanoparticles however, do stop radical production within the limits of the DCPIP assay.

5.4.3 EPR Spectra of ZnO-produced Photo-radicals

The DMPO spin-trapping method was used in EPR to trap •OH and O_2^-• radicals produced following the UV exposure of ZnO nanoparticle suspensions. Previous studies have shown that •OH and O_2^-• radicals can be produced by ZnO nanoparticles dispersed in water by spin traps in EPR (*39*). Using DMPO as a spin trap, it has been reported that the DMPO-OH adduct confirming the presence of •OH radicals, will form a 1:2:2:1 quartet with hyperfine splitting constants of $a_N = {}^{\beta}a_H$ = 14.9 G (*14, 16, 38, 39*), or slight variation from these figures of a_N = 15.19 G, ${}^{\beta}a_H$ = 15.00 G (*50*). Observed splitting in the experiments, Figure 5.12 (c-e) and Figure 5.13 (c), are the same as those observed previously for the •OH radical. The quartet may be assigned to the •OH radical production trapped by the DMPO, indicating that all four nanoparticle EPR spectra show hyperfine splitting constants in very close agreement with the previously published $a_N = {}^{\beta}a_H$ = 14.9 G.

The DMPO spin trap will also form a DMPO-OOH adduct caused by the O_2^-• radicals (*42*). This will result in a sextet EPR signal (*40*), with hyperfine 2 x 3 x 3 splitting, generated by the interaction of an uncoupled electron with the primary Nitrogen atom along with the secondary and tertiary protons, giving hyperfine splitting constants of a_N = 13.1 G, ${}^{\beta}a_H$ = 10.4 G, ${}^{\gamma}a_H$ = 1.3 G. The DMPO-OOH adduct is unstable, and decomposes to form the DMPO-OH adduct, (*39*), with a reported half-life $t_{1/2}$ = 60 seconds at pH 7.2 (*38*). It is therefore possible that the DMPO-OH hyperfine splitting constants observed are a combination of both the •OH and O_2^-• radicals, and this work has not ruled out their production. Previous work has distinguished between the production of the two radicals using DMSO to scavenge •OH radicals (*39*), although this resulted in no evidence of the formation of the O_2^-• radicals in a ZnO dispersion (*39*), while a 5-(diethoxyphosphoryl)-5-

methyl-1-pyrroline-N-oxide (DEPMPO) spin trap has also been used to show that only hydroxyl radicals were produced from ZnO nanoparticles (*39*).

In the Invisible Zinc® sunscreen, a 1:2:2:1 quartet is observed, Figure 5.14 (a) (1) (2) (3) (4), although the hyperfine splitting constants do not replicate exactly with the previous data, which can be attributed to the influence of other paramagnetic features present in the sample. An observed decrease in the DMPO-OH quartet signal has been previously observed due to the hydrogen atom contribution to the radical from the ethanol (*23*). Zweier *et al.* reported that DMPO in the presence of ethanol formed a hydroethyl radical $CH_3{\bullet}CH(OH)$, generated in the presence of the •OH radical, as the radical would extract a hydrogen atom from the ethanol (*23*). This produced a sextet signal, with hyperfine splitting of a_N = 15.8 G, a_H = 22.8 G, and may be what is observed in conjunction with the DMPO-OH radical quartet in the sun screen sample. Other background features observed appear to suggest the trapping of an alkyl-radical with the DMPO in a DMPO-R adduct (*51*), although whether it is caused by the presence of the alcohol in suspension or a component of the sun screen is unclear. The cause of the radical production in the Invisible Zinc® sun screen is undefined, but shows that exposed to UV light, radicals are formed. This indicates that when applied to skin in sunlight ROS may form at the dermal barrier with potential availability in cells, which have previously displayed toxic effects and cell death (*14, 17, 18, 23*).

Table 5.4 Showing the DMPO radical spin trap splitting constants for the hydroxyl radical quartet peaks, and other radicals formed in solution

Figure	Splitting lines 1:2:2:1				Hyperfine splitting constants (G)		
Nanosun (80nm) Zinc Oxide	3349.22	3364.001	3379.062	3393.832	14.783	15.061	14.77
Z-cote (150nm) Zinc Oxide	3349.83	3364.586	3379.478	3394.371	14.729	14.892	14.893
Z-cote (150nm) Zinc Oxide in soil	3351.11	3365.915	3380.865	3395.663	14.807	14.941	14.807
Cobalt doped Nanosun Zinc Oxide	3350.83	3365.659	3380.592	3395.419	14.827	14.933	14.827
Sunscreen	3350.07	3366.883	3381.993	3397.622	16.817	15.11	15.629
	Other splitting lines						
Sunscreen	3344.63	3359.916	3370.271	3375.203	3379.616	3391.679	

5.5 Conclusions

The observed data confirm a number of key findings in ZnO nanoparticle behaviour in the environment. The DCPIP assay has been developed to measure the photo-radical production properties of nanoparticles and has shown that the radical generation potential is dependent on nanoparticle concentration and size in the suspension. The assay can be used over a large concentration range with a detection limit of 1 µg / mL, and the assay is able to self-adjust itself for the aggregation properties of individual samples. The DCPIP assay has shown the presence of soil in suspension to cause a decrease in radical production, attributed to shadowing and particle interface interaction. The EPR data confirmed the presence of the radical generation observed using the DCPIP assay. The data was not quantitative, but did clearly show that under UV light radicals were formed and trapped using DMPO as a spin trap. The data also highlighted the issue that the Invisible Zinc® sun screen does produce radicals under UV light, and this must be cause for concern when looking at nanoparticle bioavailability and toxicity from pharmaceutical products, both in humans and aquatic organisms.

Limitations of the assay can be seen with the contrasting results observed for the cobalt doped ZnO nanoparticles. The DCPIP assay indicated that reduction is quenched, preventing the electrons generated from forming toxic radicals in suspension. However, EPR results produced radical generation. As a development of the DCPIP assay, future work needs to test the assay in sunscreen, to confirm whether the observed affects can be seen, although the DCPIP redox stability in sunscreen is unclear; an assay limitation. Assay development would extend to more complex media introducing different soil dispersions and various ionic strength suspensions, and increasing assay sensitivity for use in environmentally relevant concentrations. Other limitations of the assay are the assumptions that radicals generated transfer electrons to the DCPIP molecules, rather than merely disrupting the π- system, and the assumption that the concentration of DCPIP used in the assay allows for all photo-electrons produced to reduce the redox dye.

It is proposed that the DCPIP assay is the first, simple species-dependent assay that could be used in more complex samples and produces new information on the photo-radical generation properties of ZnO nanoparticles and potentially all photo-active nanoparticles.

References

1. Arnold, M S, Avouris, P, Pan, Z W, and Wang, Z L. (2002) Field-Effect Transistors Based on Single Semiconducting Oxide Nanobelts, *The Journal of Physical Chemistry B 107*, 659-663.
2. Bian, S-W, Mudunkotuwa, I A, Rupasinghe, T, and Grassian, V H. (2011) Aggregation and Dissolution of 4 nm ZnO Nanoparticles in Aqueous Environments: Influence of pH, Ionic Strength, Size, and Adsorption of Humic Acid, *Langmuir 27*, 6059-6068.
3. Nohynek, G J, Lademann, J r, Ribaud, C, and Roberts, M S. (2007) Grey Goo on the Skin? Nanotechnology, Cosmetic and Sunscreen Safety, *Critical Reviews in Toxicology 37*, 251-277.
4. Lachheb, H, Puzenat, E, Houas, A, Ksibi, M, Elaloui, E, Guillard, C, and Herrmann, J-M. (2002) Photocatalytic degradation of various types of dyes (Alizarin S, Crocein Orange G, Methyl Red, Congo Red, Methylene Blue) in water by UV-irradiated titania, *Applied Catalysis B: Environmental 39*, 75-90.
5. Serpone, N, Dondi, D, and Albini, A. (2007) Inorganic and organic UV filters: Their role and efficacy in sunscreens and suncare products, *Inorganica Chimica Acta 360*, 794-802.
6. Markham, S C. (1955) Photocatalytic properties of oxides, *Journal of Chemical Education 32*, 540-null.
7. Egerton, T, A, and King, C, J. (1979) The influence of light intensity on photoactivity in TiO2 pigmented systems, *Journal of the Oil and Colour Chemists Association 62* 386-391
8. Kamat, P V, and Meisel, D. (2003) Nanoscience opportunities in environmental remediation, *Comptes Rendus Chimie 6*, 999-1007.
9. Farag, H, K,, hanafi, Z, M,, Dawy, M, and Aziz, E, M,. (2010) Characterization of ZnO nanopaowders synthesized by the direct precipitation method, *Canadian journal of pure and applied science 4*, 1303-1309.

10. Turchi, C S, and Ollis, D F. (1990) Photocatalytic degradation of organic water contaminants: Mechanisms involving hydroxyl radical attack, *Journal of Catalysis 122*, 178-192.
11. Nel, A, Xia, T, Madler, L, and Li, N. (2006) Toxic Potential of Materials at the Nanolevel, *Science 311*, 622-627.
12. Shibata, H, Ogura, Y, and Sawa, Y. (1998) Hydroxyl radical generation depending on O2 or H2O by a photocatalyzed reaction in an aqueous suspension of titanium dioxide, *Bioscience, biotechnology, and biochemistry 62*, 2306-2311.
13. Ollis, D F, and Al-Ekabi, H. (1993) Photocatalytic Purification and treatment of water and Air, *Elevier, Amsterdam*.
14. Togashi, H, Shinzawa, H, Matsuo, T, Takeda, Y, Takahashi, T, Aoyama, M, Oikawa, K, and Kamada, H. (2000) Analysis of hepatic oxidative stress status by electron spin resonance spectroscopy and imaging, *Free Radical Biology and Medicine 28*, 846-853.
15. Daneshvar, N, Salari, D, and Khataee, A R. (2004) Photocatalytic degradation of azo dye acid red 14 in water on ZnO as an alternative catalyst to TiO2, *Journal of Photochemistry and Photobiology A: Chemistry 162*, 317-322.
16. Vestad, T. (1999) ESR Spin Trapping, *University of Oslo*.
17. Zhu, S, Oberdörster, E, and Haasch, M L. (2006) Toxicity of an engineered nanoparticle (fullerene, C60) in two aquatic species, Daphnia and fathead minnow, *Marine Environmental Research 62*, S5-S9.
18. Blaise, C, Gagné, F, Férard, J F, and Eullaffroy, P. (2008) Ecotoxicity of selected nano-materials to aquatic organisms, *Environmental Toxicology 23*, 591-598.
19. Hisao, H, Hiroyuki, K, Takayoshi, K, Tsugio, S, and Nick, S. (2006) DNA Damage Photoinduced by Cosmetic Pigments and Sunscreen Agents under Solar Exposure and Artificial UV Illumination, *Journal of Oleo Science 55*, 249-261.

20. Geng, J, Tang, W, Wan, X, Zhou, Q, Wang, X J, Shen, P, Lei, T C, and Chen, X D. (2008) Photoprotection of bacterial-derived melanin against ultraviolet A–induced cell death and its potential application as an active sunscreen, *Journal of the European Academy of Dermatology and Venereology 22*, 852-858.

21. Federici, G, Shaw, B J, and Handy, R D. (2007) Toxicity of titanium dioxide nanoparticles to rainbow trout (Oncorhynchus mykiss): Gill injury, oxidative stress, and other physiological effects, *Aquatic Toxicology 84*, 415-430.

22. Hu, C W, Li, M, Cui, Y B, Li, D S, Chen, J, and Yang, L Y. (2009) Toxicological effects of TiO2 and ZnO nanoparticles in soil on earthworm Eisenia fetida, *Soil Biology and Biochemistry 42*, 586-591.

23. Zweier, J L, Duke, S S, Kuppusamy, P, Sylvester, J T, and Gabrielson, E W. (1989) Electron paramagnetic resonance evidence that cellular oxygen toxicity is caused by the generation of superoxide and hydroxyl free radicals, *FEBS Letters 252*, 12-16.

24. Reddy, K M, Feris, K, Bell, J, Wingett, D G, Hanley, C, and Punnoose, A. (2007) Selective toxicity of zinc oxide nanoparticles to prokaryotic and eukaryotic systems, *Applied Physics Letters 90*, 213902-213902-213903.

25. Jemec, A, Drobne, D, Remškar, M, Sepčić, K, and Tišler, T. (2008) Effects of ingested nano-sized titanium dioxide on terrestrial isopods (Porcellio scaber), *Environmental Toxicology and Chemistry 27*, 1904-1914.

26. Mortimer, M, Kasemets, K, Heinlaan, M, Kurvet, I, and Kahru, A. (2008) High throughput kinetic Vibrio fischeri bioluminescence inhibition assay for study of toxic effects of nanoparticles, *Toxicology in Vitro 22*, 1412-1417.

27. Warheit, D B, Hoke, R A, Finlay, C, Donner, E M, Reed, K L, and Sayes, C M. (2007) Development of a base set of toxicity tests using ultrafine TiO2 particles as a component of nanoparticle risk management, *Toxicology Letters 171*, 99-110.

28. Lu, C M, Zhang, C Y, Wen, J Q, Wu, G R, and Tao, M X. (2002) Research of the effect of nanometer materials on germination and growth enhancement of Glycine max and its mechanism, *Soybean Science 21(3)*, 168-171.

29. Huang, H H, Ni, X P, Loy, G L, Chew, C H, Tan, K L, Loh, F C, Deng, J F, and Xu, G Q. (1996) Photochemical Formation of Silver Nanoparticles in Poly(N-vinylpyrrolidone), *Langmuir 12*, 909-912.
30. Lin, D, and Xing, B. (2008) Root Uptake and Phytotoxicity of ZnO Nanoparticles, *Environmental Science & Technology 42*, 5580-5585.
31. Wang, C, Wang, X, Xu, B-Q, Zhao, J, Mai, B, Peng, P a, Sheng, G, and Fu, J. (2004) Enhanced photocatalytic performance of nanosized coupled ZnO/SnO2 photocatalysts for methyl orange degradation, *Journal of Photochemistry and Photobiology A: Chemistry 168*, 47-52.
32. Jang, Y J, Simer, C, and Ohm, T. (2006) Comparison of zinc oxide nanoparticles and its nano-crystalline particles on the photocatalytic degradation of methylene blue, *Materials Research Bulletin 41*, 67-77.
33. Chakrabarti, S, Chaudhuri, B, Bhattacharjee, S, Das, P, and Dutta, B K. (2008) Degradation mechanism and kinetic model for photocatalytic oxidation of PVC ZnO composite film in presence of a sensitizing dye and UV radiation, *Journal of Hazardous Materials 154*, 230-236.
34. Kok, B, Gassner, E S, and Rurainski, H J. (1965) Photoinhibition of Chloroplast reactions, *Photochemistry and Photobiology 4*, 215-227.
35. Yang, L, and Watts, D J. (2005) Particle surface characteristics may play an important role in phytotoxicity of alumina nanoparticles, *Toxicology Letters 158*, 122-132.
36. Janzen, E G, and Blackburn, B J. (1969) Detection and identification of short-lived free radicals by electron spin resonance trapping techniques (spin trapping). Photolysis of organolead, -tin, and -mercury compounds, *Journal of the American Chemical Society 91*, 4481-4490.
37. Zweier, J L, Kuppusamy, P, and Lutty, G A. (1988) Measurement of endothelial cell free radical generation: evidence for a central mechanism of free radical injury in postischemic tissues, *Proceedings of the National Academy of Sciences 85*, 4046-4050.
38. Houriez, C l, Ferré, N, Siri, D, Tordo, P, and Masella, M. (2010) Structure and Spectromagnetic Properties of the Superoxide Radical Adduct of DMPO in

Water: Elucidation by Theoretical Investigations, *The Journal of Physical Chemistry B 114*, 11793-11803.

39. Lipovsky, A, Tzitrinovich, Z, Friedmann, H, Applerot, G, Gedanken, A, and Lubart, R. (2009) EPR Study of Visible Light-Induced ROS Generation by Nanoparticles of ZnO, *The Journal of Physical Chemistry C 113*, 15997-16001.
40. Kuppusamy, P. (2002) EPR Spectroscopy, Spying on umpaired electrons - what information can we get?, In *Sunrise Free Radical School*.
41. Seber, G. (2010) EPR Spectroscopy, (Amherst, U., Ed.).
42. Zang, L Y, and Misra, H P. (1992) EPR kinetic studies of superoxide radicals generated during the autoxidation of 1-methyl-4-phenyl-2,3-dihydropyridinium, a bioactivated intermediate of parkinsonian-inducing neurotoxin 1-methyl-4-phenyl-1,2,3,6-tetrahydropyridine, *Journal of Biological Chemistry 267*, 23601-23608.
43. Tuna, F. The EPSRC National EPR Research Facility and Service, School of Chemistry and Photon Science Institute, University of Manchester, Oxford Road, Manchester, M13 9PL.
44. Gulson, B, McCall, M, Korsch, M, Gomez, L, Casey, P, Oytam, Y, Taylor, A, McCulloch, M, Trotter, J, Kinsley, L, and Greenoak, G. (2010) Small Amounts of Zinc from Zinc Oxide Particles in Sunscreens Applied Outdoors Are Absorbed through Human Skin, *Toxicological Sciences 118*, 140-149.
45. Svendsen, C. (2010) OECD Soil. Ecotoxicologist, Centre for Ecology & Hydrology, Maclean Building, Benson Lane, Crowmarsh Gifford, Wallingford, Oxfordshire, OX10 8BB.
46. Prospect. (2010) Protocol for Nanoparticle Dispersion, *Ecotoxicology Test Protocols for representative Nanomaterials in support of the OECD Sponsorship programme*.
47. Beek, W J E, Slooff, L H, Wienk, M M, Kroon, J M, and Janssen, R A J. (2005) Hybrid Solar Cells Using a Zinc Oxide Precursor and a Conjugated Polymer, *Advanced Functional Materials 15*, 1703-1707.

48. Fujishima, A, Rao, T N, and Tryk, D A. (2000) Titanium dioxide photocatalysis, *Journal of Photochemistry and Photobiology C: Photochemistry Reviews 1*, 1-21.

49. Redmond, G, Fitzmaurice, D, and Graetzel, M. (1994) Visible Light Sensitization by cis-Bis(thiocyanato)bis(2,2'-bipyridyl-4,4'-dicarboxylato)ruthenium(II) of a Transparent Nanocrystalline ZnO Film Prepared by Sol-Gel Techniques, *Chemistry of Materials 6*, 686-691.

50. Inbaraj, J J, Bilski, P, and Chignell, C F. (2002) Photophysical and Photochemical Studies of 2-Phenylbenzimidazole and UVB Sunscreen 2-Phenylbenzimidazole-5-sulfonic Acid, *Photochemistry and Photobiology 75*, 107-116.

51. Jurkiewicz, B A, and Buettner, G R. (1994) Ultraviolet light-induced free radical formation in skin: An electron paramagnetic resonance study, *Photochemistry and Photobiology 59*, 1-4.

Chapter 6

ZnO Nanoparticle Toxicity – Medium Dependent Dissolution

6.1 Introduction

Understanding the nanoparticle interface in different environmental conditions is a central theme of this thesis. It is hypothesised that the interface structure will directly influence nanoecotoxicology and should be characterised carefully. One important toxicity mechanism has been measured, the photo-electron radical production property of ZnO nanoparticles. A second ZnO toxicity mechanism is nanoparticle dissolution, the release of Zn^{2+} ions delivered locally at nanoparticle-dissolution sites. It is this mechanism that will now be considered, observing the release of and subsequent interaction of the Zn^{2+} ionic species with other molecules in suspension (*1*).

Dissolution will occur at the nanoparticle surface with molecules moving initially into the interface and finally the bulk solution at a rate determined by a number of properties in the diffuse layer surrounding individual nanoparticles (*2*). The surface area of the nanoparticles is one controlling factor (*2, 3*), with smaller nanoparticles dissolving more readily (*4-6*) given the high surface area to volume ratio (*7*). In addition, the surface morphology or roughness will influence the dissolution rate, with rougher edges dissolving faster compared to smooth surfaces (*8*). The pH and ionic strength of the dispersion medium will also contribute to the rate of dissolution (*9*), with Agren *et al.* previously demonstrating a 10 fold rise in Zn^{2+} ions observed from ZnO at pH 5.4 compared to pH 7.4 (*10*). ZnO is however amphoteric, and will dissolve both in acidic and basic conditions (*11*), leading to the formation of $Zn(OH)^+$ species in acidic solutions (*12*), while in neutral and basic solutions Zn^{2+} is the dominant dissolved species (*13*).

Ecotoxicological studies observing the effects of ZnO nanoparticle dissolution have shown the release of metal ions at toxic concentrations in bacteria (*14*). Dennis *et al.* investigated the toxicity of Zn^{2+} ions on roundworms (*nematodes*), demonstrating an enhanced stress response (*7*) and Ji *et al*. has shown toxicity of Zn^{2+} ions to green algae Chlorella (*15*). In freshwater alga, an IC_{50} value of 60 μgL^{-1} was recorded after a 72 hour exposure of ZnO nanoparticles, attributed solely to dissolved zinc (*16*). Zinc IC_{50} values published for plants, have given estimated values near 50 mgL^{-1} in radishes, and 20 mgL^{-1} for rape and ryegrass, determined by root growth termination (*17, 18*).

In humans Zn toxic levels are harder to estimate, as it is an essential trace element, present in over 300 enzymes and proteins in the body and is required for processes such as protein metabolism and cell growth (*19*). The body contains around 3 grams of zinc, mostly concentrated in the bones and muscles (*20*), with a suggested daily zinc uptake for men of 11 mg (*21*). It has been estimated that a human LD_{50} is 27 g, based on rat exposures (*22*), with symptoms of excessive zinc uptake ranging from lethargy and vomiting to amnesia and abdominal pain (*23, 24*). Because of the high levels of zinc in the body, there have been a limited number of studies on the potential uptake of zinc from cosmetics through dermal exposure, both in nanoparticulate and dissolved Zn^{2+} form. Studies have been carried out with TiO_2 (*25*) and ZnO *(26)* sunscreen products applied to pig skin, concluding that the nanoparticles did not penetrate further than the *Stratum Corneum*. Song *et al.* used non-linear optical microscopy to image nanoparticle transdermal penetration of a commercial sun screen Zinclear®, with results displaying no skin penetration, only nanoparticle detection on the surface and in skin folds, Figure 1.3 (*27*). To determine conclusively the penetration potential of ZnO nanoparticles on human skin, an isotope tracing technique using stable ^{68}Zn has been developed to distinguish from naturally occurring zinc (*28, 29*). The break-through study applied isotope labelled ZnO nanoparticle sunscreen on human skin. The results demonstrated evidence of the ^{68}Zn present in blood and urine samples, confirming passage across healthy skin, although concentrations observed were only in the region of 1 x 10^{-3} % of the applied dose (*29*).

The studies were unable to determine if the absorbed zinc was in nanoparticle form or as dissolved zinc. Being able to determine the nanoparticle speciation is important, as Zn^{2+} ions possess different properties to nanoparticles, which will influence their toxicity. It is also important to determine the time and place of dissolution, as the nanoparticles can act as a vehicle for enhanced toxic ion delivery in organs and cells. Further evidence from the same isotope labelled ZnO nanoparticle sunscreen study (*29*) indicated that the concentration of ^{68}Zn in the blood was significantly higher than initial readings, with concentrations increasing in the subsequent 5 days following exposure. This may point to slow release of the ^{68}Zn from tissue, or evidence that the nanoparticle surfaces are modified with the body producing a slow dissolution rate. Previous work has shown that both Gold and Silver nanoparticles will adsorb protein layers in blood (*30*), and this may then delay dissolution, or prevent the release of ions into the solution bulk. The protein corona has been proposed when nanoparticles are present in plasma (*14*), with constant protein exchange at the nanoparticle surface. It is proposed that the proteins may become denatured or be structurally altered, forming a stable layer around the nanoparticle; modifying surface availability to dissolve.

6.1.1 Aims and Objectives

The aim of this chapter is to measure the rate of dissolution of ZnO nanoparticles as a function of liquid medium composition. To detect dissolution, the nanoparticles need to be separated from Zn^{2+} ions. Methods for separation include centrifugation, ultra filtration and dialysis (*16, 31*). The Zn^{2+} concentrations are then measured using inductively coupled plasma atomic emission spectrometry (ICP-AMS) with its high sensitivity able to detect elemental mass as low as parts per trillion (*32*). The rate of dissolution of ZnO nanoparticles will be monitored in deionised water using dialysis and syringe filtration, and analysed using ICP-AES. This work was carried out in Sydney, Australia at the Commonwealth Scientific and Industrial Research Organisation (CSIRO), as part of the OECD PROSPEcT collaboration (*16*). The work will be extended to complex media more representative of the potential cycle of the nanoparticles, replicating environments of nanoparticles in organisms, Figure 6.1. The nanoparticles will be suspended in Foetal Bovine Serum (FBS), high in rich proteins, especially BSA, and will be exposed to Dulbecco's Modified Eagle Medium (DMEM), a salts medium used predominantly for cell culture studies containing sulphates, chlorides and phosphates.

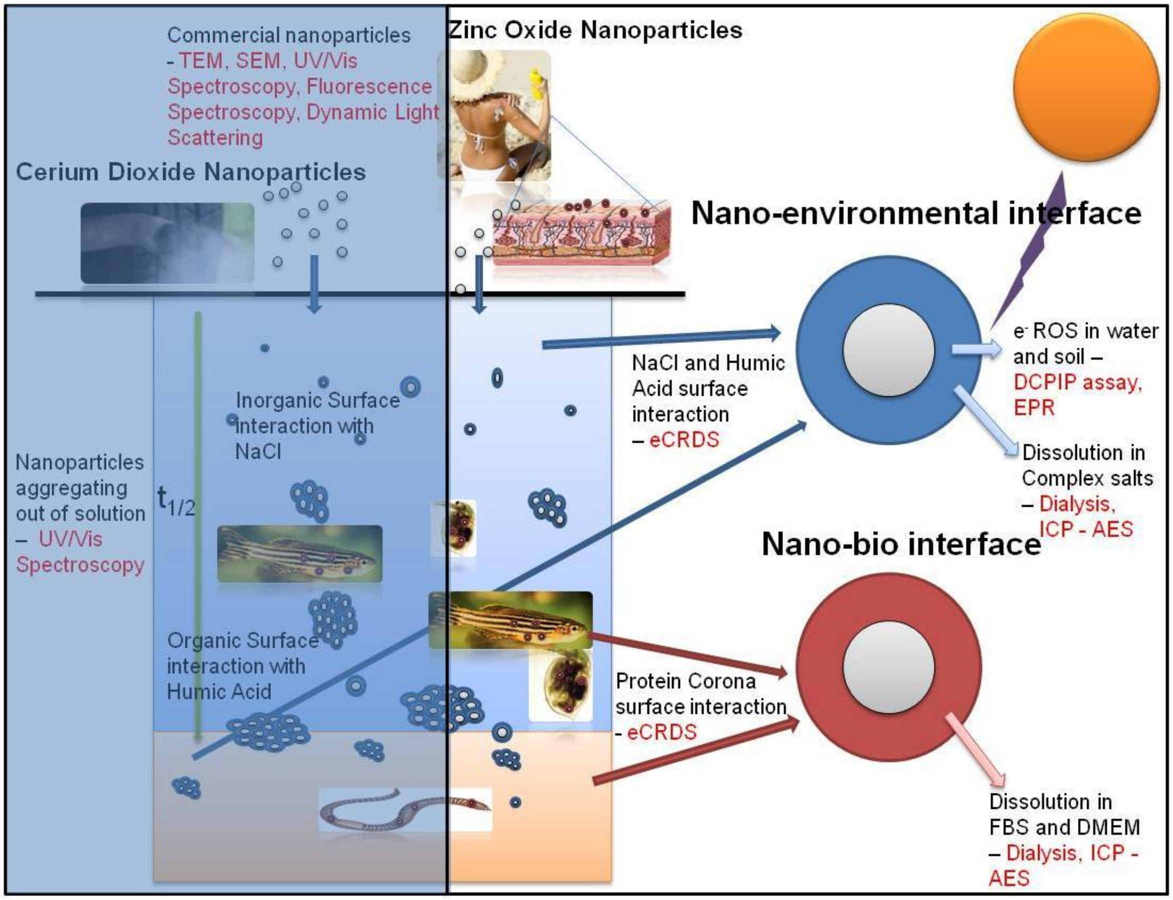

Figure 6.1 Thesis overview, highlighting the ZnO cosmetic application and the interface layers that may form on the particle surfaces once dispersed into the environment, influencing the rate and amount of dissolution observed in suspension

By contrast to the Zn^{2+} dissolution detection methods, the DCPIP photo-radical reduction assay will be used to monitor the decrease in the nanoparticle concentration over time from dissolution, Figure 6.1. This dissolution measurement will provide a standard for more complex media and will be extended to solid soil samples with new modifications to the DCPIP assay protocol.

6.2 Materials and Methods

6.2.1 Materials

Nanosun ZnO nanoparticles (30 ± 5 nm, and 200 ± 5nm) were provided by Microniser and used as received without further characterisation. Zinc Chloride ($ZnCl_2$) was purchased from Sigma Aldrich. DMEM and FBS were purchased from Invitrogen Australia Pty. Ltd. and used as supplied. The Dialysis tubing used was 1000 Dalton molecular weight cut-off giving a nominal pore size of 1 nm (Cole Palmer Spectra/Pore dialysis membranes, Extech). The Syringe filters used had a 0.1 µm pore size. The 2, 6-Dichlorophenolindophenol (DCPIP) was purchased from Fluka Analytical (33125, 90% purity), and used as received. The soil was sampled from the same batch as Chapter 5, supplied by Dr Claus Svendsen (*33*).

6.2.2 Dissolution parameters measured using Dialysis, Syringe Filtration and ICP-AES

The protocol for the dialysis measurement of nanoparticle dissolution has been described in detail elsewhere (*16*) and will only be discussed here briefly. Dialysis membrane was filled with 10 mL of deionised water to form a dialysis cell. Seven dialysis cells were placed into a 1 litre tank containing the test medium, Figure 6.2. The different test media were, 1) deionised water, 2) DMEM tissue culture medium, 3) FBS (10 % v/v) in deionised water and 4) DMEM salts solution consisting of Calcium Chloride (33.22 mgL^{-1}), Cupric Sulphate (0.0025 mgL^{-1}), Ferric Sulphate (0.934 mgL^{-1}), Potassium Chloride (223.6 mgL^{-1}), Magnesium Chloride (57.22 mgL^{-1}), Sodium Chloride (7599 mgL^{-1}), Sodium Bicarbonate (1176 mgL^{-1}), Sodium Phosphate (142 mgL^{-1}) and Zinc Sulphate (0.863 mgL^{-1}).

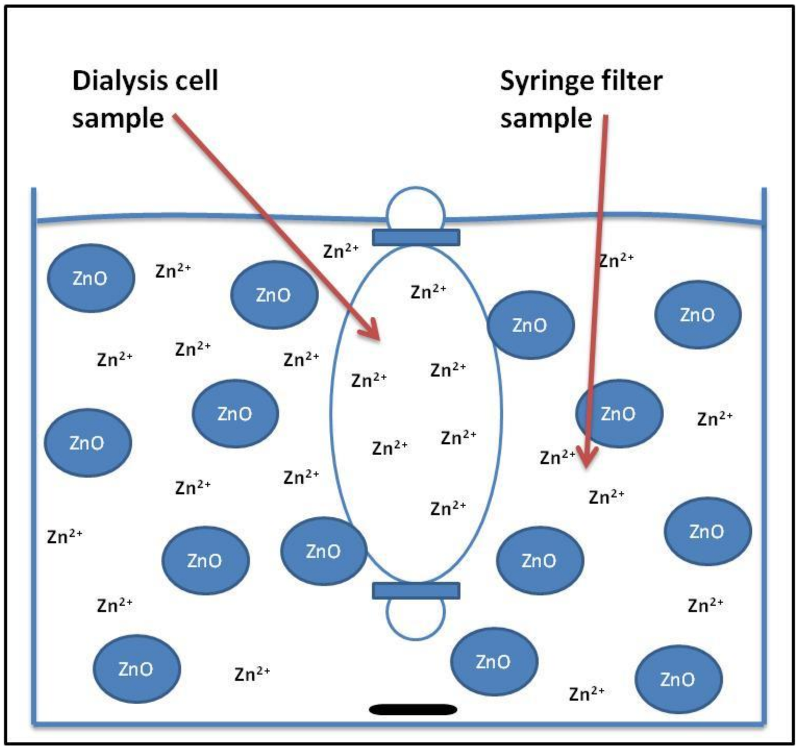

Figure 6.2 Experimental configuration showing the dissolution measurements, with samples taken for ICP-AES analysis from within dialysis cells with a 1 nm pore size cut off, and additionally taken from the surrounding volume, using a syringe filter with a 0.1 μm pore size cut off.

For each test medium triplicate dissolution experiments were performed. The test media were left to equilibrate, while being stirred continuously in a dark, temperature controlled (37 ^{O}C) incubator. Over 72 hours 5 mL aliquots were taken, (a) from the dialysis cells, and (b) syringe filtered from the tank, for dissolved zinc analysis, Figure 6.2. The samples were acidified (0.5 %) with Tracepur HNO_3 (Merck) and prepared for ICP – AES with a 5 x dilution.

6.2.3 Dissolution measured using DCPIP photo-radical assay over time

Experiments were performed to measure the dissolution of Nanosun (200 ± 5 nm) ZnO nanoparticles in a deionised water suspension over time using the DCPIP photo-radical assay developed in Chapter 5. Nanosun nanoparticles (100 mgL^{-1}) were suspended in deionised water at pH 7 and stored in the dark; the dispersion was stirred routinely to preserve the suspension. 100 mL samples of the suspension were removed at 8 different time points over a time course of ten days. At each time point DCPIP (50 µM) was added to the aliquot, and the reduction of DCPIP monitored, measuring the extinction at 595 nm over 80 minutes, in both the dark and under UV light, following the same protocol detailed in Chapter 5.

The assay was modified to include a soil sampling protocol. This allowed samples to be removed from the soil and then re-suspended to allow direct measurement of the photo-radical production rate of the nanoparticles. Samples were taken from a soil sample doped with ZnO nanoparticles over a time course of ten weeks. Nanosun (200 ± 5 nm) nanoparticles (1 g) were mixed thoroughly using a metal spatula in 100 g of previously prepared pH 7 soil (*33*). At t = 0, triplicate samples (1 g) were removed from the soil / ZnO mixture, with care taken to ensure the sample was collected throughout the soil mixture. The samples were finely broken down using a pestle and mortar, filtered to remove large soil particles and suspended in deionised water (100 mL) using the previously described protocol (Section 5.2). DCPIP (50 µM) was added to the suspension and monitored over a period of 80 minutes under UV light and under a dark control. The observed change in DCPIP absorbance was then recorded at 595 nm over this time period, with the dark control subtracted. Further samples (1 g) were removed in triplicate from the soil / ZnO mixture at 6 separate time points over a 10 week period and the reduction of DCPIP observed over the 80 minute UV exposures. To assess the accuracy of the assay, the potential to recover the nanoparticles was calculated in both a soil suspension and in deionised water. ZnO nanoparticles (100 mgL^{-1}) were added to a deionised water sample, and ZnO nanoparticles (10 mg) were added to a soil sample (1 g) and dispersed in deionised water (100 mL). These samples were assayed in conjunction with the t = 0 experimental soil samples, to give an assay recovery potential.

6.3 Results

6.3.1 Zinc Chloride Dialysis and Syringe Filter Controls

Two series of experiments were performed in parallel to compare the efficiency of separation of Zn^{2+} from any particulate material, and establish the equilibration time for the dialysis cells in suspension. The two techniques used were tank syringe filtration and dialysis. The sample recovery and capacity of the medium to interact with the Zn^{2+} ions was assessed with $ZnCl_2$ as a control experiment using the two separation techniques, presented for the four test media in Figure 6.3 and Figure 6.4.

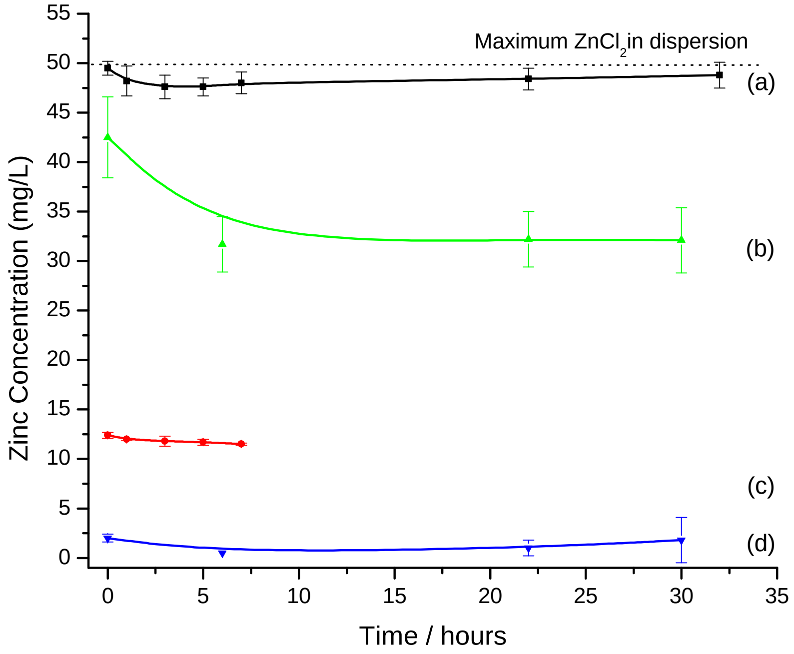

Figure 6.3 Concentration of Zn^{2+} ions ($50mgL^{-1}$) present in solution using tank-syringe filtration over time, in (a) deionised water, (b) FBS (10 %) in deionised water, (c) DMEM and (d) DMEM salts

A $ZnCl_2$ concentration of 77.1 mgL^{-1} was made up in the tank, to give a maximum of 50 mgL^{-1} Zn^{2+}. The $ZnCl_2$ tank-syringe filtered data in deionised water, Figure 6.3 (a), shows that from an initial concentration of 50 mgL^{-1} Zn^{2+}, 49 ± 1 mgL^{-1} recovery was determined by the ICP-AES. This is a percentage recovery of 98 ± 2 % over the 36 hour time course. The Zn^{2+} present in the FBS solution, Figure 6.3 (b) shows an initial recovery for the first time point of 43 ± 4 mgL^{-}1, (85 ± 8 %) and then a subsequent decreased recovery from the protein solution to a minimum of 32 ± 3 mgL^{-1} (64 ± 7 %) at 36 hours. In DMEM, Figure 6.3 (c) the concentration obtained is low, 12.4 ± 0.3 mgL^{-1} (24 ± 0.6 %) staying constant over the length of the experiment, with a concentration of 11.5 ± 0.1 mgL^{-1} (23 ± 0.2 %) recorded after 7 hours. The 22 and 32 hour time points were unreliable, and the Zn^{2+} concentration values obtained here have been omitted. At these time points, the temperature of the storage cabinet where the samples were kept rose from 37 to 54 °C overnight. This caused a significant alteration in pH of the triplicate samples a, b and c, changing from pH 7.6 in the original samples down to 6.9, 5.2 and 6.7 respectively resulting in significant changes in the rate of dissolution, reflected in the sample error. This change in temperature appeared to decrease the concentration of Zn^{2+} in solution to 7.2 ± 0.2 mgL^{-1} (14.4 ± 0.4%) after 32 hours. Finally, the Zn^{2+} concentration observed in the DMEM salts appeared low throughout the time course, with a concentration of 2 ± 0.4 mgL^{-1} (4 ± 0.8 %) obtained at *t* = 0, and a value of 2 ± 2 mgL^{-1} (4 ± 9 %) after 30 hours.

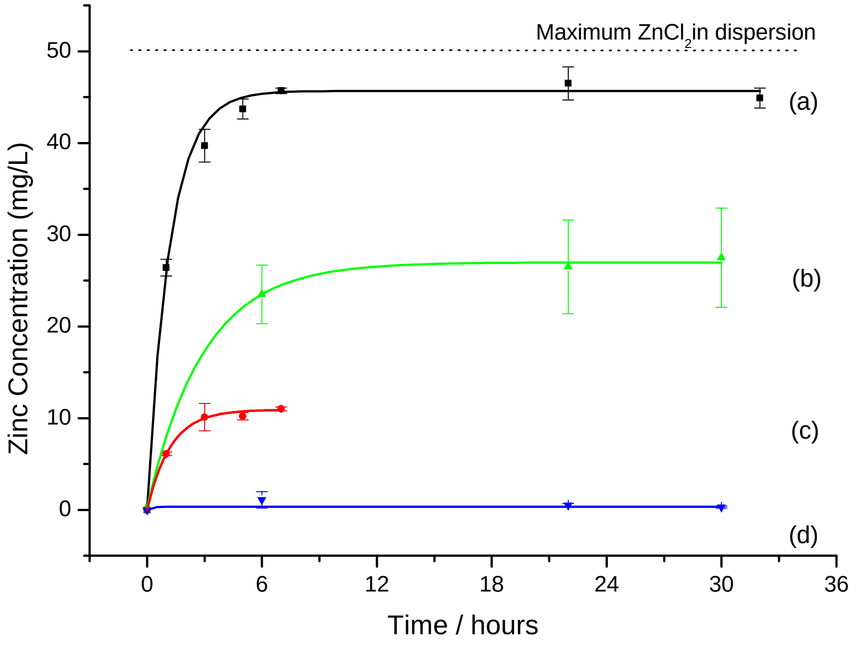

Figure 6.4 Concentration of Zn^{2+} ions ($50mgL^{-1}$) present in solution across the dialysis membrane over time, in (a) deionised water, (b) FBS (10 %) in deionised water, (c) DMEM and (d) DMEM salts

The filtration data were compared with the dialysis technique, Figure 6.4. The $ZnCl_2$ samples taken from the dialysis cells in deionised water, Figure 6.4 (a) show an exponential rise in zinc concentration present in the dialysis cells, with the zinc ions reaching a maximum of 45.7 ± 0.3 mgL^{-1} (91.4 ± 0.6 %) across the membrane after 7 hours. This indicates that equilibration takes 7 hours across the dialysis tubing; measurements taken in shorter time periods are not at equilibrium. In FBS, Figure 6.4 (b) $ZnCl_2$ initially increased from zero finding equilibrium in between 7 and 22 hours at 28 ± 5 mgL^{-1} (55 ± 10 %). When $ZnCl_2$ was added into the DMEM solution, Figure 6.4 (c) the dialysis cell equilibrium reached after 7 hours was 11 ± 0.2 mgL^{-1} (22 ± 0.4 %). This experimental time course was 32 hours, but the 22 and 32 hour time points have be excluded for the same temperature control reasons stated previously. In the DMEM salts solution, Figure 6.4 (d) it appears to show that little soluble zinc was able to be detected across the dialysis membrane, with a zinc concentration of 1.5 ± 0.4 mgL^{-1} (3 ± 0.8 %) present.

6.3.2 Zinc Oxide Nanoparticle Dialysis and Syringe Filter Dissolution

The dissolution of ZnO nanoparticles (50 mgL^{-1}) was measured in all four test media, measuring the Zn^{2+} concentration using the two filtration techniques: syringe filtering in the tank, Figure 6.5 and dialysis cell samples, Figure 6.6 over a 72 hour period.

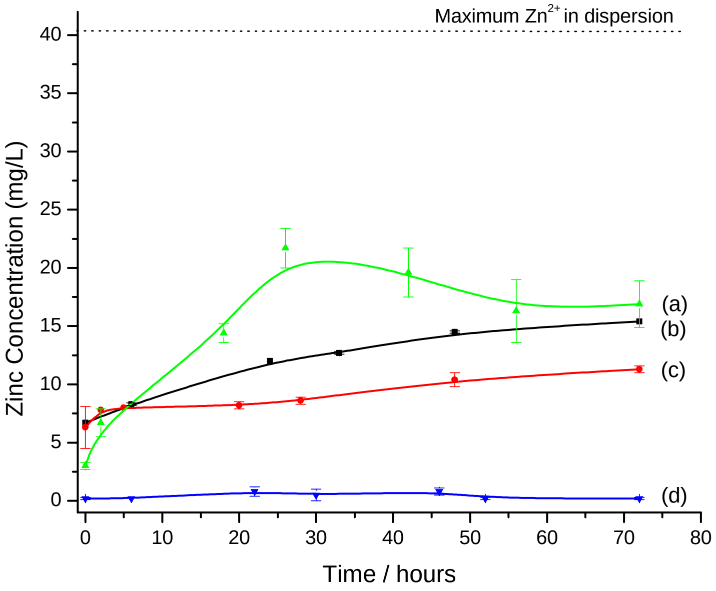

Figure 6.5 Dissolution of Nanosun ZnO nanoparticles (50 mgL^{-1}) using syringe-filtration over time, in (a) FBS (10 %) in deionised water, (b) deionised water (c) DMEM and (d) DMEM salts. The dotted line shows the maximum expected Zn^{2+} levels based on complete dissolution of the 50 mg of nanoparticles.

The tank-syringe filtered results for the Nanosun ZnO nanoparticles in FBS, Figure 6.5 (a) shows an initial rise in the Zn^{2+} ions as the particles dissolve, reaching a maximum value of 22 ± 2 mgL^{-1} (54 ± 4 %) after 26 hours, decreasing down to 17 ± 2 mgL^{-1} (42 ± 5 %) after 72 hours. In deionised water the nanoparticles dissolve steadily over time, Figure 6.5 (b), increasing the Zn^{2+} concentration in the syringe filtered samples up to 15.4 ± 0.1 mgL^{-1} (38.4 ± 0.2 %). The nanoparticles in DMEM dissolve at a slower rate than in both deionised water and FBS, reaching a Zn^{2+} concentration in the syringe filtered samples over 72 hours, of 11.3 ± 0.3 mgL^{-1}

(28.1 ± 0.8 %), Figure 6.5 (c), whilst in the DMEM salts solution there is minimal Zn^{2+} in solution, reaching a high of 0.8 ± 0.3 mgL^{-1} (1.9 ± 0.8 %) after 46 hours, Figure 6.5 (d).

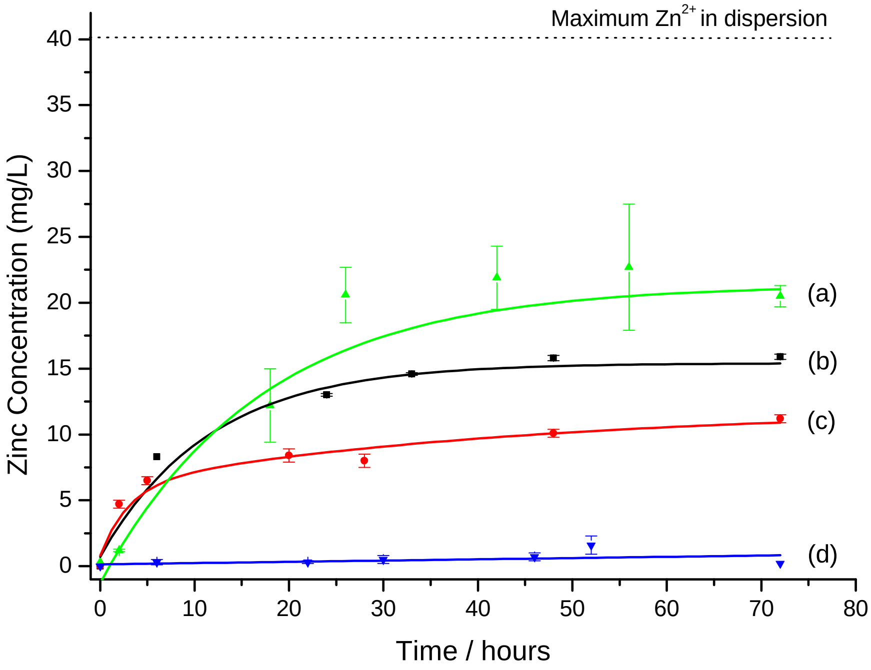

Figure 6.6 Dissolution of Nanosun ZnO nanoparticles (50 mgL^{-1}) across the dialysis membrane over time, in (a) FBS (10 %) in deionised water, (b) deionised water, (c) DMEM and (d) DMEM salts. The dotted line shows the maximum expected Zn^{2+} levels based on complete dissolution of the 50 mg of nanoparticles.

The dialysis results from the ZnO nanoparticles, Figure 6.6 occurred at a significantly slower rate than $ZnCl_2$, Figure 6.4, with the nanoparticles taking time to dissolve, perhaps not having reached a maximum after 72 hours. The medium which displayed the largest Zn^{2+} ion concentration in the dialysis cells was the FBS, Figure 6.6 (a) which showed a maximum concentration of 23 ± 5 mgL^{-1} (57 ± 12 %) after 56 hours. The nanoparticles in the deionised water, Figure 6.6 (b) reached a dialysis cell concentration level of 15.9 ± 0.2 mgL^{-1} (39.6 ± 0.5 %) showing an initial rapid dissolution process, slowing over time. The dissolution of nanoparticles in DMEM, Figure 6.6 (c) appears to be initially fast, steadily rising to a value of 11.2 ± 0.3 mgL^{-1} (27.9 ± 0.7 %). Again in the presence of the DMEM salts solution, Figure 6.6 (d) it appears to show minimal evidence of dissolution, with a Zn^{2+} concentration of 1.6 ± 0.7 mgL^{-1} (4 ± 2 %). All of the tank-syringe filtered and dissolution data are collected in Table 6.1

Table 6.1 6.1 Maximum Zn^{2+} concentrations obtained for $ZnCl_2$ and ZnO in both the Tank-syringe filtered samples and the dialysis cells

Media	$ZnCl_2$				ZnO			
	Tank-Syringe Filtered samples		Dialysis cell samples		Tank-Syringe Filtered samples		Dialysis cell samples	
	Zinc Concentration mgL^{-1}	% Recovery	Zinc Concentration mgL^{-1}	% Recovery	Zinc Concentration mgL^{-1}	% Recovery	Zinc Concentration mgL^{-1}	% Recovery
Deionised water	49 ± 1	98 ± 2	45.7 ± 0.3	91.4 ± 0.6	15.4 ± 0.1	38.4 ± 0.2	15.9 ± 0.2	39.6 ± 0.5
FBS	32 ± 3	64 ± 7	28 ± 5	55 ± 10	17 ± 2	42 ± 5	23 ± 5	57 ± 12
DMEM	11.5 ± 0.1	23 ± 0.2	11 ± 0.2	22 ± 0.4	11.3 ± 0.3	28.1 ± 0.8	11.2 ± 0.3	27.9 ± 0.7
DMEM salts solution	2 ± 2	4 ± 9	1.5 ± 0.4	3 ± 0.8	0.8 ± 0.3	1.9 ± 0.8	1.6 ± 0.7	4 ± 2

6.3.3 ZnO Nanoparticle Dissolution determined using the DCPIP Photo-radical Assay

The dissolution measurement data in the previous study required the use of techniques to separate the Zn^{2+} from the nanoparticles. The converse dissolution measurement is to measure the decrease in the concentration of the ZnO nanoparticles present. This requires a species-specific assay such as the DCPIP assay developed in Chapter 5. The photo-reduction of DCPIP by Nanosun ZnO (100 mgL^{-1}) was monitored over time. At eight time points over a ten-day period sample aliquots were removed from suspension. Each sample aliquot was monitored under UV light, observing the ΔExt at 595 nm of the suspension over an 80 minute period in both the dark and under UV light. The Dark controls were subtracted from the UV exposed data, and the absorbance change normalised to 1 at $t = 0$, Figure 6.7 (A). The DCPIP extinction change is plotted as ∆Ext (595) after 80 minutes, and fitted with an exponential function, Figure 6.7 (B) showing the suspension capacity to reduce DCPIP when exposed to UV light decreasing over time.

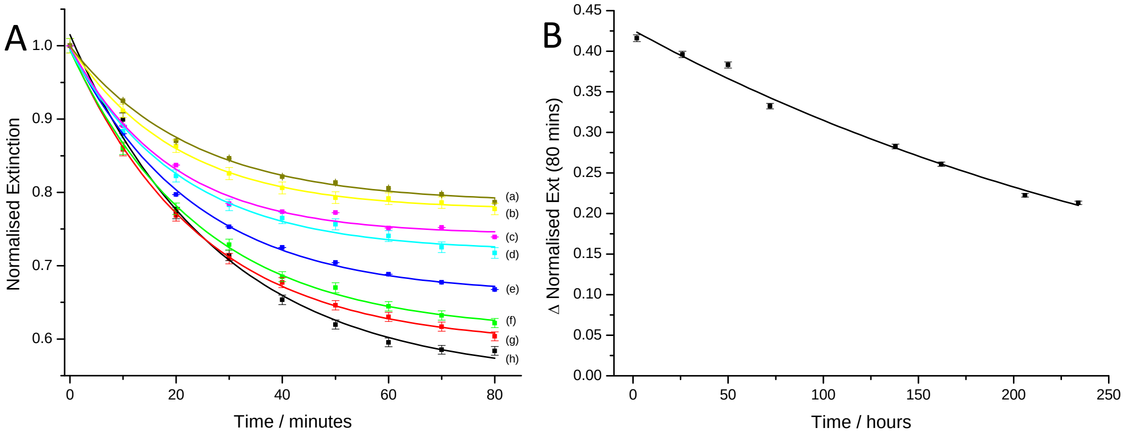

Figure 6.7 A - normalised extinction of Nanosun ZnO (100 mgL^{-1}) nanoparticles, showing the reduction of DCPIP over 80 minutes during a 10 day time course, at (a) 234 hours, (b) 206 hours, (c) 162 hours, (d) 138 hours, (e) 72 hours, (f) 50 hours, (g) 26 hours and (h) 2 hours, and B – ΔExt (595 nm) after 80 minutes over the 10 day time course. The exponential decay fit indicates a $t_{1/2}$ of the nanoparticles in the dispersion of 228 ± 22 hours, with an $R^2 = 0.988$

Finally, the rate of dissolution of ZnO nanoparticles in soil samples was measured using the DCPIP radical reduction assay. Nanosun ZnO nanoparticles (10 mgg^{-1}) were dispersed in a soil mixture over a period of 10 weeks. 1 g samples were taken in triplicate randomly throughout the soil mixture, sonicated, filtered and suspended in deionised water with DCPIP (50 µM), according to the protocol in Section 6.2. After an 80 minute irradiation with UV light, ΔExt at 595 nm measurements were plotted for each of the samples over a period of 10 weeks, with percentage recovery control spikes also shown,

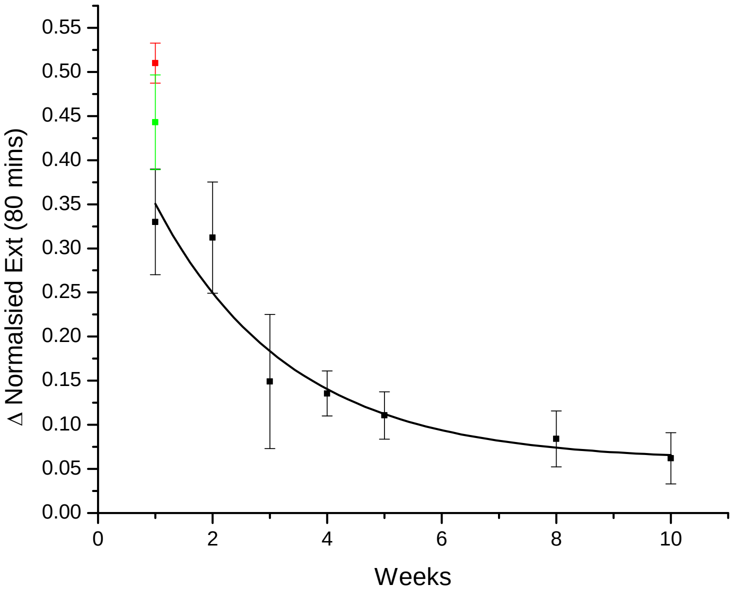

Figure 6.8 ΔExt at 595 nm for DCPIP with Nanosun ZnO dispersed in soil exposed to UV light over 80 minutes, plotted over the time course. The ZnO nanoparticle recovery controls are shown at *t* = 0, in deionised water (Red), and a soil / deionised water suspension (Green). The exponential decay fit indicates a nanoparticle half-life of 508 ± 20 hours with an R^2 = 0.946

The sampling is limited by the homogeneous dispersion of nanoparticles in the soil and reproducibility in sampling. Once the nanoparticles have been mixed into the soil, the organic components will attach to the nanoparticle surfaces, meaning that preparation of the sample for suspension is complicated. The samples were sonicated to break up the large nanoparticle / soil complexes and filtered to remove the large soil particles. The recovery controls indicate only a 65 ± 9 % ZnO nanoparticle recovery at $t = 0$, with a 13 ± 8 % shadowing effect attributed to the soil Figure 6.8. This low recovery figure is indicative of the fact that the nanoparticles will immediately form complex organic structures with the soil making the nanoparticles unavailable to UV light, as well as nanoparticle clustering in the sample.

6.4 Discussion

The dissolution of ZnO nanoparticles has been extensively studied as a toxicity mechanism (*6, 34*) with nanoparticle inhalation or ingestion followed by the dissolution of the nanoparticles to deliver potentially high local concentrations of Zn^{2+} next to a cell membrane. The oral LD_{50} value for zinc is 3 gkg^{-1} body weight, calculated from a sulphate salts exposure (*22, 24*), typically 279 g for an average person which is an unlikely load from any cosmetic or commercial nanotechnology application. Locally however, this concentration may be exceeded close to a cell membrane or in a specific organ from nanoparticle dissolution, giving rise to localised nanoparticle-specific Zn^{2+} toxicity. In humans, Zn^{2+} is an essential metal cofactor forming many enzymes (*24*), and is heavily regulated with both import and export processes present within cells (*24*) to maintain cellular concentrations. When these processes become saturated then the levels of Zn^{2+} may build up in the cells and lead to redox stress.

Before reaching the body however, ZnO nanoparticles may dissolve in the water column at a rate that depends on the pH, composition and ionic strength of the local medium. Importantly for this thesis, dissolution will also depend on the structure of the nano-environmental interface. Highly charged surfaces can attract counter -ions resulting in an interfacial pH that may be two orders of magnitude larger than in the bulk and consequentially modify the rate of dissolution. Furthermore, the solubility of Zn^{2+} in a collection of counter-ion salts may result in rapid precipitation or co-precipitation from the water column rendering the dissolving nanoparticle harmless. Nanoparticle dissolution rates and the influence on toxicity has previously been studied (*6, 16, 34*), and here nanoparticle dissolution will be extended to the influence of complex media on the dissolution rate observed. Dissolution will be measured from the total Zn^{2+} concentration through ICP-AES and conversely measuring the nanoparticles themselves using the ZnO nanoparticle specific DCPIP assay.

6.4.1 $ZnCl_2$ and ZnO nanoparticle Tank-syringe Filtration Analysis

One method for measuring nanoparticle dissolution is the separation of the nanoparticles from Zn^{2+} ions using tank-syringe filtration, followed by ultra-sensitive detection of total Zn^{2+} by ICP-AES. The experimental controls using the tank-syringe filtration technique for Zn^{2+} detection from $ZnCl_{2,}$ Figure 6.3, indicated a decrease in Zn^{2+} recovery efficiency in the more complex media. For 100 % efficiency, a molar concentration of 614 µM of Zn^{2+} could be expected. In deionised water the concentration observed after 32 hours was 600 ± 12 µM. This decreased to 394 ± 28 µM in FBS and 88 ± 2 µM in DMEM. In the DMEM salts solution, the concentration observed was 25 ± 5 µM, 4% of the initial Zn^{+} concentration. The likely cause of the concentration deficits may be attributed to the surface adsorption capacity of the proteins and amino acids in the media, as well as adsorption onto the membrane of the dialysis cells and the tank walls.

The ZnO nanoparticle dissolution measurements collected from the tank-syringe filtration, Figure 6.5 can be corrected for the removed Zn^{2+} capacity. In all four media the capacity observed in the $ZnCl_2$ is assumed to be constant for the ZnO dissolution exposure. In deionised water, correction for capacity gives a concentration of 204 ± 5 µM Zn^{2+} collected from the tank after 72 hours from which a dissolution half-life of 87 ± 2 hours is derived, Table 6.2. This concentration is comparable with previous results collected by Franklin *et al.* (*16*), measured over the same time period, which displayed an estimated half-life of 80 ± 30 hours, for ZnO ($100 mgL^{-1}$) nanoparticles. An alternative method using centrifugation, observing dissolution of 4 nm ZnO nanoparticle, demonstrated a dissolution half-life of 210 ± 50 hours (*6*).

The FBS medium was used to consider the effect of a protein corona (*35*) on the dissolution rate and has a pH of 7.25, marginally higher than deionised water, and an ionic strength of 161 mM (*36*). The capacity corrected Zn^{2+} concentration in FBS is 427 ± 47 µM after 72 hours, and gives a half-life of 41 ± 5 hours compared to 87 ± 2 hours in deionised water, Table 6.2. Dissolution of ZnO nanoparticles in the cell culture medium, DMEM, has also been observed. DMEM consists of a high concentration of amino acids and salts as well as glucose and vitamins, and has a pH of 7.6 and an ionic strength of 166 mM (*37*). Correcting for the reduced capacity effect, the observed concentration of Zn^{2+} after 72 hours in the DMEM was 664 ± 54 µM, which gave an estimated half-life of 27 ± 3 hours, Table 6.2. This half-life is 3.2 times shorter than in deionised water.

The results demonstrate an increase in dissolution rate for ZnO nanoparticles in FBS and DMEM compared to deionised water. A change in pH has previously demonstrated to increase the rate of dissolution of nanoparticles (*10*), however here, the pH of all three suspensions is ~pH 7. The enhanced dissolution of ZnO nanoparticles in the presence of biological components such as amino acids and proteins has previously been observed (*34, 38*). The increased dissolution was attributed to the ability of the proteins to improve the separation of nanoparticles, preventing large nanoparticle aggregates forming (*39*), with Xia *et al*. observing a decrease in aggregate size from 413 nm in water, down to 36 nm in DMEM. The increased mono-dispersion of nanoparticles will increase the nanoparticle mass to surface area, resulting in faster dissolution compared to the larger aggregates (*6*), with the organic complexes enhancing the dissolution process.

To observe the influence of salts on the rate of dissolution with no proteins present, the ZnO nanoparticles were dispersed in a solution containing various salts including Magnesium Chloride, Sodium Bicarbonate, Sodium Phosphate and Sodium Chloride. This solution had an ionic strength of 324 mM, higher than in both the FBS and DMEM. The total Zn^{2+} observed over time was very low, resulting in a large capacity corrected concentration of 609 ± 122 µM, giving a half-life of 29 ± 8 hours, Table 6.2. The low total Zn^{2+} capacity observed can be attributed to aggregation and precipitation driven by the high ionic strength of the solution. (*9, 40*) This aggregation does not account for the almost complete reduction in Zn^{2+} observed however, as the large aggregates will still dissolve, releasing ions with a longer half-life. However, the concentration of ions remains very low over long hours indicating perhaps the dissolution is stopped by a surface modification. One such candidate for surface passivation chemistry comes from the interaction with phosphate producing a zinc phosphate corona which has a very low K_{sp} of 9×10^{-33} (*41*). To confirm this hypothesis, further work needs to be carried out, with the individual phosphate salts to monitor the release of Zn^{2+} in suspension. If the salts demonstrate Zn^{2+} ion quenching in suspension, then simple layers around the nanoparticles in the production process will allow for the Zn^{2+} toxicity mechanism to be prevented in suspension.

6.4.2 $ZnCl_2$ and ZnO nanoparticle Dialysis Filtration Analysis

Similar dissolution measurements have been made with the dialysis membrane which has a nominal pore size of 1 nm, compared with the tank-syringe filter cut-off of 100 nm. The 100 nm filter in the tank syringe sampling allows larger particles to pass through the membrane which are only partially dissolved but contribute to the total zinc measurement; this will be significantly smaller for the dialysis membrane. In the $ZnCl_2$ dialysis experiments, the Zn^{2+} concentration reached equilibrium after 7 hours with a similar adsorption capacity compared with the tank-syringe method. Correcting the measured Zn^{2+} concentrations for the capacity gives half-life determinations of 69 ± 2 hours in deionised water, 34 ± 7 hours in FBS, 29 ± 1 hours in DMEM, and 28 ± 6 hours in DMEM salts, Table 6.2.

The dialysis cell half-life values are comparable with the syringe filtration, although the half-life in the dialysis cells is shorter, in particular for the deionised water. This may be a feature of the nanoparticle aggregation on the dialysis membrane on and around the dialysis pores, giving an enhanced concentration around the dialysis cells compared to in the tank suspension. From the dialysis cell walls the nanoparticles may then dissolve and pass through the membrane.

Although the filtration technique has a significantly larger pore size, it does not appear to have overestimated the dissolution compared to the dialysis concentrations, indicating that the nanoparticles in suspension consist of quite large aggregates. Both of these techniques may still allow small nanoparticles to pass through the pore filters, leading to enhanced Zn^{2+} concentrations, and faster dissolution rates using ICP-AES. To prevent this, an alternative way to measure the rate of nanoparticle dissolution is to monitor the decrease in particles, instead of an increase in Zn^{2+} ions. This can be achieved by using a species specific assay.

Table 6.2 Dissolution half-life times in different media using tank syringe filtration, dialysis and DCPIP reduction assay

Suspension Medium	**Tank Syringe Half-life / hours**	**Dialysis Half-life / hours**	**DCPIP Assay Half-life / hours**
Deionised water	87 ± 2	69 ± 2	229 ± 37
FBS	41 ± 5	34 ± 7	
DMEM	27 ± 3	29 ± 1	
DMEM Salts	29 ± 8	28 ± 6	
Soil			580 ± 20

6.4.3 DCPIP Photo-radical Assay monitoring Nanoparticle Dissolution in suspension over time

The nanoparticle photo-radical generation is a direct nanoparticle property, meaning the DCPIP assay can be used to monitor the rate of nanoparticle dissolution in solution over time, the disappearance of the nanoparticle compared to the arrival of the Zn^{2+} ion in solution. The ΔExt (595 nm) after 80 minutes plotted against the 10-day time course, Figure 6.7 (B) displayed a decreasing trend over time. The data were fitted with an exponential decay, from which the half-life can be estimated. The fit indicated that the half-life derived from the radical reduction was 229 ± 37 hours, Table 6.2. This half-life estimation appears to be 3 times larger than the measure of dissolved Zn^{2+}. This is because the photo-radical reduction will not vary rapidly with nanoparticle diameter, with the nanoparticles still having the ability to reduce the DCPIP as they dissolve, and the photo-electron production rate falling rapidly only when the nanoparticle becomes very small. It should also be noted that the results are not directly comparable as the nanoparticles used in this experiment were 200 ± 5 nm in diameter, compared to the 30 ± 5 nm particles used in the dialysis and syringe filtered experiments. These larger particles will take longer to dissolve (*6*), resulting in an increased half-life observed.

The nanoparticle half-life can be estimated from a second method, observing the initial rate of DCPIP reduction over time, Figure 6.9. Early time points display minimal variation in reduction rate, postulated to be the initial dissolution of the rough particle edges, with the fast rate decreasing at latter time points attributed to complete particle dissolution, and a larger discrepancy in particle size.

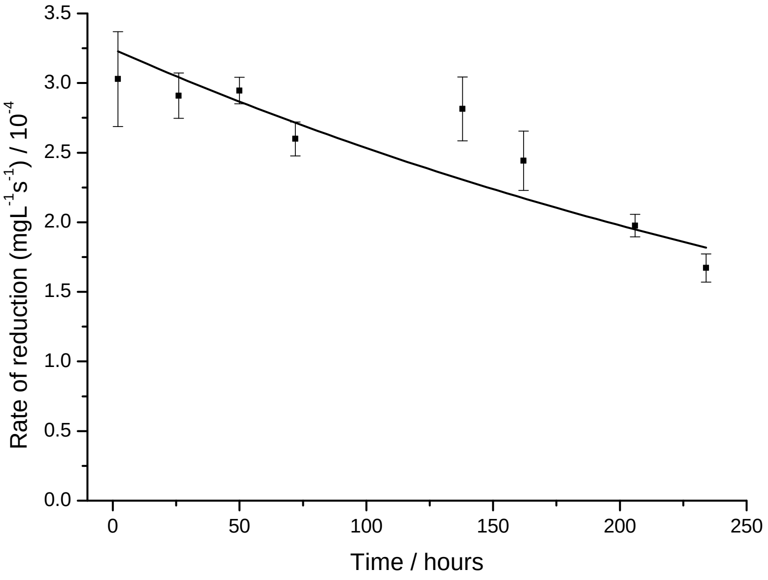

Figure 6.9 The initial-rate analysis of DCPIP reduction as a function of time for a Nanosun ZnO suspension. The fit gives an estimated half-life of 280 ± 26 hours with an R^2 value of 0.912

The exponential fit parameters gave a comparable half-life within the error, of nanoparticle radical production of 280 ± 16 hours, compared to 229 ± 37 hours for ΔExt (595 nm). The fit accuracy of 0.912 is lower compared to 0.988 for ΔExt (595 nm), attributed to the complex change in rate. The rate analysis gives a more exact measurement of nanoparticle dissolution in suspension, as the measurements are derived from a larger number of data points over an 80 minute exposure.

The nanoparticle dissolution half-life parameters have so far only been assessed in suspension. Nanoparticles mixed in sediment and soils will still dissolve, at a rate dependent on the inorganic and organic surface layers around them and the water content available in their local environment. In the sample used here the soil has a maximum water holding capacity (WHC) determined as 766 $mLkg^{-1}$, dry weight, 76.6% v/w (*33*). The dissolution half-life $t_{1/2}$ of the nanoparticles in the soil sample was calculated as 580 ± 20 hours, Table 6.2. This half-life is twice as long as the nanoparticle dissolution measured using the DCPIP assay in deionised water. The particles dissolve slowly in soil because of the low water content which will become rapidly saturated, while stable organic coronae may also form around the particles preventing the release of Zn^{2+}.

6.5 Conclusions

The nanoparticle dissolution mechanism for ZnO nanoparticles was investigated as a function of medium composition from simple DDI water to more complex cell growth media such as FBS and DMEM. For both the tank-syringe filtered and dialysis techniques, the half-life measurements are in good agreement, but give much shorter half-lives compared to the DCPIP assay. Measuring the decrease in nanoparticles present in suspension generates longer half-life times with particles able to decrease in size without completely dissolving, maintaining their specific nanoparticle properties. Measuring the photo-radical yield over time is arguably a more reliable technique as it measures direct speciation of the nanoparticles in suspension, and it is reasonable to extend this assay to more complex media. The significance of these half-life parameters on the ecotoxicology of the nanoparticles is that the nanoparticles are likely to rapidly sediment out of the water column, where the dissolution mechanism of toxicity will be significantly reduced. Dissolution at membrane surfaces may also be slow and there is the possibility of zinc phosphate formation to completely stabilise the particle, meaning the ZnO dissolution is likely to be a fairly slow process and therefore not a significant toxic mechanism of nanoecotoxicology.

References

1. Tombacz, E. (2009) pH-dependent surface charging of metal oxides, *Periodica Polytechnica, Chemical Engineering 52*, 77-86.
2. Borm, P, Klaessig, F C, Landry, T D, Moudgil, B, Pauluhn, J r, Thomas, K, Trottier, R, and Wood, S. (2006) Research Strategies for Safety Evaluation of Nanomaterials, Part V: Role of Dissolution in Biological Fate and Effects of Nanoscale Particles, *Toxicological Sciences 90*, 23-32.
3. Tang, R, Orme, C A, and Nancollas, G H. (2004) Dissolution of crystallites: surface energetic control and size effects, *Chemphyschem : a European journal of chemical physics and physical chemistry 5*, 688-696.
4. Yang, Z, and Xie, C. (2006) Zn2+ release from zinc and zinc oxide particles in simulated uterine solution, *Colloids and Surfaces B: Biointerfaces 47*, 140-145.
5. Auffan, M, Rose, J, Bottero, J-Y, Lowry, G V, Jolivet, J-P, and Wiesner, M R. (2009) Towards a definition of inorganic nanoparticles from an environmental, health and safety perspective, *Nat Nano 4*, 634-641.
6. Bian, S-W, Mudunkotuwa, I A, Rupasinghe, T, and Grassian, V H. (2011) Aggregation and Dissolution of 4 nm ZnO Nanoparticles in Aqueous Environments: Influence of pH, Ionic Strength, Size, and Adsorption of Humic Acid, *Langmuir 27*, 6059-6068.
7. Dennis, J L, Mutwakil, M H A Z, Lowe, K C, and de Pomerai, D I. (1997) Effects of metal ions in combination with a non-ionic surfactant on stress responses in a transgenic nematode, *Aquatic Toxicology 40*, 37-50.
8. Tinke, A P, Vanhoutte, K, De Maesschalck, R, Verheyen, S, and De Winter, H. (2005) A new approach in the prediction of the dissolution behavior of suspended particles by means of their particle size distribution, *Journal of Pharmaceutical and Biomedical Analysis 39*, 900-907.
9. Lok, C-N, Ho, C-M, Chen, R, He, Q-Y, Yu, W-Y, Sun, H, Tam, P, Chiu, J-F, and Che, C-M. (2007) Silver nanoparticles: partial oxidation and antibacterial activities, *Journal of Biological Inorganic Chemistry 12*, 527-534.

10. Agren, M S. (1990) Percutaneous absorption of zinc from zinc oxide applied topically to intact skin in man, *Dermatologica 180*, 36-39.
11. Strumm, and Morgan (1995) *Chemical Equilibria and Rates in Natural Waters*, Vol. 3rd edition, Wiley-Interscience, New York.
12. Gupta, S, Kumar, P, Chakkaravathi, A A, Craciun, D, and Singh, R K. Investigation of chemical mechanical polishing of zinc oxide thin films, *Applied Surface Science 257*, 5837-5843.
13. Degen, A, and Kosec, M. (2000) Effect of pH and impurities on the surface charge of zinc oxide in aqueous solution, *Journal of the European Ceramic Society 20*, 667-673.
14. Neal, A L, Kabengi, N, Grider, A, and Bertsch, P M. Can the soil bacterium Cupriavidus necator sense ZnO nanomaterials and aqueous Zn2+ differentially?, *Nanotoxicology 0*, 1-10.
15. Ji, J, Long, Z, and Lin, D. Toxicity of oxide nanoparticles to the green algae Chlorella sp, *Chemical Engineering Journal 170*, 525-530.
16. Franklin, N M, Rogers, N J, Apte, S C, Batley, G E, Gadd, G E, and Casey, P S. (2007) Comparative Toxicity of Nanoparticulate ZnO, Bulk ZnO, and ZnCl2 to a Freshwater Microalga (Pseudokirchneriella subcapitata): The Importance of Particle Solubility, *Environmental Science & Technology 41*, 8484-8490.
17. Lin, D, and Xing, B. (2007) Phytotoxicity of nanoparticles: Inhibition of seed germination and root growth, *Environmental Pollution 150*, 243-250.
18. Lin, D, and Xing, B. (2008) Root Uptake and Phytotoxicity of ZnO Nanoparticles, *Environmental Science & Technology 42*, 5580-5585.
19. Vallee, B L, and Falchuk, K H. (1993) The biochemical basis of zinc physiology, *Physiological Reviews 73*, 79-118.
20. Wastney, M E, Aamodt, R L, Rumble, W F, and Henkin, R I. (1986) Kinetic analysis of zinc metabolism and its regulation in normal humans, *American Journal of Physiology - Regulatory, Integrative and Comparative Physiology 251*, R398-R408.

21. (2009) Health Professional Fact Sheet, (Health, N. I. o., Ed.), Office of Dietary Supplements.

22. (ATSDR), A f T S a D R, (Ed.) (2005) *Toxicological profile for Zinc*, U.S. Department of Health and Human Services, Public Health Service, Atlanta, GA.

23. Porea, T J, Belmont, J W, and Mahoney, J D H. (2000) Zinc-induced anemia and neutropenia in an adolescent, *The Journal of pediatrics 136*, 688-690.

24. Plum, L M, Rink, L, and Haase, H. (2010) The Essential Toxin: Impact of Zinc on Human Health, *International Journal of Environmental Research and Public Health 7*, 1342-1365.

25. Sadrieh, N, Wokovich, A M, Gopee, N V, Zheng, J, Haines, D, Parmiter, D, Siitonen, P H, Cozart, C R, Patri, A K, McNeil, S E, Howard, P C, Doub, W H, and Buhse, L F. (2010) Lack of Significant Dermal Penetration of Titanium Dioxide from Sunscreen Formulations Containing Nano- and Submicron-Size TiO2 Particles, *Toxicological Sciences 115*, 156-166.

26. Monteiro-Riviere, N A, Wiench, K, Landsiedel, R, Schulte, S, Inman, A O, and Riviere, J E. (2011) Safety Evaluation of Sunscreen Formulations Containing Titanium Dioxide and Zinc Oxide Nanoparticles in UVB Sunburned Skin: An In Vitro and In Vivo Study, *Toxicological Sciences 123*, 264-280.

27. Song, Z, Kelf, T A, Sanchez, W H, Roberts, M S, Rika, J, Frenz, M, and Zvyagin, A V. (2011) Characterization of optical properties of ZnO nanoparticles for quantitative imaging of transdermal transport, *Biomed. Opt. Express 2*, 3321-3333.

28. Larner, F, and Rehkamper, M. Evaluation of Stable Isotope Tracing for ZnO Nanomaterials: New Constraints from High Precision Isotope Analyses and Modeling, *Environmental Science & Technology 46*, 4149-4158.

29. Gulson, B, McCall, M, Korsch, M, Gomez, L, Casey, P, Oytam, Y, Taylor, A, McCulloch, M, Trotter, J, Kinsley, L, and Greenoak, G. (2010) Small Amounts of Zinc from Zinc Oxide Particles in Sunscreens Applied Outdoors Are Absorbed through Human Skin, *Toxicological Sciences 118*, 140-149.

30. Lundqvist, M, Stigler, J, Elia, G, Lynch, I, Cedervall, T, and Dawson, K A. (2008) Nanoparticle size and surface properties determine the protein corona with possible implications for biological impacts, *Proceedings of the National Academy of Sciences 105*, 14265-14270.

31. Miao, A-J, Zhang, X-Y, Luo, Z, Chen, C-S, Chin, W-C, Santschi, P H, and Quigg, A. Zinc oxide–engineered nanoparticles: Dissolution and toxicity to marine phytoplankton, *Environmental Toxicology and Chemistry 29*, 2814-2822.

32. Thomas, R (2004) *Practical guide to ICP-MS*, Vol. , Marcel Dekker.

33. Svendsen, C. (2010) OECD Soil. Ecotoxicologist, Centre for Ecology & Hydrology, Maclean Building, Benson Lane, Crowmarsh Gifford, Wallingford, Oxfordshire, OX10 8BB.

34. Xia, T, Kovochich, M, Liong, M, Madler, L, Gilbert, B, Shi, H, Yeh, J I, Zink, J I, and Nel, A E. (2008) Comparison of the Mechanism of Toxicity of Zinc Oxide and Cerium Oxide Nanoparticles Based on Dissolution and Oxidative Stress Properties, *ACS Nano 2*, 2121-2134.

35. Lynch, I, and Dawson, K A. (2008) Protein-nanoparticle interactions, *Nano Today 3*, 40-47.

36. Altunbas, A, Lee, S J, Rajasekaran, S A, Schneider, J P, and Pochan, D J. (2011) Encapsulation of curcumin in self-assembling peptide hydrogels as injectable drug delivery vehicles, *Biomaterials 32*, 5906-5914.

37. Toppazzini, M, Coslovi, A, Boschelle, M, Marsich, E, Benincasa, M, Gennaro, R, and Paoletti, S. (2011) Can the interaction between the antimicrobial peptide LL-37 and alginate be exploited for the formulation of new biomaterials with antimicrobial properties?, *Carbohydrate Polymers 83*, 578-585.

38. Moreau, J W, Weber, P K, Martin, M C, Gilbert, B, Hutcheon, I D, and Banfield, J F. (2007) Extracellular Proteins Limit the Dispersal of Biogenic Nanoparticles, *Science 316*, 1600-1603.

39. Sager, T M, Porter, D W, Robinson, V A, Lindsley, W G, Schwegler-Berry, D E, and Castranova, V. (2007) Improved method to disperse nanoparticles for in vitro and in vivo investigation of toxicity, *Nanotoxicology 1*, 118-129.

40. French, R A, Jacobson, A R, Kim, B, Isley, S L, Penn, R L, and Baveye, P C. (2009) Influence of Ionic Strength, pH, and Cation Valence on Aggregation Kinetics of Titanium Dioxide Nanoparticles, *Environmental Science & Technology 43*, 1354-1359.

41. Heung, W F, Yang, Y P, Zhou, M Y, Wong, P C, Mitchell, K A R, and Foster, T. (1994) X-ray photoelectron spectroscopy and corrosion studies of zinc phosphate coated on 7075-T6 aluminium alloy, *Journal of Materials Science 29*, 3653-3657.

Chapter 7
Conclusions and Further work

7.1 Conclusions

The extraordinary rise of nanotechnology in industry, particularly cosmetics (*1-3*), brings with it an associated increase in the mass of nanoparticles released into the environment. Limited data and fear of enhanced reactivity and bio-availability of nanoparticles has led to a presumption of high risk on release into the environment (*4*). This thesis aimed to determine the nanoparticle fate in the environment through characterisation of the molecular interactions at the interface in complex environmental suspensions. By understanding the nanoparticle interface, direct assumptions on nanoecotoxicology can be determined, allowing specific and relevant risk assessment.

Characterisation of the nano-environmental interface presents a significant challenge for physical and analytical chemists. Metal oxide nanoparticles in particular, and charged interfaces in general, are rather complex and yet are fundamental to understanding the dispersion stability and subsequent chemistry. The interrogation of chromophore species on the model silica-water charged interface using EW-CRDS (*5-9*), led directly to the observation of the GCS layer formation and provided evidence of different molecular binding structures closest to the surface. These measurements were extended to include the formation of stable inorganic and organic layers co-deposited with the CV chromophore on the surface.

The EW-CRDS technique allowed for direct observation of nanoparticle adsorption and aggregation at a charged surface, representative of a soil surface found in the environment. Key nanoparticle characteristics were able to be established from the interface interaction, including the CeO_2 nanoparticle extinction coefficient of $8.5 \pm 1.4 \times 10^{10}$ M^{-1} cm^{-1}, and the nanoparticle surface charge density of 1.6 ± 0.3 e^- nm^{-2}.

The surface charge density is a unique property of the nanoparticle, which will remain constant regardless of the environment. Fundamental properties such as this are important and need to be established before particles can subsequently be related to test conditions, setting benchmark parameters for the nano-environmental risks. For standardised nanoparticle characterisation, a stable nanoparticle dispersion protocol has also been established, designed for homogeneous nanoparticle suspensions. The dispersion protocol can be used to test nanoparticle suspension parameters, and indicated a half-life in excess of 330 hours for a CeO_2 (100 mgL^{-1}) suspension. Having a set nanoparticle protocol is important for nanoparticle comparison work, and reproducibility of data.

Nanoparticle toxicity has been interrogated at the ZnO particle surface in different environments. Under UV light, the photo-electron production rate from Z-cote ZnO nanoparticles was quantified as 709 $e^{-}s^{-1}np^{-1}$ produced with a photo-electron yield of 19 ± 2%. The photo-electron production is a specific nanoparticle property, and enables nanoparticle speciation in complex suspensions, which can be related conversely to nanoparticle dissolution. The rate of dissolution has been measured in five different media, and the dissolution half-life has been established as a parameter for characterising dissolution rates across various test media and contrasting dissolution techniques. The environmental half-life of ZnO nanoparticles in our test media ranged from 29 hours in DMEM to 580 hours in soil, demonstrating the importance of the local environment on dissolution, and points to maximum exposure times of organisms to dissolved metal ion toxicity mechanisms. Further assays for direct speciation of nanoparticles in environmental samples are needed, measuring nanoparticles in suspension, instead of total zinc measurements in ICP-AES. Although the DCPIP assay developed in this work is one such nanoparticle-specific assay, it is unlikely that this will be suitable in more complex test media.

Other techniques have been used in this thesis, which do not aid in the understanding of the nanoparticle characterisation. The nanoparticle zeta potential as a characterisation technique is highly medium dependent. Derived from the

Smoluchowski equation (*10*), the drift velocity parameters become inaccurate in complex environments. DLS gives direct measurements of nanoparticle size in suspension, although it is highly biased towards large particles. The alternative techniques for determining nanoparticle size parameters in suspension are all based on imaging such as SEM and TEM, with the obvious problems of aggregated sample preparation, so the technique is predominantly used to establish sample shape. Future development should improve imaging techniques to enable observation of nanoparticles in the different complex suspensions directly without the need for sample collection or drying.

For accurate understanding of nanoparticles, characterisation of the surface independent of the environment is required, Figure 7.1 (A), as discussed previously. These properties may then be related to ecotoxicity work through specific *in vivo* assays on a genetic organism to determine their fate. A defined set of toxicity tests may be carried out, with system metabolic stress responses and other inflammation responses monitored. Key toxicity mechanisms that should be focussed on are the nanoparticle dissolution lifetimes and mass accumulation in organs, Figure 7.1 (B). Where nanoparticles have a short dissolution half-life such as ZnO, the nanoparticles will be removed from the systems after a matter of days. Contrastingly, CeO_2 nanoparticles will not dissolve, and may persist in the environment over a long period, subsequently leading to particle mass build up *in vivo*.

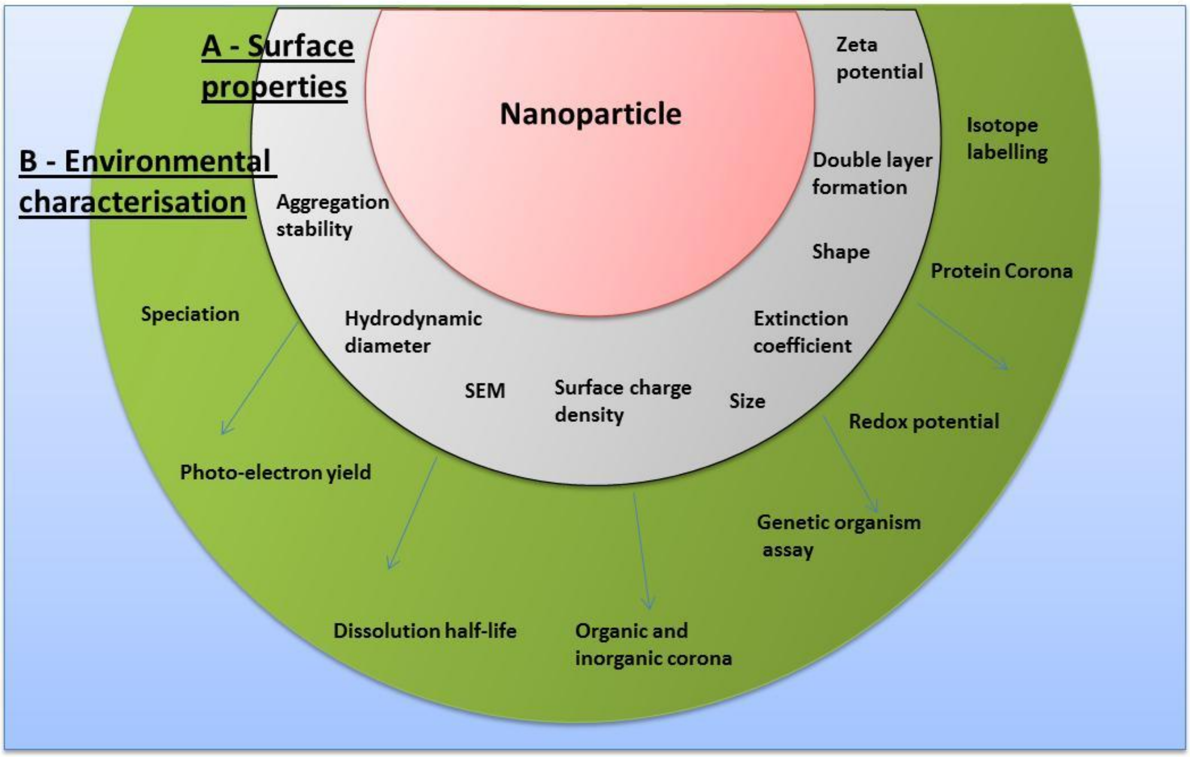

Figure 7.1 Key nanoparticle surface properties that will allow for subsequent characterisation of nanoecotoxicology.

On release into the environment nanoparticle surfaces will be covered with cosmetic ligands in ZnO, or soot particles in $CeO_{2.}$ These layers will prevent surface toxicity mechanisms, with further organic and inorganic shells likely to form around the nanoparticles. The nanoparticles will have a short life-time in the environment, aggregating into large clusters and sedimenting out of suspension or dissolving within a few days, with the long term exposure unlikely to be a relevant environmental issue. To establish the nanoparticle interaction and subsequent toxic dangers in the environment, the nanoparticle interface and surface properties need to be fully understood; only then, can the ecotoxic consequences be properly assessed.

7.2 Future work

The EW-CRDS measurements observing the co-formation of the CV and NaCl at the charged interface indicated that the Na^+ ions did not completely prevent the CV association at the surface, which might have been expected at high salt concentrations. This points towards unstable Na^+ interaction, with a low binding affinity. Future work will introduce more complex salts into the inorganic interface model, such as K^+, Cs^+ and Ca^{2+} to determine the stability of the different inorganic coronae formed. Full characterisation of the silica surface will also allow for neutralisation properties to be measured as a parameter for different nanoparticles. This can produce key interfacial charge characteristics for individual nanoparticles. Other developments using EW-CRDS will observe the $Ce^{4+/3+}$ redox properties measuring the half-cell interfacial properties. Previous work has combined an electrochemical cell intra cavity, observing the oxidation of Ferrocyanide, as a function of adsorption with charge reversal (*11*), and a similar experimental configuration may be possible, to observe the CeO_2 redox properties.

The dissolution half-life parameters for individual organic and inorganic constituents will be determined. Breaking the complex organic media down and observing the influence of BSA as a function of concentration on the rate of nanoparticle dissolution will determine the properties of the protein corona. Similarly, breaking the inorganic suspensions down, and monitoring dissolution rates with phosphate will establish the ability to form insoluble complexes. This will confirm the phosphate hypothesis and could lead to the quenching of toxic Zn^{2+} ions. Once the nanoparticle corona formation in understood in different environments, they can be introduced into organisms to monitor the change in toxicity potential, with a view to developing a standard set of test coronae for nanoparticles. Development of this shell around the nanoparticle could subsequently be incorporated into the manufacturing process, optimising the nanoparticle interface to prevent known toxicity mechanisms on release into the environment. This would however be limited by the specific nanoparticle characteristics required for that product.

At present, the number of techniques used to characterise nanoparticles is too large and gives inconsistent results between techniques. The characterisation should be reduced to a few important relevant parameters. By having a set of techniques which can directly assess the risk factor of the nanoparticles, the nanoecotoxicology can be understood, allowing for the future safe development of nanotechnology.

References

1. Ray, P C, Yu, H, and Fu, P P. (2009) Toxicity and Environmental Risks of Nanomaterials: Challenges and Future Needs, *Journal of Environmental Science and Health, Part C 27*, 1-35.
2. Nel, A, Xia, T, Madler, L, and Li, N. (2006) Toxic Potential of Materials at the Nanolevel, *Science 311*, 622-627.
3. Lux, R. (2009) Nanomaterials State of the Market QI, *Lux research Inc, New York*.
4. Bian, S-W, Mudunkotuwa, I A, Rupasinghe, T, and Grassian, V H. (2011) Aggregation and Dissolution of 4 nm ZnO Nanoparticles in Aqueous Environments: Influence of pH, Ionic Strength, Size, and Adsorption of Humic Acid, *Langmuir 27*, 6059-6068.
5. Fisk, J D, Batten, R, Jones, G, O'Reilly, P, and Shaw, A M. (2005) pH Dependence of the Crystal Violet Adsorption Isotherm at the Silica-Water Interface, *J. Phys. Chem. B 109*, 14475-14480.
6. Fisk, J D, Rooth, M, and Shaw, A M. (2007) Gold Nanoparticle Adsorption and Aggregation Kinetics at the Silica−Water Interface, *The Journal of Physical Chemistry C 111*, 2588-2594.
7. O'Reilly, J P, Butts, C P, I'Anso, I A, and Shaw, A M. (2005) Interfacial pH at an Isolated Silica Water Surface, *Journal of the American Chemical Society 127*, 1632-1633.
8. Rooth, M, and Shaw, A M. (2006) Interfacial pH and surface pKa of a thioctic acid self-assembled monolayer, *Physical Chemistry Chemical Physics 8*, 4741-4743.
9. Shaw, A M, Hannon, T E, Li, F, and Zare, R N. (2003) Adsorption of Crystal Violet to the Silica-Water Interface Monitored by Evanescent Wave Cavity Ring-Down Spectroscopy, *J. Phys. Chem. B*.
10. Sze, A, Erickson, D, Ren, L, and Li, D. (2003) Zeta-potential measurement using the Smoluchowski equation and the slope of the current time

relationship in electroosmotic flow, *Journal of Colloid and Interface Science 261*, 402-410.

11. Mazurenka, M, Wilkins, L, Macpherson, J V, Unwin, P R, and Mackenzie, S R. (2006) Evanescent Wave Cavity Ring-Down Spectroscopy in a Thin-Layer Electrochemical Cell, *Analytical Chemistry 78*, 6833-6839.